Acceleration and Stabilization Methods for Monte Carlo Reactor Core *k*-Eigenvalue Problems

by

Kendra P. Keady

A dissertation submitted in partial fulfillment
of the requirements for the degree of
Doctor of Philosophy
(Nuclear Engineering and Radiological Sciences)
in the University of Michigan
2016

Doctoral Committee:

Professor Edward W. Larsen, Chair
Assistant Professor Brian C. Kiedrowski
Professor William R. Martin
Professor John C. Schotland

"I almost wish I hadn't gone down that rabbit-hole –

and yet – and yet – it's rather curious, you know, this sort of life!"

–Lewis Carroll, Alice in Wonderland

For Umpop

ACKNOWLEDGMENTS

First and foremost, I owe enormous thanks to my advisor, Dr. Ed Larsen. Dr. Larsen, you're a veritable mathemagician – but perhaps more importantly, you're a kind, patient, thoroughly good human being. Working with you these past five years (ok, five and a *half*) has been a pleasure.

Thanks also to the rest of my committee, for your valuable insight and precious time. Professor/"Supreme Ruler" Brian gets points for making me laugh aloud on numerous occasions.

Mom and Dad, where do I even begin? You clothed me, fed me, loved me, and put up with me all the way through undergrad (a Herculean task, I suspect). Without your patient guidance, I wouldn't be where I am today. Special thanks for supporting me as I waffled from major to major in college. See? I finally found one that stuck! ☺

Thank you to my older brother, Rob, for being ridiculously intelligent and talented and an all-around good role model. You've always kept me on my toes, especially that one time you smashed my face into a pile of Legos.

Grams and Umpop, thank you for a lifetime of love and baked goods! Also, for telling all your friends that I "work at NASA." Boy, that makes me feel cool.

To the good people of 1928 Cooley – thanks for not exiling me when I tried to burn the office down with my chicken pot pie a few weeks ago. I'm sorry the microwave still smells funny.

Huge kudos to Jeff Weatherup and Ed Birdsall for springing into action when Chimichanga departed for the big electronics store in the sky (a mere two weeks before my dissertation was due). Between their heroic effort and the department's generous funding, I had a new laptop (Enchilada) in less than 48 hours.

Finally, a big thanks to anyone who is actually reading this! If you find a typo, look me up and I'll send you a dollar or a candy bar or something.

TABLE OF CONTENTS

Chapter

LIST OF FIGURES

LIST OF TABLES

ABSTRACT

Typical Monte Carlo (MC) reactor core k-eigenvalue simulations are large and complex, requiring many inactive cycles to converge the fission source. In a 2009 publication, a hybrid MC method was proposed in which the fission source convergence is "accelerated" at the end of each inactive MC cycle using the solution of a discrete low-order Coarse Mesh Finite-Difference (CMFD) equation. This method has been implemented in several codes, but is sometimes unstable. It was hypothesized that the instability was driven by statistical error in the MC-calculated CMFD correction factors. Two independent variants of the method were developed to address this issue, with mixed results.

In this work, we extend existing research on this CMFD-MC method and its variants. To delve deeper into the numerical stability issue, we perform a Fourier analysis on the "non-random" CMFD-MC iteration scheme (which assumes an infinite number of particles per cycle). Spectral radius results indicate that the CMFD-MC method becomes unstable for certain coarse-grid/scattering ratio combinations, even in the infinite-particle limit. Thus, it is unlikely that statistical error is the primary driver of CMFD-MC instability, though it appears that stochastic noise can drive a "barely-stable" simulation into the unstable regime.

While the CMFD-MC method is effective in accelerating fission source convergence during inactive cycles, it has no effect on the dominant source of

active cycle noise (i.e. the transport process itself). This motivates a second goal of our research: to modify the traditional iteration scheme in a way that makes more efficient use of stochastic information, while maintaining compatibility with CMFD feedback.

To this end, we investigate a new MC iteration strategy, in which particles are allowed to undergo a fixed maximum number of collisions per cycle. We call this the Limited-Collision Monte Carlo (LCMC) method. This particular strategy was chosen to significantly shorten the computation time per MC cycle; however, a Fourier analysis predicts (and numerical results support) that this iteration is less stable than CMFD-MC for a given coarse grid size when the number of permitted collisions per cycle is small. Thus, the LCMC source distribution may require a large number of cycles to reach adequate convergence for high dominance-ratio problems.

This observation led us to design and implement a new simulation procedure, which makes use of both the CMFD-MC and LCMC iterations. Our iteration scheme employs standard CMFD-MC during inactive cycles to efficiently converge the fission source, then transitions to the modified Limited-Collision Monte Carlo (LCMC) algorithm to improve the efficiency of active cycles.

By implementing this procedure, we show that it is possible to solve reactor core *k*-eigenvalue problems using two different MC algorithms; one that is designed to quickly and efficiently converge the fission source, and one that is designed to make more efficient use of stochastic information during active cycles. We refer to this simulation strategy as the “mixed” method (indicating a hybrid simulation, employing both the CMFD-MC and LCMC iteration schemes). Results for a large 1-D problem indicate a factor of 3-5 improvement in the solution Figure of Merit (FOM) over the current “state of the art”

method. Mixed method FOMs for the 2-D problems presented in this thesis are comparable to existing methods; however, we show that the mixed method may still provide a benefit when run with a sufficiently large number of particles per cycle.

CHAPTER 1

Introduction

1.1 Background

1.1.1 The Reactor Core *k*-Eigenvalue Problem

The steady-state reactor core *k*-eigenvalue problem involves the solution of a modified Boltzmann transport equation for the neutron angular flux as a function of space, angle, and energy. This angular flux solution is usually integrated over all angles to obtain the space and energy-dependent neutron scalar flux, which can be used to obtain reaction rates and power profiles throughout the reactor core.

Reactor core *k*-eigenvalue calculations are an important component of nuclear reactor design and analysis. The neutron flux solution obtained from a reactor core calculation can be used to characterize steady-state reactor operation, determine the effect of various accident scenarios on reactor power, and iteratively design new reactor cores for future construction. However, full-core calculations generally involve complicated space, angle, and energy dependence; as a result, these simulations are computationally expensive. In addition, a significant amount of nuclear data (in the form of cross sections) must be used to adequately describe energy-dependent neutron reactions in the core and surrounding material. These factors make the development of accurate, efficient full-core neutronics solvers a formidable task.

Existing full-core *k*-eigenvalue simulation methods can be classified in two broad categories. The first category, known as *Monte Carlo* methods, involves the random sampling and tallying of a large number of independent particles (commonly referred to as neutron "histories"). The second category, *deterministic* methods, discretizes the *k*-eigenvalue iteration equations in space, angle, and energy. We briefly describe each of these categories in the following sections, as well as their strengths and weaknesses with regard to the reactor core *k*-eigenvalue problem.

1.1.2 The Monte Carlo Method

The Monte Carlo method is a broad term for numerical algorithms that employ pseudorandom numbers to sample individual realizations of quantities from their governing distribution functions. The random sampling process is repeated a large number of times to generate an estimate of some sample mean, along with its standard deviation.

The Monte Carlo method is used to simulate complex problems in a number of areas, including fluid dynamics, financial engineering, and numerical integration of complex functions in mathematics. In nuclear engineering, Monte Carlo is used to simulate radiation transport for a variety of problem types, including shielding, source-detector and reactor problems. In this research, we focus on the k-eigenvalue reactor core problem.

The Monte Carlo k-eigenvalue reactor core calculation begins with an initial guess of the fission bank shape, which is updated each iteration cycle (a single cycle involves the simulation of a large, fixed number of neutron histories). Histories are drawn from a fission bank and transported through the problem domain, with path lengths and collision parameters sampled according to the probability distribution functions that govern neutron physics.

After a number of cycles, the global shape of the Monte Carlo fission bank becomes roughly stationary (no longer changing its basic overall shape from cycle to cycle). This concludes the "inactive cycle" portion of the Monte Carlo simulation. The second phase of the simulation, known as the "active cycle" phase, involves tallying Monte Carlo histories on a specified space-angle-energy grid to obtain an estimate of the converged flux solution. This solution contains statistical error, which is estimated and reported along with the solution.

In large reactor core calculations, the standard Monte Carlo estimate of the fission source converges very slowly. As a result, many inactive cycles are needed before tallying of the solution can begin. In some cases, the fission source shape never converges completely, instead continuing to "wobble" slowly during active cycles. Solution estimates from these large simulations are subject to a phenomenon known as inter-cycle correlation, which can lead to unphysical solutions and inaccurate estimates of statistical error [1].

1.1.3 Determinstic Methods

In contrast with the Monte Carlo method, determinstic methods do not employ random sampling to generate solution estimates. Instead, these methods rely on phase-space discretization to create large, discrete systems of equations that can be solved for an approximate estimate of the true, continuous solution. Deterministic methods generally employ finite-difference approximations and auxiliary equations to close the system. Because the discrete solution provides no error estimate, additional uncertainty quantification must be carried out to investigate the relationship between the accuracy of the solution and the chosen discretization.

Different types of deterministic methods exist in nearly every branch of engineering, science and mathematics. A variety of these methods are used in nuclear engineering, especially in the area of computational reactor physics.

In the field of computational reactor physics, deterministic methods are characterized by discretization of the governing k-eigenvalue equation in space, energy and angle. A large number of discretization schemes exist in reactor analysis codes, and myriad combinations of space, angle and energy discretizations can be found in the literature [2, 3, 4].

A common angular treatment is the discrete-ordinates method, which approximates the continuous angular variable using a set of discrete angles and corresponding weights. Discrete-ordinates codes usually employ auxiliary equations to relate cell-center and cell-edge angular flux terms (thus closing the system in the spatial variable), and approximate energy dependence with a multigroup formulation (discussed below). The multigroup discrete-ordinates method converges to the true transport solution as the space-angle-energy grid becomes infinitesmally fine.

Some deterministic reactor analysis codes employ the diffusion approximation to reduce computational cost. The diffusion approximation assumes that the neutron current is proportional to the spatial derivative of the flux, which removes angular dependence from the calculation. In addition, the time-independent diffusion equation is elliptic, and can be solved very efficiently (when compared to the transport equation). However, diffusion calculations do not converge to the true transport solution as the grid is refined.

One feature common to all deterministic methods is the presence of systematic error (also known as truncation error) in the solution. As previously noted, solutions obtained via deterministic methods do not include an estimate of solution error. Instead, separate uncertainty quantification must be performed to estimate truncation error in the system of equations. Deterministic iteration methods can also experience numerical instability, often as a result of discretizations that are too coarse.

Finally, all deterministic methods in reactor physics employ a multigroup approximation to treat the energy variable. The calculation of multigroup cross sections is far from straightforward, requires intuition on the part of the user, and is generally more art than science. As a result, all energy-dependent deterministic solutions contain some amount of systematic error from the multigroup approximation.

1.1.4 Hybrid Methods

Although Monte Carlo and deterministic *k*-eigenvalue methods for reactor core problems have largely evolved independently, in recent years there has been increasing interest in combining elements of both strategies to produce "hybrid methods." These hybrid formulations aim to preserve the best features of each method (e.g. the continuous energy treatment of Monte Carlo, or the efficiency of diffusion-like deterministic methods), while minimizing their drawbacks. A number of hybrid methods have been developed, but few have progressed beyond relatively simple proof-of-concept implementations.

A notable exception is the hybrid weight-window FW-CADIS method, which exists in at least one production-scale reactor analysis code [5]. In this method, an inexpensive estimate of the forward or adjoint flux solution is obtained using a deterministic solver. This estimate is then processed to determine permissible weight bounds for Monte Carlo histories traveling through specified regions of the problem domain. The weight-window method helps to flatten the distribution of Monte Carlo histories across the spatial domain; however, it has minimal effect on the convergence rate of the fission source distribution.

A second hybrid method that has received considerable attention is the CMFD-MC iteration strategy, which is considered in this work [6]. In the CMFD-MC strategy, the elements of a low-order diffusion-like system are tallied during each Monte Carlo cycle. At the conclusion of the cycle, the low-rder system is solved for an updated flux estimate, which is then used to adjust the Monte Carlo fission bank for the following cycle. A variant of the CMFD-MC method exists in the open-source MC code OpenMC. The CMFD-MC method and its variants are discussed at length in Chapter 3.

Other hybrid methods for reactor problems exist in the literature; however, most of these were developed and tested only for reasonably simple (1-D, monoenergetic) problems. One notable exception is the COarse MEsh Transport (COMET) method, which uses Monte Carlo to generate a response function library for a variety of local source terms (i.e. a set of fixed-source problems) [7]. A coarse-mesh deterministic method is then used to iterate on the partial currents and eigenvalue of the global reactor problem.

1.1.5 Other Previous Work

In this section, we briefly discuss previous work in the area of non-hybrid stabilization and acceleration methods for Monte Carlo reactor core *k*-eigenvalue simulations. These techniques primarily involve modifications to the standard MC *k*-eigenvalue iteration (discussed in Chapter 2), which were carried out in an effort to accelerate fission source convergence.

The first Monte Carlo acceleration technique is known as Wielandt's method, and was originally developed for deterministic methods [8]. In the deterministic interpretation, Wielandt's method involves modifying the eigenvalue problem using a "shifted" eigenvalue k'. If the eigenvalue "shift" parameter is chosen judiciously, this method accelerates the deterministic calculation by decreasing the dominance ratio of the system.

The Monte Carlo interpretation of Wielandt's method involves tracking some portion of fission daughter particles during the cycle of their creation, rather than banking them all for the following cycle (as is done in the standard MC method). This decreases the number of cycles required to approach fission source convergence; however, it increases the length of each cycle considerably. Hence, Wielandt's method is not a true Monte Carlo "acceleration" scheme, as it does not decrease the total time required to converge the fission source distribution. However, it has been shown to improve the reliability of fission source convergence for high dominance-ratio problems [9].

A second strategy used to modify the Monte Carlo fission source convergence rate is the superhistory method [10]. In the superhistory method, more than one fission neutron generation is simulated per Monte Carlo cycle. Like the Wielandt method, the superhistory method decreases the number of inactive cycles required to achieve a stationary fission source distribution. Also, like the Wielandt method, the superhistory method significantly increases the computing time per cycle. This effectively cancels any potential time savings. In fact, it has been theoretically shown that the Wielandt and superhistory methods cannot decrease the computational time required to converge the fission source [11].

Finally, we briefly describe the fission matrix method. In the fission matrix method, a spatial mesh is applied to the problem, which must include all fissile regions. During Monte Carlo cycles, tallies are used to record the cumulative number of particles that are born in one mesh region and create fission bank sites in another region (in some cases, the birth and bank regions are the same). It has recently been shown that the fission matrix can be stored in a compressed format to reduce memory requirements [12].

Once a sufficient number of cycles have been simulated, the accumulated fission matrix can be used to redistribute the Monte Carlo fission bank sites. However, if the number of histories per cycle is too small (or the fission source distribution has strong spatial gradients), elements of the fission matrix may be very noisy. When this is the case, fission matrix acceleration can cause the Monte Carlo simulation to become unstable [13].

1.2 Motivation

The two primary goals of this work are as follows. First, we seek to investigate the stability of various hybrid Monte Carlo iteration schemes. We do this by introducing the concept of the "non-random" Monte Carlo calculation, which describes the convergence rate of the fission source distribution in the limit as the number of histories becomes infinite.

While it is not readily apparent how to analyze the stability of methods with statistical error, the "non-random" versions of these methods can be linearized and Fourier-analyzed in a straightforward way. In doing this, we gain valuable insight into the convergence behavior of the method in cases where statistical error is negligible. While we cannot quantify the effect of random error on the spectral radius of the non-random method, we hypothesize that the presence of sufficient random error can destabilize a simulation that is stable in the infinite-particle limit. We support this hypothesis with numerical results from direct Monte Carlo simulations.

If a particular set of parameters is found to be unstable in the infinite-particle limit, we would expect it to be unstable for a practical simulation with a finite number of particles. If this is the case, the Fourier stability analysis provides insight into how the parameters might be changed to stabilize an unstable simulation.

The second goal of this work is to introduce and characterize a new iteration strategy for Monte Carlo *k*-eigenvalue simulations. This iteration strategy, which we call "Limited-Collision Monte Carlo" (LCMC), limits each random history to a fixed maximum number of collisions per cycle. Histories that survive the maximum number of collisions are banked for the following cycle. This iteration scheme vastly reduces the time per cycle, but in some cases is less stable than the standard CMFD-MC iteration (in the non-random limit). In practice, the decrease in LCMC simulation time is largely outweighed by the corresponding increase in the number of cycles required to converge the fission and scattering source distributions. In addition, extra computation time is spent solving the CMFD system, on account of finer coarse grid requirements and increased stochastic noise (this is especially true for multidimensional simulations).

To leverage the strengths of both the CMFD-MC and LCMC strategies, we have developed and implemented a "hybrid" of the two methods, which aims to maximize the efficiency of both the inactive and active cycle portions of the *k*-eigenvalue calculation. To do this, we employ the CMFD-MC iteration equations during inactive cycles to efficiently converge the fission source, then switch to the new LCMC iteration equations during active cycles to shorten total simulation time.

To motivate our methodology in developing this new iteration strategy, we assert that the two phases of the Monte Carlo *k*-eigenvalue calculation pose different computational challenges. During inactive cycles, systematic error in the fission source source is the dominant source of solution error; thus, the iteration equations used during inactive cycles should be designed to converge the global shape of the Monte Carlo fission source as efficiently as possible.

By contrast, during the active cycle phase of the calculation, statistical noise from the transport process is dominant (any remaining error in the fission source shape is assumed negligible). Tally data from each active cycle is stored and averaged to obtain the final solution estimate; as a result, the active-cycle iteration scheme should be designed to make efficient use of stochastic information from Monte Carlo histories.

We believe that the CMFD-MC method is well-suited for inactive cycles (when run on a sufficiently fine "coarse" grid), because it converges the fission source distribution in a small number of cycles for most problems. However, the CMFD-MC method has no effect on high-frequency statistical noise, which is the dominant source of active-cycle error.

By contrast, the LCMC method requires a large number of cycles to converge the fission and scattering source distributions, but it takes considerably less time per cycle than CMFD-MC. Consequently, the LCMC method can improve the efficiency of active cycles.

1.3 Thesis Outline

The remainder of this document is organized as follows. In Chapter 2, we describe the standard Monte Carlo *k*-eigenvalue iteration scheme, which is widely used in Monte Carlo reactor analysis codes. We Fourier-analyze the non-random Monte Carlo iteration scheme for a special homogeneous problem, and compare our theoretical predictions to numerical experiments to better understand the fission source convergence behavior of the Monte Carlo iteration. We also present standard Monte Carlo numerical results for several representative core problems, which serve as benchmarks for the other methods considered in this research.

In Chapter 3, we describe the existing CMFD-MC method, originally proposed by Lee et. al. [6]. Numerical stability issues are described, as well as existing methods that were developed to address these issues. We then propose a new explanation for the observed stability behavior, and we present a Fourier analysis to defend our hypothesis. Finally, we present numerical results for the CMFD-MC method and its variants.

Next, in Chapter 4 we introduce the new LCMC method, which was developed as part of this research. The method is described and Fourier-analyzed. Numerical results are presented to characterize the fission source convergence behavior of the LCMC method, as well as demonstrate its performance for the representative core problems.

A new hybrid iteration method for MC *k*-eigenvalue problems is presented and implemented in Chapter 5, which we call the "mixed" method. This hybrid strategy combines the CMFD-MC and LCMC methods in a single simulation, using the CMFD-MC method to efficiently converge the fission source during inactive cycles, then transitioning to the LCMC method to improve the efficiency of active cycles. We present numerical results for the representative problem set, and compare the results to those from the standard, CMFD-MC, and LCMC methods presented in previous chapters.

In Chapter 6.4, we present parametric Figure of Merit (FOM) studies for the mixed method. These results are compared to FOM results for the Wolters method, to better understand the relative efficiency of the mixed method over a range of problems.

Finally, in Chapter 7 we summarize our findings and discuss their importance. We then suggest future work in the area of stabilization and acceleration methods for Monte Carlo reactor core *k*-eigenvalue problems.

CHAPTER 2

The MC Method

2.1 Introduction

In this chapter, we describe the widely-used standard Monte Carlo (MC) k-eigenvalue iteration scheme, which was originally developed over half a century ago. In contrast to deterministic methods, which discretize the transport equation (or a diffusion approximation) in phase space, the Monte Carlo method requires no discretizations. In general, a mesh structure exists to accumulate tally results, but this mesh does not affect the underlying transport in any way. Thus, the accuracy of the Monte Carlo calculation is limited only by knowledge of underlying physics, the accuracy of neutron cross-section data, and the computation time available.

To begin, we introduce the concept of the “non-random” Monte Carlo method, which describes Monte Carlo iteration equations in the limit as the number of particles becomes infinite. This method is fully continuous in space, angle, and energy. We then linearize and Fourier-analyze the non-random system, which represents new research. Next, theoretical spectral radius predictions from the Fourier analysis are compared to numerical results from direct simulation. Finally, we assess the performance of the standard Monte Carlo method for a set of representative problems. This problem set will be used throughout the thesis for straightforward comparisons between methods.

2.2 MC Iteration Strategy

In this section, the MC iteration strategy for solving k-eigenvalue problems is described. The equations presented here contain no random error terms; thus, they describe the Monte Carlo iteration strategy only in the limit as the number of histories approaches infinity. We consider the following one-group, planar-geometry k-eigenvalue problem on the domain

$0 \leq x \leq X$, with periodic boundary conditions and isotropic scattering:

$$\mu\frac{d}{dx}\psi(x,\mu) + \Sigma_t(x)\psi(x,\mu) - \frac{\Sigma_s(x)}{2}\phi(x) = \frac{\nu\Sigma_f(x)}{2k}\phi(x)\,,$$

$$0 \leq x \leq X\,,\ -1 \leq \mu \leq 1\,, \tag{2.1a}$$

$$\psi(0,\mu) = \psi(X,\mu)\,,\ -1 \leq \mu \leq 1\,, \tag{2.1b}$$

where

$$\phi(x) = \int_{-1}^{1} \psi(x,\mu)d\mu\,. \tag{2.1c}$$

The ℓ^{th} MC iteration (or "cycle") begins with Eqs. (2.1), written with iteration superscripts as follows:

$$\mu\frac{d}{dx}\psi^{(\ell+1/2)}(x,\mu) + \Sigma_t(x)\psi^{(\ell+1/2)}(x,\mu) - \frac{\Sigma_s(x)}{2}\phi^{(\ell+1/2)}(x) = \frac{\nu\Sigma_f(x)}{2k^{(\ell)}}\phi^{(\ell)}(x)\,, \tag{2.2a}$$

$$0 \leq x \leq X\,,\ -1 \leq \mu \leq 1\,,$$

$$\psi^{(\ell+1/2)}(0,\mu) = \psi^{(\ell+1/2)}(X,\mu)\,,\ -1 \leq \mu \leq 1\,, \tag{2.2b}$$

where

$$\phi^{(\ell+1/2)}(x) = \int_{-1}^{1} \psi^{(\ell+1/2)}(x,\mu)d\mu\,. \tag{2.2c}$$

If $\ell = 0$, the fission source is populated from an initial guess. Often, the initial guess is flat or simply-varying in space. Next, the updated eigenvalue estimate is computed using:

$$k^{(\ell+1)} = k^{(\ell)}\frac{\int_0^X \nu\Sigma_f(x)\phi^{(\ell+1/2)}(x)dx}{\int_0^X \nu\Sigma_f(x)\phi^{(\ell)}(x)dx}\,. \tag{2.2d}$$

To complete the MC iteration cycle, the fission source is normalized such that:

$$\nu\Sigma_f(x)\phi^{(\ell+1)}(x) = \frac{\nu\Sigma_f(x)\phi^{(\ell+1/2)}(x)}{\frac{1}{X}\int_0^X \nu\Sigma_f(x)\phi^{(\ell+1/2)}(x)dx}\,. \tag{2.2e}$$

Because this is an eigenvalue problem, the eigenfunction $\phi(x)$ is known only to a multiplicative constant; thus, the choice of normalization is arbitrary.

In contrast to standard deterministic methods, the MC transport simulation shown in Eqs. (2.2) treats scattering *implicitly*; the scattering source is *fully converged* during the high-order transport calculation, because the standard MC method simulates full particle histories (from birth until death) within each cycle. Eqs. (2.2) are not discretized in space or angle, because MC simulations involve no such discretizations. We reiterate that Eqs. (2.2) have no terms that describe random errors. These equations apply to MC simulations only in the limit in which the number of particles per cycle is sufficiently large that statistical errors can be ignored.

In summary, a standard MC *k*-eigenvalue iteration cycle proceeds as follows: (i) a large number of particles are sampled from a fission bank and transported until they leak from the domain or are absorbed, (ii) an updated estimate of the multiplication factor is calculated, and (iii) the fission source bank is normalized for the next cycle. During step (i), random numbers are used to sample distance to collision (or material boundary), collision type, and energy/angle change from mathematical representations of physical probability distribution functions.

Next, we linearize the non-random MC iteration equations. This facilitates the Fourier analysis in Section 2.3.2.

2.3 Stability Analysis

In this section, we Fourier-analyze the standard MC iteration scheme for *k*-eigenvalue problems, in the limit as the number of MC histories approaches infinity. To our knowledge, no previous attempts have been made to Fourier-analyze the MC iteration scheme; thus, all research in this section is new.

We begin by linearizing the MC iteration equations presented in Section 2.2. We then introduce a Fourier ansatz and obtain an analytical expression for the non-random MC spectral radius. In Section 2.4.1, our theoretical predictions are compared to direct numerical estimates of the spectral radius.

Before we proceed, we note that the standard MC Fourier analysis is not discretized in space, in contrast with the discrete CMFD-MC and FCPI Fourier analyses presented later in this thesis. This continuous representation is possible because the standard MC method involves no discretization; it is fully continuous in space, angle, and energy (in the infinite-history limit). Tally grids are imposed on MC problems only to bin results; they do not introduce truncation error, and do not affect the underlying MC transport process in any way.

2.3.1 The Linearized Non-Random MC Iteration

We begin with the standard monoenergetic MC iteration equations introduced in Section 2.2, for a homogeneous problem with periodic boundaries:

$$\mu\frac{d}{dx}\psi^{(\ell+1/2)}(x,\mu)+\Sigma_t\psi^{(\ell+1/2)}(x,\mu)-\frac{\Sigma_s}{2}\phi^{(\ell+1/2)}(x)=\frac{\nu\Sigma_f}{2k^{(\ell)}}\phi^{(\ell)}(x)\,, \tag{2.3a}$$

$$0\le x\le X\,,\ -1\le\mu\le 1\,,$$

$$\psi^{(\ell+1/2)}(0,\mu)=\psi^{(\ell+1/2)}(X,\mu)\,,\ -1\le\mu\le 1\,, \tag{2.3b}$$

$$\phi^{(\ell+1/2)}(x)=\int_{-1}^{1}\psi^{(\ell+1/2)}(x,\mu)d\mu\,, \tag{2.3c}$$

$$k^{(\ell+1)}=k^{(\ell)}\frac{\int_0^X\nu\Sigma_f\phi^{(\ell+1/2)}(x)dx}{\int_0^X\nu\Sigma_f\phi(x)dx}\,, \tag{2.3d}$$

$$\nu\Sigma_f\phi^{(\ell+1)}(x)=\frac{\nu\Sigma_f\phi^{(\ell+1/2)}(x)}{\frac{1}{X}\int_0^X\nu\Sigma_f\phi^{(\ell+1/2)}(x)dx}\,. \tag{2.3e}$$

We reiterate that the choice of normalization is arbitrary, because the eigenfunction is known only to a multiplicative constant. On convergence, Eqs. (2.3) have the exact solution:

$$\psi(x,\mu)=\frac{1}{2}\,,$$

$$\phi(x)=1\,,$$

$$\frac{1}{k}=\frac{\Sigma_a}{\nu\Sigma_f}\,.$$

Next, relevant quantities are expanded linearly around the exact solution, using a small parameter $\epsilon\ll 1$:

$$\psi^{(\ell+1/2)}(x,\mu)=\frac{1}{2}+\epsilon\hat{\psi}^{(\ell+1/2)}(x,\mu)\,,$$

$$\phi^{(\ell+1/2)}(x)=1+\epsilon\hat{\phi}^{(\ell+1/2)}(x)\,,$$

$$\phi^{(\ell)}(x)=1+\epsilon\hat{\phi}^{(\ell)}(x)\,,$$

$$\frac{1}{k^{(\ell+1)}} = \frac{\Sigma_a}{\nu\Sigma_f} + \epsilon\delta^{(\ell+1)} .$$

Introducing these expansions into Eqs. (2.3), equating $\mathcal{O}(\epsilon)$ terms, and neglecting $\mathcal{O}(\epsilon^2)$ terms yields:

$$\mu\frac{d}{dx}\hat{\psi}^{(\ell+1/2)}(x,\mu) + \Sigma_t\hat{\psi}^{(\ell+1/2)}(x,\mu) - \frac{\Sigma_s}{2}\hat{\phi}^{(\ell+1/2)}(x) = \frac{\nu\Sigma_f}{2}\delta^{(\ell)} + \frac{\Sigma_a}{2}\hat{\phi}^{(\ell)}(x) , \tag{2.4a}$$

$$0 \le x \le X , \ -1 \le \mu \le 1 ,$$

$$\hat{\psi}^{(\ell+1/2)}(0,\mu) = \hat{\psi}^{(\ell+1/2)}(X,\mu) , \ -1 \le \mu \le 1 , \tag{2.4b}$$

$$\hat{\phi}^{(\ell+1/2)}(x) = \int_{-1}^{1} \hat{\psi}^{(\ell+1/2)}(x,\mu)d\mu , \tag{2.4c}$$

$$\delta^{(\ell+1)} = \delta^{(\ell)} - \frac{\Sigma_a}{\nu\Sigma_f}\frac{1}{X}\int_0^X \nu\Sigma_f\hat{\phi}^{(\ell+1/2)}(x)dx , \tag{2.4d}$$

$$\nu\Sigma_f\hat{\phi}^{(\ell+1)}(x) = \nu\Sigma_f\hat{\phi}^{(\ell+1/2)}(x) - \frac{1}{X}\int_0^X \nu\Sigma_f\hat{\phi}^{(\ell+1/2)}(x)dx . \tag{2.4e}$$

Eqs. (2.4) comprise the linearized MC k-eigenvalue iteration scheme. The rate at which the original Eqs. (2.3) converge is equal to the rate at which the unknowns in Eqs. (2.4) limit to zero.

We note that some terms have changed as a result of the linearization procedure. In particular, the right-hand side of the transport equation now contains two terms, one that is proportional to the eigenvalue error, and one that is proportional to the eigenfunction error.

In Section 2.3.2, we Fourier-analyze the linearized non-random MC k-eigenvalue system.

2.3.2 Fourier Analysis

In this section, we complete the Fourier analysis of the MC iteration equations. We obtain an equation for the convergence rate of the system as a function of the Fourier frequency (λ), which can then be used to find the spectral radius of the iteration scheme.

We begin the analysis by defining the Fourier ansatz:

$$\hat{\psi}^{(\ell+1/2)}(x,\mu) = a(\mu)\omega^{\ell}e^{i\Sigma_t\lambda x} , \tag{2.5a}$$

$$\hat{\phi}^{(\ell+1/2)}(x) = A\omega^{\ell}e^{i\Sigma_t\lambda x} , \tag{2.5b}$$

$$\hat{\phi}^{(\ell)}(x) = B\omega^{\ell}e^{i\Sigma_t\lambda x} , \tag{2.5c}$$

$$\delta^{(\ell+1)} = \mathcal{C}\omega^{\ell+1}e^{i\Sigma_t\lambda x} . \tag{2.5d}$$

Here, $a(\mu)$ is an undetermined function of the polar angle, while A, B and C are constants. For clarity, we note that the ω terms in our ansatz (the "eigenvalues") are raised to powers of ℓ, while the superscripts of the original quantities (enclosed in parentheses) are iteration indices. The solution defined by Eqs. (2.5) limits to zero if $|\omega| < 1$. The maximum value of $|\omega|$ is called the *spectral radius*, ρ; if $0 < \rho < 1$, the method is stable, and if $\rho \geq 1$, it is unstable.

Inserting the ansatz into the linearized system (Eqs. (2.4)) and simplifying, we obtain the following system of equations:

$$(i\lambda\mu + 1)\Sigma_t a(\mu)e^{i\Sigma_t\lambda x} - \frac{\Sigma_s}{2}Ae^{i\Sigma_t\lambda x} = \frac{\nu\Sigma_f}{2}\mathcal{C} + \frac{\Sigma_a}{2}Be^{i\Sigma_t\lambda x} \tag{2.6a}$$

$$e^0 = e^{i\Sigma_t\lambda X} \tag{2.6b}$$

$$A = \int_{-1}^{1} a(\mu)d\mu \tag{2.6c}$$

$$B\omega e^{i\Sigma_t\lambda x} = e^{i\Sigma_t\lambda x} - \frac{1}{X}\int_0^X Ae^{i\Sigma_t\lambda x'}dx' \tag{2.6d}$$

$$\mathcal{C}\omega = \mathcal{C} - \frac{\Sigma_a}{\nu\Sigma_f}\frac{1}{X}\int_0^X Ae^{i\Sigma_t\lambda x}dx \tag{2.6e}$$

The periodic boundaries impose a condition on the Fourier frequency:

$$\begin{aligned} e^0 = 1 &= e^{i\Sigma_t\lambda X}\,, \\ &= \cos(\Sigma_t\lambda X) + i\,\sin(\Sigma_t\lambda X)\,, \\ \lambda_s &= \frac{2s\pi}{\Sigma_t X}\,,\ \ s = 0, 1, 2\ldots \end{aligned} \tag{2.7}$$

The effect of the periodic boundary is to restrict values of the Fourier frequency (λ) to a set of discrete points λ_s. There are a countably infinite number of λ_s values, with their spacing dependent on the optical thickness of the system ($\Sigma_t X$). Because the discrete Fourier modes are independent of one another, we separate Eqs. (2.6) into spatially varying terms (corresponding to $\lambda_s \neq 0$) and spatially constant terms ($\lambda_s = 0$).

We begin with the spatially varying equations, and solve for $\omega(\lambda_s)$ for $s \neq 0$. This system of equations takes the form:

$$(i\lambda_s\mu + 1)\Sigma_t a(\mu) - \frac{\Sigma_s}{2}A = \frac{\Sigma_a}{2}B\,, \tag{2.8a}$$

$$A = \int_{-1}^{1} a(\mu)d\mu\,, \tag{2.8b}$$

$$B\omega - A = \frac{1}{X} A i\lambda_s \Sigma_t (e^{i\lambda_s \Sigma_t X} - 1) \,. \tag{2.8c}$$

The boundary equation is omitted in Eqs. (2.8), because it has already been used to determine the permissible values of λ_s. Also, our choice of λ_s causes the right side of Eq. (2.8c) to be exactly zero. Next, we rearrange Eq. (2.8a) and integrate over the polar angle μ, which yields:

$$\int_{-1}^{1} a(\mu) d\mu = \left(\frac{(1-c)}{2} B + \frac{c}{2} A \right) \int_{-1}^{1} \frac{1}{1 + i\lambda_s \mu} d\mu \,. \tag{2.9}$$

In Eq. (2.9), we have introduced the *scattering ratio*, c:

$$c = \frac{\Sigma_s}{\Sigma_t} \,.$$

Substituting Eq. (2.8b) into Eq. (2.9), evaluating the integral term, and simplifying yields:

$$A = \left(\frac{(1-c)}{2} B + \frac{c}{2} A \right) \frac{2}{\lambda_s} \tan^{-1}(\lambda_s) \,, \tag{2.10}$$

$$A = ((1-c)B + cA) \frac{1}{\lambda_s} \tan^{-1}(\lambda_s) \,. \tag{2.11}$$

We rearrange Eq. (2.8c) to solve for ω,

$$\omega = \frac{A}{B} \,,$$

divide Eq. (2.10) through by B, and substitute in the above expression for the ratio $\frac{A}{B}$. After some algebra, we obtain the final expression for ω as a function of λ_s ($s \neq 0$):

$$\omega = \frac{\left(\frac{1-c}{\lambda_s} \right) \tan^{-1}(\lambda_s)}{1 - \frac{c}{\lambda_s} \tan^{-1}(\lambda_s)} \,. \tag{2.12}$$

(In Figure 2.1, Eq. (2.12) is plotted as a function of λ_s for several values of the scattering ratio, c. This plot can be found in Section 2.4.1.)

Next, we return to the original system in Eqs. (2.6), this time considering only the $s = 0$ case. The system becomes:

$$\Sigma_t a(\mu) - \frac{\Sigma_s}{2} A = \frac{\nu \Sigma_f}{2} \mathcal{C} + \frac{\Sigma_a}{2} B \,, \tag{2.13a}$$

$$A = \int_{-1}^{1} a(\mu) d\mu \,, \tag{2.13b}$$

$$B\omega = 0 \ , \tag{2.13c}$$

$$\mathcal{C}(\omega - 1) = -\frac{\Sigma_a}{\nu\Sigma_f} A \ . \tag{2.13d}$$

Eq. (2.13c) immediately yields $B = 0$ (assuming the non-trivial solution for ω). If we apply this result to Eq. (2.13a), then integrate over the polar angle and insert Eq. (2.13b), we obtain:

$$\begin{aligned} \Sigma_t A - \Sigma_s A &= \nu\Sigma_f \mathcal{C} \ , \\ (1-c)A &= \frac{\nu\Sigma_f}{\Sigma_t}\mathcal{C} \ . \end{aligned} \tag{2.14}$$

From Eq. (2.13d), we know that

$$A = \frac{\nu\Sigma_f}{\Sigma_a}(1-\omega)\mathcal{C} \ . \tag{2.15}$$

Substituting this expression for A in Eq. (2.14) and simplifying, we arrive at the final result for $s = 0$:

$$\begin{aligned} (1-c)\frac{\nu\Sigma_f}{\Sigma_a}(1-\omega)\mathcal{C} &= \frac{\nu\Sigma_f}{\Sigma_t}\mathcal{C} \ , \\ \frac{(1-c)}{\Sigma_a}(1-\omega) &= \frac{1}{\Sigma_t} \ , \\ (1-c)(1-\omega) &= \frac{\Sigma_a}{\Sigma_t} \ , \\ (1-c)(1-\omega) &= (1-c) \ , \\ 1-\omega &= 1 \ , \\ \omega &= 0 \ . \end{aligned} \tag{2.16}$$

From Eq. (2.16), the convergence rate of the non-spatially-varying Fourier frequency ($s = 0$, also known as the "flat mode") is zero. This indicates that the $\mathcal{O}(\epsilon)$ component of the k-eigenvalue converges immediately, because the $\mathcal{O}(\epsilon)$ eigenvalue error term depends only on the flat mode value of ω. The eigenfunction, however, depends on both the flat and spatially-varying Fourier modes, and does not converge instantly. To determine the spectral radius of the MC eigenfunction (denoted here by ρ), we determine the maximum ω as a function of λ_s:

$$\rho = \sup_{s>0} |\omega(\lambda_s)| \ . \tag{2.17}$$

If the spectral radius ρ in Eq. (2.17) is larger than unity, error in the eigenfunction will increase as the iteration index ℓ increases; this indicates an unstable simulation. Conversely, if ρ is less than unity, error in the eigenfunction will decrease as the iteration index increases, and the simulation will converge. Assuming $\rho < 1$, simulations with smaller values of ρ will converge faster than simulations with larger values of ρ.

Having arrived at an analytic expression for the convergence rate of the non-random MC k-eigenvalue iteration scheme, we can take limits of this equation to better understand the behavior of this method. In the pure scattering limit ($c \to 1$), the right-hand side of Eq. (2.12) limits to zero for all λ_s. In other words, the solution of a purely-scattering problem would converge instantly in the infinite-particle limit.

In the purely-absorbing limit, Eq. (2.12) reduces to simply

$$\omega = \frac{1}{\lambda_s}\tan^{-1}(\lambda_s) , \tag{2.18}$$

which approaches a maximum of $\omega = 1$ as the discrete λ_s values approach zero. (In practice, the smallest λ_s value is greater than zero, but approaches zero as the problem size tends to infinity.) The purely-absorbing case represents an upper bound on the spectral radius as a function of the scattering ratio, c. The presence of scattering always acts to reduce the spectral radius of the non-random MC iteration scheme for finite problems, a result which will be shown numerically in the next section.

2.4 Numerical Results

Two types of numerical results are presented for the MC iteration strategy. First, we describe numerical experiments which were carried out to demonstrate the validity of the Fourier stability analysis. Then, we introduce a set of benchmark problems which are used to test the performance of the standard MC method. These results, in turn, provide a baseline for comparison with the hybrid methods presented later in this thesis.

2.4.1 Stability Analysis

In this section, we present numerical results from our Fourier analysis of the linearized MC k-eigenvalue iteration equations. Theoretical predictions from the Fourier analysis in Section 2.3.2 are compared to numerical estimates from two sources: (i) a “surrogate” S_N code, and (ii) direct MC simulation. The surrogate S_N simulations are, in essence, a high-resolution discrete approximation to the MC iteration scheme; they converge the scattering source to a small tolerance, and employ a very fine space-angle grid to minimize systematic error.

From Eq. (2.12), it is clear that the convergence rate of the spatially-varying modes is a function of the scattering ratio, c. In addition, permissible values of the Fourier frequency (λ_s) are determined by the total optical thickness of the slab, $\Sigma_t X$. We reiterate that the non-random MC equations are fully continuous; the convergence rate of the problem does not depend on the size of the tally grid. However, it does depend on the problem size, because the discrete λ_s values depend on X.

To demonstrate these relationships visually, we plot continuous convergence-rate curves for several values of the scattering ratio (c) in Figure 2.1. These curves represent the limit as the problem size approaches infinity; in this limit, the discrete frequencies λ_s approach a continuous distribution.

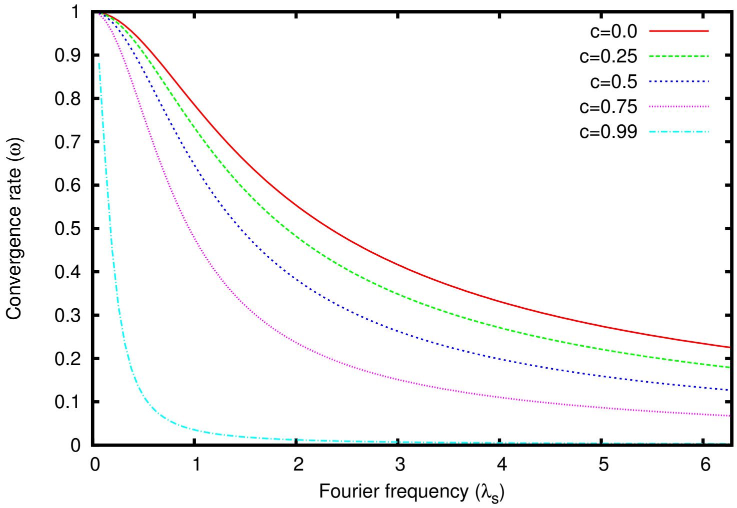

Figure 2.1: MC convergence rate as a function of Fourier frequency (λ_s)

The curves in Figure 2.1 are continuous for $0 < \lambda_s < \infty$. Here, we have plotted them on the interval $[0, 2\pi]$, because spatially-varying modes with small values of λ_s dominate the convergence rate of the MC iteration. We see that the maximum convergence rate for all values of c approaches (but does not exceed) unity in the limit as $\lambda_s \rightarrow 0$; thus, the non-random MC iteration scheme is unconditionally stable, regardless of the problem size or cross sections. That said, real MC simulations inevitably contain some amount of random error. As a result, MC k-eigenvalue calculations (which are stable in the infinite-particle limit) may still fail to fully converge the fission source. This is especially true for problems with high spectral radii in the non-random limit. Because these simulations converge very slowly in the absence of statistical noise, one can hypothesize that they will converge even more slowly (or not at all) when statistical error is present.

We consider two homogeneous problems to examine the convergence rate of the non-random MC k-eigenvalue iteration scheme; case A is 10 mean free paths thick, while case B is 50 mean free paths thick. The large size difference between these two cases will help to demonstrate the strong dependence of the MC spectral radius on slab optical thickness. The total cross section is held at unity for all cases, while the scattering cross section is varied. Problem parameters can be found in Table 2.1. In addition, Figure 2.2 shows convergence rates for permissible values of the discrete frequency for cases A and B.

Table 2.1: Test problem specifications

Case	X (cm)	h (cm)	Σ_t (cm^{-1})	Σ_s (cm^{-1})	$\nu\Sigma_f$ (cm^{-1})
A	10	1.0	1.0	0.0 - 0.99	0.01
B	50	1.0	1.0	0.0 - 0.99	0.01

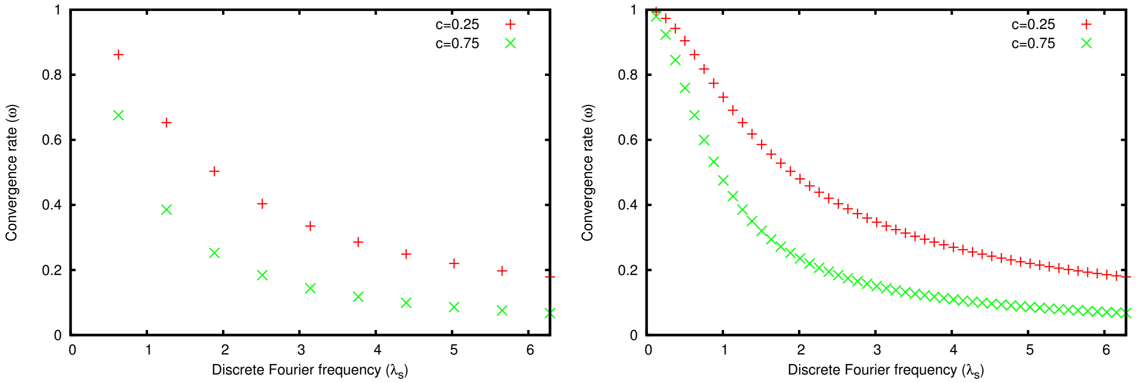

(a) Case A (X = 10 cm)

(b) Case B (X = 50 cm)

Figure 2.2: MC convergence rate for permissible values of λ_s

The convergence rate (ω) is a monotonically-decreasing function of the Fourier frequency λ_s. Recalling the spectral radius formula presented in Section 2.3.2,

$$\rho = \sup_{s>0} |\omega(\lambda_s)| \ ,$$

we infer that the spectral radius of the MC k-eigenvalue simulation is always determined by the smallest value of λ_s. Optically thin slabs will have more widely-spaced λ_s values than optically thick slabs; thus, for a fixed value of the scattering ratio, the spectral radius is a monotonically increasing function of slab optical thickness.

The values of h (the MC grid size) and $\nu\Sigma_f$ presented in Table 2.1 have no effect on the spectral radius of the non-random MC scheme; we include them only to provide a complete description of our MC input. Our surrogate discrete-ordinates code uses the S_{32} Gauss-Legendre quadrature set, with step characteristic spatial differencing and a 0.01-cm spatial discretization. We converge the S_N scattering iteration to 10^{-9} during each transport solve, to ensure that the surrogate simulation closely resembles the true MC k-eigenvalue iteration.

Next, we compare theoretical predictions from the Fourier analysis to results from our S_N surrogate, as well as direct MC simulations. Numerical estimates of the spectral radius are calculated using the well-known expression

$$\rho = \frac{||\phi^{(\ell+1)} - \phi^{(\ell)}||}{||\phi^{(\ell)} - \phi^{(\ell-1)}||} . \tag{2.19}$$

In general, Eq. (2.19) is only valid for large ℓ, as it represents the asymptotic convergence behavior of the iteration strategy. Unfortunately, direct MC estimates of the spectral radius must be calculated during early inactive cycles (when ℓ is small) to ensure that systematic error in the fission source clearly dominates stochastic error.

Spectral radius estimates obtained from direct MC are both very noisy and expensive to obtain. First of all, three consecutive cycles of flux data are required before an estimate can be calculated. Also, a large number of particles per cycle ($\mathcal{O}(10^7)$) must be simulated to suppress random error in the estimates, and 25 independent simulations are needed to determine accurate error bounds. Finally, when the spectral radius of the non-random method is close to unity ($\rho \sim 0.9$ or greater), estimates from real simulations become highly susceptible to random fluctuation. In these cases, spectral radius calculations using direct MC are too noisy to be useful.

By contrast, spectral radius estimates from the surrogate code contain no statistical error; systematic error is also minimized through the use of a very fine space-angle grid and tight scattering source convergence. With this in mind, we expect results from the surrogate discrete-ordinates code to more closely match theoretical predictions.

Numerical results for case A (the 10-centimeter slab problem) are shown in Figure 2.3. As expected, direct MC estimates of the spectral radius are exceedingly noisy. However, we note that all MC estimates fall within a single standard deviation of the theoretical spectral radius value, and generally follow the trend predicted by the Fourier analysis. Surrogate discrete-ordinates estimates of the spectral radius lie almost exactly on top of theoretical predictions from the Fourier analysis. As previously noted, we observe that the non-random MC spectral radius is a monotonically decreasing function of the scattering ratio, c.

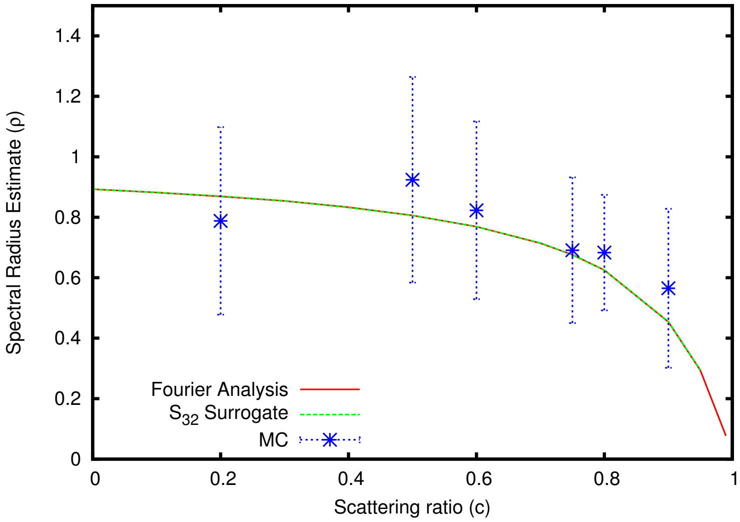

Figure 2.3: Spectral radius (ρ) vs. scattering ratio, case A

Results for case B (the 50-centimeter slab problem) are shown in Figure 2.4. Because the theoretical case B spectral radius is close to unity for nearly all values of the scattering ratio, we were unable to obtain direct MC spectral radius estimates in a reasonable amount of time (we show an example MC estimate in Figure 2.4, for the amusement of the reader). Instead, we consider only the theoretical and surrogate S_N predictions. These two curves agree closely, again demonstrating the validity of the Fourier analysis in predicting the convergence rate of the non-random MC *k*-eigenvalue iteration.

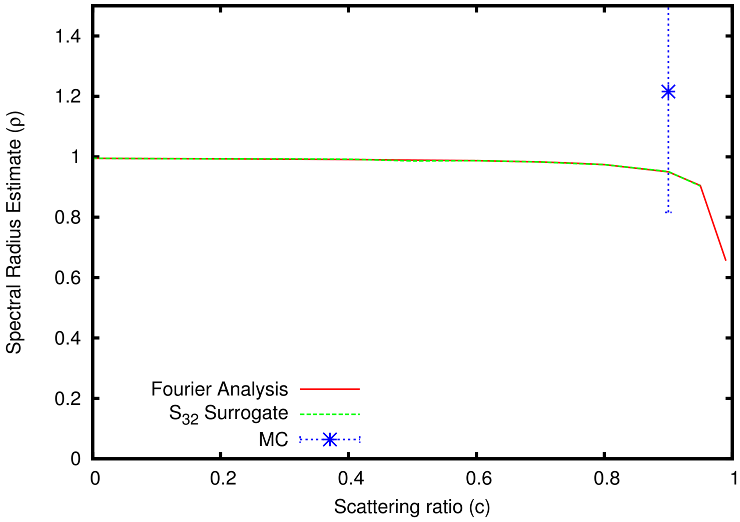

Figure 2.4: Spectral radius (ρ) vs. scattering ratio, case B

At this time, it is not known how to include the effects of statistical noise in a Fourier analysis. This is a candidate for future work, and will be discussed further in Chapter 7

2.4.2 Benchmark Problem Performance

Next, we assess the performance of the MC k-eigenvalue iteration scheme using a set of benchmark test problems, which are used in later chapters to allow straightforward comparison with the baseline results presented here.

We begin with an optically thick, monoenergetic, homogeneous k-eigenvalue slab problem with vacuum boundaries. This problem is introduced in Section 2.4.2.1 below, and accompanied by numerical results for the standard MC iteration strategy.

2.4.2.1 Homogeneous Problem

In this section, we present results for a homogeneous fissile problem originally used by Wolters [14]. The system is a 40 centimeter thick slab with vacuum boundaries, and will hereafter be referred to as problem #1. Cross sections and other parameters for problem #1 are presented in Table 2.2.

Table 2.2: Cross sections, problem #1

X (cm)	h (cm)	Σ_t (cm^{-1})	Σ_s (cm^{-1})	$\nu\Sigma_f$ (cm^{-1})
40	0.5	1.0	0.5	0.48

Using diffusion theory, Wolters estimated the first two eigenvalues of problem #1, then took their ratio to determine an approximate dominance ratio of 0.9887 for the system. A dominance ratio near unity indicates that the first two eigenvalues are closely spaced, which in turn makes the fundamental eigenfunction (which represents the steady-state fission source shape) difficult to converge. The fundamental k-eigenvalue of problem #1 is approximately 0.9563.

First, we use problem #1 to investigate the dependence of the solution apparent RSD on the number of active cycles simulated. This is done to verify that the standard MC k-eigenvalue iteration behaves in a manner consistent with the *Central Limit Theorem* (CLT) as the number of active cycles becomes large.

The CLT states that a large number of independent, identically-distributed samples of a random variable will assume a normal distribution, even if the random variable itself is not normally distributed. While we are not able to theoretically show that MC cycle tallies meet the requirements of the CLT, we can empirically demonstrate that these tallies converge at a rate roughly proportional to $\frac{C}{\sqrt{N}}$ (the rate predicted by the CLT), where C is a constant and N is the number of active cycles.

To do this, we ran three cases, each with a different number of active cycles. These cases are outlined in Table 2.3.

Table 2.3: Simulation parameters, problem #1

Case	Inactive cycles	Active Cycles	Histories/Cycle
A	70	50	1e6
B	70	100	1e6
C	70	200	1e6

A large number of particles per cycle are simulated for problem #1. This minimizes high-frequency error in the solution, which in turn makes it simpler to examine convergence trends. We use a 0.5-centimeter tally grid for all cases.

First, we compare the MC eigenfunction estimate to a high-resolution S_N benchmark solution. This comparison is shown in Figure 2.5. The benchmark solution was generated using the S_{32} Gauss-Legendre quadrature set, with step characteristic spatial differencing and a 0.05-centimeter spatial discretization. The two solutions agree reasonably well, though the MC eigenfunction is tipped slightly to the right (that is, it overpredicts the solution in the right half of the problem, and underpredicts it in the left half). This "tipped" solution behavior is commonly observed in MC *k*-eigenvalue simulations of high dominance-ratio problems.

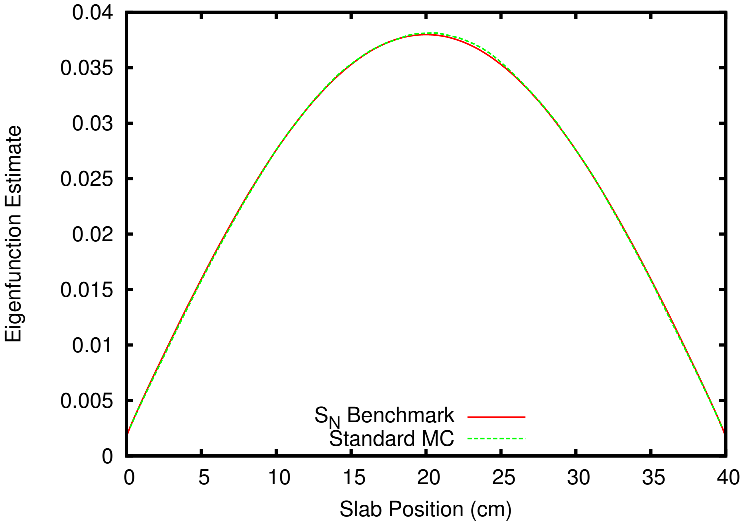

Figure 2.5: Std. MC eigenfunction estimate, problem #1, case A

Next, we consider the relationship between the eigenfunction apparent relative standard deviation (RSD) and number of active cycles. If the MC k-eigenvalue iteration scheme behaves according to the CLT, increasing the number of active cycles by a factor of 2 should decrease the apparent RSD by a factor of $\sqrt{2}$ (≈ 1.414). Equivalently,

$$\frac{\mathrm{RSD}_N(x)}{\mathrm{RSD}_{2N}(x)} = \frac{\frac{C}{\sqrt{N}}}{\frac{C}{\sqrt{2N}}} = \frac{\sqrt{2N}}{\sqrt{N}} = \sqrt{2}\,. \tag{2.20}$$

Figure 2.6 shows apparent RSD ratios for Problem 1, with a line at $\sqrt{2}$ included for reference. Both the case A/case B and case B/case C ratios are, on average, slightly less than the $\sqrt{2}$ ratio predicted by the CLT. We hypothesize that this is due in part to the relatively small number of active cycles used in these cases. Because the CLT assumes a large number of samples, we would expect better results for larger runs. In addition, the active cycles suffer from some degree of inter-cycle correlation, which violates the independent sample assumption of the CLT.

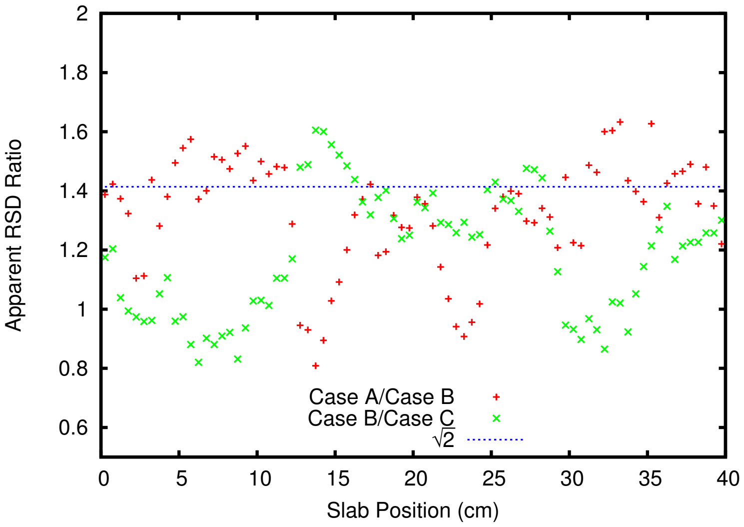

Figure 2.6: Std. MC apparent RSD ratios for problem #1

We also use problem #1 to investigate the standard MC real-to-apparent RSD ratio. As discussed in Section 1.1.2, strong inter-cycle correlation effects often exist in large, high dominance ratio MC simulations. (In low dominance ratio problems, the fission source shape can change significantly from cycle to cycle, limiting the amount of observed inter-cycle correlation.) This phenomenon occurs when the global MC fission source shape fails to converge sufficiently during inactive cycles, instead continuing to "wobble" during the active cycle phase. Because the MC fission bank is formed using histories from the previous cycle, adjacent cycle solutions are not truly independent. As previously mentioned, this violates the independent sample assumption of the CLT.

To obtain an estimate of the real solution RSD, we repeat case A 25 times, each with a different random number seed. In doing this, we ensure that the simulations are independent of one another (though the cycles within a single simulation are not). After the simulations have run, statistics are calculated on the independent solution estimates and compared to the apparent RSD estimate from a single simulation. If the real RSD is higher than the apparent RSD, inter-cycle correlation is likely present. This, in turn, implies that active cycle tallies from a single simulation are not sufficiently independent to meet the assumptions of the CLT.

The real-to-apparent RSD ratio for case A is shown in Figure 2.7, with unity plotted as a reference. The average real-to-apparent RSD ratio for the standard MC iteration scheme is roughly 4.5 for problem #1. This indicates that a large amount of inter-cycle correlation is present in problem #1, which is consistent with observations in the literature [15].

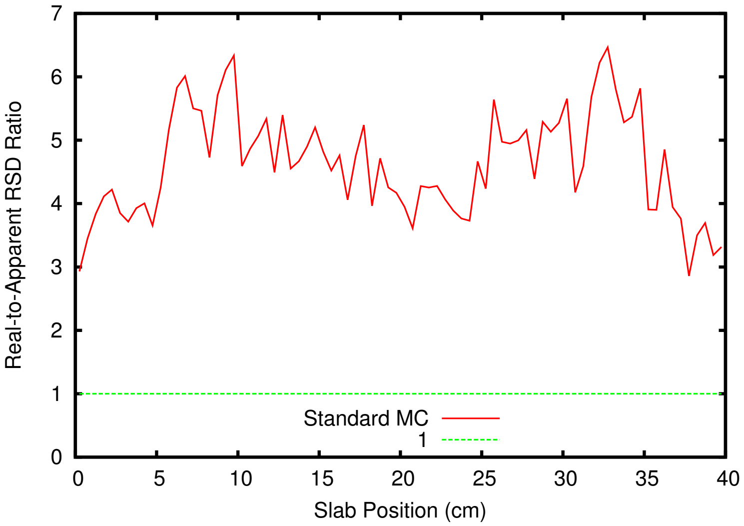

Figure 2.7: Std. MC real-to-apparent RSD ratio, problem #1

The inter-cycle correlations lead to untrustworthy apparent RSD estimates when standard MC is used to simulate large, high dominance-ratio *k*-eigenvalue problems.

2.4.2.2 1-D Core Problem

In addition to the homogeneous problem presented above, we consider a one-dimensional monoenergetic core problem (originally developed by H.G. Joo at Seoul National University). This problem is designed to represent the spatial heterogeneity of a real reactor core, while retaining simplified energy and angular dependence.

Five different assembly types are modeled, including a homogeneous reflector assembly. Each of the assemblies contains 16 pin cells, and each pin cell is composed of three 0.425-cm material regions. The 1-D core problem is hereafter designated as problem #2.

Figure 2.8 shows the spatial arrangement of assembly types in problem #2. We note the asymmetric distribution of fuel assemblies in the core, which removes half-core symmetry from the solution shape. There are 17 assemblies in the 1-D core, for a total slab width of 346.8 cm. The fundamental eigenvalue of problem #2 is approximately 1.2122 (from our high-resolution S_N benchmark solution).

R	C	C	B	B	M	B	B	M	B	B	M	B	B	A	C	R

Figure 2.8: Core layout for problem #2 [16]

Figure 2.9 shows the spatial distribution of pin-cell types within each assembly type. The pin-cell material layouts are listed in Table 2.4; reflector and water-hole pin cells are homogeneous, while fuel pin cells are heterogeneous. Finally, material cross sections for problem #2 are given in Table 2.5.

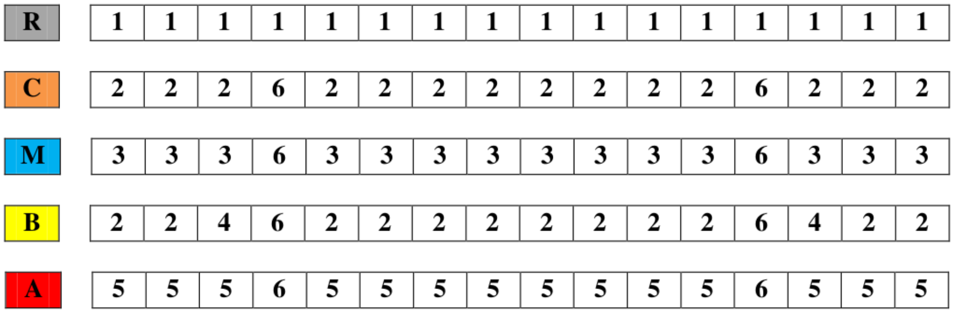

R	1	1	1	1	1	1	1	1	1	1	1	1	1	1	1	1
C	2	2	2	6	2	2	2	2	2	2	2	2	6	2	2	2
M	3	3	3	6	3	3	3	3	3	3	3	3	6	3	3	3
B	2	2	4	6	2	2	2	2	2	2	2	2	6	4	2	2
A	5	5	5	6	5	5	5	5	5	5	5	5	6	5	5	5

Figure 2.9: Assembly layouts for problem #2 [16]

We begin by examining the standard MC eigenfunction solution for problem #2. A benchmark solution was generated using a discrete-ordinates code with a very fine space-angle grid (S_{32} quadrature, 0.0425-cm spatial mesh) and step characteristic spatial discretization. Parameters for the MC simulation are shown in Table 2.6; we note the large number of inactive cycles required to approach fission source convergence. To determine the number of inactive cycles, we run a test case and examine the value of the Shannon entropy (see Figure 2.13). When the Shannon entropy approaches a stationary value, we

Table 2.4: Pin-cell layouts for problem #2

Pin ID	Description	Mat. 1	Mat. 2	Mat. 3
1	Reflector	m6	m6	m6
2	UO_2 Pin A	m1	m2	m1
3	MOX Pin	m1	m3	m1
4	Gd-doped UO_2	m1	m4	m1
5	UO_2 Pin B	m1	m5	m1
6	Water Hole	m7	m7	m7

Table 2.5: Cross sections, problem #2

Material	Description	Σ_t (cm^{-1})	Σ_s (cm^{-1})	Σ_a (cm^{-1})	$\nu\Sigma_f$ (cm^{-1})
m1	Water (Pin-cell)	1.74712e-01	1.73779e-01	9.33242e-04	n/a
m2	UO_2 Fuel A	3.32736e-01	2.74910e-01	5.78256e-02	7.97840e-02
m3	MOX Fuel	2.82549e-01	2.14888e-01	6.76607e-02	8.64238e-02
m4	UO_2 Fuel w/ Gd	8.58461e-02	4.32728e-02	4.25733e-02	1.85589e-03
m5	UO_2 Fuel B	3.33356e-01	2.755534e-01	5.78218e-02	7.96455e-02
m6	Water (Reflector)	7.85602e-02	7.77942e-02	7.65957e-04	n/a
m7	Water (Water Hole)	9.01554e-02	9.96296e-02	5.25823e-04	n/a

assume the fission source is converged. The MC and benchmark eigenfunctions for problem #2 are shown in Figure 2.10, with a close-up view in Figure 2.11. The MC estimate is averaged over all 100 active cycles.

Table 2.6: Simulation parameters, problem #2

Inactive cycles	Active Cycles	Histories/Cycle
150	100	1e5

The MC eigenfunction agrees reasonably well with the benchmark solution in the left-hand portion of the core; however, it significantly overpredicts the flux in the core center, and underpredicts the flux near the right-hand edge. This is clearly seen in Figure 2.11.

To further assess the performance of the standard MC iteration, we also compare eigenfunction estimates averaged over cycles 150-200 and 200-250 to the benchmark solution (see Figure 2.12). The 50-cycle MC eigenfunction estimates more clearly demonstrate the fission source "wobble" effect observed in high dominance-ratio problems. The two 50-cycle averages are tipped in opposite directions, indicating that the fission source shape is not fully converged. In this case, errors in the 50-cycle eigenfunction estimates largely cancel out, which results in a considerably more accurate 100-cycle eigenfunction estimate.

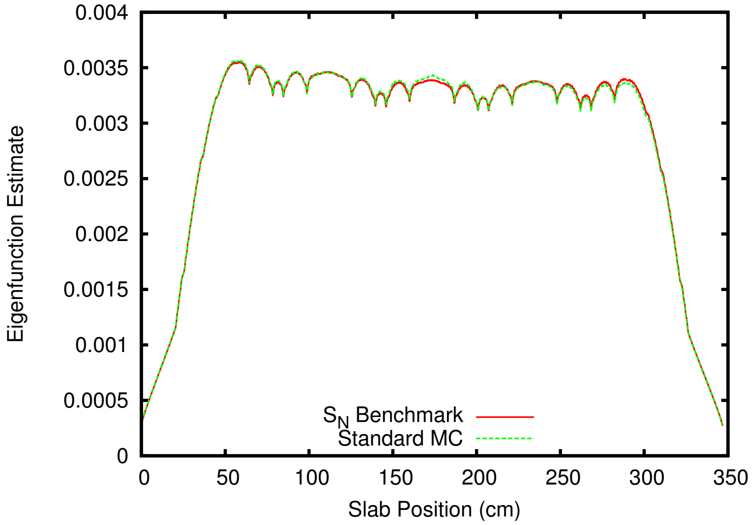

Figure 2.10: Std. MC eigenfunction estimate, problem #2

However, this type of error cancellation is not guaranteed, as it depends on the number of active cycles and the cycle-to-cycle variation of the fission source “wobble.”

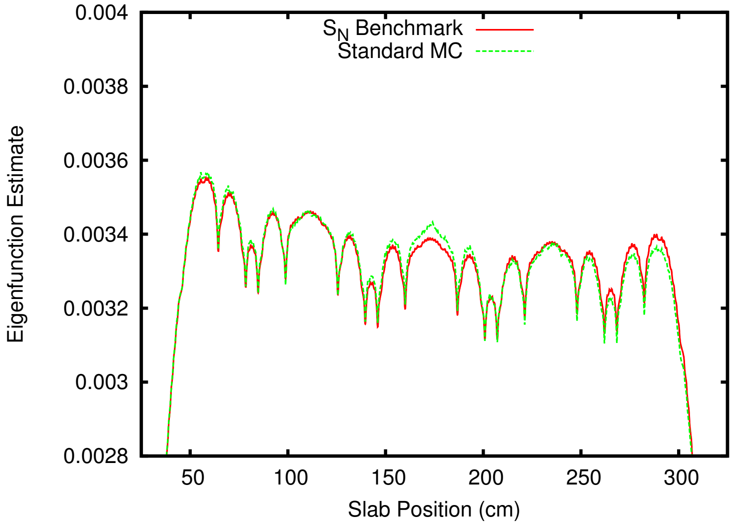

Figure 2.11: Std. MC close-up of eigenfunction estimate, problem #2

Figure 2.13 shows the cycle Shannon entropy of the fission bank for problem #2. The Shannon entropy [17] is used as a rough measure of fission source convergence, and is calculated using

$$H = \sum_{k=1}^{K} -F_k \ln F_k \,, \tag{2.21}$$

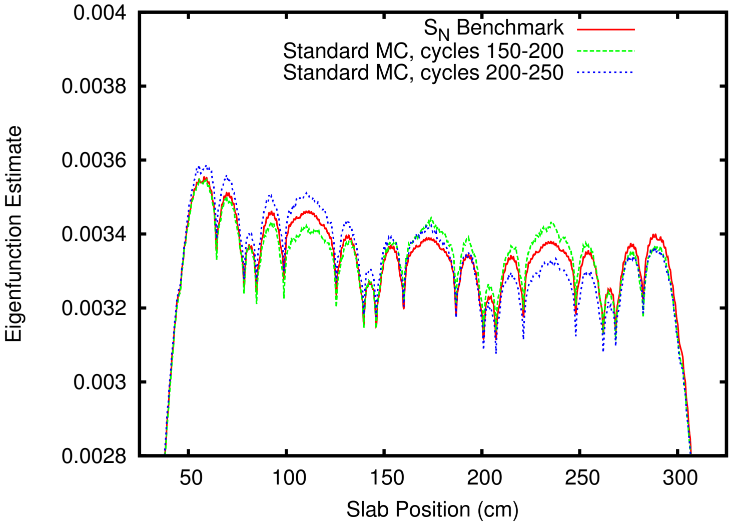

Figure 2.12: Std. MC close-up of 50-cycle eigenfunction estimates, problem #2

where F_k is the fraction of the fission source in spatial cell k, and K is the total number of cells. If the fission source is fully converged (i.e. not changing at all from cycle to cycle), the Shannon entropy is nearly a (problem-dependent) constant value. In reality, some degree of random error is always present in the Monte Carlo fission bank, which introduces random fluctuation in the Shannon entropy. On inspection of Figure 2.13, we observe that fluctuations in the Shannon entropy for problem #2 are not completely random, even during active cycles (when the fission bank is assumed to be converged). Instead, the fission source drifts slowly around a mean value. This indicates that the standard MC k-eigenvalue iteration does not completely "converge" the fission source for problem #2.

Finally, in Figure 2.14 we compare the apparent MC RSD for problem #2 to the relative error in the solution (with respect to the S$_N$ benchmark). The apparent RSD is calculated using cycle-wise results from the active-cycle phase of the MC calculation, while the solution relative error in spatial cell k is calculated using

$$RE_k = \frac{|\phi_{k,S_N} - \phi_{k,MC}|}{\phi_{k,S_N}} \, . \tag{2.22}$$

In Eq. (2.22), $\phi_{k,MC}$ is the MC eigenfunction estimate in cell k, averaged over all active cycles.

If active-cycle error in the MC simulation is dominated by stochastic error (i.e. the fission source is sufficiently converged), the apparent RSD should be an unbiased estimate of the fluctuation in the fine cell average eigenfunction. If, however, the fission source is not sufficiently converged by the onset of active cycles, the apparent RSD will tend to

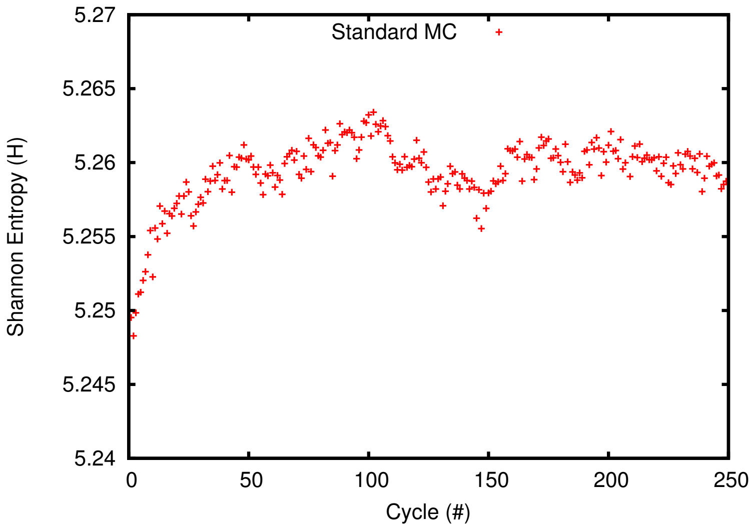

Figure 2.13: Std. MC Shannon entropy vs. cycle number, problem #2

underestimate the fluctuation in the eigenfunction. In this case, the real relative error in the solution will generally be larger than the apparent RSD predicts.

In Figure 2.14, the relative solution error (Figure 2.14b) is considerably higher than the apparent RSD (Figure 2.14a) over most of the spatial domain. In addition, the two error shapes are considerably different across the problem domain. The apparent RSD predicts a reasonably smooth error distribution across the core, with slight increases in the reflector assemblies. In reality, the relative error (with respect to the benchmark solution) has a distinct oscillating shape, with peaks in the center and outer edges of the core. This shape reflects the underlying "wobble" of the fission source, and confirms that the standard MC *k*-eigenvalue iteration fails to converge the fission source for problem #2.

2.4.2.3 2-D Quarter-Assembly Problem

We now present results for a 2-D UO_2 quarter-assembly problem with seven energy groups, hereafter referred to as problem #3. The problem geometry is shown in Figure 2.15, with a different color for each material. UO_2 fuel is shown in blue, guide tubes are peach, the central fission chamber is green, and the surrounding water reflector is teal. The north and west boundaries of the domain are reflective, while the south and east boundaries are vacuum. The reflector region is one quarter-assembly in width.

Problem #3 uses cross sections and pin-cell layouts for the C5G7 benchmark UO_2 assembly; this data are given in Appendix .

Standard MC simulation parameters for problem #3 are listed in Table 2.7. Since no

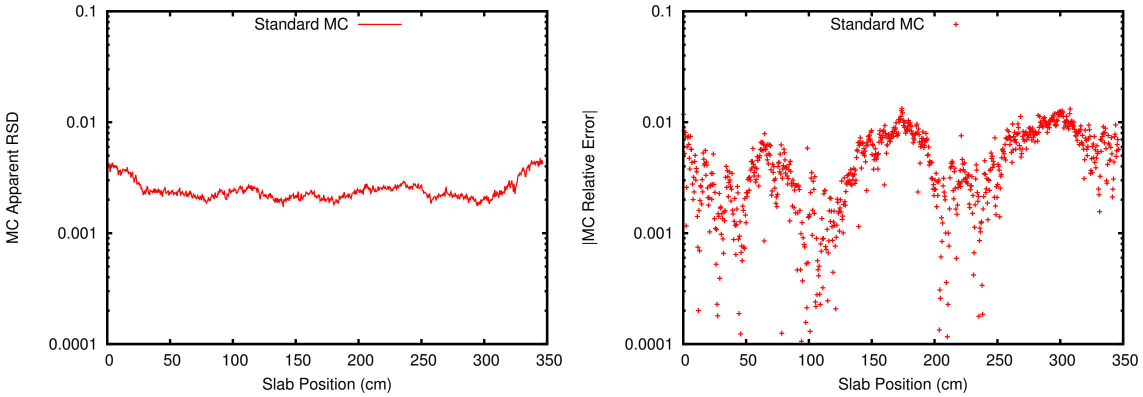

(a) Apparent RSD (b) Relative error from benchmark

Figure 2.14: Std. MC solution error curves, problem #2

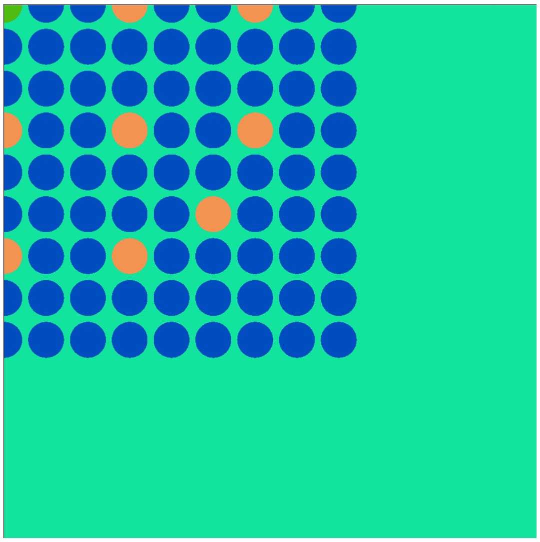

Figure 2.15: Problem #3 geometry

reference solution is available for problem #3, we ran a large number of particles per cycle to ensure an accurate eigenfunction solution. This problem is not optically thick, and thus it should not suffer from large inter-cycle correlation effects. As a result, we expect apparent RSD estimates to be reasonably accurate. The *k*-eigenvalue for problem #3 is roughly 0.767.

Table 2.7: Simulation parameters, problem #3

Inactive Cyc.	Active Cyc.	Hist./Cyc.
50	50	2e5

In Figure 2.16, we present fast and thermal flux distributions for problem #3. In this work, the “fast” group contains C5G7 energy groups 1 through 3, while the “thermal” group contains C5G7 energy groups 4 through 7. (The logic behind this group structure is discussed in Section 3.5.2.5.) The flux distributions are plotted on a uniform 20×20 grid, which tends to “smear” fine spatial variations near the guide tubes and fuel-reflector interface. This grid size was chosen to minimize statistical noise, while preserving major features of the flux shape.

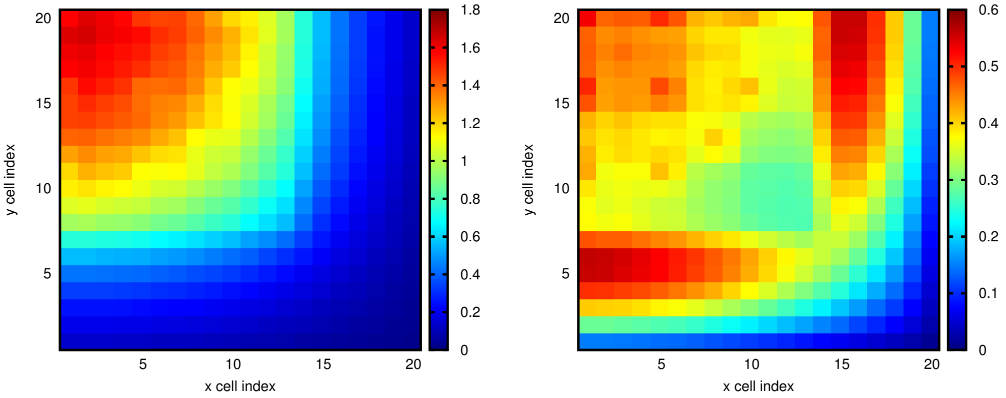

(a) Fast flux (C5G7 grp. 1-3)

(b) Thermal flux (C5G7 grp. 4-7)

Figure 2.16: Std. MC fast and thermal flux distributions, problem #3

The global shape of the fast flux distribution is dominated by leakage, which is significant in a problem of this size. The fast flux is highest near the reflecting boundaries, and lowest near the vacuum boundaries. There is a slight fast flux dip in the upper left-hand cell, as a result of the fission chamber (which produces fewer fast neutrons than the fuel pins, because the fission rate is very low).

The global thermal flux shape is peaked near the upper-left corner of the problem geometry. In addition, local thermal flux peaks occur in the portion of the reflector region closest to the fuel. These peaks are a result of fast and epithermal neutrons that exit the fuel and downscatter in the reflector.

Next, we consider quarter-pin power tallies for problem #3. In this work, quarter-pin power is defined as the total fission rate in each fuel quarter-pin. In other words, the “power” of a quarter-pin with x-position i and y-position j (denoted $P_{pin,i,j}$) is calculated using:

$$P_{pin,i,j} = \sum_{g=1}^{7} \int_{V_{pin}} \Sigma_{f,g}(\vec{x})\phi_g(\vec{x})dV \,, \tag{2.23}$$

where V_{pin} is the quarter-pin volume, $\Sigma_{f,g}(\vec{x})$ is the group- and position-dependent fission cross section, and $\phi_g(\vec{x})$ is the group- and position-dependent scalar flux.

Quarter-pin power and quarter-pin power apparent RSD distributions for problem #3 are given in Figure 2.17. As expected, power is highest near the upper-left corner of the problem domain (adjacent to the reflecting boundaries). Small power increases occur near the guide tube regions, which act as a source of thermal neutrons for fission. The same is true near the south and east edges of the fuel assembly, where neutrons thermalized in the reflector cause an increase in thermal fission along the edge of the assembly.

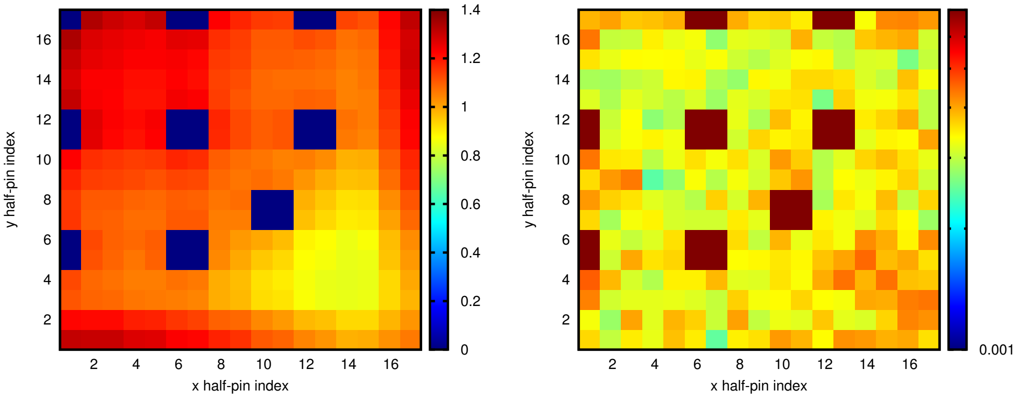

(a) Pin power (b) Apparent RSD

Figure 2.17: Std. MC pin power and apparent RSD, problem #3

The quarter-pin power apparent RSD distribution is relatively flat across the fuel region, with a slight increase near the lower-right edge of the fuel.

2.4.2.4 2-D Assembly Problem

Here, we consider a 2-D MOX assembly problem with seven-group cross sections. The assembly problem will hereafter be referred to as problem #4. As in problem #3, we use material cross-sections and assembly layouts from the C5G7 benchmark definition; problem geometry is shown in Figure 2.18. There are three enrichments of MOX fuel in problem #4, which are shown in brown, red, and purple in Figure 2.18. The central fission chamber is green, guide tubes are peach, and the surrounding water reflector is teal. The north and west boundaries of problem #4 are reflective, while the south and east boundaries are vacuum. The reflector region is one half assembly in width.

Standard MC simulation parameters for problem #4 are listed in Table 2.8. The *k*-eigenvalue for this problem is approximately 0.972.

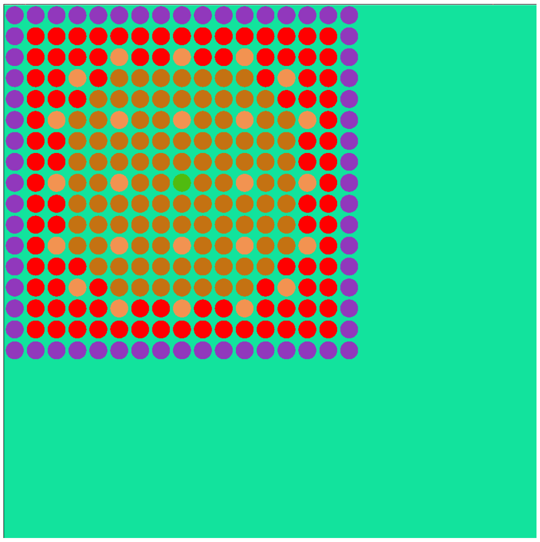

Figure 2.18: Problem #4 geometry

Table 2.8: Simulation parameters, problem #4

Inactive Cyc.	Active Cyc.	Hist./Cyc.
50	50	2e5

Fast and thermal flux distributions for problem #4 are shown in Figure 2.19. Similar to problem #3, the global fast flux shape is peaked near the upper-left corner of the problem domain, adjacent to the reflecting boundaries. The fast flux decreases relatively smoothly across the problem, with a minimum near the south and east vacuum boundaries. Slight fast flux dips are observed near the guide tubes, where no fast neutrons are produced.

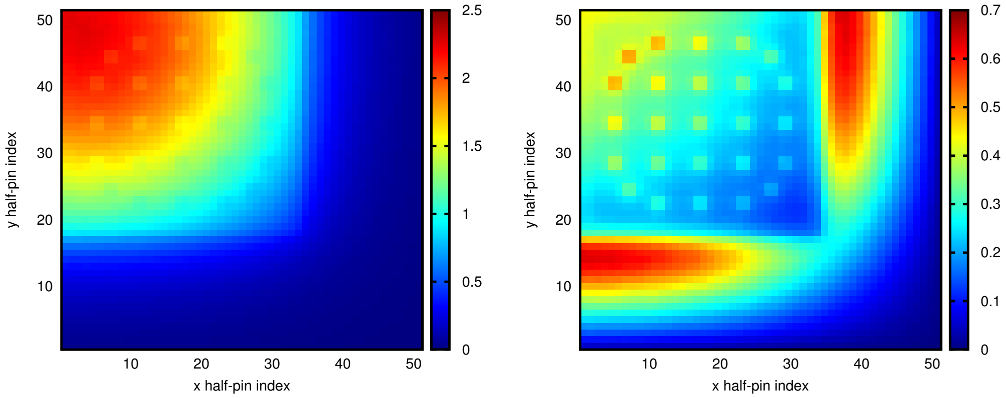

(a) Fast flux (C5G7 grp. 1-3)

(b) Thermal flux (C5G7 grp. 4-7)

Figure 2.19: Std. MC fast and thermal flux distributions, problem #4

The thermal flux is strongly peaked along the fuel-reflector interface, as a result of fast and epithermal neutrons that leak from the fuel and downscatter in the reflector region. We also observe local thermal flux peaks in guide tube regions, where no thermal fission occurs.

Figure 2.20 shows standard MC pin power and pin power apparent RSD distributions for problem #4. As in problem #3, we plot only the fuel region, because the reflector is non-fissile.

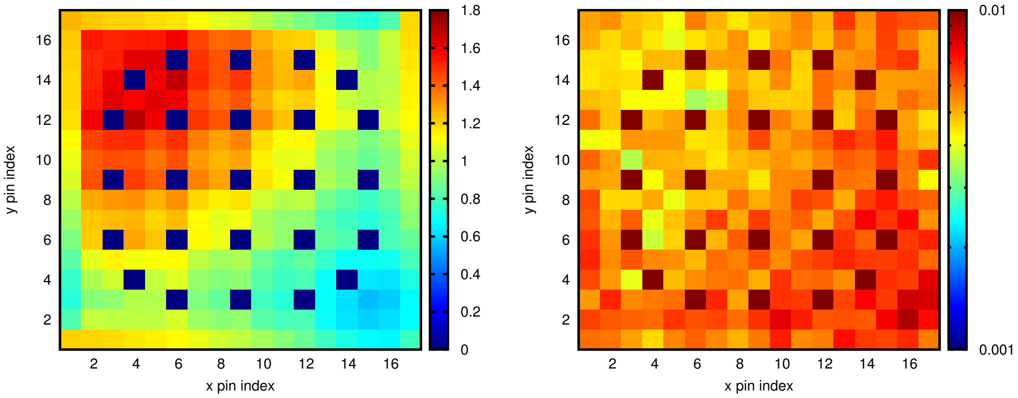

(a) Pin power

(b) Apparent RSD

Figure 2.20: Std. MC pin power and apparent RSD, problem #4

The pin power is highest in the upper-left corner of the problem domain, near the reflecting boundaries. The outside ring of fuel pins contains a lower enrichment of MOX fuel than the rest of the assembly, which results in a pin power dip immediately adjacent to the north and west boundaries.

In general, the pin power decreases smoothly from the upper-left corner of the assembly to the lower-right (with the exception of the guide tubes and fission chamber). On average, the pin-power apparent RSD is smaller in the upper-left portion of the problem, and larger in the lower-right.

2.4.2.5 2-D C5G7 Benchmark

Finally, we consider the 2-D C5G7 benchmark problem. This problem was originally developed to evaluate the accuracy of pin power solutions obtained using deterministic methods without spatial homogenization (these solutions invariably contain systematic error as a result of spatial discretization, approximate geometry representation, and, in some codes, the diffusion approximation).

The C5G7 problem is composed of 4 fuel assemblies, surrounded by 5 fully homogeneous reflector "assemblies." The north and west boundary conditions are reflective, which creates quarter-core symmetry (the south and east boundaries are vacuum). With a total core size of 16 fuel assemblies (taking the reflecting boundaries into account), the C5G7 problem geometry is not as large as a full-size power reactor core. However, it *is* optically thick enough to present a computational challenge for hybrid MC methods, while maintaining reasonable runtimes on a personal computer.

In addition, the C5G7 benchmark uses 7-group cross sections, which allow us to test our methods for a problem with some energy dependence. While real-world MC simulations almost always use continuous-energy cross sections, the multigroup treatment limits to continuous energy as the number of energy groups approaches infinity. Thus, performance comparisons for the C5G7 benchmark are more applicable to real-world reactor core simulations than results from monoenergetic problems. The 2-D 7-group C5G7 benchmark problem is hereafter designated as problem #5.

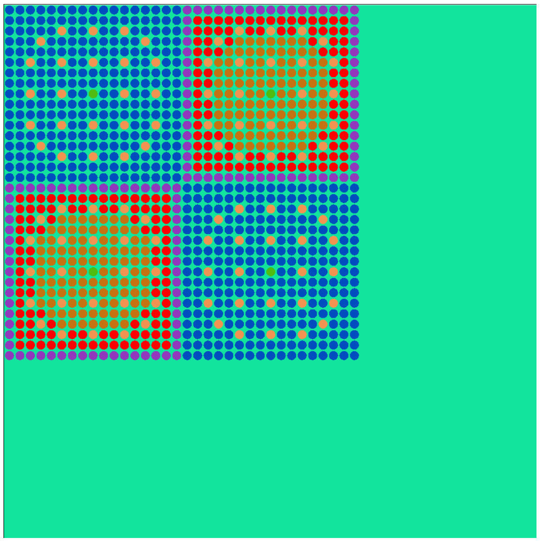

Figure 2.21: Problem #5 geometry

Problem #5 contains three fuel types: one UO_2 fuel, and three different MOX enrichments. Fuel and cladding materials are homogenized together. As a result, each 1.26 cm×1.26 cm pin cell contains only two material regions (the homogenized fuel-clad mixture and surrounding moderator). Figure 2.21 shows the geometry of problem #5, with different colors corresponding to different materials. Fuel assemblies are in the upper left, with reflector regions (teal) along the right and bottom edges of the spatial domain. Each fuel assembly is comprised of a 17×17 array of pin cells, with a symmetric array of control rod guide tubes (brownish-orange), as well as a central fission chamber (green). The upper left and lower right fuel assemblies contain UO_2 fuel, while the lower left and upper right assemblies contain MOX fuel of varying enrichment.

Material cross sections for problem #5 are given in Appendix , and simulation parameters are listed in Table 2.9. The observant reader may note that we use a relatively small number of histories per cycle (given the size of the C5G7 tally space). This is done intentionally, to mimic the low particle density dictated by memory limitations when full-size core problems are run on a personal computer.

Table 2.9: Simulation parameters, problem #5

Inactive cycles	Active Cycles	Histories/Cycle
100	100	5e4

In our standard MC simulation of problem #5, we tally group-wise fluxes and pin powers on a pin-cell grid. We are then able to compare pin power results with the provided benchmark solution, which was generated using the production-scale radiation transport code MCNP [18]. The MCNP code employs the standard MC *k*-eigenvalue iteration, and as such the benchmark solution contains statistical error. The MCNP reference solution was generated using approximately 300 million histories; thus, it should have considerably lower error than our solutions (which use 5 million histories).

Fast and thermal group pin-cell fluxes are shown in Figure 2.22. Here, the original seven-group fluxes have been summed into two coarse groups; the group boundaries are chosen to match the coarse group structure used in our CMFD simulations (see Chapter 3.6).

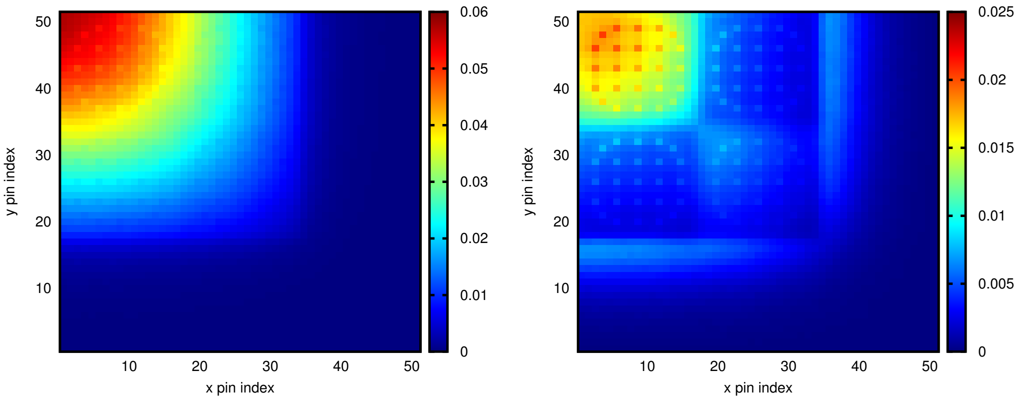

(a) Fast (C5G7 grp. 1-3) (b) Thermal (C5G7 grp. 4-7)

Figure 2.22: Std. MC fast and thermal flux distributions, problem #5

The fast flux shape (Figure 2.22a) is smoothly-varying across most of the domain, and is peaked in the upper left corner (adjacent to the two reflecting boundaries). Because problem #5 appears relatively optically thin to fast neutrons, the fast flux shape is strongly influenced by leakage through the east and south boundaries of the problem. We observe slight depressions in the fast flux in guide tube regions, because fast neutrons are produced only in the fuel pin regions of the assembly.

The spatial shape of the thermal flux (Figure 2.22b) is considerably more complicated than the fast flux. While the overall shape is somewhat similar (peaked near the reflective boundaries and minimized near the vacuum boundaries), the thermal flux has local peaks near the fuel-reflector interface. Thermal neutrons in this region are largely a product of fast and epithermal neutrons that exit the fuel, then downscatter in the reflector. The thermal flux is higher in the guide tube and fission chamber cells than in the surrounding fuel pins, because these fuel pins act as a sink for thermal neutrons. Finally, the thermal flux is relatively lower in the MOX assemblies than the UO_2 assemblies, because the MOX fuel has higher cross sections for thermal fission.

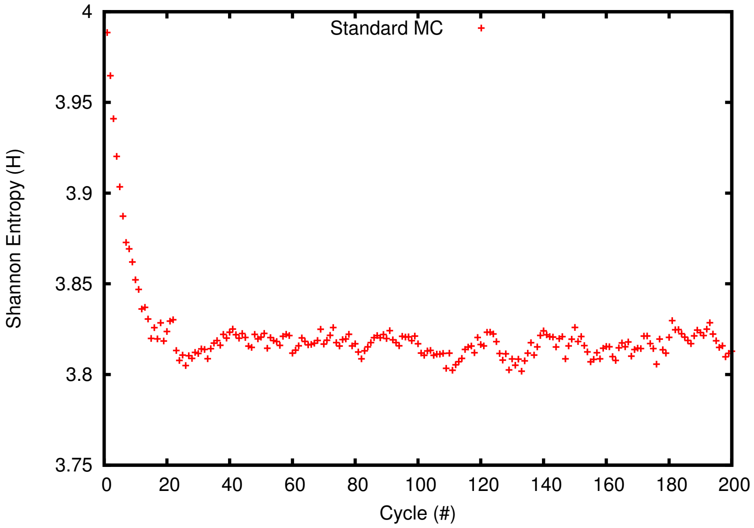

Figure 2.23: Std. MC Shannon entropy vs. cycle number, problem #5

To assess the convergence of the fission source for problem #5, we plot the MC Shannon entropy in Figure 2.23. As we observed in problem #2, we see that the Shannon entropy for problem #5 continues to oscillate slowly around a mean value during active cycles (cycles 100-200), indicating that the fission source is not completely stationary. The fluctuations are relatively small; thus, we expect this simulation to produce reasonably accurate results, though the apparent RSD may still underpredict real solution error.

Figure 2.24 plots the standard MC pin power distribution for problem #5, normalized so that the average pin power is unity. We note that Figure 2.24 shows only the four fuel assemblies, because pin power in the reflector assemblies is zero.

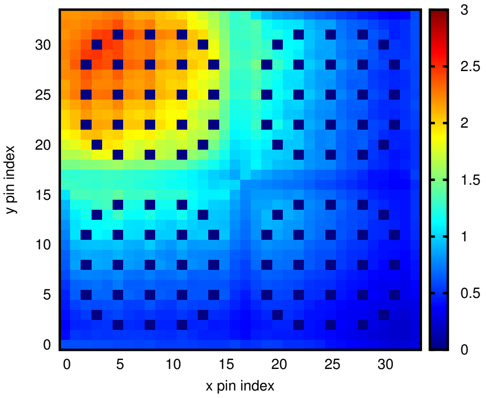

Figure 2.24: Std. MC pin power distribution, problem #5

The pin power is maximized in the upper-left fuel assembly, near the reflecting boundaries. Conversely, it is minimized near the eastern and southern edges of the fuel region (near the fuel-reflector interface). This is consistent with the overall shape of the thermal and fast flux distributions presented in Figure 2.22.

Since the benchmark solution provides a pin power distribution, we are able to calculate relative error in our MC results with respect to the benchmark. As previously mentioned, the benchmark solution for the C5G7 problem was also generated using MC; however, the benchmark simulation uses many more histories, and should thus have considerably lower error than our results.

In Figure 2.25, we present the MC pin power apparent RSD and relative error distributions for problem #5. As in Figure 2.24, these plots include only the four fuel assemblies.

Both plots in Figure 2.25 use the same color scale for straightforward comparison. Pin power errors are not calculated for the guide tubes, which are non-fissile.

In general, the shape of the apparent RSD trend matches the relative solution error reasonably well. On average, the relative error is lower in the upper-left fuel assembly (where the density of histories is highest), and higher near the fuel-reflector interface (where the density of particles is lowest). When averaged over the slab, the relative error (calculated with respect to the benchmark) appears to be slightly higher than the apparent RSD; this is difficult to determine visually using the data in Figure 2.25.

Agreement observed between the relative error and apparent RSD plots in Figure 2.25 implies that inter-cycle correlation is relatively weak in problem #5. The limited amount of Shannon entropy fluctuation shown in Figure 2.23 supports this hypothesis. This is not a

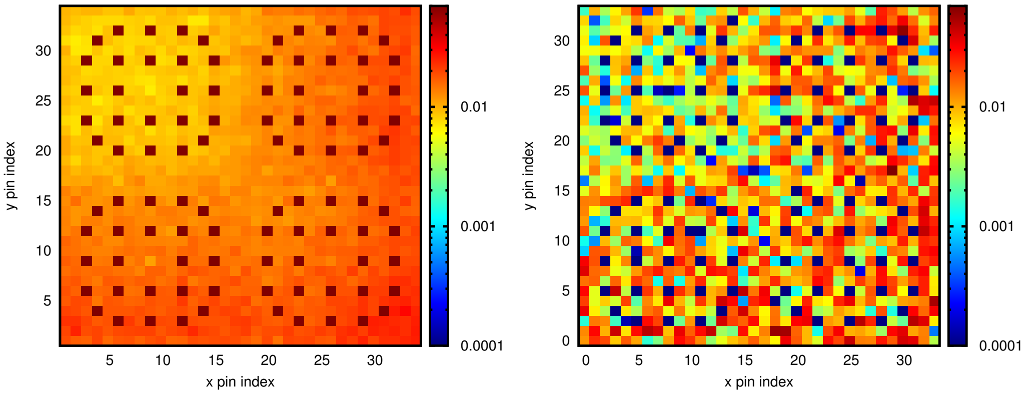

(a) Apparent RSD (b) Relative error

Figure 2.25: Std. MC pin power apparent RSD and relative error from benchmark, problem #5

surprising observation; while problem #2 is 17 assemblies wide, the C5G7 problem is only a six-by-six array of assemblies (when the reflecting boundaries are taken into account). In addition, the two-dimensional C5G7 geometry allows for more leakage, which tends to decrease the spectral radius of the calculation.

To better present error information for problem #5, we also compute errors for the four fuel assembly regions. In Table 2.10, we list assembly apparent RSD, as well as relative error with respect to the benchmark. Data is arranged in a matrix format, with row and column indices to identify each assembly.

Table 2.10: Std. MC assembly apparent RSD and relative error (|%|), problem #5

	1	2
1	0.055	0.091
2	0.090	0.101

(a) Apparent RSD

	1	2
1	0.097	0.462
2	0.055	0.441

(b) Relative error

By the Central Limit Theorem (CLT), we expect roughly 68% of relative error values to fall at or below the apparent RSD values listed in Table 2.10. Thus, for the four assembly data points, we expect two or three of the relative error values to be less than (or equal to) their corresponding apparent RSD. However, only one of the relative error values (for assembly [1,1], which is the upper-left UO_2 assembly) falls within this interval.

There are several possible explanations for this observation. First of all, we expect some degree of inter-cycle correlation in problem #5, even though it is not particularly optically thick. Inter-cycle correlation can cause the standard MC apparent RSD to underpredict error in the solution.

In addition, the problem #5 benchmark solution was generated using standard MC, and thus has statistical error. Even though error in the benchmark should be considerably lower than error in our results, it may still be significant enough to affect our relative error calculation.

Finally, our MC simulation uses a relatively small number of particles per cycle, considering the large tally space of the C5G7 problem. Thus, it is possible that our simulation does not adequately satisfy the law of large numbers (an assumption of the CLT). This might also explain why the apparent RSD estimate in the upper-left fuel assembly appears to be the most accurate; a large fraction of histories contribute to tallies in this fuel assembly, which means that quantities in this region are more likely to satisfy the large number requirement of the CLT.

Table 2.11 shows the maximum and mean pin power relative error, calculated with respect to the MC benchmark solution. The fuel pin with maximum error is located in the lower-right fuel assembly, near the fuel-reflector interface. In addition, we note that the maximum pin power error is a factor of ∼ 5.7 larger than the average pin power error of 1.20%.

Table 2.11: Std. MC pin power max and mean relative error, problem #5

Max (|%|)	Mean (|%|)
6.86	1.20

2.5 Summary

This chapter began with a description of the standard MC iteration method for *k*-eigenvalue calculations. The iteration scheme (for an infinite number of particles) was then linearized and Fourier-analyzed, yielding an analytical expression for the standard MC spectral radius. Using this expression, we showed that the standard MC iteration is unconditionally stable (in the infinite-particle limit).

Two categories of numerical results were then presented. First, we compared the theoretical predictions of the Fourier analysis to numerical results from a surrogate discrete-ordinates simulation, as well as estimates obtained using direct MC. Numerical results from the surrogate simulation closely matched predictions. Direct MC estimates were quite noisy, but generally matched the predicted spectral radius trend.

Next, we assessed the performance of the MC k-eigenvalue iteration for a set of benchmark problems. We verified several findings previously published in the literature; namely, that the MC apparent RSD behaves roughly as predicted by the CLT, and that MC apparent RSD estimates severely underestimate the real RSD for high dominance-ratio problems. The MC method was also tested on four heterogeneous reactor core problems. Results from these simulations are, in later chapters, compared to results from hybrid methods considered in this thesis.

CHAPTER 3

The CMFD-MC Method

3.1 Introduction

In this chapter, we describe the CMFD-MC method for reactor core *k*-eigenvalue calculations. This was originally developed to accelerate deterministic methods, and has been used to this end in a number of production-scale reactor analysis codes [4, 19]. In 2009, Lee et. al. demonstrated that CMFD feedback could also be used to accelerate fission source convergence for Monte Carlo simulations [6].

While the original CMFD-MC method produced promising results for simple 1-D problems, results were mixed for 2- and 3-D problems [20, 21, 14]. Large, multidimensional MC simulations have a more inherently complex tally space, which can lead to considerable stochastic errors in sparsely-populated regions of the domain [22]. This led to the assumption that instabilities observed in CMFD-MC simulations were primarily driven by stochastic noise, which in turn motivated the Lee-Joo-Lee-Smith (LJLS) and Wolters modifications (which are described below in Section 3.3).

The remainder of this chapter is organized as follows. First, we describe the original CMFD-MC iteration scheme [6]. Then, we briefly outline the two major variants that exist in the literature: (i) the LJLS multi-set tally accumulation method [21], and (ii) the Wolters correction factor method [14]. Next, we Fourier-analyze the non-random CMFD-MC iteration strategy to better understand the stability behavior of the method (this and subsequent work in this chapter is new research). We then present results from the Fourier analysis, and analyze the performance of the CMFD-MC method and its variants for the problem set introduced in Chapter 2.

3.2 CMFD-MC Iteration Strategy

Here we describe the non-random CMFD-MC iteration strategy for solving MC k-eigenvalue problems. (This method is simply the CMFD-MC method [6], assuming an infinite number of particles per cycle.) We consider the monoenergetic, planar-geometry k-eigenvalue problem with periodic boundaries introduced in Chapter 2.

The ℓ^{th} CMFD-MC iteration (or "cycle") begins with Eqs. (2.1), written with iteration superscripts as follows:

$$\mu\frac{d}{dx}\psi^{(\ell+1/2)}(x,\mu)+\Sigma_t(x)\psi^{(\ell+1/2)}(x,\mu)-\frac{\Sigma_s(x)}{2}\phi^{(\ell+1/2)}(x)=\frac{\nu\Sigma_f(x)}{2k^{(\ell)}}\phi^{(\ell)}(x)\,, \tag{3.1a}$$

$$0\le x\le X\,,\ -1\le\mu\le 1\,,$$

$$\psi^{(\ell+1/2)}(0,\mu)=\psi^{(\ell+1/2)}(X,\mu)\,,\ -1\le\mu\le 1\,, \tag{3.1b}$$

where

$$\phi^{(\ell+1/2)}(x)=\int_{-1}^{1}\psi^{(\ell+1/2)}(x,\mu)d\mu\,. \tag{3.1c}$$

As noted in Chapter 2, the MC transport simulation shown in Eqs. (3.1) treats scattering implicitly. In addition, Eqs. (3.1) are not discretized in space or angle, because MC simulations involve no such discretizations. Since these equations contain no random terms, they apply to MC simulations only in the limit in which the number of particles per cycle is sufficiently large that statistical errors can be ignored.

To proceed, we impose a "coarse" spatial grid on the system, with J cells of width Δ_j ($1\le j\le J$). During the solution of Eqs. (3.1), the following quantities are tallied on the coarse grid for $1\le j\le J$. (Capital letters (Φ, Δ) denote coarse-grid quantities, while lower-case letters (ψ, ϕ) denote continuous quantities.)

$$\Phi_j^{(\ell+1/2)}=\frac{1}{\Delta_j}\int_{x_{j-1/2}}^{x_{j+1/2}}\phi^{(\ell+1/2)}(x)dx\,, \tag{3.2a}$$

$$\Phi_{1,j\pm1/2}^{(\ell+1/2)}=\int_{-1}^{1}\mu\psi^{(\ell+1/2)}(x_{j\pm1/2},\mu)d\mu\,, \tag{3.2b}$$

$$\Sigma_{a,j}^{(\ell+1/2)}=\frac{\int_{x_{j-1/2}}^{x_{j+1/2}}\Sigma_a(x)\phi^{(\ell+1/2)}(x)dx}{\int_{x_{j-1/2}}^{x_{j+1/2}}\phi^{(\ell+1/2)}(x)dx}\,, \tag{3.2c}$$

$$\Sigma_{t,j}^{(\ell+1/2)}=\frac{\int_{x_{j-1/2}}^{x_{j+1/2}}\Sigma_t(x)\phi^{(\ell+1/2)}(x)dx}{\int_{x_{j-1/2}}^{x_{j+1/2}}\phi^{(\ell+1/2)}(x)dx}\,, \tag{3.2d}$$

$$\nu\Sigma_{f,j}^{(\ell+1/2)} = \frac{\int_{x_{j-1/2}}^{x_{j+1/2}} \nu\Sigma_f(x)\phi^{(\ell+1/2)}(x)dx}{\int_{x_{j-1/2}}^{x_{j+1/2}} \phi^{(\ell+1/2)}(x)dx} . \tag{3.2e}$$

Also, the following interior-edge quantities are calculated:

$$\tilde{D}_{j+1/2}^{(\ell+1/2)} = \frac{2}{3}\left(\frac{1}{\Sigma_{t,j}^{(\ell+1/2)}\Delta_j + \Sigma_{t,j+1}^{(\ell+1/2)}\Delta_{j+1}}\right) , \tag{3.2f}$$

$$\hat{D}_{j+1/2}^{(\ell+1/2)} = \frac{\Phi_{1,j+1/2}^{(\ell+1/2)} + \tilde{D}_{j+1/2}^{(\ell+1/2)}(\Phi_{j+1}^{(\ell+1/2)} - \Phi_j^{(\ell+1/2)})}{\Phi_{j+1}^{(\ell+1/2)} + \Phi_j^{(\ell+1/2)}} , \tag{3.2g}$$

and the exterior edge quantities are calculated using the periodic boundary condition:

$$\begin{aligned}\tilde{D}_{1/2}^{(\ell+1/2)} &= \tilde{D}_{J+1/2}^{(\ell+1/2)} \\ &= \frac{2}{3}\left(\frac{1}{\Sigma_{t,1}^{(\ell+1/2)}\Delta_1 + \Sigma_{t,J}^{(\ell+1/2)}\Delta_J}\right) ,\end{aligned} \tag{3.2h}$$

$$\begin{aligned}\hat{D}_{1/2}^{(\ell+1/2)} &= \hat{D}_{J+1/2}^{(\ell+1/2)} \\ &= \frac{\Phi_{1,1/2}^{(\ell+1/2)} + \tilde{D}_{1/2}^{(\ell+1/2)}(\Phi_1^{(\ell+1/2)} - \Phi_J^{(\ell+1/2)})}{\Phi_1^{(\ell+1/2)} + \Phi_J^{(\ell+1/2)}} .\end{aligned} \tag{3.2i}$$

The MC estimates of $\Sigma_{a,j}^{(\ell+1/2)}$, $\nu\Sigma_{f,j}^{(\ell+1/2)}$, $\hat{D}_{j+1/2}^{(\ell+1/2)}$, and $\tilde{D}_{j+1/2}^{(\ell+1/2)}$ are used to build the coefficients of the CMFD system. The low-order discrete CMFD equations are:

$$\Phi_{1,j+1/2}^{(\ell+1)} - \Phi_{1,j-1/2}^{(\ell+1)} + \Sigma_{a,j}^{(\ell+1/2)}\Phi_j^{(\ell+1)}\Delta_j = \frac{\nu\Sigma_{f,j}^{(\ell+1/2)}}{k^{(\ell+1)}}\Phi_j^{(\ell+1)}\Delta_j , \quad 1 \le j \le J , \tag{3.3a}$$

$$\Phi_{1,j+1/2}^{(\ell+1)} = -\tilde{D}_{j+1/2}^{(\ell+1/2)}(\Phi_{j+1}^{(\ell+1)} - \Phi_j^{(\ell+1)}) + \hat{D}_{j+1/2}^{(\ell+1/2)}(\Phi_{j+1}^{(\ell+1)} + \Phi_j^{(\ell+1)}) , \tag{3.3b}$$

$$\Phi_{1,1/2}^{(\ell+1)} = \Phi_{1,J+1/2}^{(\ell+1)} , \tag{3.3c}$$

$$1 = \frac{1}{J}\sum_{j=1}^{J}\Phi_j^{(\ell+1)} . \tag{3.3d}$$

On convergence, Eq. (3.3a) is simply the *neutron balance equation*, obtained by integrating Eq. (2.1a) over angle and the j^{th} coarse cell. Also on convergence, Eq. (3.3b) reduces to the identity $\Phi_{1,j+1/2} = \Phi_{1,j+1/2}$. (The motivation behind the specific construction of Eq. (3.3b) is Fick's Law.) Finally, on convergence Eq. (3.3c) reduces to the condition from Eq. (2.1b) that the converged scalar flux must be periodic. For these reasons, the low-order discrete Eqs. (3.3) are fully consistent with the high-order continuous Eqs. (2.1), and on convergence, the solution of these equations would be the true scalar fluxes, volume-averaged over each coarse cell.

To proceed, the current terms $\Phi_{1,j+1/2}^{(\ell+1)}$ in Eqs. (3.3a) and (3.3b) are eliminated to form an algebraic system involving only the coarse-grid scalar fluxes, $\Phi_j^{(\ell+1)}$ (this system is not tridiagonal because of the periodic boundary condition). The solution of Eqs. (3.3) yields a new estimate of the k-eigenvalue and coarse-grid scalar flux, the latter of which is used to scale the continuous fine-grid fission source for the next cycle:

$$\nu\Sigma_f(x)\phi^{(\ell+1)}(x) = \nu\Sigma_f(x)\phi^{(\ell+1/2)}(x)\left[\frac{\Phi_j^{(\ell+1)}}{\Phi_j^{(\ell+1/2)}}\right] , \quad x_{j-1/2} \le x \le x_{j+1/2} \, , \quad 1 \le j \le J \, . \tag{3.4}$$

(The $\nu\Sigma_f$ terms in Eq. 3.4 cancel for the simple case shown here, but we retain them to indicate that we are scaling the fission source.)

This completes the description of the CMFD-MC iteration strategy [6]. To summarize, a single iteration "cycle" has the following steps: (i) perform an MC calculation, using the previous-cycle estimate of the fission source term (or initial guess if $l = 0$) [Eqs. (3.1)], (ii) use MC tallies to form the coefficients of the CMFD system [Eqs. (4.2)], (iii) solve the CMFD system [Eqs. (3.3)] to obtain an updated estimate of the coarse-grid scalar flux and eigenvalue, and (iv) scale the MC fission source using the updated coarse-grid scalar flux [Eq. (3.4)]. In a real MC simulation, step (iv) can be carried out by adjusting the weight of MC fission bank sites, or by duplicating/deleting bank sites.

In the following section, we discuss the two primary variants of CMFD-MC: the Wolters method, and the LJLS "multi-set" method.

3.3 Variants of the CMFD-MC Iteration Strategy

3.3.1 The LJLS Method

The LJLS method employs the same MC transport solve and coarse-grid tallies as the original CMFD-MC method described in Section 3.2; however, the coefficients of the low-order system are formed using the *average* of MC tallies over several cycles. For example, if tallies are averaged over the previous N_{avg} cycles, the coarse-grid cross sections become:

$$\Phi_j^{(\ell+1/2)} = \frac{1}{N_{avg}\Delta_j} \sum_{\ell'=(l-N_{avg})}^{\ell} \int_{x_{j-1/2}}^{x_{j+1/2}} \phi^{(\ell'+1/2)}(x)dx \,, \tag{3.5}$$

$$\Phi_{1,j\pm1/2}^{(\ell+1/2)} = \frac{1}{N_{avg}} \sum_{\ell'=(\ell-N_{avg})}^{\ell} \int_{-1}^{1} \mu\psi^{(\ell'+1/2)}(x_{j\pm1/2},\mu)d\mu \,, \tag{3.6}$$

$$\Sigma_{a,j}^{(\ell+1/2)} = \frac{\frac{1}{N_{avg}\Delta_j} \sum_{\ell'=(\ell-N_{avg})}^{\ell} \int_{x_{j-1/2}}^{x_{j+1/2}} \Sigma_a(x)\phi^{(\ell'+1/2)}(x)dx}{\Phi_j^{(\ell+1/2)}} \,, \tag{3.7}$$

$$\Sigma_{t,j}^{(\ell+1/2)} = \frac{\frac{1}{N_{avg}\Delta_j} \sum_{\ell'=(\ell-N_{avg})}^{\ell} \int_{x_{j-1/2}}^{x_{j+1/2}} \Sigma_t(x)\phi^{(\ell'+1/2)}(x)dx}{\Phi_j^{(\ell+1/2)}} \,, \tag{3.8}$$

$$\nu\Sigma_{f,j}^{(\ell+1/2)} = \frac{\frac{1}{N_{avg}\Delta_j} \sum_{\ell'=(\ell-N_{avg})}^{\ell} \int_{x_{j-1/2}}^{x_{j+1/2}} \nu\Sigma_f(x)\phi^{(\ell'+1/2)}(x)dx}{\Phi_j^{(\ell+1/2)}} \,. \tag{3.9}$$

The averaged tallies are flushed periodically to minimize bias, a strategy referred to as the "multi-set" method in recent work by Lee et. al. [23]. CMFD feedback is skipped during the first cycle of each set (when the tally bins contain only one cycle of MC data). The multi-set method is shown visually in Figure 3.1, for a set size of 5 cycles. (This is the set size recommended in [23]).

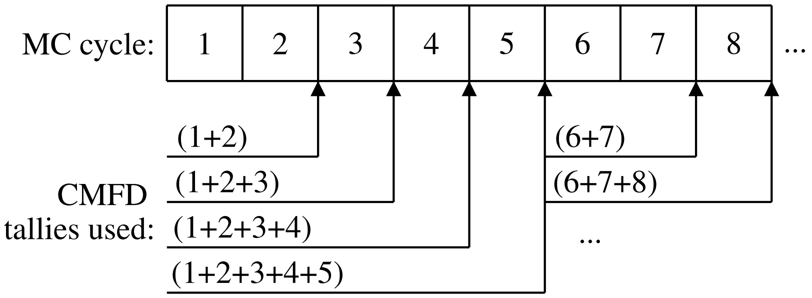

Figure 3.1: Visual description of the LJLS multi-set iteration strategy for CMFD-MC

Because more MC information is used to calculate the coarse-grid coefficients, the LJLS multi-set method effectively suppresses random noise in the CMFD system. However, when the CMFD flux solution is used to update the MC fission source during the feedback step, adjacent MC cycles are no longer independent from one another (one of the key features of the original CMFD-MC iteration scheme). Adjacent cycles in the LJLS method are not as strongly correlated as adjacent cycles in the standard MC method, but

LJLS solutions still tend to significantly underestimate solution error for high dominance ratio problems. This observation will be discussed further in Section 3.5.2.

3.3.2 The Wolters Method

The Wolters variant of CMFD-MC uses the same MC transport iteration as the original CMFD-MC method [Eqs. (3.1)]. In the Wolters method, higher-order quantities and spatially weighted current-like terms are tallied during the MC solve (in addition to the coarse grid flux-weighted cross sections and edge currents needed for the standard CMFD calculation). These quantities are used to form a correction to the CMFD $\hat{D}$ term, which helps suppress stochastic noise in the low-order system. The underlying assumption of the Wolters correction is that, if the same random neutron histories contribute to both the original $\hat{D}$ and the correction term, the two quantities will be correlated. Thus, when the correction term is subtracted from the numerator of the $\hat{D}$ value, the result will have less relative stochastic error than the original expression. To describe the Wolters method mathematically, we begin with the monoenergetic, planar-geometry transport equation:

$$\mu\frac{d}{dx}\psi(x,\mu)+\Sigma_t(x)\psi(x,\mu)-\frac{\Sigma_s(x)}{2}\phi(x)=\frac{\nu\Sigma_f(x)}{2k}\phi(x)\,.$$

We then operate on this equation by $\int_{-1}^{1}\mu(\cdot)d\mu$ to obtain:

$$\frac{d}{dx}\phi_2(x)+\Sigma_t(x)\phi_1(x)=0\,, \tag{3.10}$$

where

$$\phi_n(x)=\int_{-1}^{1}\mu^n\psi(x,\mu)d\mu\,.$$

Next, we multiply Eq. (3.10) by a spatial weighting function. The choice of the weighting function is arbitrary. Here, we present the two simplest functions considered in Wolters' work: (i) a histogram function, and (ii) a linear "tent" function.

First, we define a coarse grid with cells of width Δ_j, where

$$x_j=\text{midpoint of cell } j=\frac{1}{2}\left(x_{j-1/2}+x_{j+1/2}\right)\,. \tag{3.11}$$

This coarse grid is shown in Figure 3.2.

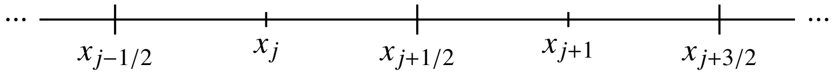

Figure 3.2: Coarse grid structure

In the histogram case, we operate on Eq. (3.10) by

$$\int_{x_{j-1/2}}^{x_{j+3/2}} (\cdot) dx \tag{3.12}$$

to get

$$\phi_{2,j+3/2} - \phi_{2,j-1/2} + \int_{x_{j-1/2}}^{x_{j+3/2}} \Sigma_t(x)\phi_1(x)dx = 0 \, .$$

If we divide this expression by

$$\int_{x_{j-1/2}}^{x_{j+3/2}} \Sigma_t(x)dx \, , \tag{3.13}$$

we obtain:

$$\frac{\phi_{2,j+3/2} - \phi_{2,j-1/2}}{\int_{x_{j-1/2}}^{x_{j+3/2}} \Sigma_t(x)dx} + \frac{\int_{x_{j-1/2}}^{x_{j+3/2}} \Sigma_t(x)\phi_1(x)dx}{\int_{x_{j-1/2}}^{x_{j+3/2}} \Sigma_t(x)dx} = 0 \, . \tag{3.14}$$

The second term in Eq. (3.14) can be interpreted as an approximation to the cell-edge current at $x_{j+1/2}$, which limits to the exact cell-edge current as the coarse grid becomes infinitesmally small. Because the left side of Eq. (3.14) is exactly zero for the true transport solution, it can be subtracted from the numerator of the CMFD $\hat{D}$ equation without bias. This yields a new expression for the CMFD correction term, which should be less noisy than the original $\hat{D}$ expression shown in Eq. (3.2g).

For the tent function case, we define the following function:

$$T_{j+1/2}(x) = \begin{cases} \frac{1}{\Delta_j}(x - x_{j-1/2}) \, , & x_{j-1/2} < x < x_{j+1/2} \, , \\ \frac{1}{\Delta_{j+1}}(x_{j+3/2} - x) \, , & x_{j+1/2} < x < x_{j+3/2} \, , \\ 0 \, , & \text{otherwise} \, . \end{cases} \tag{3.15}$$

This function is shown in Figure 3.3. Then, we multiply both sides of Eq. (3.10) by the tent function $T_{j+1/2}(x)$ defined in Eq. (3.15) and integrate from $x_{j-1/2} < x < x_{j+3/2}$ (using

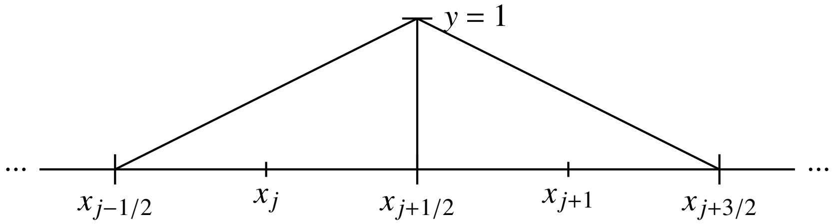

Figure 3.3: Linear tent function

integration by parts on the first term). This yields

$$\phi_{2,j+1} - \phi_{2,j} + \int_{x_{j-1/2}}^{x_{j+3/2}} T_{j+1/2}(x)\Sigma_t(x)\phi_1(x)dx = 0 \,.$$

We then divide through by the tent-weighted total cross section,

$$\int_{x_{j-1/2}}^{x_{j+3/2}} T_{j+1/2}(x)\Sigma_t(x)dx \,,$$

which yields the following expression:

$$\frac{\phi_{2,j+1} - \phi_{2,j}}{\int_{x_{j-1/2}}^{x_{j+3/2}} T_{j+1/2}(x)\Sigma_t(x)dx} + \frac{\int_{x_{j-1/2}}^{x_{j+3/2}} T_{j+1/2}(x)\Sigma_t(x)\phi_1(x)dx}{\int_{x_{j-1/2}}^{x_{j+3/2}} T_{j+1/2}(x)\Sigma_t(x)dx} = 0 \,. \tag{3.16}$$

Similar to the histogram case, the second term in Eq. (3.16) can be interpreted as an approximate estimate of the cell-edge current at $x_{j+1/2}$. We would expect the edge current estimate in Eq. (3.16) to be more accurate than the corresponding term in Eq. (3.14), because greater weight is given to histories passing near the cell edge at $x_{j+1/2}$.

When the Wolters correction factors are applied to multi-dimensional problems, additional terms must be calculated. First of all, the multi-dimensional form of the "current-like" term [i.e. the second term in Eq. (3.14)] consists of three components, which must be calculated and stored separately.

In addition, the ϕ_2 term becomes a 3×3 tensor,

$$\phi_2(\vec{x}) = \int_{4\pi} \begin{bmatrix} \Omega_x\Omega_x & \Omega_x\Omega_y & \Omega_x\Omega_z \\ \Omega_y\Omega_x & \Omega_y\Omega_y & \Omega_y\Omega_z \\ \Omega_z\Omega_x & \Omega_z\Omega_y & \Omega_z\Omega_z \end{bmatrix} \psi(\vec{x},\vec{\Omega})d\vec{\Omega} \,, \tag{3.17}$$

the components of which must be tallied and stored on the specified coarse grid. In Eq.

3.17,

$$\vec{\Omega} = \Omega_x \vec{i} + \Omega_y \vec{j} + \Omega_z \vec{k} \tag{3.18}$$

is an angular vector describing the direction of particle travel. Depending on the weighting function used, the ϕ_2 values may be volume or edge quantities.

In general, we find that the "histogram" Wolters method works very well for 1-D problems, but is less effective for 2- and 3-D simulations (see Section 3.5.2). This is probably due in part to a weaker correlation between edge and volume tallies in multidimensional geometry.

The more complicated Wolters correction factors (e.g. the tent-function-based expression) do not extend to multiple spatial dimensions in a straightforward way, and, in fact, these weighting functions provide only a modest benefit over the histogram function in 1-D simulations. For these reasons, we have implemented only the histogram-weighted Wolters correction factor for multidimensional problems.

In summary, we have concluded that the Wolters correction alone is not sufficient to stabilize a realistic multi-dimensional full-core simulation. However, this method is relatively straightforward and inexpensive to implement, and can be used in conjunction with other stabilization methods as part of a comprehensive approach.

3.4 Stability Analysis

In this section, two CMFD-MC iteration schemes are linearized and Fourier-analyzed (assuming an infinite number of MC particles per cycle [24]). First, we consider a monoenergetic case. The monoenergetic stability analysis provides us with relatively straightforward relationships between coarse-grid optical thickness, scattering ratio, and spectral radius. However, the monoenergetic stability analysis alone is not sufficient to make predictions about the behavior of realistic reactor simulations (which invariably employ energy-dependent cross sections). To this end, we have also Fourier-analyzed a two-energy-group CMFD-MC iteration scheme.

Similarities exist between the monoenergetic and two-group CMFD-MC iteration equations, but Fourier analyses of the two cases are fundamentally different (consequently, so are the results). Because the two-group Fourier analysis does not reduce to the monoenergetic case, we present both cases separately.

To our knowledge, this is the first attempt to theoretically analyze the numerical stability of the CMFD-MC method; hence, all of the work presented in this section is new research.

3.4.1 Monoenergetic Case

3.4.1.1 The Linearized Non-Random CMFD-MC Method

To linearize the non-random CMFD-MC k-eigenvalue iteration method defined in Section 3.2, we consider a special problem in which the exact eigenfunction is constant (independent of space and angle). Specifically, we consider a spatially uniform system with periodic boundary conditions:

$$\mu\frac{d}{dx}\psi^{(\ell+1/2)}(x,\mu)+\Sigma_t\psi^{(\ell+1/2)}(x,\mu)-\frac{\Sigma_s}{2}\phi^{(\ell+1/2)}(x)=\frac{\nu\Sigma_f}{2k^{(\ell)}}\phi^{(\ell)}(x)\,, \tag{3.19a}$$

$$0\le x\le X\,,\ -1\le\mu\le 1\,,$$

$$\psi^{(\ell+1/2)}(0,\mu)=\psi^{(\ell+1/2)}(X,\mu)\,,\ -1\le\mu\le 1\,. \tag{3.19b}$$

The CMFD grid is assumed to be uniform, with J cells of width Δ. The coarse-grid cross sections and diffusivities ($\tilde{D}$) are known exactly:

$$\Sigma_{a,j}^{(\ell+1/2)}=\Sigma_a\,, \tag{3.20a}$$

$$\Sigma_{t,j}^{(\ell+1/2)}=\Sigma_t\,, \tag{3.20b}$$

$$\nu\Sigma_{f,j}^{(\ell+1/2)}=\nu\Sigma_f\,, \tag{3.20c}$$

$$\tilde{D}_{j+1/2}^{(\ell+1/2)}=\tilde{D}=\frac{1}{3\Sigma_t\Delta}\,, \tag{3.20d}$$

while the remainder of the equations become:

$$\phi^{(\ell+1/2)}(x)=\int_{-1}^{1}\psi^{(\ell+1/2)}(x,\mu)d\mu\,, \tag{3.21a}$$

$$\Phi_j^{(\ell+1/2)}=\frac{1}{\Delta}\int_{x_{j-1/2}}^{x_{j+1/2}}\int_{-1}^{1}\psi^{(\ell+1/2)}(x,\mu)d\mu dx\,, \tag{3.21b}$$

$$\Phi_{1,j+1/2}^{(\ell+1/2)}=\int_{-1}^{1}\mu\psi^{(\ell+1/2)}(x_{j+1/2},\mu)d\mu\,, \tag{3.21c}$$

$$\hat{D}_{j+1/2}^{(\ell+1/2)}=\frac{\Phi_{1,j+1/2}^{(\ell+1/2)}+\tilde{D}(\Phi_{j+1}^{(\ell+1/2)}-\Phi_j^{(\ell+1/2)})}{\Phi_{j+1}^{(\ell+1/2)}+\Phi_j^{(\ell+1/2)}}\,, \tag{3.21d}$$

$$\Phi_{1,j+1/2}^{(\ell+1)}-\Phi_{1,j-1/2}^{(\ell+1)}+\Sigma_a\Phi_j^{(\ell+1)}\Delta=\frac{\nu\Sigma_f}{k^{(\ell+1)}}\Phi_j^{(\ell+1)}\Delta\,,\ 1\le j\le J\,, \tag{3.21e}$$

$$\Phi_{1,j+1/2}^{(\ell+1)}=-\tilde{D}(\Phi_{j+1}^{(\ell+1)}-\Phi_j^{(\ell+1)})+\hat{D}_{j+1/2}^{(\ell+1/2)}(\Phi_{j+1}^{(\ell+1)}+\Phi_j^{(\ell+1)})\,, \tag{3.21f}$$

$$\Phi^{(\ell+1/2)}_{1,1/2} = \Phi^{(\ell+1/2)}_{1,J+1/2} \,, \tag{3.21g}$$

$$1 = \frac{1}{J}\sum_{j=1}^{J} \Phi^{(\ell+1)}_{j} \,. \tag{3.21h}$$

On convergence, this problem has the following exact solution:

$$\psi(x,\mu) = \frac{1}{2} \,, \tag{3.22a}$$

$$\Phi_j = \phi(x) = 1 \,, \tag{3.22b}$$

$$\Phi_{1,j+1/2} = 0 \,, \tag{3.22c}$$

$$\frac{1}{k} = \frac{\Sigma_a}{\nu\Sigma_f} \,. \tag{3.22d}$$

To proceed, we define the following linear expansions around the exact solution (with $\epsilon \ll 1$):

$$\psi^{(\ell+1/2)}(x,\mu) = \frac{1}{2} + \epsilon\tilde{\psi}^{(\ell+1/2)}(x,\mu) \,, \tag{3.23a}$$

$$\phi^{(\ell+1/2)}(x) = 1 + \epsilon\tilde{\phi}^{(\ell+1/2)}(x) \,, \tag{3.23b}$$

$$\phi^{(\ell+1)}(x) = 1 + \epsilon\tilde{\phi}^{(\ell+1)}(x) \,, \tag{3.23c}$$

$$\Phi^{(\ell+1/2)}_j = 1 + \epsilon\tilde{\Phi}^{(\ell+1/2)}_j \,, \tag{3.23d}$$

$$\Phi^{(\ell+1)}_j = 1 + \epsilon\tilde{\Phi}^{(\ell+1)}_j \,, \tag{3.23e}$$

$$\Phi^{(\ell+1/2)}_{1,j+1/2} = 0 + \epsilon\tilde{\Phi}^{(\ell+1/2)}_{1,j+1/2} \,, \tag{3.23f}$$

$$\Phi^{(\ell+1)}_{1,j+1/2} = 0 + \epsilon\tilde{\Phi}^{(\ell+1)}_{1,j+1/2} \,, \tag{3.23g}$$

$$\hat{D}^{(\ell+1/2)}_{j+1/2} = 0 + \epsilon\hat{d}^{(\ell+1/2)}_{j+1/2} \,, \tag{3.23h}$$

$$\frac{1}{k^{(\ell+1)}} = \frac{\Sigma_a}{\nu\Sigma_f} + \epsilon\delta^{(\ell+1)} \,. \tag{3.23i}$$

Since the coarse-grid cross sections and diffusion coefficients are known exactly, these quantities are not expanded. Inserting Eqs. (3.23) into Eqs. (3.19) and (3.21), and equating $O(\epsilon)$ terms, we obtain:

$$\mu\frac{d}{dx}\tilde{\psi}^{(\ell+1/2)}(x,\mu)+\Sigma_t\tilde{\psi}^{(\ell+1/2)}(x,\mu) - \frac{\Sigma_s}{2}\tilde{\phi}^{(\ell+1/2)}(x) = \frac{\nu\Sigma_f}{2}\delta^{(\ell)} + \frac{\Sigma_a}{2}\tilde{\phi}^{(\ell)}(x) \,, \quad 0 \le x \le X \,,\ -1 \le \mu \le 1 \,, \tag{3.24a}$$

$$\tilde{\psi}^{(\ell+1/2)}(0,\mu) = \tilde{\psi}^{(\ell+1/2)}(X,\mu) \,,\ -1 \le \mu \le 1 \,, \tag{3.24b}$$

$$\tilde{\phi}^{(\ell+1/2)}(x) = \int_{-1}^{1} \tilde{\psi}^{(\ell+1/2)}(x,\mu)d\mu \ , \tag{3.24c}$$

$$\tilde{\Phi}_j^{(\ell+1/2)} = \frac{1}{\Delta}\int_{x_{j-1/2}}^{x_{j+1/2}} \int_{-1}^{1} \tilde{\psi}^{(\ell+1/2)}(x,\mu)d\mu dx \ , \tag{3.24d}$$

$$\tilde{\Phi}_{1,j+1/2}^{(\ell+1/2)} = \int_{-1}^{1} \mu\tilde{\psi}^{(\ell+1/2)}(x_{j+1/2},\mu)d\mu \ , \tag{3.24e}$$

$$\hat{\tilde{d}}_{j+1/2}^{(\ell+1/2)} = \frac{1}{2}\left[\tilde{\Phi}_{1,j+1/2}^{(\ell+1/2)} + \tilde{D}(\tilde{\Phi}_{j+1}^{(\ell+1/2)} - \tilde{\Phi}_j^{(\ell+1/2)})\right] \ , \tag{3.24f}$$

$$\nu\Sigma_f\delta^{(\ell+1)}\Delta = (\tilde{\Phi}_{1,j+1/2}^{(\ell+1)} - \tilde{\Phi}_{1,j-1/2}^{(\ell+1)}) \ , \ \ 1 \le j \le J \ , \tag{3.24g}$$

$$\tilde{\Phi}_{1,j+1/2}^{(\ell+1)} = -\tilde{D}(\tilde{\Phi}_{j+1}^{(\ell+1)} - \tilde{\Phi}_j^{(\ell+1)}) + 2\hat{\tilde{d}}_{j+1/2}^{(\ell+1/2)} \ , \tag{3.24h}$$

$$\tilde{\Phi}_{1,1/2}^{(\ell+1/2)} = \tilde{\Phi}_{1,J+1/2}^{(\ell+1/2)} \ , \tag{3.24i}$$

$$0 = \frac{1}{J}\sum_{j=1}^{J} \tilde{\Phi}_j^{(\ell+1)} \ , \tag{3.24j}$$

and

$$\tilde{\phi}^{(\ell+1)}(x) = \tilde{\phi}^{(\ell+1/2)}(x) + \tilde{\Phi}_j^{(\ell+1)} - \tilde{\Phi}_j^{(\ell+1/2)} \ , \tag{3.24k}$$
$$x_{j-1/2} \le x \le x_{j+1/2} \ , \ \ 1 \le j \le J \ .$$

We note that several of the linearized equations differ in form from Eqs. (3.1) - (3.3), because the original equations contained nonlinear terms.

After some straightforward algebra (omitted here for brevity), we find:

$$\delta^{(\ell+1)} = 0 \ . \tag{3.25}$$

This shows that the non-random CMFD-MC method converges the $O(\epsilon)$ component of the system eigenvalue after only one iteration. However, the $O(\epsilon)$ component of the eigenfunction is not converged after one iteration; the Fourier analysis predicts the rate of convergence of this component of the eigenfunction.

Inserting Eq. (3.25) into Eqs. (3.24) and rearranging to algebraically eliminate $\hat{\tilde{d}}_{j+1/2}^{(\ell+1/2)}$, we obtain the following system of equations for the linearized non-random CMFD-MC method:

$$\mu\frac{d}{dx}\tilde{\psi}^{(\ell+1/2)}(x,\mu) + \Sigma_t\tilde{\psi}^{(\ell+1/2)}(x,\mu) - \frac{\Sigma_s}{2}\tilde{\phi}^{(\ell+1/2)}(x) = \frac{\Sigma_a}{2}\tilde{\phi}^{(\ell)}(x) \ , \tag{3.26a}$$
$$0 \le x \le X, -1 \le \mu \le 1 \ ,$$

$$\tilde{\psi}^{(\ell+1/2)}(0,\mu) = \tilde{\psi}^{(\ell+1/2)}(X,\mu)\ , \ \ -1 \le \mu \le 1\ , \tag{3.26b}$$

$$\tilde{\phi}^{(\ell+1/2)}(x) = \int_{-1}^{1} \tilde{\psi}^{(\ell+1/2)}(x,\mu)d\mu\ , \tag{3.26c}$$

$$\tilde{\Phi}_j^{(\ell+1/2)} = \frac{1}{\Delta}\int_{x_{j-1/2}}^{x_{j+1/2}} \tilde{\phi}^{(\ell+1/2)}(x)dx\ , \tag{3.26d}$$

$$\tilde{\Phi}_{1,j+1/2}^{(\ell+1/2)} = \int_{-1}^{1} \mu\tilde{\psi}^{(\ell+1/2)}(x_{j+1/2},\mu)d\mu\ , \tag{3.26e}$$

$$\begin{aligned}\tilde{\Phi}_{j+1}^{(\ell+1)} - 2\tilde{\Phi}_{j}^{(\ell+1)} + \tilde{\Phi}_{j-1}^{(\ell+1)} = {} & \frac{1}{\tilde{D}}(\tilde{\Phi}_{1,j+1/2}^{(\ell+1/2)} - \tilde{\Phi}_{1,j-1/2}^{(\ell+1/2)}) \\ & + \tilde{\Phi}_{j+1}^{(\ell+1/2)} - 2\tilde{\Phi}_{j}^{(\ell+1/2)} + \tilde{\Phi}_{j-1}^{(\ell+1/2)}\ , \ \ 1 \le j \le J\ ,\end{aligned} \tag{3.26f}$$

$$\tilde{\Phi}_1^{(\ell+1)} = \tilde{\Phi}_{J+1}^{(\ell+1)}\ , \tag{3.26g}$$

$$0 = \frac{1}{J}\sum_{j=1}^{J} \tilde{\Phi}_j^{(\ell+1)}\ , \tag{3.26h}$$

$$\tilde{\phi}^{(\ell+1)}(x) = \tilde{\phi}^{(\ell+1/2)}(x) + \tilde{\Phi}_j^{(\ell+1)} - \tilde{\Phi}_j^{(\ell+1/2)}\ , \tag{3.26i}$$

$$x_{j-1/2} \le x \le x_{j+1/2}\ , \ \ 1 \le j \le J\ .$$

In Eqs. (3.26), the eigenvalue is converged exactly [Eq. (3.25)], but the eigenfunction is not converged. The Fourier analysis of the linearized equations, performed next in Section 3.4.1.2, determines the rate of convergence of the eigenfunction. We emphasize again that the Fourier analysis contains no terms that account for statistical errors; the analysis applies only when the statistical noise in the solution is sufficiently small that it can be ignored.

3.4.1.2 Fourier Analysis

To carry out the Fourier analysis, we discretize the MC portion of the linearized system in angle and space. This is an approximation to the continuous MC problem, but it enables us to formulate and solve a block matrix system numerically for the spectral radius. To ensure that the discrete results are accurate enough to closely approximate the original problem, we carry out a parametric study to determine an adequately fine space-angle grid (see Section 3.5.1.1).

Thus, we approximate the MC k-eigenvalue problem by a discrete ordinates problem formulated on a fine space-angle grid, with N discrete angles from $1 \le n \le N$ and K fine spatial cells of thickness h ($1 \le k \le K$). We use the "coarse-grid parameter" $p = \frac{\Delta}{h}$ to denote the number of fine cells per coarse cell, and we introduce the notation

$$\sum_{k\in j}(\cdot)\,, \tag{3.27}$$

to describe a sum over the fine cells k belonging to coarse cell j. Also, we use Gauss-Legendre quadrature sets, which satisfy:

$$\sum_{n=1}^{N} w_n = 2\,. \tag{3.28}$$

Using this notation, the discretized version of Eq. (3.26a) can be written in the form:

$$\frac{\mu_n}{h}(\tilde{\psi}^{(\ell+1/2)}_{k+1/2,n} - \tilde{\psi}^{(\ell+1/2)}_{k-1/2,n}) + \Sigma_t \tilde{\psi}^{(\ell+1/2)}_{k,n} - \frac{\Sigma_s}{2}\tilde{\phi}^{(\ell+1/2)}_k = \frac{\Sigma_a}{2}\tilde{\phi}^{(\ell)}_k\,, \tag{3.29a}$$

$$1 \le n \le N,\ \ 1 \le k \le K\,,$$

$$\tilde{\psi}^{(\ell+1/2)}_{1/2,n} = \tilde{\psi}^{(\ell+1/2)}_{K+1/2,n}\,,\ \ 1 \le n \le N\,. \tag{3.29b}$$

Similarly, the linearized scalar flux expression becomes:

$$\tilde{\phi}^{(\ell+1/2)}_k = \sum_{n=1}^{N} w_n \tilde{\psi}^{(\ell+1/2)}_{k,n}\,. \tag{3.29c}$$

To close the system, we introduce the weighted diamond auxiliary equations:

$$\tilde{\psi}^{(\ell+1/2)}_{k,n} = \left(\frac{1+\alpha_n}{2}\right)\tilde{\psi}^{(\ell+1/2)}_{k+1/2,n} + \left(\frac{1-\alpha_n}{2}\right)\tilde{\psi}^{(\ell+1/2)}_{k-1/2,n}\,,$$

$$1 \le n \le N\,,\ \ 1 \le k \le K\,. \tag{3.29d}$$

In this work, we use the *Step Characteristic* spatial discretization, with

$$\alpha_n = \frac{1+e^{-\Sigma_t h/\mu_n}}{1-e^{-\Sigma_t h/\mu_n}} - \frac{2\mu_n}{\Sigma_t h}\,,\ \ 1 \le n \le N\,. \tag{3.29e}$$

The equations that "link" the MC problem to CMFD [Eqs. (3.26d), (3.26e) and (3.27)] must also be discretized, while the CMFD equations themselves [Eqs. (3.26f) and (3.26g)] remain essentially unchanged:

$$\tilde{\Phi}^{(\ell+1/2)}_j = \frac{1}{p}\sum_{k\in j}\tilde{\phi}^{(\ell+1/2)}_k\,, \tag{3.29f}$$

$$\tilde{\Phi}^{(\ell+1/2)}_{1,j+1/2} = \sum_{n=1}^{N} w_n \mu_n \tilde{\psi}^{(\ell+1/2)}_{(jp)+1/2,n} \,, \tag{3.29g}$$

$$\begin{aligned}\tilde{\Phi}^{(\ell+1)}_{j+1} - 2\tilde{\Phi}^{(\ell+1)}_{j} + \tilde{\Phi}^{(\ell+1)}_{j-1} = \frac{1}{\tilde{D}}(\tilde{\Phi}^{(\ell+1/2)}_{1,j+1/2} - \tilde{\Phi}^{(\ell+1/2)}_{1,j-1/2})& \\ + \tilde{\Phi}^{(\ell+1/2)}_{j+1} - 2\tilde{\Phi}^{(\ell+1/2)}_{j} + \tilde{\Phi}^{(\ell+1/2)}_{j-1} \,,&\end{aligned} \tag{3.29h}$$

$$\tilde{\Phi}^{(\ell+1)}_{1,1/2} = \tilde{\Phi}^{(\ell+1)}_{1,J+1/2} \,, \tag{3.29i}$$

$$0 = \frac{1}{J}\sum_{j=1}^{J} \tilde{\Phi}^{(\ell+1)}_{j} \,, \tag{3.29j}$$

$$\tilde{\phi}^{(\ell+1)}_{k} = \tilde{\phi}^{(\ell+1/2)}_{k} + \tilde{\Phi}^{(\ell+1)}_{j} - \tilde{\Phi}^{(\ell+1/2)}_{j} \,, \;\; 1 \le j \le J \,, \;\; k \in j \,. \tag{3.29k}$$

To simplify the Fourier ansatz, a new *relative* coordinate system is introduced [25]:

$$k = (j-1)p + r \,. \tag{3.30}$$

Here, k is the global fine cell index, j is the index of the coarse cell in which fine cell k resides, p is the number of fine cells per coarse cell, and r is the position of fine cell k within coarse cell j. With this coordinate system in place, we introduce the Fourier ansatz:

$$\tilde{\psi}^{(\ell+1/2)}_{k-1/2,n} = \omega^l a_{r,n} e^{i\Sigma_t \lambda x_j} \,, \tag{3.31a}$$

$$\tilde{\psi}^{(\ell+1/2)}_{k,n} = \omega^l b_{r,n} e^{i\Sigma_t \lambda x_j} \,, \tag{3.31b}$$

$$\tilde{\phi}^{(\ell+1/2)}_{k} = \omega^l B_r e^{i\Sigma_t \lambda x_j} \,, \tag{3.31c}$$

$$\tilde{\Phi}^{(\ell+1/2)}_{j} = \omega^l D e^{i\Sigma_t \lambda x_j} \,, \tag{3.31d}$$

$$\tilde{\Phi}^{(\ell+1)}_{j} = \omega^l F e^{i\Sigma_t \lambda x_j} \,, \tag{3.31e}$$

$$\tilde{\phi}^{(\ell+1)}_{k} = \omega^{l+1} G_r e^{i\Sigma_t \lambda x_j} \,. \tag{3.31f}$$

The fine-grid error coefficients are assumed to be periodic on the coarse grid, such that:

$$\tilde{\psi}^{(\ell+1/2)}_{(k+p)-1/2,n} = \left(\tilde{\psi}^{(\ell+1/2)}_{k-1/2,n}\right) e^{i\Sigma_t \lambda \Delta} = \omega^l a_{r,n} e^{i\Sigma_t \lambda (x_j + \Delta)} \,. \tag{3.32}$$

Inserting the ansatz into Eqs. (3.29) and simplifying, we obtain the following system of equations:

$$\begin{cases} \frac{\mu_n}{h}\left(a_{r+1,n} - a_{r,n}\right) + \Sigma_t b_{r,n} - \frac{\Sigma_s}{2} B_r = \frac{\Sigma_a}{2} G_r \,, & 1 \le r < p \,, \\ \frac{\mu_n}{h}\left(a_{1,n} e^{i\Sigma_t \lambda \Delta} - a_{r,n}\right) + \Sigma_t b_{r,n} - \frac{\Sigma_s}{2} B_r = \frac{\Sigma_a}{2} G_r \,, & r = p \,, \end{cases} \tag{3.33a}$$

$$a_{1,n} = a_{1,n} e^{i\Sigma_t \lambda X} \ , \tag{3.33b}$$

$$\begin{cases} b_{r,n} = \left[\frac{1+\alpha_n}{2}\right] a_{r+1,n} + \left[\frac{1-\alpha_n}{2}\right] a_{r,n} \ , & 1 \leq r < p \ , \\ b_{r,n} = \left[\frac{1+\alpha_n}{2}\right] a_{1,n} e^{i\Sigma_t \lambda \Delta} + \left[\frac{1-\alpha_n}{2}\right] a_{r,n} & r = p \ , \end{cases} \tag{3.33c}$$

$$B_r = \sum_{n=1}^{N} w_n b_{r,n} \ , \tag{3.33d}$$

$$D = \frac{1}{p} \sum_{r=1}^{p} B_r \ , \tag{3.33e}$$

$$2(F - D)(\cos(\Sigma_t \lambda \Delta) - 1) = 3\Sigma_t \Delta \sum_{n=1}^{N} w_n \mu_n a_{1,n} (e^{i\Sigma_t \lambda \Delta} - 1) \ , \tag{3.33f}$$

$$\sum_{n=1}^{N} w_n \mu_n a_{1,n} = e^{i\Sigma_t \lambda X} \sum_{n=1}^{N} w_n \mu_n a_{1,n} \ , \tag{3.33g}$$

$$0 = \sum_{j=1}^{J} e^{i\Sigma_t \lambda x_j} \ , \tag{3.33h}$$

$$\omega G_r - B_r = (F - D) \ . \tag{3.33i}$$

From the boundary equations (3.33b) and (3.33g), we determine permissible values of the Fourier frequency λ for the discrete system:

$$\lambda_s = \frac{2s\pi}{\Sigma_t X} \ , \ \ 1 \leq s < J \ . \tag{3.34}$$

This set of Fourier frequencies automatically satisfies the normalization condition in Eq. (3.33h). Next, Eqs. (3.33d) and (3.33i) are used to eliminate F, D, and B_r in the remainder of Eqs. (3.33). We also define the scattering ratio,

$$c = \frac{\Sigma_s}{\Sigma_t} \ . \tag{3.35}$$

Inserting Eq. (3.35) and carrying out further simplification yields the following discrete system of equations:

$$\begin{cases} \frac{\mu_n}{\Sigma_t h} \left(a_{r+1,n} - a_{r,n}\right) + b_{r,n} - \frac{c}{2} \sum_{n'=1}^{N} w_{n'} b_{r,n'} - \frac{(1-c)}{2} G_r = 0 \ , & 1 \leq r < p \ , \\ \frac{\mu_n}{\Sigma_t h} \left(a_{1,n} e^{i\Sigma_t \lambda_s \Delta} - a_{r,n}\right) + b_{r,n} - \frac{c}{2} \sum_{n'=1}^{N} w_{n'} b_{r,n'} - \frac{(1-c)}{2} G_r = 0 \ , & r = p \ , \end{cases} \tag{3.36a}$$

$$\begin{cases} \left[\frac{1+\alpha_n}{2}\right] a_{r+1,n} + \left[\frac{1-\alpha_n}{2}\right] a_{r,n} - b_{r,n} = 0\,, & 1 \leq r < p\,, \\ \left[\frac{1+\alpha_n}{2}\right] a_{1,n} e^{i\Sigma_t \lambda_s \Delta} + \left[\frac{1-\alpha_n}{2}\right] a_{r,n} - b_{r,n} = 0 & r = p\,, \end{cases} \tag{3.36b}$$

$$\sum_{n=1}^{N} w_n \left(E\mu_n a_{1,n} + b_{r,n}\right) - \omega G_r = 0\,, \tag{3.36c}$$

where

$$E = \frac{3\Sigma_t \Delta}{2} \left[1 + \frac{i \sin(\Sigma_t \lambda_s \Delta)}{(\cos(\Sigma_t \lambda_s \Delta) - 1)}\right]. \tag{3.36d}$$

Eqs. (3.36) can be written in block matrix form [25]:

$$\begin{bmatrix} \mathbf{A} & \mathbf{B} \\ \mathbf{C} & -\omega\mathbf{I} \end{bmatrix} \begin{bmatrix} \mathbf{x} \\ \mathbf{y} \end{bmatrix} = \begin{bmatrix} \mathbf{0} \\ \mathbf{0} \end{bmatrix}. \tag{3.37}$$

Here $\mathbf{A}$ is a $2Np \times 2Np$ matrix containing the coefficients of $a_{r,n}$ and $b_{r,n}$ from Eqs. (3.36a) and (3.36b), $\mathbf{B}$ is a $2Np \times p$ matrix composed of the coefficients of G_r from Eqs. (3.36a) and (3.36b), and $\mathbf{C}$ is a $p \times 2Np$ matrix containing the coefficients of $a_{r,n}$ and $b_{r,n}$ from Eq. (3.36c). The final matrix $(-\omega\mathbf{I})$ is a $p \times p$ diagonal matrix containing the negative of the eigenvalues ω_r, which comprise the coefficients of G_r in Eqs. (3.36c). The size-$2Np$ column vector $\mathbf{x}$ contains the $a_{r,n}$ and $b_{r,n}$ values, while the size-p column vector $\mathbf{y}$ contains the G_r values. To solve for the system eigenvalues ω_r, we follow the procedure outlined in [25]. The block matrix system is first decomposed:

$$\begin{bmatrix} \mathbf{A} & \mathbf{B} \\ \mathbf{C} & -\omega\mathbf{I} \end{bmatrix} = \begin{bmatrix} \mathbf{A} & \mathbf{0} \\ \mathbf{C} & \mathbf{I} \end{bmatrix} \begin{bmatrix} \mathbf{I} & \mathbf{A}^{-1}\mathbf{B} \\ \mathbf{0} & -\mathbf{C}\mathbf{A}^{-1}\mathbf{B} - \omega\mathbf{I} \end{bmatrix}. \tag{3.38}$$

The determinant of the original system is then calculated using

$$\begin{vmatrix} \mathbf{A} & \mathbf{0} \\ \mathbf{C} & \mathbf{I} \end{vmatrix} \begin{vmatrix} \mathbf{I} & \mathbf{A}^{-1}\mathbf{B} \\ \mathbf{0} & -\mathbf{C}\mathbf{A}^{-1}\mathbf{B} - \omega\mathbf{I} \end{vmatrix} = |\mathbf{A}||-\mathbf{C}\mathbf{A}^{-1}\mathbf{B} - \omega\mathbf{I}| = \mathbf{0}\,. \tag{3.39}$$

From inspection, the determinant of the original block matrix system is zero, while the determinant of matrix $\mathbf{A}$ is non-zero. Thus, we can infer that

$$|-\mathbf{C}\mathbf{A}^{-1}\mathbf{B} - \omega\mathbf{I}| = \mathbf{0}\,, \tag{3.40}$$

where $\mathbf{C}\mathbf{A}^{-1}\mathbf{B}$ and $\mathbf{I}$ are $p \times p$ matrices.

Using Eq. (3.40), the eigenvalues ω_r can be calculated numerically for $1 \leq r \leq p$ and permitted values of the discrete Fourier frequency, λ_s. Once the eigenvalues are known, the spectral radius ρ is determined using

$$\rho = \sup_{1\leq s<J}\left(\sup_{1\leq r\leq p}|\omega_r(\lambda_s)|\right). \tag{3.41}$$

3.4.2 Two-group Case

3.4.2.1 The Linearized Non-Random Two-Group CMFD-MC Method

To extend the Fourier analysis to a more realistic case, we also consider a two-energy-group version of the CMFD-MC iteration strategy. While the overall analysis procedure is similar to the monoenergetic case, the two-group Fourier analysis yields additional information regarding the effect of (simplified) energy dependence on the spectral radius. In keeping with standard reactor physics terminology, group 1 is referred to as the "fast" energy group, while group 2 is referred to as the "thermal" energy group. To simplify the two-group stability analysis, we assume that (i) upscattering from the thermal group to the fast group is negligible, (ii) all fission neutrons are born in the fast group, and (iii) fast fission is negligible.

We consider a spatially uniform system with periodic boundary conditions, and follow the procedure outlined in Section 3.4.1.1 to linearize the non-random two-group CMFD-MC k-eigenvalue iteration scheme. The exact groupwise eigenfunction solution to this problem is constant (independent of space and angle). Specifically, we consider:

$$\mu\frac{d}{dx}\psi_1^{(\ell+1/2)}(x,\mu)+\Sigma_{t,1}\psi^{(\ell+1/2)}(x,\mu)-\frac{\Sigma_{s,1\to1}}{2}\phi_1^{(\ell+1/2)}(x)=\frac{\nu\Sigma_{f,2}}{2k^{(\ell)}}\phi_2^{(\ell)}(x)\,, \tag{3.42a}$$

$$\mu\frac{d}{dx}\psi_2^{(\ell+1/2)}(x,\mu)+\Sigma_{t,2}\psi_2^{(\ell+1/2)}(x,\mu)-\frac{\Sigma_{s,1\to2}}{2}\phi_1^{(\ell+1/2)}(x)-\frac{\Sigma_{s,2\to2}}{2}\phi_2^{(\ell+1/2)}(x)=0\,, \tag{3.42b}$$

$$0\leq x\leq X\,,\ -1\leq\mu\leq1\,,$$

$$\psi^{(\ell+1/2)}(0,\mu)=\psi^{(\ell+1/2)}(X,\mu)\,,\ -1\leq\mu\leq1\,. \tag{3.42c}$$

The prescribed coarse grid is uniform, with J cells of width Δ. The coarse-grid groupwise cross sections and diffusivities ($\tilde{D}_g$) are known exactly:

$$\Sigma_{t,j,g}^{(\ell+1/2)}=\Sigma_t\,, \tag{3.43a}$$

$$\Sigma_{s,j,g'\to g}^{(\ell+1/2)}=\Sigma_{s,g'\to g}\,, \tag{3.43b}$$

$$\nu\Sigma_{f,j,g}^{(\ell+1/2)}=\nu\Sigma_{f,g}\,, \tag{3.43c}$$

$$\tilde{D}^{(\ell+1/2)}_{j+1/2,g} = \tilde{D}_g = \frac{1}{3\Sigma_{t,g}\Delta} \,, \tag{3.43d}$$

while the remainder of the equations become:

$$\phi^{(\ell+1/2)}_g(x) = \int_{-1}^{1} \psi^{(\ell+1/2)}_g(x,\mu)d\mu \,, \tag{3.44a}$$

$$\Phi^{(\ell+1/2)}_{j,g} = \frac{1}{\Delta}\int_{x_{j-1/2}}^{x_{j+1/2}} \int_{-1}^{1} \psi^{(\ell+1/2)}_g(x,\mu)d\mu dx \,, \tag{3.44b}$$

$$\Phi^{(\ell+1/2)}_{1,j+1/2,g} = \int_{-1}^{1} \mu\psi^{(\ell+1/2)}_g(x_{j+1/2},\mu)d\mu \,, \tag{3.44c}$$

$$\hat{D}^{(\ell+1/2)}_{j+1/2,g} = \frac{\Phi^{(\ell+1/2)}_{1,j+1/2,g} + \tilde{D}(\Phi^{(\ell+1/2)}_{j+1,g} - \Phi^{(\ell+1/2)}_{j,g})}{\Phi^{(\ell+1/2)}_{j+1,g} + \Phi^{(\ell+1/2)}_{j,g}} \,, g = 1,2 \,, \tag{3.44d}$$

$$\begin{gathered} \Phi^{(\ell+1)}_{1,j+1/2,1} - \Phi^{(\ell+1)}_{1,j-1/2,1} + \Sigma_{r,1}\Phi^{(\ell+1)}_{j,1}\Delta = \frac{\nu\Sigma_{f,2}}{k^{(\ell+1)}}\Phi^{(\ell+1)}_{j,2}\Delta \,, \\ \Phi^{(\ell+1)}_{1,j+1/2,2} - \Phi^{(\ell+1)}_{1,j-1/2,2} + \Sigma_{r,2}\Phi^{(\ell+1)}_{j,2}\Delta - \Sigma_{s,1\to 2}\Phi^{(\ell+1)}_{j,1}\Delta = 0 \,, \; 1 \le j \le J \,, \end{gathered} \tag{3.44e}$$

$$\Phi^{(\ell+1)}_{1,j+1/2,g} = -\tilde{D}_g(\Phi^{(\ell+1)}_{j+1,g} - \Phi^{(\ell+1)}_{j,g}) + \hat{D}^{(\ell+1/2)}_{j+1/2,g}(\Phi^{(\ell+1)}_{j+1,g} + \Phi^{(\ell+1)}_{j,g}) \,, \tag{3.44f}$$

$$\Phi^{(\ell+1/2)}_{1,1/2,g} = \Phi^{(\ell+1/2)}_{1,J+1/2,g} \,, \tag{3.44g}$$

$$1 = \frac{1}{J}\sum_{g=1}^{2}\sum_{j=1}^{J}\Phi^{(\ell+1)}_{j,g} \,, \tag{3.44h}$$

$$\begin{gathered} \tilde{\phi}^{(\ell+1)}_g(x) = \tilde{\phi}^{(\ell+1/2)}_g(x) + \tilde{\Phi}^{(\ell+1)}_{j,g} - \tilde{\Phi}^{(\ell+1/2)}_{j,g} \,, \\ x_{j-1/2} \le x \le x_{j+1/2} \,, \; 1 \le j \le J \,, \; g = 1,2 \;. \end{gathered} \tag{3.44i}$$

On convergence, this problem has the following exact solution:

$$\psi_1(x,\mu) = \frac{1}{2} \,, \tag{3.45a}$$

$$\psi_2(x,\mu) = \frac{1}{2}\left(\frac{\Sigma_{s,1\to 2}}{\Sigma_{r,2}}\right) = \frac{\mathcal{C}}{2} \,, \tag{3.45b}$$

$$\Phi_{j,1} = \phi_1(x) = 1 \,, \tag{3.45c}$$

$$\Phi_{j,2} = \phi_2(x) = \mathcal{C} \,, \tag{3.45d}$$

$$\Phi_{1,j+1/2,g} = 0 \,, \; g = 1,2 \,, \tag{3.45e}$$

$$\frac{1}{k} = \frac{\Sigma_{r,1}\Sigma_{r,2}}{\nu\Sigma_{f,2}\Sigma_{s,1\to 2}} = \frac{1}{k_{ex}} \;. \tag{3.45f}$$

Next, we define the following linear expansions around the exact solution (with $\epsilon \ll 1$):

$$\psi_1^{(\ell+1/2)}(x,\mu) = \frac{1}{2} + \epsilon\tilde{\psi}^{(\ell+1/2)}(x,\mu) \,, \tag{3.46a}$$

$$\psi_2^{(\ell+1/2)}(x,\mu) = \frac{\mathcal{C}}{2} + \epsilon\tilde{\psi}^{(\ell+1/2)}(x,\mu) \,, \tag{3.46b}$$

$$\phi_1^{(\ell+1/2)}(x) = 1 + \epsilon\tilde{\phi}^{(\ell+1/2)}(x) \,, \tag{3.46c}$$

$$\phi_2^{(\ell+1/2)}(x) = \mathcal{C} + \epsilon\tilde{\phi}^{(\ell+1/2)}(x) \,, \tag{3.46d}$$

$$\phi_1^{(\ell+1)}(x) = 1 + \epsilon\tilde{\phi}^{(\ell+1)}(x) \,, \tag{3.46e}$$

$$\phi_2^{(\ell+1)}(x) = \mathcal{C} + \epsilon\tilde{\phi}^{(\ell+1)}(x) \,, \tag{3.46f}$$

$$\Phi_{j,1}^{(\ell+1/2)} = 1 + \epsilon\tilde{\Phi}_j^{(\ell+1/2)} \,, \tag{3.46g}$$

$$\Phi_{j,2}^{(\ell+1/2)} = \mathcal{C} + \epsilon\tilde{\Phi}_j^{(\ell+1/2)} \,, \tag{3.46h}$$

$$\Phi_{j,1}^{(\ell+1)} = 1 + \epsilon\tilde{\Phi}_j^{(\ell+1)} \,, \tag{3.46i}$$

$$\Phi_{j,2}^{(\ell+1)} = \mathcal{C} + \epsilon\tilde{\Phi}_j^{(\ell+1)} \,, \tag{3.46j}$$

$$\Phi_{1,j+1/2,g}^{(\ell+1/2)} = 0 + \epsilon\tilde{\Phi}_{1,j+1/2,g}^{(\ell+1/2)} \,, \tag{3.46k}$$

$$\Phi_{1,j+1/2,g}^{(\ell+1)} = 0 + \epsilon\tilde{\Phi}_{1,j+1/2,g}^{(\ell+1)} \,, \tag{3.46l}$$

$$\hat{D}_{j+1/2,g}^{(\ell+1/2)} = 0 + \epsilon\hat{d}_{j+1/2,g}^{(\ell+1/2)} \,, \tag{3.46m}$$

$$\frac{1}{k^{(\ell+1)}} = \frac{1}{k_{ex}} + \epsilon\delta^{(\ell+1)} \,. \tag{3.46n}$$

The coarse-grid cross sections and diffusion coefficients are known exactly for the homogeneous problem, so these quantities are not expanded. Inserting Eqs. (3.46) into Eqs. (3.42) and (3.44), we equate $\mathcal{O}(\epsilon)$ terms to obtain:

$$\begin{gathered}
\mu\frac{d}{dx}\tilde{\psi}_1^{(\ell+1/2)}(x,\mu) + \Sigma_{t,1}\tilde{\psi}_1^{(\ell+1/2)}(x,\mu) - \frac{\Sigma_{s,1\to 1}}{2}\tilde{\phi}_1^{(\ell+1/2)}(x) = \frac{\nu\Sigma_{f,2}}{2}\left(\delta^{(\ell)}\mathcal{C} + \frac{1}{k_{ex}}\tilde{\phi}_2^{(\ell)}(x)\right) \,, \\
\mu\frac{d}{dx}\tilde{\psi}_2^{(\ell+1/2)}(x,\mu) + \Sigma_{t,2}\tilde{\psi}_2^{(\ell+1/2)}(x,\mu) - \frac{\Sigma_{s,1\to 2}}{2}\tilde{\phi}_1^{(\ell+1/2)}(x) - \frac{\Sigma_{s,2\to 2}}{2}\tilde{\phi}_2^{(\ell+1/2)}(x) = 0 \,, \\
0 \le x \le X \,, \ -1 \le \mu \le 1 \,,
\end{gathered} \tag{3.47a}$$

$$\tilde{\psi}_g^{(\ell+1/2)}(0,\mu) = \tilde{\psi}_g^{(\ell+1/2)}(X,\mu) \,, \ -1 \le \mu \le 1 \,, \tag{3.47b}$$

$$\tilde{\phi}_g^{(\ell+1/2)}(x) = \int_{-1}^{1} \tilde{\psi}_g^{(\ell+1/2)}(x,\mu)d\mu \,, \tag{3.47c}$$

$$\tilde{\Phi}_{j,g}^{(\ell+1/2)} = \frac{1}{\Delta}\int_{x_{j-1/2}}^{x_{j+1/2}} \int_{-1}^{1} \tilde{\psi}_g^{(\ell+1/2)}(x,\mu)d\mu dx \,, \tag{3.47d}$$

$$\tilde{\Phi}^{(\ell+1/2)}_{1,j+1/2,g} = \int_{-1}^{1} \mu\tilde{\psi}^{(\ell+1/2)}_g(x_{j+1/2},\mu)d\mu \, , \tag{3.47e}$$

$$\hat{d}^{(\ell+1/2)}_{j+1/2,g} = \frac{1}{2}(\tilde{\Phi}^{(\ell+1/2)}_{1,j+1/2,g} + \tilde{D}_g(\tilde{\Phi}^{(\ell+1/2)}_{j+1,g} - \tilde{\Phi}^{(\ell+1/2)}_{j,g})) \, , \tag{3.47f}$$

$$\begin{gathered}\tilde{\Phi}^{(\ell+1)}_{1,j+1/2,1} - \tilde{\Phi}^{(\ell+1)}_{1,j-1/2,1} + \Sigma_{r,1}\tilde{\Phi}^{(\ell+1)}_{j,1}\Delta = \nu\Sigma_{f,2}\Delta\left(\delta^{(\ell+1)}\mathcal{C} + \frac{1}{k_{ex}}\tilde{\Phi}^{(\ell+1/2)}_{j,2}\right) , \\ \tilde{\Phi}^{(\ell+1)}_{1,j+1/2,2} - \tilde{\Phi}^{(\ell+1)}_{1,j-1/2,2} + \Sigma_{r,2}\tilde{\Phi}^{(\ell+1)}_{j,2}\Delta - \Sigma_{s,1\to 2}\tilde{\Phi}^{(\ell+1)}_{j,1}\Delta = 0 \, , \; 1 \le j \le J \, ,\end{gathered} \tag{3.47g}$$

$$\tilde{\Phi}^{(\ell+1)}_{1,j+1/2,g} = -\tilde{D}_g(\tilde{\Phi}^{(\ell+1)}_{j+1,g} - \tilde{\Phi}^{(\ell+1)}_{j,g}) + 2\hat{d}^{(\ell+1/2)}_{j+1/2,g} \, , \tag{3.47h}$$

$$\tilde{\Phi}^{(\ell+1/2)}_{1,1/2,g} = \tilde{\Phi}^{(\ell+1/2)}_{1,J+1/2,g} \, , \tag{3.47i}$$

$$0 = \sum_{g=1}^{2}\sum_{j=1}^{J}\tilde{\Phi}^{(\ell+1)}_{j,g} \, , \tag{3.47j}$$

and

$$\begin{gathered}\tilde{\phi}^{(\ell+1)}_g(x) = \tilde{\phi}^{(\ell+1/2)}_g(x) + \tilde{\Phi}^{(\ell+1)}_{j,g} - \tilde{\Phi}^{(\ell+1/2)}_{j,g} \, , \\ x_{j-1/2} \le x \le x_{j+1/2} \, , \; 1 \le j \le J \, , \; g = 1,2 \, .\end{gathered} \tag{3.47k}$$

As we observed in the monoenergetic case, several of the linearized equations differ in form from Eqs. (3.42) - (3.44), because the original equations contained nonlinear terms.

If we sum the thermal and fast group balance equations [Eqs. (3.47g)] over all coarse spatial cells, and then solve for $\delta^{(\ell+1)}$, we obtain:

$$\delta^{(\ell+1)} = 0 \, . \tag{3.48}$$

This shows that the non-random two-group CMFD-MC method converges the $O(\epsilon)$ component of the system eigenvalue after only one iteration (as does the monoenergetic CMFD-MC method). The $O(\epsilon)$ component of the eigenfunction is not converged after one iteration, however; the Fourier analysis predicts the rate of convergence of this component of the eigenfunction.

In Section 3.4.2.2, we define the Fourier ansatz, insert the ansatz into Eqs. (3.47), and solve for the spectral radius. As before, we reiterate that this analysis applies only when stochastic noise in the solution is sufficiently small that it can be ignored.

3.4.2.2 Fourier Analysis

To carry out the Fourier analysis, we discretize the MC portion of the linearized two-group CMFD-MC system in angle and space. This is done using the procedure presented in Section 3.4.1.2; we replace the MC k-eigenvalue problem by a discrete ordinates problem formulated on a fine space-angle grid, with N discrete angles from $1 \leq n \leq N$ and K fine spatial cells of thickness h $(1 \leq k \leq K)$. This is an approximation to the continuous system, but it allows us to solve a block matrix system numerically for the linearized two-group CMFD-MC spectral radius. We use the "coarse-grid parameter" $p = \frac{\Delta}{h}$ to denote the number of fine cells per coarse cell, and we use the notation

$$\sum_{k \in j} (\cdot) \,, \tag{3.49}$$

to describe a sum over the fine cells k belonging to coarse cell j. Also, we use Gauss-Legendre quadrature sets, which satisfy:

$$\sum_{n=1}^{N} w_n = 2 \,. \tag{3.50}$$

With this notation, the discretized version of Eq. (3.47a) can be written in the form:

$$\frac{\mu_n}{h}(\tilde{\psi}^{(\ell+1/2)}_{k+1/2,n,1} - \tilde{\psi}^{(\ell+1/2)}_{k-1/2,n,1}) + \Sigma_{t,1}\tilde{\psi}^{(\ell+1/2)}_{k,n,1} - \frac{\Sigma_{s,1\to1}}{2}\tilde{\phi}^{(\ell+1/2)}_{k,1} = \frac{\Sigma_{r,1}\Sigma_{r,2}}{2\Sigma_{s,1\to2}}\tilde{\phi}^{(\ell)}_{k} \,, \tag{3.51a}$$

$$\frac{\mu_n}{h}(\tilde{\psi}^{(\ell+1/2)}_{k+1/2,n,2} - \tilde{\psi}^{(\ell+1/2)}_{k-1/2,n,2}) + \Sigma_{t,2}\tilde{\psi}^{(\ell+1/2)}_{k,n,2} - \frac{\Sigma_{s,1\to2}}{2}\tilde{\phi}^{(\ell+1/2)}_{k,1} - \frac{\Sigma_{s,2\to2}}{2}\tilde{\phi}^{(\ell+1/2)}_{k,2} = 0 \,, \tag{3.51b}$$

$$1 \leq n \leq N, \ 1 \leq k \leq K \,,$$

$$\tilde{\psi}^{(\ell+1/2)}_{1/2,n,g} = \tilde{\psi}^{(\ell+1/2)}_{K+1/2,n,g} \,, \ \ 1 \leq n \leq N \,, \ g = 1,2 \,. \tag{3.51c}$$

In Eqs. (3.51), we make use of Eq. (3.48) to eliminate the $\delta^{(\ell+1)}$ term. The discretized form of the linearized scalar flux expression becomes:

$$\tilde{\phi}^{(\ell+1/2)}_{k,g} = \sum_{n=1}^{N} w_n \tilde{\psi}^{(\ell+1/2)}_{k,n,g} \,. \tag{3.51d}$$

To close the system, we introduce the weighted diamond auxiliary equations:

$$\tilde{\psi}^{(\ell+1/2)}_{k,n,g} = \left(\frac{1+\alpha_{n,g}}{2}\right)\tilde{\psi}^{(\ell+1/2)}_{k+1/2,n,g} + \left(\frac{1-\alpha_{n,g}}{2}\right)\tilde{\psi}^{(\ell+1/2)}_{k-1/2,n,g} \,,$$

$$1 \leq n \leq N \,, \ \ 1 \leq k \leq K \,, \ g = 1,2 \,, \tag{3.51e}$$

where $\alpha_{n,g}$ are calculated using the Step Characteristic spatial discretization introduced in Section 3.4.1.2.

The equations that connect the MC problem to CMFD [Eqs. (3.47c)-(3.47e) and (3.47k)] must also be discretized. However, the CMFD equations themselves remain essentially unchanged:

$$\tilde{\Phi}^{(\ell+1/2)}_{j,g} = \frac{1}{p}\sum_{k\in j}\tilde{\phi}^{(\ell+1/2)}_{k,g} \,, \tag{3.51f}$$

$$\tilde{\Phi}^{(\ell+1/2)}_{1,j+1/2,g} = \sum_{n=1}^{N} w_n\mu_n\tilde{\psi}^{(\ell+1/2)}_{(jp)+1/2,n,g} \,, \tag{3.51g}$$

$$\begin{gathered}\tilde{\Phi}^{(\ell+1)}_{1,j+1/2,1} - \tilde{\Phi}^{(\ell+1)}_{1,j-1/2,1} + \Sigma_{r,1}\tilde{\Phi}^{(\ell+1)}_{j,1}\Delta = \frac{\Sigma_{r,1}\Sigma_{r,2}}{\Sigma_{s,1\to2}}\tilde{\Phi}^{(\ell+1/2)}_{j,2}\Delta \,, \\ \tilde{\Phi}^{(\ell+1)}_{1,j+1/2,2} - \tilde{\Phi}^{(\ell+1)}_{1,j-1/2,2} + \Sigma_{r,2}\tilde{\Phi}^{(\ell+1)}_{j,2}\Delta - \Sigma_{s,1\to2}\tilde{\Phi}^{(\ell+1)}_{j,1}\Delta = 0 \,,\ 1 \le j \le J \,,\end{gathered} \tag{3.51h}$$

$$\tilde{\Phi}^{(\ell+1)}_{1,1/2,g} = \tilde{\Phi}^{(\ell+1)}_{1,J+1/2,g} \,, \tag{3.51i}$$

$$0 = \sum_{g=1}^{2}\sum_{j=1}^{J}\tilde{\Phi}^{(\ell+1)}_{j,g} \,, \tag{3.51j}$$

$$\tilde{\phi}^{(\ell+1)}_{k,g} = \tilde{\phi}^{(\ell+1/2)}_{k,g} + \tilde{\Phi}^{(\ell+1)}_{j,g} - \tilde{\Phi}^{(\ell+1/2)}_{j,g} \,,\ \ 1 \le j \le J \,,\ \ k \in j \,,\ g = 1,2 \,. \tag{3.51k}$$

In Eqs. (3.51f), we again make use of Eq. (3.48) to eliminate the $\delta^{(\ell+1)}$ term.

To simplify the Fourier ansatz, we again introduce the relative coordinate system used in the monoenergetic case:

$$k = (j-1)p + r \,. \tag{3.52}$$

Here, k is the global fine cell index, j is the index of the coarse cell in which fine cell k resides, p is the number of fine cells per coarse cell, and r is the position of fine cell k within coarse cell j. With this coordinate system in place, we introduce the Fourier ansatz:

$$\tilde{\psi}^{(\ell+1/2)}_{k-1/2,n,g} = \omega^l a_{r,n,g} e^{i\lambda x_j} \,, \tag{3.53a}$$

$$\tilde{\psi}^{(\ell+1/2)}_{k,n,g} = \omega^l b_{r,n,g} e^{i\lambda x_j} \,, \tag{3.53b}$$

$$\tilde{\phi}^{(\ell+1/2)}_{k,g} = \omega^l B_{r,g} e^{i\lambda x_j} \,, \tag{3.53c}$$

$$\tilde{\Phi}^{(\ell+1/2)}_{j,g} = \omega^l \mathcal{D}_g e^{i\lambda x_j} \,, \tag{3.53d}$$

$$\tilde{\Phi}^{(\ell+1)}_{j,g} = \omega^l F_g e^{i\lambda x_j} \,, \tag{3.53e}$$

$$\tilde{\Phi}^{(\ell+1)}_{1,j+1/2,g} = \omega^l K_g e^{i\lambda x_{j+1/2}} \ , \tag{3.53f}$$

$$\tilde{\phi}^{(\ell+1)}_{k,g} = \omega^{l+1} E_{r,g} e^{i\lambda x_j} \ . \tag{3.53g}$$

We note that the two-group ansatz does not include the total cross section in the exponential term, as this value is now group-dependent. The fine-grid error coefficients are assumed to be periodic on the coarse grid, such that:

$$\tilde{\psi}^{(\ell+1/2)}_{(k+p)-1/2,n,g} = \left(\tilde{\psi}^{(\ell+1/2)}_{k-1/2,n,g}\right) e^{i\lambda\Delta} = \omega^l a_{r,n,g} e^{i\lambda(x_j+\Delta)} \ . \tag{3.54}$$

Inserting the ansatz into Eqs. (3.51) and simplifying, we obtain the following system of equations:

$$\begin{cases} \frac{\mu_n}{h}\left(a_{r+1,n,1} - a_{r,n,1}\right) + \Sigma_{t,1} b_{r,n,1} - \frac{\Sigma_{s,1\to1}}{2} B_{r,1} = \frac{\Sigma_{r,1}\Sigma_{r,2}}{2\Sigma_{s,1\to2}} E_{r,2} \ , & 1 \le r < p \ , \\ \frac{\mu_n}{h}\left(a_{1,n,1} e^{i\lambda\Delta} - a_{r,n,1}\right) + \Sigma_{t,1} b_{r,n,1} - \frac{\Sigma_{s,1\to1}}{2} B_{r,1} = \frac{\Sigma_{r,1}\Sigma_{r,1}}{2\Sigma_{s,1\to2}} E_{r,2} \ , & r = p \ , \end{cases} \tag{3.55a}$$

$$\begin{cases} \frac{\mu_n}{h}\left(a_{r+1,n,2} - a_{r,n,2}\right) + \Sigma_{t,2} b_{r,n,2} - \frac{\Sigma_{s,1\to2}}{2} B_{r,1} - \frac{\Sigma_{s,2\to2}}{2} B_{r,2} = 0 \ , & 1 \le r < p \ , \\ \frac{\mu_n}{h}\left(a_{1,n,2} e^{i\lambda\Delta} - a_{r,n,2}\right) + \Sigma_{t,2} b_{r,n,2} - \frac{\Sigma_{s,1\to2}}{2} B_{r,1} - \frac{\Sigma_{s,2\to2}}{2} B_{r,2} = 0 \ , & r = p \ , \end{cases} \tag{3.55b}$$

$$a_{1,n,g} = a_{1,n,g} e^{i\lambda X} \ , \tag{3.55c}$$

$$\begin{cases} b_{r,n,g} = \left[\frac{1+\alpha_{n,g}}{2}\right] a_{r+1,n,g} + \left[\frac{1-\alpha_{n,g}}{2}\right] a_{r,n,g} \ , & 1 \le r < p \ , \\ b_{r,n,g} = \left[\frac{1+\alpha_{n,g}}{2}\right] a_{1,n,g} e^{i\lambda\Delta} + \left[\frac{1-\alpha_{n,g}}{2}\right] a_{r,n,g} & r = p \ , \end{cases} \tag{3.55d}$$

$$B_{r,g} = \sum_{n=1}^{N} w_n b_{r,n,g} \ , \tag{3.55e}$$

$$\mathcal{D}_g = \frac{1}{p} \sum_{r=1}^{p} B_{r,g} \ , \tag{3.55f}$$

$$K_1\left(e^{i\lambda\frac{\Delta}{2}} - e^{-i\lambda\frac{\Delta}{2}}\right) + \Sigma_{r,1}\Delta F_1 = \frac{\Sigma_{r,1}\Sigma_{r,2}}{\Sigma_{s,1\to2}} \Delta F_2 \ , \tag{3.55g}$$

$$K_2\left(e^{i\lambda\frac{\Delta}{2}} - e^{-i\lambda\frac{\Delta}{2}}\right) + \Sigma_{r,2}\Delta F_2 - \Sigma_{s,1\to2}\Delta F_1 = 0 \ , \ 1 \le j \le J \ , \tag{3.55h}$$

$$K_g = -\tilde{D}_g(F_g - \mathcal{D}_g)\left(e^{i\lambda\frac{\Delta}{2}} - e^{-i\lambda\frac{\Delta}{2}}\right) + \sum_{n=1}^{N} w_n \mu_n a_{1,n,g} e^{i\lambda\frac{\Delta}{2}} \tag{3.55i}$$

$$\sum_{n=1}^{N} w_n \mu_n a_{1,n,g} = e^{i\lambda X} \sum_{n=1}^{N} w_n \mu_n a_{1,n,g} \ , \tag{3.55j}$$

$$0 = \sum_{j=1}^{J} e^{i\lambda x_j} \,, \tag{3.55k}$$

$$\omega E_{r,g} - B_{r,g} = (F_g - \mathcal{D}_g) \,. \tag{3.55l}$$

From the boundary equations (3.55c) and (3.55j), we determine permissible values of the Fourier frequency λ for the discrete system:

$$\lambda_s = \frac{2s\pi}{X} \,, \;\; 1 \le s < J \,. \tag{3.56}$$

This set of Fourier frequencies automatically satisfies the normalization condition in Eq. (3.55k). Next, we use Eq. (3.55i) to eliminate the current error coefficients K_g in Eqs. (3.55g) and (3.55h). We also algebraically eliminate $\mathcal{D}$ from the remainder of Eqs. (3.55), using a combination of Eqs. (3.55e), (3.55f), and (3.55d):

$$\begin{aligned}
\mathcal{D} &= \frac{1}{p} \sum_{r=1}^{p} B_{r,g} \,, \\
&= \frac{1}{p} \sum_{r=1}^{p} \sum_{n=1}^{N} w_n b_{r,n,g} \,, \\
&= \frac{1}{p} \sum_{r=1}^{p} \sum_{n=1}^{N} w_n \left[\frac{1+\alpha_{n,g}}{2} \right] a_{r+1,n,g} + \left[\frac{1-\alpha_{n,g}}{2} \right] a_{r,n,g} \,, \\
&= \frac{1}{p} \sum_{n=1}^{N} w_n \left(a_{1,n,g} \left(e^{i\lambda_s \Delta} + 1 \right) + 2 \sum_{r=2}^{p-1} a_{r,n,g} \right) \,.
\end{aligned} \tag{3.57}$$

Inserting Eq. (3.57) into Eqs. (3.55g) and (3.55h) and carrying out further simplification yields the following system of equations:

$$\begin{cases}
\left(\frac{\mu_n}{h} + \Sigma_{t,1}\left[\frac{1+\alpha_{n,1}}{2}\right]\right) a_{r+1,n,1} - \frac{\Sigma_{s,1\to1}}{2} \sum_{n'=1}^{N} \left(w_{n'} \left[\frac{1+\alpha_{n',1}}{2} \right] a_{r+1,n',1} \right) \\
\quad + \left(-\frac{\mu_n}{h} + \Sigma_{t,1}\left[\frac{1-\alpha_{n,1}}{2}\right]\right) a_{r,n,1} - \frac{\Sigma_{s,1\to1}}{2} \sum_{n'=1}^{N} \left(w_{n'} \left[\frac{1-\alpha_{n',1}}{2} \right] a_{r,n',1} \right) - \frac{\Sigma_{r,1}\Sigma_{r,2}}{2\Sigma_{s,1\to2}} E_{r,2} = 0 \,, \quad 1 \le r < p \,, \\
\left(\frac{\mu_n}{h} + \Sigma_{t,1}\left[\frac{1+\alpha_{n,1}}{2}\right]\right) a_{1,n,1} e^{i\lambda_s \Delta} - \frac{\Sigma_{s,1\to1}}{2} \sum_{n'=1}^{N} \left(w_{n'} \left[\frac{1+\alpha_{n',1}}{2} \right] a_{1,n',1} \right) e^{i\lambda_s \Delta} \\
\quad + \left(-\frac{\mu_n}{h} + \Sigma_{t,1}\left[\frac{1-\alpha_{n,1}}{2}\right]\right) a_{r,n,1} - \frac{\Sigma_{s,1\to1}}{2} \sum_{n'=1}^{N} \left(w_{n'} \left[\frac{1-\alpha_{n',1}}{2} \right] a_{r,n',1} \right) - \frac{\Sigma_{r,1}\Sigma_{r,2}}{2\Sigma_{s,1\to2}} E_{r,2} = 0 \,, \quad r = p \,,
\end{cases} \tag{3.58a}$$

$$\begin{cases} \left(\frac{\mu_n}{h}+\Sigma_{t,2}\left[\frac{1+\alpha_{n,2}}{2}\right]\right)a_{r+1,n,2}-\frac{\Sigma_{s,2\to 2}}{2}\sum_{n'=1}^{N}\left(w_{n'}\left[\frac{1+\alpha_{n',2}}{2}\right]a_{r+1,n',2}\right) & \\ \quad +\left(-\frac{\mu_n}{h}+\Sigma_{t,2}\left[\frac{1-\alpha_{n,2}}{2}\right]\right)a_{r,n,2}-\frac{\Sigma_{s,2\to 2}}{2}\sum_{n'=1}^{N}\left(w_{n'}\left[\frac{1-\alpha_{n',2}}{2}\right]a_{r,n',2}\right) & \\ \quad -\frac{\Sigma_{s,1\to 2}}{2}\sum_{n'=1}^{N}w_{n'}\left(\left[\frac{1+\alpha_{n',1}}{2}\right]a_{r+1,n',1}+\left[\frac{1-\alpha_{n',1}}{2}\right]a_{r,n',1}\right)=0\,, & 1\le r<p\,, \\ \left(\frac{\mu_n}{h}+\Sigma_{t,2}\left[\frac{1+\alpha_{n,2}}{2}\right]\right)a_{1,n,2}e^{i\lambda_s\Delta}-\frac{\Sigma_{s,2\to 2}}{2}\sum_{n'=1}^{N}\left(w_{n'}\left[\frac{1+\alpha_{n',2}}{2}\right]a_{1,n',2}\right)e^{i\lambda_s\Delta} & \\ \quad +\left(-\frac{\mu_n}{h}+\Sigma_{t,2}\left[\frac{1-\alpha_{n,2}}{2}\right]\right)a_{r,n,2}-\frac{\Sigma_{s,2\to 2}}{2}\sum_{n'=1}^{N}\left(w_{n'}\left[\frac{1-\alpha_{n',2}}{2}\right]a_{r,n',2}\right) & \\ \quad -\frac{\Sigma_{s,1\to 2}}{2}\sum_{n'=1}^{N}w_{n'}\left(\left[\frac{1+\alpha_{n',1}}{2}\right]a_{1,n',1}e^{i\lambda_s\Delta}+\left[\frac{1-\alpha_{n',1}}{2}\right]a_{r,n',1}\right)=0\,, & r=p\,, \end{cases} \tag{3.58b}$$

$$\sum_{n=1}^{N}w_n\left(\mu_n a_{1,n,1}(e^{i\lambda_s\Delta}-1)+\frac{G_1}{p}a_{1,n,1}(e^{i\lambda_s\Delta}+1)+\frac{2}{p}\sum_{r=2}^{p-1}a_{r,n,1}\right) \\ +(\Sigma_{r,1}\Delta-G_1)F_1-\frac{\Sigma_{r,1}\Sigma_{r,2}}{\Sigma_{s,1\to 2}}\Delta F_2=0\,, \tag{3.58c}$$

$$\sum_{n=1}^{N}w_n\left(\mu_n a_{1,n,2}(e^{i\lambda_s\Delta}-1)+\frac{G_2}{p}a_{1,n,2}(e^{i\lambda_s\Delta}+1)+\frac{2}{p}\sum_{r=2}^{p-1}a_{r,n,2}\right) \\ +(\Sigma_{r,2}\Delta-G_2)F_2-\Sigma_{s,1\to 2}\Delta F_1=0\,, \tag{3.58d}$$

where

$$G_g=\frac{2}{3\Sigma_{t,g}\Delta}(\cos(\lambda_s\Delta)-1)\,,\ g=1,2\,,$$

and

$$\begin{cases} \sum_{n=1}^{N}w_n\left(\left[\frac{1+\alpha_{n,g}}{2}\right]a_{r+1,n,g}+\left[\frac{1-\alpha_{n,g}}{2}\right]a_{r,n,g}\right)+F_g & \\ \quad -\frac{1}{p}\sum_{n=1}^{N}w_n\left(a_{1,m,g}(e^{i\lambda_s\Delta}+1)+2\sum_{r=2}^{p-1}a_{r,n,g}\right)-E_{r,g}\omega=0\,, & 1\le r<p\,,\ g=1,2\,, \\ \sum_{n=1}^{N}w_n\left(\left[\frac{1+\alpha_{n,g}}{2}\right]a_{1,n,g}e^{i\lambda_s\Delta}+\left[\frac{1-\alpha_{n,g}}{2}\right]a_{r,n,g}\right)+F_g & \\ \quad -\frac{1}{p}\sum_{n=1}^{N}w_n\left(a_{1,m,g}(e^{i\lambda_s\Delta}+1)+2\sum_{r=2}^{p-1}a_{r,n,g}\right)-E_{r,g}\omega=0\,, & r=p\,,\ g=1,2\,. \end{cases} \tag{3.58e}$$

Similar to the monoenergetic case, Eqs. (3.58) can be written in block matrix form [25]:

$$\begin{bmatrix} \mathbf{A} & \mathbf{B} \\ \mathbf{C} & -\omega\mathbf{I} \end{bmatrix}\begin{bmatrix} \mathbf{x} \\ \mathbf{y} \end{bmatrix}=\begin{bmatrix} \mathbf{0} \\ \mathbf{0} \end{bmatrix}\,. \tag{3.59}$$

Here, **A** is a $(2Np+2)\times(2Np+2)$ matrix containing the coefficients of $a_{r,n,g}$ and F_g from Eqs. (3.58a)-(3.58d). Similarly, **B** is a $(2Np+2)\times 2p$ matrix composed of the coefficients of $E_{r,g}$ from Eqs. (3.58a)-(3.58d), and **C** is a $2p\times(2Np+2)$ matrix containing the coefficients of $a_{r,n,g}$ and F_g from Eq. (3.58e). The final matrix $(-\omega\mathbf{I})$ is a $2p \times 2p$ diagonal matrix containing the negative of the eigenvalues $\omega_{r,g}$, which are the coefficients of $E_{r,g}$ in Eqs. (3.58e). The size-$(2Np+2)$ column vector $\mathbf{x}$ contains the $a_{r,n,g}$ and F_g values, while the size-$2p$ column vector $\mathbf{y}$ contains the $E_{r,g}$ values. To solve for the system eigenvalues $\omega_{r,g}$, we follow the procedure outlined in Section 3.4.1.2. From inspection, the determinant of the original block matrix system is zero, while the determinant of matrix $\mathbf{A}$ is non-zero. Thus, we can infer that

$$|-\mathbf{C}\mathbf{A}^{-1}\mathbf{B} - \omega\mathbf{I}| = \mathbf{0}\,, \tag{3.60}$$

where $\mathbf{C}\mathbf{A}^{-1}\mathbf{B}$ and $\mathbf{I}$ are $2p \times 2p$ matrices. In this form, it is clear that Eq. (3.60) is an eigenvalue problem, with $2p$ eigenvalues $\omega_{r,g}$.

Using Eq. (3.60), the eigenvalues $\omega_{r,g}$ can be calculated numerically for $1 \le r \le p$, $g = 1,2$ and permitted values of the discrete Fourier frequency, λ_s. Once the eigenvalues are known, the spectral radius ρ is determined using

$$\rho = \sup_{g=1,2}\left[\sup_{1\le s<J}\left(\sup_{1\le r\le p}\left|\omega_{r,g}(\lambda_s)\right|\right)\right]. \tag{3.61}$$

3.5 Numerical Results

In this section, we present numerical results for the CMFD-MC method. We begin with numerical results from the stability analysis. Then, we assess the performance of the CMFD-MC method (along with the Wolters and LJLS variants) for a set of benchmark problems. These are the same problems that were introduced in Section 2.4.2; they are later used in Chapter 5 to provide an overall comparison of the methods presented in this thesis.

3.5.1 Stability Analysis

3.5.1.1 Monoenergetic Case

As a first test of the validity of the monoenergetic Fourier analysis, we compare its predictions to spectral radius estimates obtained from a “surrogate” discrete ordinates - CMFD (CMFD-$\mathrm{S_N}$) code. The surrogate code treats the scattering source implicitly, as in the non-random CMFD-MC method. Instead of performing a fixed number of inner scattering source iterations per outer fission source iteration, the surrogate code performs as many inner scattering source iterations as is necessary to converge the scattering source to a very small tolerance. When run on a fine space-angle grid, the surrogate code should behave just like MC in the limit as the number of histories approaches infinity. Thus, the spectral radius estimate produced using a fine space-angle grid should well-approximate the desired estimate.

To determine a sufficiently fine space-angle grid, we performed a parametric study using the Fourier analysis script developed for this work. Values of the coarse-grid parameter p and angular order N were successively increased for a problem with fixed cross sections $\Sigma_t = 1\ \text{cm}^{-1}$, $\nu\Sigma_f = 0.01\ \text{cm}^{-1}$, and $\Sigma_s = 0.5\ \text{cm}^{-1}$. The study was repeated twice, for coarse grids $\Delta = 1$ cm and $\Delta = 5$ cm. Resulting spectral radius estimates were then plotted as a function of the coarse-grid parameter and number of discrete angles. These plots are shown in Fig. 3.4.

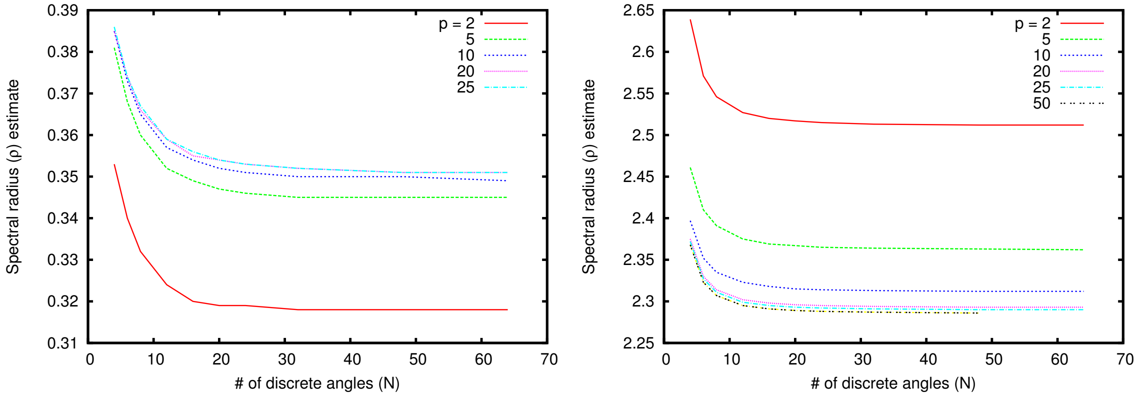

(a) $\Delta = 1$ cm (b) $\Delta = 5$ cm

Figure 3.4: Discrete spectral radius estimate (ρ) as a function of angular order N and coarse-grid parameter p

In both cases, the spectral radius curve changes significantly when the number of discrete angles N is small, but becomes flat for $N \geq 16$. For the $\Delta = 1$ cm case, we see a large shift in the spectral radius estimate between the $p = 2$ and $p = 5$ curves, but for $p \geq 10$ the change in the spectral radius is small (on the order of 10^{-3}). For $\Delta = 5$ cm, the change in the spectral radius estimate becomes small for $p \geq 25$.

Based on this study, we opted to use $p = 50$ and the S_{32} quadrature set for our calculations. This particular discretization provided sufficient accuracy for the discrete approximation across a wide range of coarse grid sizes, while maintaining reasonable runtimes and memory demands for the Fourier analysis script. Due to the size of the block matrix system ($[2Np+p] \times [2Np+p]$), the spectral radius calculation becomes intractable for large values of N and p. While there is inevitably a discretization error in the discrete results, this error should be small.

Next, in our direct CMFD-MC and surrogate CMFD-S$_\text{N}$ simulations, we employed the same spectral radius esimator used in Section 2.3.2:

$$\rho = \frac{||\Phi^{(\ell+1)} - \Phi^{(\ell)}||}{||\Phi^{(\ell)} - \Phi^{(\ell-1)}||} \,. \tag{3.62}$$

This expression requires estimates of Φ for three consecutive iterations, and is accurate for large values of ℓ. For small values of ρ, this is slightly problematic for the surrogate CMFD-S$_\text{N}$ simulations, since roundoff errors can significantly affect the accuracy of Eq. (3.62) after only a few iterations. It is much more problematic for the random CMFD-MC simulations, since the error in the fission source can quickly become reduced to the magnitude of the statistical errors.

Fortunately, small values of ρ, which are the most difficult to estimate, are not so interesting because the iteration method converges very rapidly. Larger values of ρ, closer to or greater than unity, are much more interesting, and for these Eq. (3.62) is more accurate.

The k-eigenvalue test problem considered in this section is a homogeneous 50-centimeter slab with periodic boundaries. The total and fission cross sections are fixed, while the scattering cross section takes one of four values. The coarse grid size varies between 1.0 and 12.5 mean free paths (mfp), keeping in mind that there must be an integer number of coarse cells. Numerical data for the problem are provided in Table 3.1.

Table 3.1: Test problem specifications

Σ_t (cm^{-1})	$\nu\Sigma_f$ (cm^{-1})	Σ_s (cm^{-1})	Δ (cm)
1.0	0.01	0.5, 0.75, 0.9, 0.99	1.0 - 12.5

For each coarse grid/scattering ratio combination, we calculate the theoretical spectral radius using $p = 50$ with the S_{32} Gauss-Legendre quadrature set. The numerical spectral radius is then estimated using our surrogate CMFD-S$_\text{N}$ code. We reiterate that the discrete ordinates code performs many sweeps (inner iterations) to converge the scattering source to a tight tolerance (10^{-9}) before proceeding to the CMFD calculation, in order to mimic the non-random CMFD-MC method.

We were also able to estimate the spectral radius directly using a CMFD-MC code. Unfortunately, it is difficult to estimate ρ when the spectral radius is small (i.e. the fission source converges very quickly), because the magnitude of the fission source error becomes comparable to the stochastic error after very few cycles. Eq. (3.62) requires three cycles of flux data to numerically estimate the spectral radius; if ρ is small, the fission source error may already be small compared to the random error before an estimate can be calculated!

Difficulties also occur when ρ is less than but close to unity; for these problems the random statistical errors in CMFD-MC can drive the barely-stable non-random CMFD-MC method unstable.

To estimate the CMFD-MC spectral radius numerically, the code was initialized with a random fission source guess. We then used Eq. (3.62) to generate a single value of ρ after the fourth cycle. This procedure was repeated for twenty-five independent simulations to obtain an average CMFD-MC ρ value, which is plotted along with its standard deviation in the subsequent figures. Evidence from multiple trials shows that reasonably accurate estimates of ρ can only be obtained during the first few inactive cycles of each simulation (when the fission source error is larger than the random error). Because three cycles of coarse-grid fluxes are required to generate an estimate of ρ, the first value is not available until the end of the third iteration cycle. This estimate tends to be slightly biased (likely due to contamination from the initial guess), and we discard it. As a result, the earliest usable spectral radius estimate is calculated after the fourth iteration cycle.

In spite of these difficulties, we were able to calculate direct CMFD-MC spectral radius estimates for problems in which $0.5 < \rho < 0.98$. Again, if $\rho < 0.5$, the fission source converges too rapidly for Eq. (3.62) to become accurate. Also, if $\rho > 0.98$, then the random statistical errors in CMFD-MC can drive the barely-stable non-random CMFD-MC method unstable. For this reason, our direct estimates of ρ from CMFD-MC simulations become *very* noisy when $\rho \approx 1$.

But perhaps most importantly, our direct numerical simulations show that for a given scattering ratio, the Fourier analysis accurately predicts the coarse grid size at which the simulation becomes unstable.

Figures 3.5 through 3.8 compare the theoretical, CMFD-S_N and CMFD-MC spectral radius results for $c = 0.5$, 0.75, 0.9 and 0.99, respectively. The CMFD-S_N spectral radius very closely matches the theoretical prediction for most cases, with the exception of problems in which the true spectral radius is very low. In these cases, the CMFD-S_N solution converges to machine precision too quickly to obtain an asymptotic ρ estimate.

There are several interesting trends in the CMFD-MC spectral radius data. First, the spectral radius increases monotonically as the coarse grid size increases. There appear to no be no coarse grid sizes between $\Delta = 1$ mfp and $\Delta = 12.5$ mfp for which the CMFD-MC method is stable for all values of the scattering ratio $0 \leq c < 1$, even in the limit as the number of particles becomes infinite.

Also, the Fourier analysis predicts that for a fixed coarse grid size, the spectral radius decreases (the method converges more rapidly) as the scattering ratio increases. This trend can be explained by examination of the CMFD-MC iteration strategy. As previously

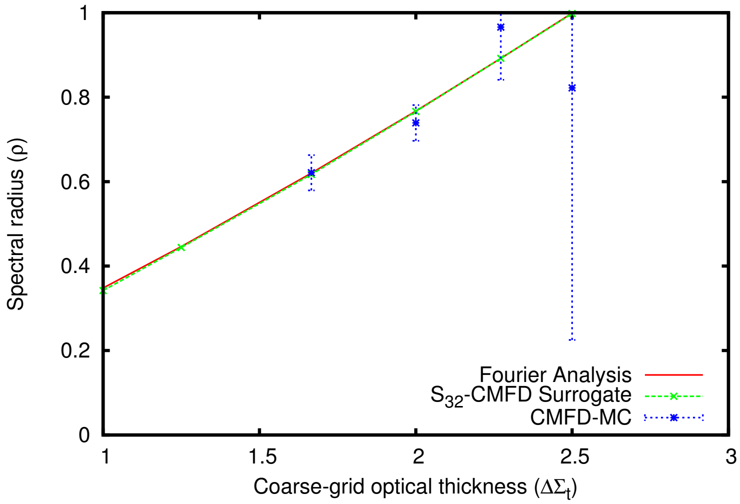

Figure 3.5: Spectral radius (ρ) vs. coarse-grid optical thickness for $c = 0.5$

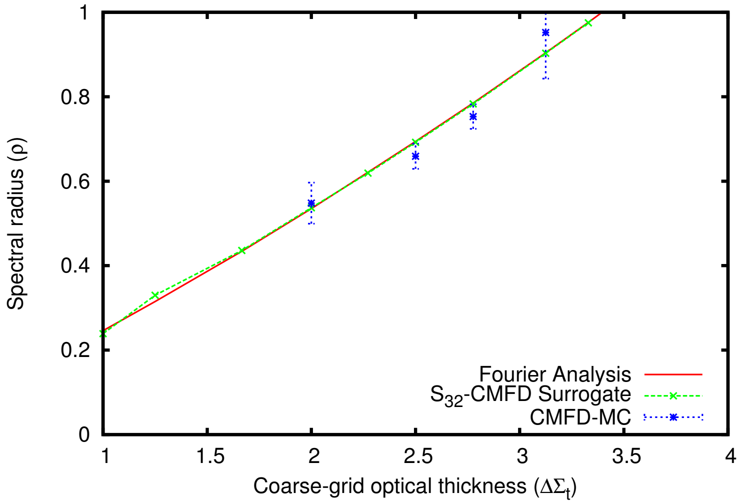

Figure 3.6: Spectral radius (ρ) vs. coarse-grid optical thickness for $c = 0.75$

described, the MC method treats scattering implicitly; the scattering source is converged entirely during the MC sweep. If the scattering ratio is near unity, the MC simulation does more "work" during a single iteration than it would for a low-scattering problem. This transfers a considerable amount of the convergence burden to the inner MC sweep, which results in outer (CMFD) fission source convergence after very few cycles.

In addition, Figs. 3.5 - 3.8 show that the standard deviation of the CMFD-MC spectral radius estimate becomes large when $\rho \approx 1$. As the theoretical spectral radius approaches unity, the fission source convergence rate becomes arbitrarily slow for the hypothetical case

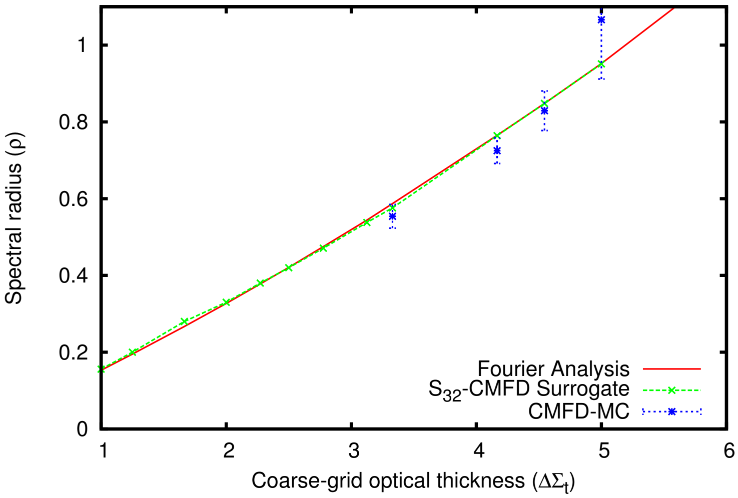

Figure 3.7: Spectral radius (ρ) vs. coarse-grid optical thickness for $c = 0.9$

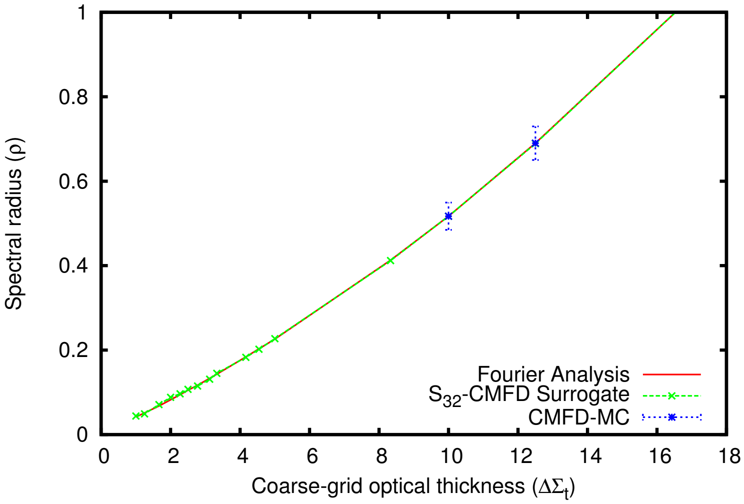

Figure 3.8: Spectral radius (ρ) vs. coarse-grid optical thickness for $c = 0.99$

with no stochastic noise. Since our MC simulations are necessarily run with a finite number of particles per cycle, our simulations have a non-negligible random error in quantities tallied during the MC sweep. This additional error term can induce an instability in problems that are theoretically stable (in the infinite-particle limit). Therefore, spectral radius estimates from our CMFD-MC code, for problems very near the predicted stability limit, tend to be noisy. This is especially obvious for the $c = 0.5$ case in Fig. 3.5.

When the CMFD-MC method is used in an unstable configuration, the coarse-grid flux shape develops a distinct cycle-to-cycle oscillation. An example of this is given in Fig. 3.9a, with a stable simulation in Fig. 3.9b for comparison. The even-cycle fluxes in Fig. 3.9a become increasingly tipped toward the left edge of the slab as the iteration cycles progress, while the odd-cycle fluxes increasingly tip toward the right. Eventually, the simulation will "crash" when the coarse-grid flux becomes negative, or when one or more coarse cells have no MC data (we disabled negative flux detection to generate data for Fig. (3.9a)). We stress that the *only* difference between the results presented in Fig. 3.9a and Fig. 3.9b is the coarse grid size; both simulations use the same random number seed, the same initial guess, the same number of particles per cycle, and the same cross sections.

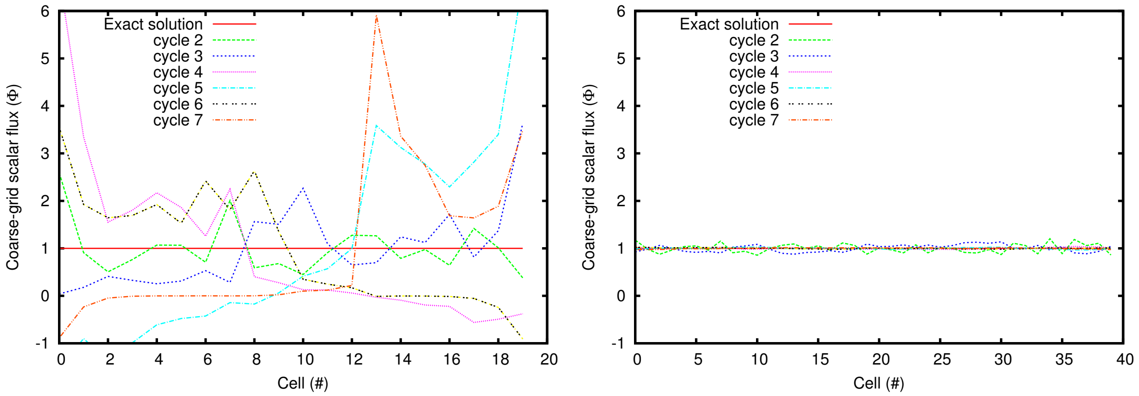

(a) $\Sigma_t\Delta = 2.5$

(b) $\Sigma_t\Delta = 1.25$

Figure 3.9: Unstable vs. stable cycle-to-cycle coarse grid fluxes, $c = 0.5$

As mentioned in Section 3.3.1, the LJLS variant of CMFD-MC [23] attempts to mitigate oscillation in the CMFD-MC method by using MC tallies from multiple cycles to form the CMFD system, a technique known as the "multi-set" method. The effect of this approach is similar to running a larger number of MC particles per iteration cycle. However, using tallies from more than one MC cycle reintroduces some of the inter-cycle correlation normally suppressed by CMFD feedback. This complicates the iteration strategy by creating a need to reset MC tallies periodically throughout the calculation. In essence, the tally accumulation technique does not address the underlying cause of the flux oscillation – a coarse grid size near or beyond the stability limit of the CMFD-MC method.

Finally, to better visualize the stability limit of the CMFD-MC method, we interpolated linearly between our Fourier analysis results to produce approximate constant-ρ curves. These curves are plotted as a function of coarse mesh size and scattering ratio, and are shown in Fig. 3.10. The phase space to the left of the $\rho = 1.0$ line represents coarse grid/scattering ratio combinations for which the one-group planar non-random CMFD-MC

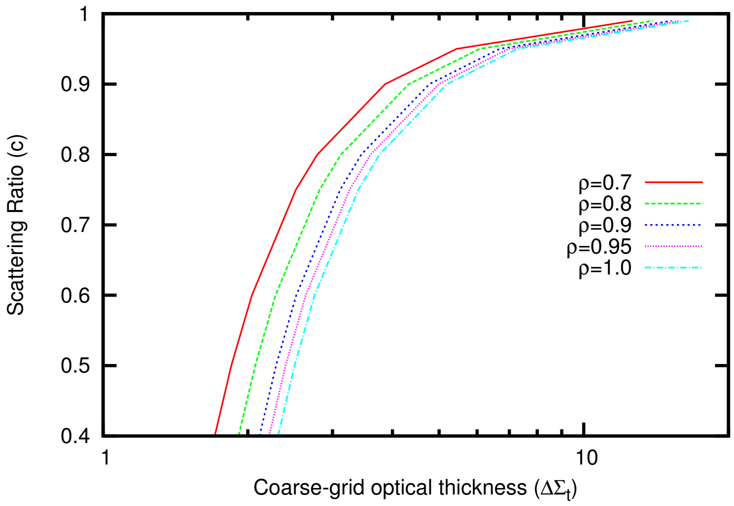

Figure 3.10: Constant spectral radius curves as a function of $\Sigma_t\Delta$ and c

method is stable. Conversely, the phase space to the right of the $\rho = 1.0$ line represents coarse grid/scattering ratio combinations for which the method is unstable. As the scattering ratio approaches unity, the non-random CMFD-MC stable grid size limit appears to tend towards infinity; for low scattering ratios ($c \leq 0.5$), the method becomes unstable for grids on the order of two mean free paths. We hypothesize that the presence of random error probably shifts these curves slightly to the left, but we cannot quantify this effect at present.

3.5.1.2 Two-group Case

To compare the theoretical predictions of the two-group Fourier analysis to numerical experiment, we use materials from the C5G7 benchmark problem. Because the C5G7 benchmark specification includes seven-group cross sections, we first flux-collapse the original cross sections to two energy groups using a discrete-ordinates code (for a homogeneous infinite-medium problem).

Using our Fourier analysis script, a small energy group parametric was performed to investigate the relationship between the theoretical spectral radius of the iteration scheme and the choice of energy bin bounds for the two-group collapse; this study showed very little change in the spectral radius as the group structure changed.

With this information, we decided to collapse C5G7 groups 1 through 3 into the fast group, with groups 4 through 7 in the thermal group. This structure was chosen with the

MC calculation in mind; in the interest of maintaining fairly comparable MC statistics between the fast and thermal groups, it is logical to include multiple fine energy groups in the thermal coarse group. In addition, this particular group structure satisfies the no-upscattering assumption made in the two-group Fourier analysis. However, we note that the other two assumptions are violated: the UO_2 fast fission cross-section is non-zero, and a small fraction of fission neutrons are born in the "thermal" group.

Table 3.2 shows the infinite-medium flux-collapsed two-group cross sections for C5G7 UO_2 fuel. The use of C5G7 cross sections allows us to investigate the spectral radius as a function of coarse grid size for more realistic reactor materials, in the hope that greater insight can be gained regarding the stability behavior of practical CMFD-MC reactor simulations.

Table 3.2: UO_2 test problem specifications (all cross sections in cm^{-1})

$\Sigma_{t,1}$	$\Sigma_{t,2}$	$\nu\Sigma_{f,1}$	$\nu\Sigma_{f,2}$	$\Sigma_{s,1\to1}$	$\Sigma_{s,1\to2}$	$\Sigma_{s,2\to2}$	χ_1	χ_2	Δ (cm)
0.328	0.524	3.81e-3	4.67e-2	0.323	1.32e-4	0.435	~1	1.17e-7	5.0 - 37.5

Here, we consider a 150-cm slab problem with periodic boundaries. This problem is phyiscally larger than the monoenergetic test problem, because total cross sections for the two-group case are considerably smaller than the monoenergetic total cross section of unity. While the 50-cm monoenergetic test problem was 50 mean free paths (mfp) thick, the 150-cm two-group test problem is ~49 mfp thick for fast neutrons, and ~79 mfp thick for thermal neutrons.

Because the two-group cross sections involve a scattering *matrix*, we can no longer derive straightforward relationships between the spectral radius and the scattering ratio. However, we can still investigate the relationship between the spectral radius and coarse grid size.

As was done in the monoenergetic case, we generate numerical spectral radius estimates using a surrogate multigroup CMFD-S_N code. CMFD-S_N cases are simulated using a very fine space-angle grid, with S_{16} quadrature and $p = 50$ fine cells per coarse cell. Ideally, we would hold the fine grid size fixed, rather than the number of fine grids per coarse; however, because the size of the matrix system depends on p, the theoretical spectral radius calculation quickly becomes intractable when the coarse grid size increases and the fine grid size is fixed.

We also generate numerical two-group spectral radius estimates using direct CMFD-MC simulations. As mentioned in Section 3.5.1.1, it is difficult to efficiently obtain estimates of the spectral radius using CMFD-MC. If the non-random spectral radius is too low

($\rho <\sim 0.5$), the fission source converges before we can obtain an accurate estimate. Likewise, if the non-random spectral radius is sufficiently close to unity, statistical errors can push the simulation into the unstable regime; this, in turn, causes the simulation to crash. Finally, a large number of particles per cycle must be simulated to minimize stochastic noise, and each case must be repeated 25 times (using different random number seeds) to estimate error bounds.

These issues are only exacerbated in the two-group case, where the number of tally bins is doubled. Two-group direct CMFD-MC spectral radius estimates are obtained using OpenMC-MG (our multigroup version of the open-source code OpenMC), which uses collision tallies for simulations with CMFD. Combined, these factors cause direct two-group CMFD-MC spectral radius estimates to be considerably noisier than their monoenergetic counterparts.

Figure 3.11 plots spectral radius versus coarse grid size for the UO_2 fuel material defined in the C5G7 benchmark. In addition to theoretical predictions, Figure 3.11 includes numerical estimates from direct CMFD-MC, as well as the CMFD-S_N surrogate.

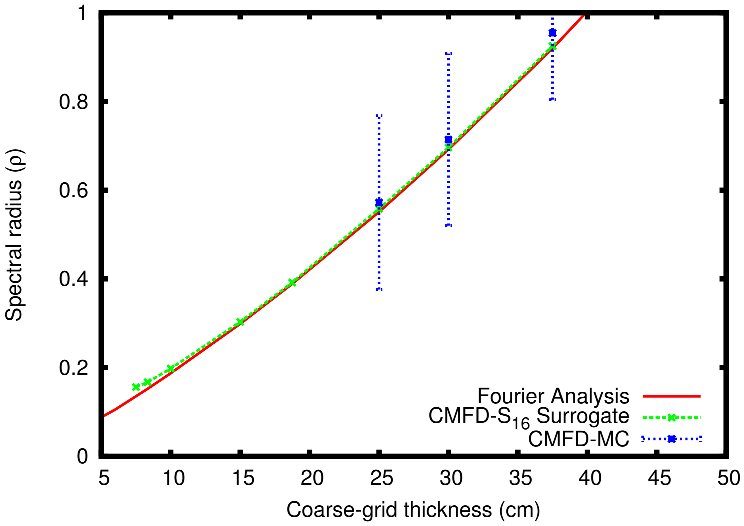

Figure 3.11: Spectral radius (ρ) vs. coarse-grid size, group-collapsed UO_2

In spite of the aforementioned difficulties, we observe very good agreement between theoretical predictions and surrogate CMFD-S_N estimates. In addition, mean CMFD-MC estimates are very close to theoretical predictions; however, standard deviations for these estimates are large, so we cannot draw definitive conclusions from this data.

The two-group UO_2 spectral radius is a monotonically increasing function of the coarse grid size, Δ. The homogeneous 150-cm UO_2 problem becomes unstable when the coarse grid is roughly 40 cm thick, which corresponds to an optical thickness of roughly 13 mfp for fast neutrons and 21 mfp for thermal neutrons.

We also investigate a group-collapse case, where the MC calculation takes place on a more detailed energy grid than the two-group CMFD calculation. To do this, we use the original seven-group C5G7 material cross sections for the MC (or surrogate S_N) transport solve. Coarse-grid quantities are tallied according to the coarse group structure, resulting in a two-group CMFD system.

We have not Fourier-analyzed this scenario, but seek to understand how well the two-group Fourier analysis predicts the convergence rate of the seven-group MC/two-group CMFD iteration scheme (hereafter referred to as the 7g/2g iteration). In the limit as the number of MC energy groups approaches infinity, the multigroup iteration scheme approaches the continuous-energy MC/two-group CMFD (CE/2g) iteration scheme. Thus, understanding how well our two-group Fourier analysis predicts the stability of the 7g/2g iteration should yield insight into how well it might predict the stability of CE/2g simulations.

Figure 3.12 plots CMFD-S_N and CMFD-MC estimates of the spectral radius for the 7g/2g iteration scheme, as a function of the coarse grid size. The theoretical two-group spectral radius curve is included for comparison.

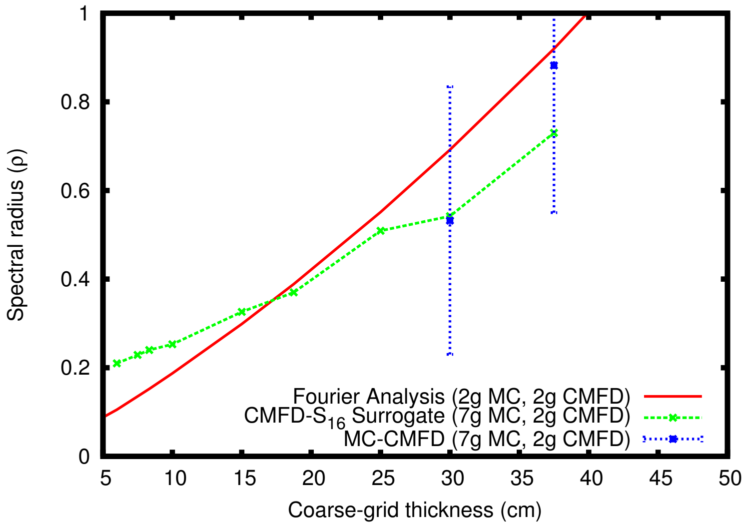

Figure 3.12: Spectral radius (ρ) vs. coarse-grid size, 7-group MC/2-group CMFD, UO_2

While both the 7g/2g and two-group spectral radius trends are monotonically increasing, it is apparent that the 7g/2g numerical spectral radius curve is flatter than the two-group theoretical curve. In other words, the seven-group/two-group CMFD-MC iteration scheme will remain stable for larger coarse grids, in the infinite-particle limit. This suggests that the use of a larger number of energy groups in the MC simulation has a stabilizing effect on the iteration scheme as a whole. The direct CMFD-MC results presented in Figure 3.12 are too noisy to provide any further insight.

3.5.2 Benchmark Problem Performance

In this section, we present numerical results assessing the performance of the CMFD-MC method for a set of benchmark *k*-eigenvalue problems. We also consider the two primary variants of this method, the Wolters method and the LJLS method, which were introduced earlier in this chapter.

First, we use a simple homogeneous problem to assess the dependence of the eigenfunction apparent relative standard deviation (RSD) on the number of active cycles simulated. This is done to empirically verify that the method behaves according to the Central Limit Theorem (CLT), which was introduced in Chapter 2. We then assess the real-to-apparent RSD ratio for the same problem.

Finally, we present numerical results for the four representative heterogeneous problems introduced in Chapter 2: the 1-D monoenergetic core problem, the 2-D UO_2 quarter assembly, the 2-D MOX assembly, and the 2-D C5G7 benchmark problem.

3.5.2.1 Homogeneous Problem

The problem considered here is the same homogeneous fissile slab presented in Chapter 2 (problem #1 in Section 2.4.2.1). Because the CMFD-MC method and its variants converge the fission source much more efficiently than the standard MC method, we use considerably fewer inactive cycles for our problem #1 CMFD-MC calculations. Simulation parameters can be found in Table 3.3 below; problem size and cross-section data was previously presented in Table 2.2. We use the same simulation parameters for CMFD-MC and the two variants (LJLS and the Wolters method). There are two possible coarse grid sizes for case A.

Table 3.3: Simulation parameters, problem #1

Case	Inactive Cyc.	Active Cyc.	Histories/Cyc.	Fine Grid (cm)	Coarse Grid (cm)
A	25	50	1e6	0.5	0.5, 2.0
B	25	100	1e6	0.5	0.5
C	25	200	1e6	0.5	0.5

First, we compare eigenfunction estimates from the three CMFD-MC variants to a high-resolution S_N benchmark. The three methods all agree reasonably well with the benchmark solution across the spatial domain, though small discrepancies are present (likely due to the high dominance ratio of the problem).

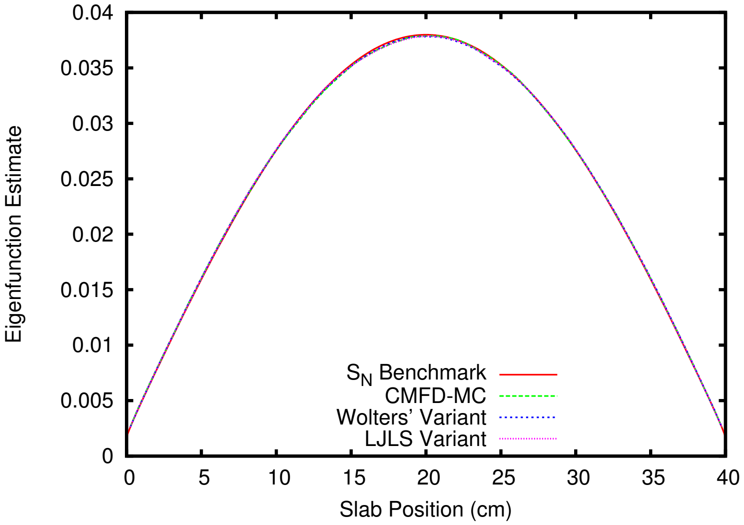

Figure 3.13: CMFD-MC and variants eigenfunction estimate, problem #1, case A (0.5-cm grid)

To determine how the apparent RSD changes as a function of the number of active batches, we simulate case A (with a 0.5-cm grid), case B and case C using the original CMFD-MC method, as well as the LJLS and Wolters variants. We then take the ratio of the the apparent RSD for case A to the apparent RSD for case B, as well as the ratio for case B to case C. If, in fact, the behavior of the method is consistent with the CLT, we expect both of the apparent RSD ratios to average roughly $\sqrt{2}$ across the slab. The apparent RSD ratios can be found in Figures 3.14a - 3.14c below, with a line at $\sqrt{2}$ for reference.

On average, apparent RSD ratios for the CMFD-MC method are reasonably close to the value predicted by the CLT. The case A/case B ratio is slightly lower than expected, which may be due to the small number of active cycles simulated in case A (the CLT assumes a large number of samples; it is likely that the number of active cycles in case A is not "sufficiently large"). The case B/case C ratio is very close to $\sqrt{2}$ when averaged across the spatial domain.

Apparent RSD ratios for the Wolters variant of CMFD-MC are also very close to the expected value when averaged across the slab, indicating that the apparent RSD of the eigenfunction decreases roughly at the rate predicted by the CLT.

The LJLS apparent RSD ratios are slightly higher than the expected value, for both case A/case B and case B/case C. This may be due to the presence of inter-cycle correlation in the LJLS simulation, which averages the tally results of several previous cycles to form the

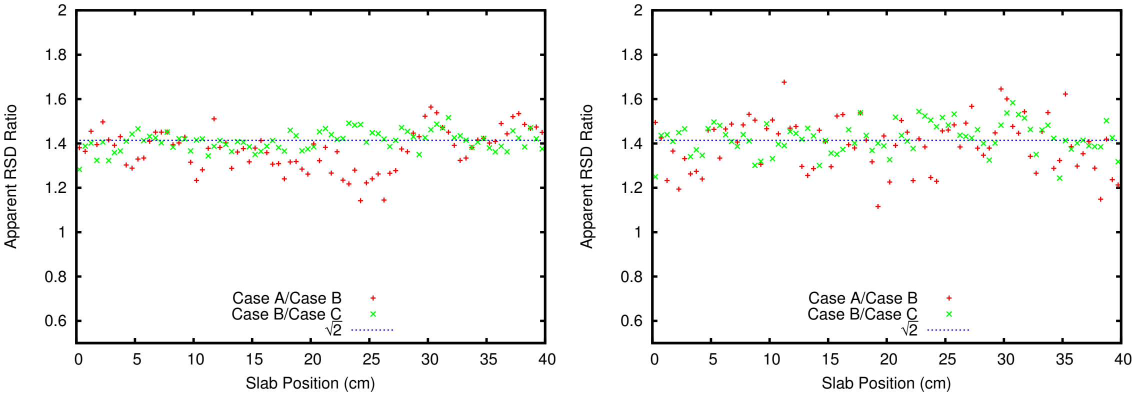

(a) CMFD-MC (b) Wolters variant

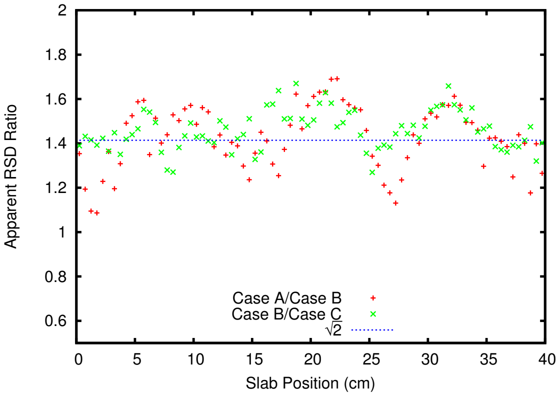

(c) LJLS variant

Figure 3.14: CMFD-MC and variants apparent RSD ratios, problem #1

CMFD system. This reasoning is supported by the shape of the apparent RSD ratio, which oscillates across the slab. This inter-cycle correlation violates the independence assumption of the CLT.

Next, we consider the real-to-apparent RSD ratio for the CMFD-MC method and its variants. These curves are shown in Figures 3.15a - 3.15c. To estimate the real-to-apparent RSD ratio, we simulate case A 25 times for each method, with a different random number seed for each simulation. Statistics can then be calculated across the 25 cases to yield an estimate of the real RSD, which is compared to the apparent RSD obtained from a single simulation. These calculations are carried out using both a 0.5-cm and a 2.0-cm coarse grid, to better understand the effect of the coarse grid size on the real-to-apparent RSD ratio.

Figure 3.15 shows two significant results. First, apparent RSD estimates from standard CMFD-MC and the Wolters variant slightly *overestimate* the real RSD for the 2.0-cm case.

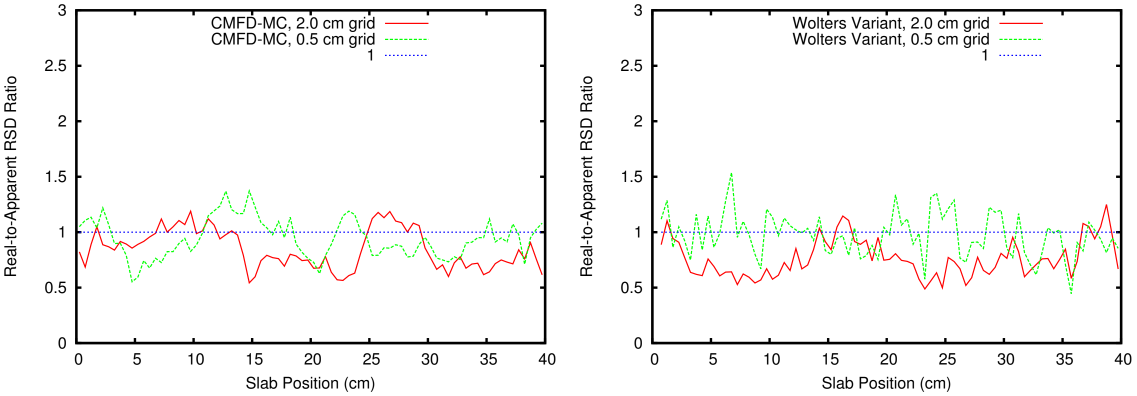

(a) CMFD-MC (b) Wolters variant

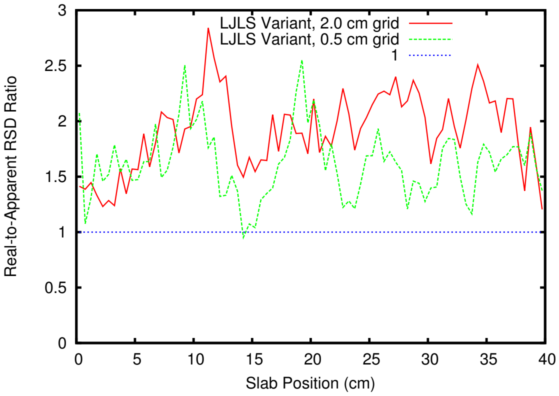

(c) LJLS variant

Figure 3.15: CMFD-MC and variants real-to-apparent RSD ratios, problem #1

Second, the LJLS variant *underestimates* the real RSD for both the 0.5 and 2.0-cm cases.

To better understand why CMFD-MC and the Wolters variant overpredict the RSD for the 2.0-cm case, we first emphasize that the 2.0-cm coarse grid case with $c = 0.5$ is near the infinite-particle stability limit ($\rho \approx 0.8$ for a 50-cm periodic problem; see Section 3.5.1.1). Consequently, the real simulation (which uses considerably fewer than ∞ histories per cycle) is likely very near the stability limit. As was shown previously, cycle-to-cycle flux estimates from unstable CMFD-MC simulations tend to exhibit growing spatial oscillations. Simular behavior is observed in CMFD-MC simulations *near* the stability limit; however, cycle-to-cycle oscillations do not grow in amplitude in this case. Instead, the solution simply tips back and forth from cycle to cycle; as a result, adjacent cycle solutions are “anti-correlated,” in a sense. At the end of the simulation, errors in individual cycle estimates of the flux largely cancel, yielding a reasonably accurate average eigenfunction over all active cycles.

When the apparent RSD is calculated, however, these cycle-to-cycle flux oscillations are taken into account. This leads to an unrealistically high estimate of solution error. (While this is undesirable behavior, we believe that this overestimation of the real RSD is, at the very least, conservative.)

If the coarse grid is refined, the non-random spectral radius decreases significantly, which leads to a corresponding decrease in the spectral radius of the real CMFD-MC simulation. This largely eliminates the oscillating behavior of the low-order solution, and results in real-to-apparent RSD ratios of roughly unity for both CMFD-MC and the Wolters variant.

In contrast, apparent RSD estimates from the LJLS method underestimate the real RSD for both the 0.5-cm and 2.0-cm cases. This occurs because the LJLS low-order system reuses tally data from previous MC cycles, which reintroduces inter-cycle correlation. The average LJLS real-to-apparent RSD ratio decreases slightly from the 2.0-cm case to the 0.5-cm case. While the LJLS real-to-apparent RSD ratio is considerably lower than the standard MC case (~1.5 - 2.5, versus 4.5 for standard MC), the LJLS apparent RSD still does not provide a conservative estimate of the real solution RSD.

3.5.2.2 1-D Core Problem

We next consider the performance of CMFD and its variants on problem #2, the large, heterogeneous 1-D core introduced in Section 2.4.2.2. Simulation parameters are shown in Table 3.5. For problem #2, we use assembly-size coarse grids for the CMFD-MC and LJLS methods (as suggested in the literature [23]), and a quarter-assembly coarse grid for the Wolters method. Coarse-grid tallies are flushed every 5 cycles in the LJLS simulation (as suggested in [23]), and CMFD feedback is skipped during the first cycle of each LJLS set.

Table 3.4: Simulation parameters, problem #2

Method	Inactive cycles	Active Cycles	Coarse Grid (cm)	Histories/Cycle
CMFD-MC	25	100	20.4	1e5
Wolters	25	100	5.1	1e5
LJLS	25	100	20.4	1e5

As before, we first compare eigenfunction estimates for CMFD-MC, the Wolters variant and the LJLS variant to the S_N benchmark solution. This comparison is plotted in Figure 3.16, with a close-up view in Figure 3.17. While solution estimates from all three methods match the overall shape of the benchmark, it is evident (especially in Figure 3.17) that

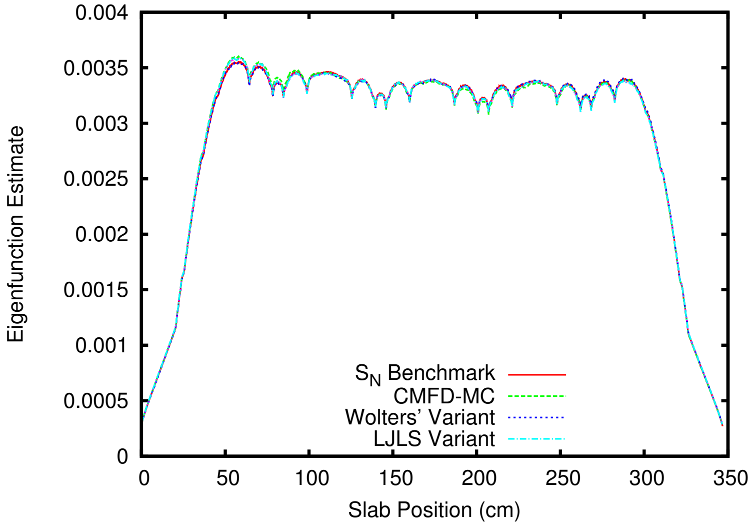

Figure 3.16: CMFD-MC and variants eigenfunction estimates, problem #2

CMFD-MC and the LJLS variant significantly overpredict the solution in the left-hand side of the core, and underpredict the solution in the right-hand side. The Wolters method, on the other hand, closely matches the benchmark solution over most of the domain. Figure 3.18 shows 50-cycle eigenfunction estimates for CMFD-MC, the Wolters variant and the LJLS variant. These show behavior similar to Figure 3.17: 50-cycle estimates from the CMFD-MC and LJLS methods are considerably less accurate than 50-cycle estimates from the Wolters variant. These results suggest that the Wolters variant is significantly more

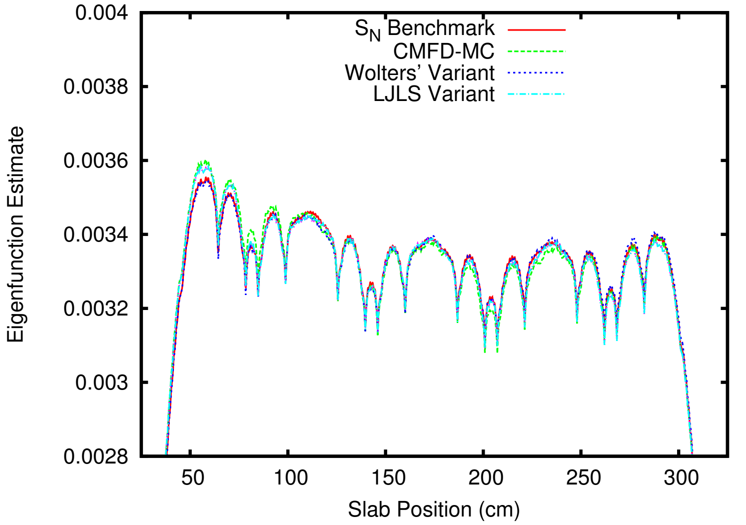

Figure 3.17: CMFD-MC and variants close-up of eigenfunction estimates, problem #2

effective at converging the fission source in problem #2.

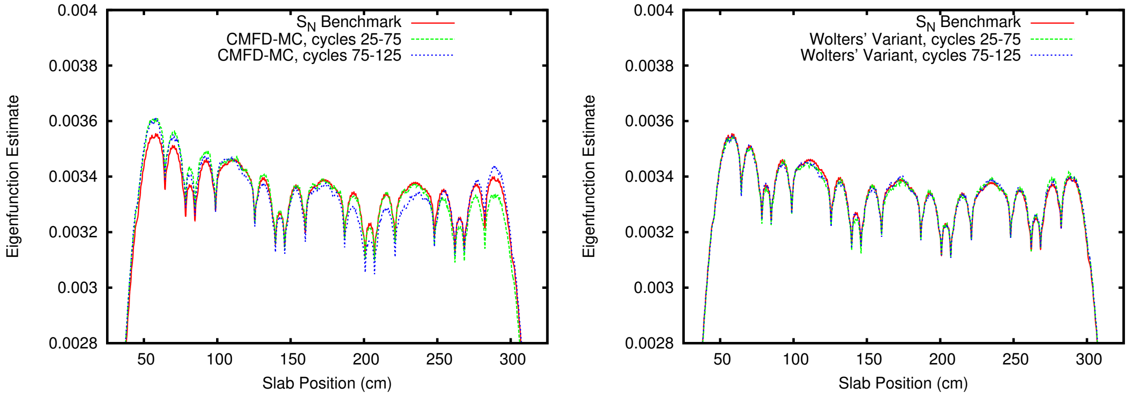

(a) CMFD-MC

(b) Wolters variant

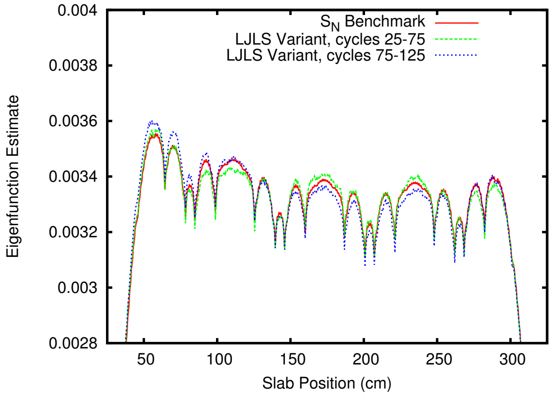

(c) LJLS variant

Figure 3.18: CMFD-MC and variants close-up of 50-cycle eigenfunction estimates, problem #2

Next, Shannon entropy versus cycle is compared in Figure 3.19. Shannon entropy for the CMFD-MC method fluctuates considerably from cycle to cycle throughout the calculation. The LJLS Shannon entropy is more tightly grouped than the CMFD-MC data, but five-cycle "clusters" of correlated values can be observed as a result of the multi-set approach. Because tallies are accumulated and reused across multiple cycles, the LJLS Shannon entropy does not display the stochastic behavior expected for a fully converged fission source. Shannon entropy values for the Wolters variant appear to vary randomly about a stationary mean throughout the active-cycle phase of the calculation (from cycles 25-125). This is the expected behavior for a sufficiently converged fission source distribution, which supports results presented in previous figures.

Finally, Figure 3.20 presents both the apparent RSD curves and the relative solution error for problem #2. Relative solution error is calculated with respect to the benchmark

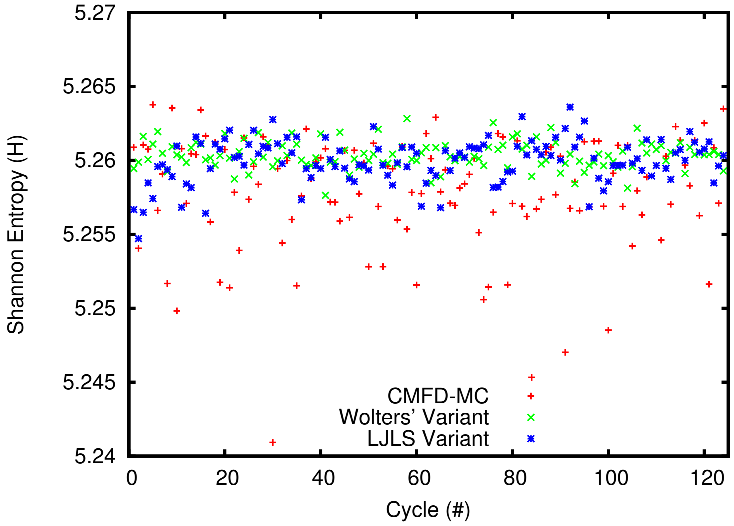

Figure 3.19: CMFD-MC and variants Shannon entropy vs. cycle number, problem #2

solution, and gives a measure of the "real" error in the CMFD-MC eigenfunctions. Apparent RSD curves are calculated using cycle flux estimates from the active-cycle portion of the simulation. If the apparent RSD is an unbiased estimator of real solution error for a

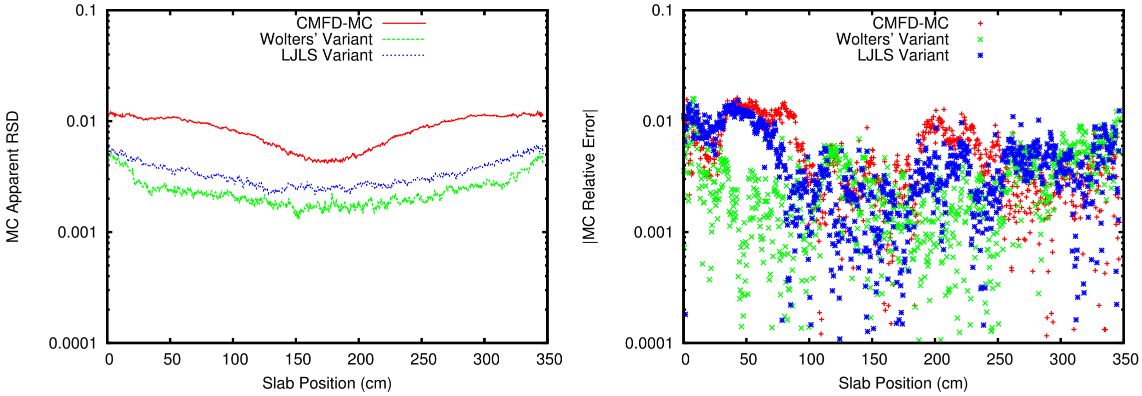

(a) Apparent RSD

(b) Relative error from benchmark

Figure 3.20: CMFD-MC and variants eigenfunction error curves, problem #2

particular method, we would expect the apparent and relative error curves in Figure 3.20 to agree reasonably well (on average). This is clearly not the case for the CMFD-MC method apparent RSD curve (shown in red), which overpredicts relative solution error considerably across most of the problem. This is likely a result of the flux oscillation phenomenon described previously, whereby the cycle-to-cycle fluxes exhibit predictable error cancellation behavior. This leads to reasonable accuracy when results are averaged over active cycles, but causes apparent RSD estimates to overpredict real solution error.

The apparent RSD estimate produced by the LJLS variant underpredicts relative error with respect to the benchmark solution. This is similar to the observed real-to-apparent RSD behavior of the LJLS variant for problem #1, and is likely due to inter-cycle correlation from a poorly converged fission source distribution. In addition, the global shape of the LJLS relative error distribution does not match the apparent RSD curve.

Finally, the apparent RSD estimate produced by the Wolters variant provides a reasonably accurate prediction of real solution error (on average). While the relative error with respect to the benchmark shows a considerable amount of high-frequency noise, the global trend in this quantity matches the trend predicted by the apparent RSD.

3.5.2.3 2-D Quarter-Assembly Problem

The next benchmark problem considered in this work is the quarter-assembly UO_2 problem originally introduced in Section 2.4.2 (problem #3). Because problem #3 is not optically thick, we expect all of the CMFD-MC variants to perform comparably. Thus, we only present results for the Wolters variant of CMFD-MC.

Simulation parameters for problem #3 are listed in Table 3.5. While the MC simulation uses seven-group cross sections, the CMFD formulation used to accelerate fission source convergence for problem #3 is monoenergetic; in other words, the CMFD calculation involves only one energy group. This is done to allow comparison with the LCMC and mixed method results presented later in this thesis.

Table 3.5: Simulation parameters, problem #3

Method	Inactive cycles	Active Cycles	Coarse Grid (cm)	Histories/Cycle
Wolters	25	50	3.213	2e5

The CMFD system for problem #3 is formed using track-length tallies. Standard track-length tallies cannot be used to calculate quantities that depend on post-collision particle properties (e.g. average scattering cosine and fission neutron production). However, track-length tallies *can* be used in the special case where CMFD feedback is monoenergetic and scattering is isotropic. The use of track-length tallies will be discussed in further detail in Section 4.4.2.3.

Figure 3.21 shows the fast and thermal flux distributions for problem #3, tallied on a uniform 20×20 grid. These flux distributions agree very closely with the problem #3 results presented in Chapter 2. The fast flux shape is highest in the upper-left corner of the fuel, and decreases relatively smoothly across the problem domain. The thermal flux has

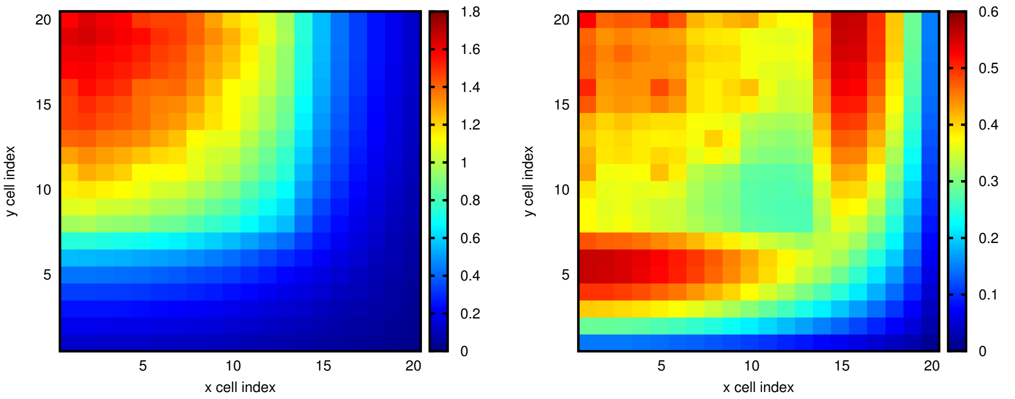

(a) Fast flux (C5G7 grp. 1-3)

(b) Thermal flux (C5G7 grp. 4-7)

Figure 3.21: Wolters variant fast and thermal flux distributions, problem #3

local peaks in the portion of the reflector nearest the fuel, where a portion of the fast and epithermal neutrons leaking from the fuel assembly downscatter into the thermal energy group.

Next, in Figure 3.22 we plot the quarter-pin power and quarter-pin power apparent RSD distributions for problem #3. Only the fuel region is included in Figure 3.22, because no power is produced in the reflector region. On average, the quarter-pin power apparent RSD

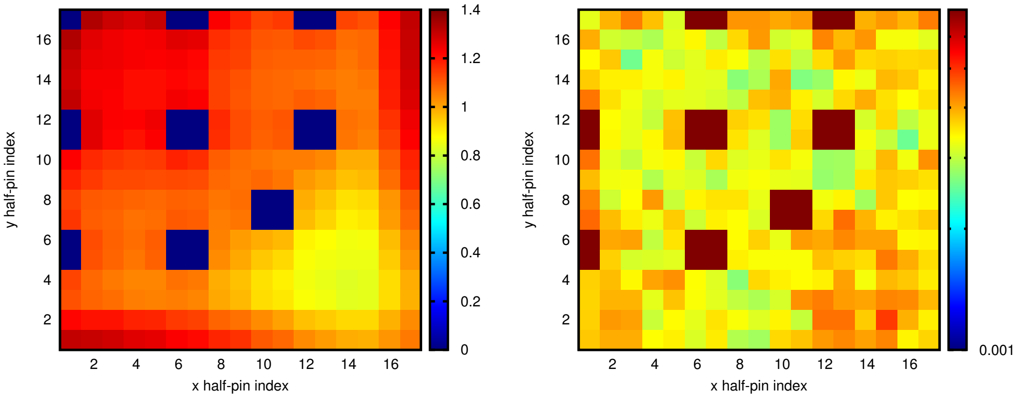

(a) Quarter-pin power

(b) Apparent RSD

Figure 3.22: Wolters variant quarter-pin power and apparent RSD, problem #3

is slightly higher for the Wolters method when compared to standard MC. The primary purpose of the Wolters method (and other CMFD-MC variants) is to efficiently converge the fission source in high dominance-ratio problems; since problem #3 is optically thin in comparison to a full-core problem, it does not benefit from the use of CMFD feedback. In this case, in fact, the use of CMFD feedback is slightly detrimental to the calculation.

3.5.2.4 2-D Assembly Problem

In this section, we provide flux and pin-power results for problem #4, the MOX assembly problem introduced in Section 2.4.2.4. The MOX assembly is surrounded by a half-assembly thick reflector region, and uses cross sections and geometry from the C5G7 benchmark (see Appendix). Like problem #3, we expect all three CMFD-MC variants to perform comparably for problem #4; thus, we present only results for the Wolters method.

Simulation parameters are listed in Table 3.6.

Table 3.6: Simulation parameters, problem #4

Method	Inactive cycles	Active Cycles	Coarse Grid (cm)	Histories/Cycle
Wolters	25	50	4.01625	2e5

Fast and thermal flux distributions for problem #4 are shown in Figure 3.23. These distributions match closely with the standard MC results presented in Section 2.4.2.4. Finally, pin-power and pin-power apparent RSD distributions are plotted in Figure 3.24. The pin power is peaked near the north and west reflecting boundaries, as expected. A slight pin power dip is evident in the outermost ring of fuel, where the MOX enrichment is lowest. These results agree closely with the standard MC distribtion in 2.4.2.4.

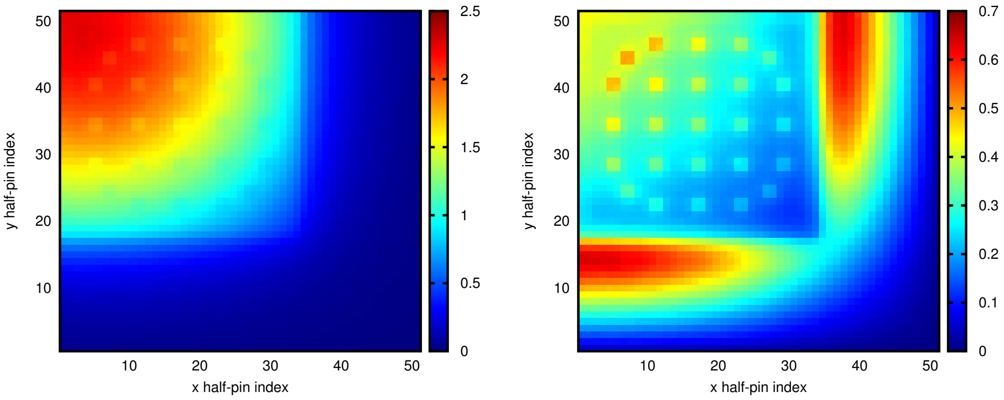

(a) Fast flux (C5G7 grp. 1-3)

(b) Thermal flux (C5G7 grp. 4-7)

Figure 3.23: Wolters variant fast and thermal flux distributions, problem #4

3.5.2.5 2-D C5G7 Benchmark

The final test problem for the CMFD-MC method (along with the Wolters and LJLS variants) is the C5G7 benchmark introduced in Section 2.4.2.5, which we refer to as problem

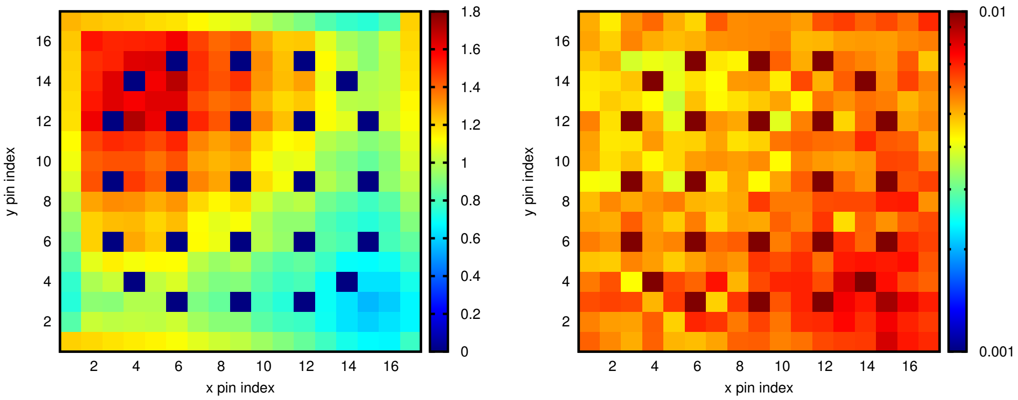

(a) Pin power

(b) Apparent RSD

Figure 3.24: Wolters variant pin power and apparent RSD, problem #4

#5. As previously described, problem #5 uses seven-group cross sections for the MC simulation. The CMFD problem is formulated using two energy groups; consequently, we group-collapse the seven-group MC tally data to form the coefficients of the low-order system. In this work, we have chosen to collapse C5G7 groups 1 through 3 into the "fast" CMFD group, with C5G7 groups 4 through 7 comprising the "thermal" CMFD group. In Section 3.5.1.2, we described the reasoning behind this group structure: because the spectral radius of real CMFD-MC simulations is sensitive to stochastic noise, it is best to balance tally information between the two coarse groups as evenly as possible. This particular choice reduces statistical noise in the thermal group, while largely maintaining the expected flux shape.

First, we present simulation parameters for problem #5 (see Table 3.7). A description of problem geometry can be found in Section 2.4.2.5, while material cross sections are located in Appendix .

Table 3.7: Simulation parameters, problem #5

Method	Inactive cycles	Active Cycles	Coarse Grid (cm)	Histories/Cycle
CMFD-MC	50	100	10.71	5e4
Wolters	50	100	10.71	5e4
LJLS	50	100	21.42	5e4

In these simulations, CMFD-MC and the Wolters variant both employ a quarter-assembly coarse grid, while LJLS employs an assembly coarse grid. We attempted to simulate the CMFD-MC method using an assembly coarse grid, but the simulation became unstable after only a few cycles (this will be discussed later in this section).

Figures 3.25 - 3.27 show fast and thermal MC pin-cell fluxes averaged across all active cycles for the CMFD-MC, Wolters and LJLS methods.

Flux solutions from the three methods are nearly indistinguishable, indicating that all three agree reasonably well. The LJLS variant appears to predict higher thermal flux in the inner reflector region than either CMFD-MC or the Wolters variant, but this is the only notable difference between the flux trends.

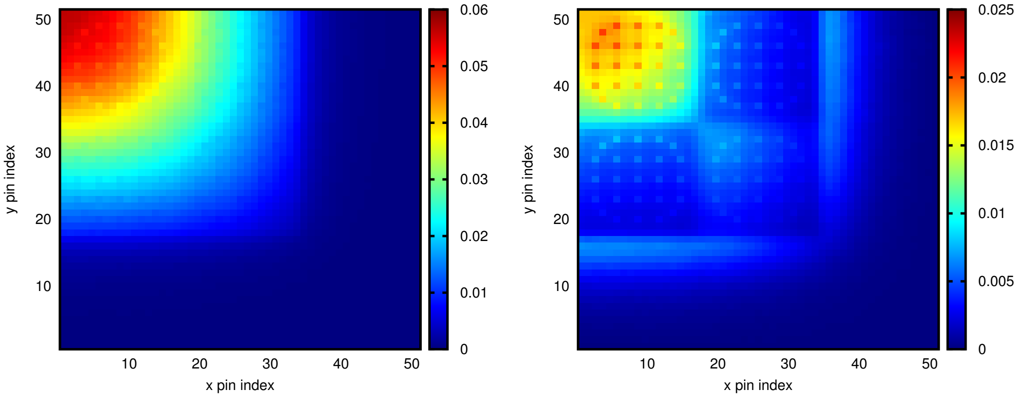

(a) Fast (C5G7 grp. 1-3)   (b) Thermal (C5G7 grp. 4-7)

Figure 3.25: CMFD-MC fast and thermal flux distributions, problem #5

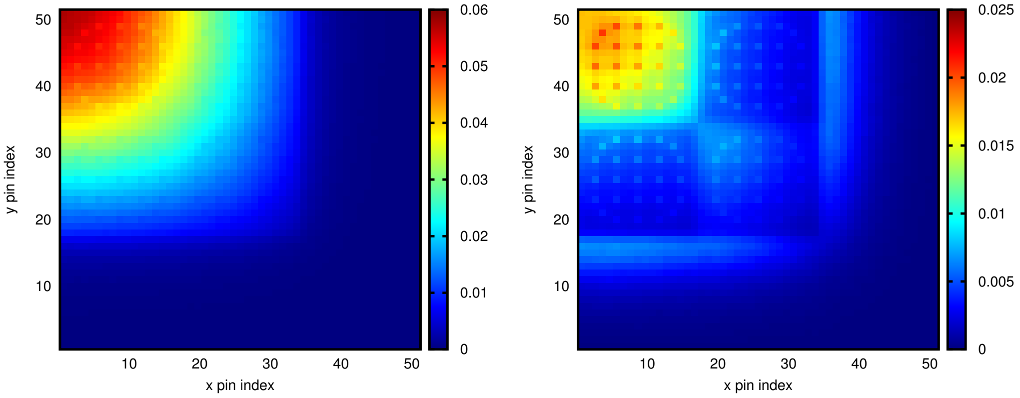

(a) Fast (C5G7 grp. 1-3)   (b) Thermal (C5G7 grp. 4-7)

Figure 3.26: Wolters variant fast and thermal flux distributions, problem #5

Shannon entropy as a function of cycle number is plotted in Figure 3.28a for CMFD-MC, the Wolters variant and the LJLS variant. Trends for CMFD-MC and the Wolters variant are reasonably similar, with stochastic variation around a mean value of ∼ 3.82. There appears to be a slightly larger spread in the cycle-to-cycle Wolters variant Shan-

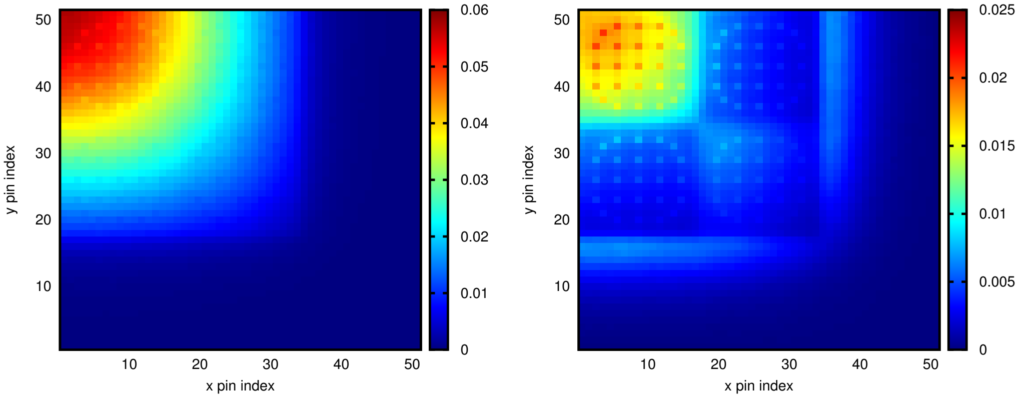

(a) Fast (C5G7 grp. 1-3) (b) Thermal (C5G7 grp. 4-7)

Figure 3.27: LJLS variant fast and thermal flux distributions, problem #5

non entropy, especially in later cycles. The LJLS Shannon entropy values are correlated between adjacent cycles, as a result of the multi-set tally accumulation method.

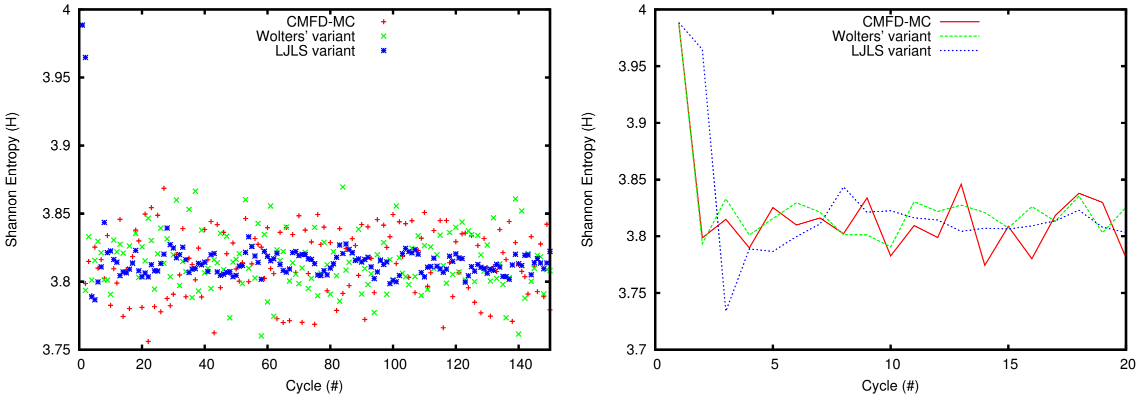

(a) All cycles (b) Cycles 1-20

Figure 3.28: CMFD-MC and variants Shannon entropy versus cycle, problem #5

Figure 3.28b shows Shannon entropy data for the first 20 inactive cycles, to better display fission source convergence behavior for the three CMFD variants. Cycle-to-cycle values are plotted using connecting lines to clearly show "see-sawing" behavior in the CMFD-MC Shannon entropy. We note that use of the Wolters correction largely suppresses this behavior, leading to a considerably smoother convergence trend.

The LJLS method exhibits large Shannon entropy jumps for the first few cycles, but quickly settles into a trend as a result of tally accumulation across cycles.

Next, pin power distributions for the CMFD-MC, Wolters and LJLS methods are plotted in Figure 3.29. Only the fuel assemblies are included in these figures, because the reflector regions are non-fissile. Pin power distributions for the three methods look largely the same, with higher pin power near the north and west (reflecting) boundaries, and lower pin power near the east and south edges of the fuel region.

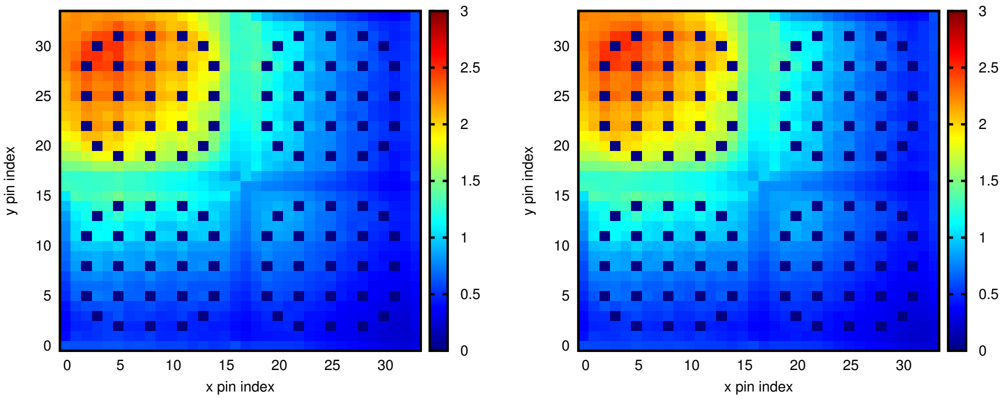

(a) CMFD-MC

(b) Wolters variant

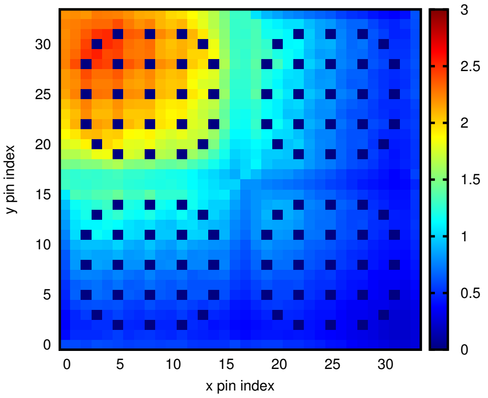

(c) LJLS variant

Figure 3.29: CMFD-MC and variants pin power, problem #5

We next provide apparent pin-power RSD distributions for the three CMFD-MC variants, which are calculated using active-cycle eigenfunction estimates from the simulations performed in this research. Because a high-fidelity reference MC pin power solution is available for problem #5, we also calculate relative pin power error for the CMFD-MC, Wolters and LJLS methods. Figures 3.30 - 3.32 show the pin power apparent RSD and relative error distributions for the three CMFD-MC variants considered in this work.

Pin-power apparent RSD distributions appear to be very similar for all three methods (in fact, at a glance they might be mistaken for multiple copies of the same plot). This contrasts with results from problem #2, in which the Wolters variant of CMFD-MC produced considerably lower apparent RSDs than the standard CMFD-MC method. This may be

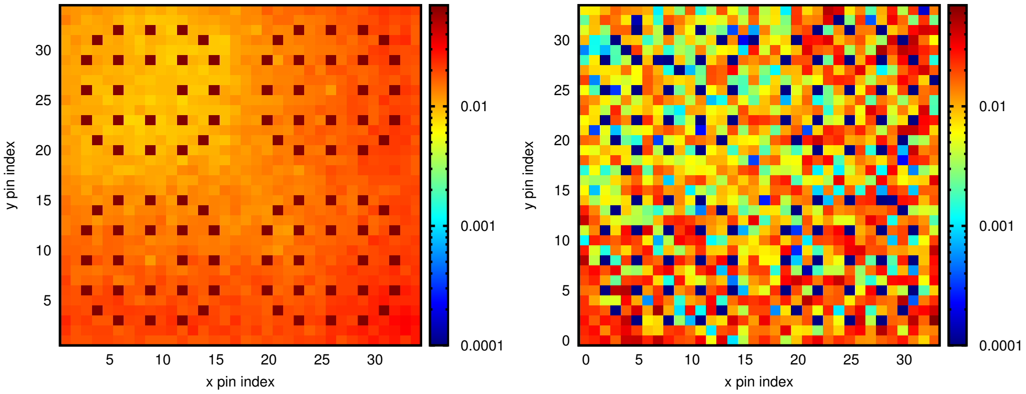

(a) Apparent RSD

(b) Relative error

Figure 3.30: CMFD-MC pin power app. RSD and relative error, problem #5

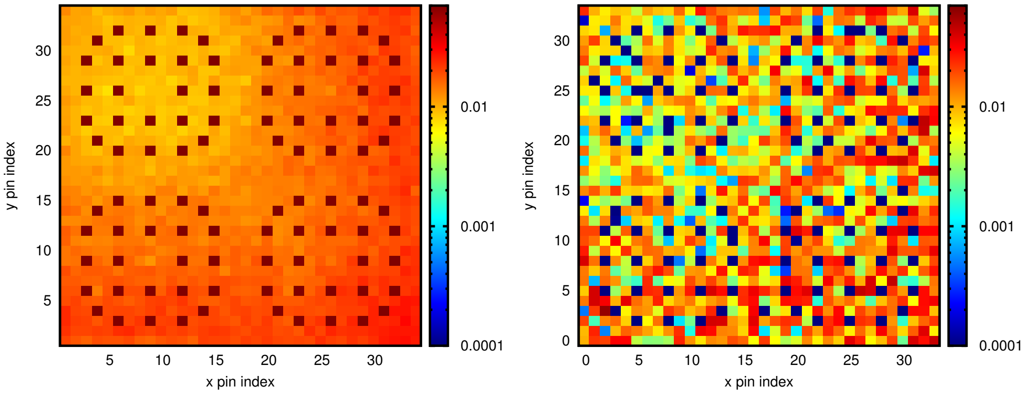

(a) Apparent RSD

(b) Relative error

Figure 3.31: Wolters method pin power app. RSD and relative error, problem #5

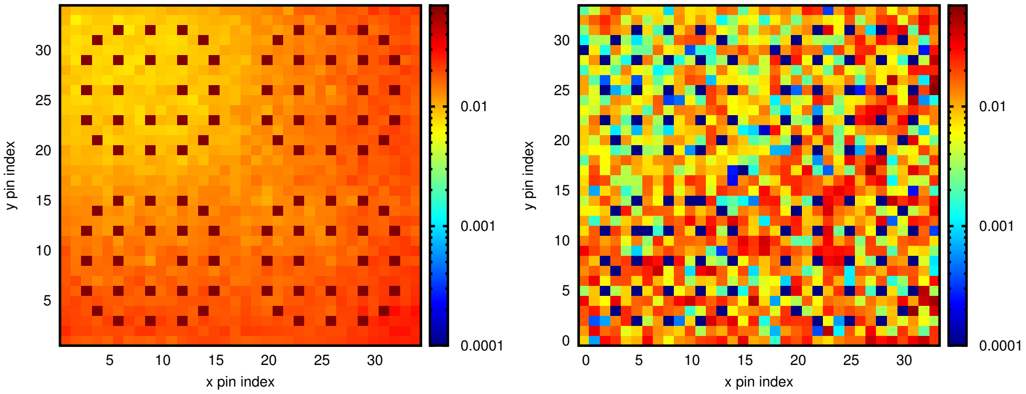

(a) Apparent RSD

(b) Relative error

Figure 3.32: LJLS method pin power app. RSD and relative error, problem #5

due in part to the fact that the CMFD-MC grid was considerably coarser than the Wolters variant grid for problem #2; here, the two methods use the same coarse grid.

In addition, one of the underlying assumptions of the Wolters variant is that a correlation exists between histories contributing to volume tallies and histories contributing to edge tallies. This assumption may be less valid in multidimensional geometry, where spatial cells are bounded in more than one dimension. For this reason, the Wolters method may be less effective for 2- and 3-D problems than for 1-D problems.

Table 3.8: CMFD-MC assembly apparent RSD and relative error (|%|), problem #5

	1	2
1	0.063	0.095
2	0.096	0.109

(a) Apparent RSD

	1	2
1	0.006	0.594
2	0.660	0.119

(b) Relative error

Table 3.9: Wolters method assembly apparent RSD and relative error (|%|), problem #5

	1	2
1	0.061	0.095
2	0.096	0.109

(a) Apparent RSD

	1	2
1	0.226	0.247
2	0.057	0.336

(b) Relative error

Table 3.10: LJLS method assembly apparent RSD and relative error (|%|), problem #5

	1	2
1	0.054	0.091
2	0.090	0.103

(a) Apparent RSD

	1	2
1	0.372	0.132
2	0.464	0.810

(b) Relative error

Table 3.11: Pin power max and mean error for CMFD-MC and variants, problem #5

Max (|%|)	Mean (|%|)
6.49	1.30

(a) CMFD-MC

Max (|%|)	Mean (|%|)
6.04	1.18

(b) Wolters variant

Max (|%|)	Mean (|%|)
6.52	1.24

(c) LJLS variant

Next, we present a case in which the CMFD-MC method is unstable for a particular grid size, but can be made stable simply by refining the coarse grid. This clearly demonstrates the relationship between spectral radius and coarse grid size predicted by our Fourier analysis of the CMFD-MC method. We emphasize that both of the simulations presented use the same number of particles per cycle; the only parameter that changes between the two is the coarse grid size, which decreases from an assembly to a quarter-assembly.

In Figure 3.33, CMFD thermal group fluxes are plotted for the first six cycles of the assembly-grid case. We observe a multidimensional analog of the flux oscillation phenomenon seen in optically thick 1-D problems. The location of maximum thermal flux changes from cycle to cycle, alternating between the upper-left and lower-right fuel assemblies. In addition, the maximum thermal flux grows in amplitude through cycle 4, when fluxes elsewhere in the problem become negative.

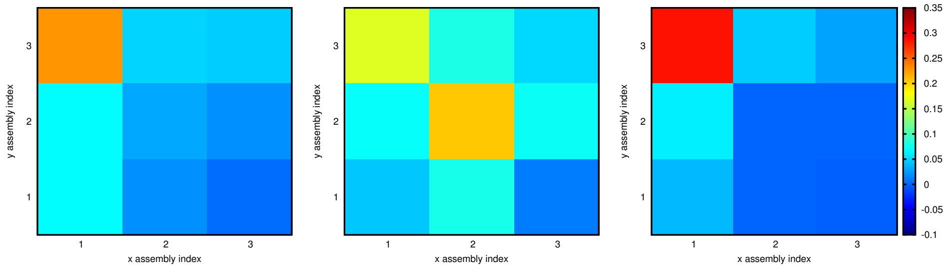

(a) Cycle 1 (b) Cycle 2 (c) Cycle 3

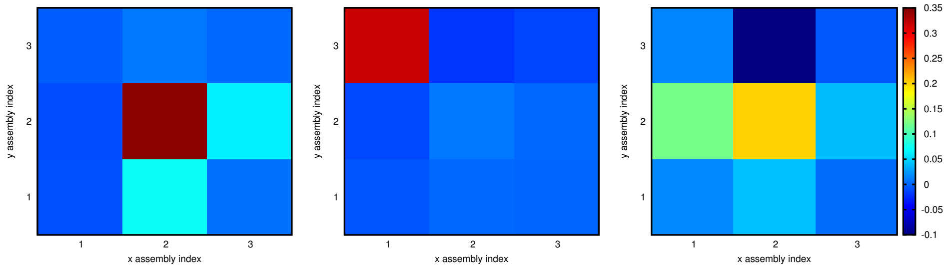

(d) Cycle 4 (e) Cycle 5 (f) Cycle 6

Figure 3.33: C5G7 thermal group flux, cycles 1-6, assembly-grid CMFD-MC

In Figure 3.34, CMFD thermal group fluxes are plotted for the first six cycles of the quarter-assembly-grid case. Here, the CMFD flux shape remains physical from cycle to cycle. A slight cycle-to-cycle flux oscillation is still visible in the upper left-hand corner of the problem domain. However, because this oscillation does not grow, the simulation remains stable.

Again, we emphasize that we did not increase the number of particles per cycle when the coarse grid size was refined from an assembly to a quarter-assembly. As a result, the MC tallies used to calculate coarse-grid quantities in the quarter-assembly case contain *more* statistical noise than the MC tallies used in the assembly-grid case. If stochastic noise

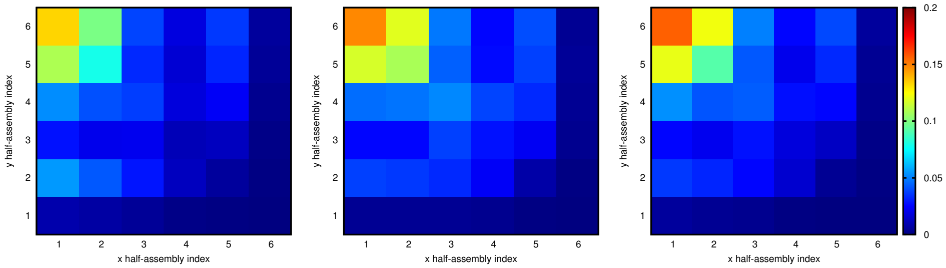

(a) Cycle 1 (b) Cycle 2 (c) Cycle 3

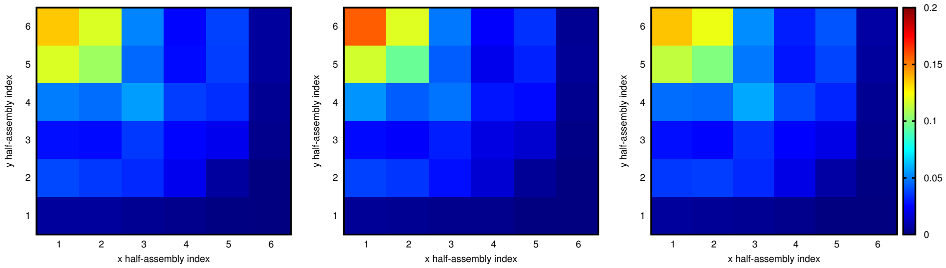

(d) Cycle 4 (e) Cycle 5 (f) Cycle 6

Figure 3.34: C5G7 thermal group flux, cycles 1-6, quarter-assembly-grid CMFD-MC

were the primary driver of CMFD-MC instability, we would expect refining the coarse grid to further destabilize the method. Instead, we observe the opposite behavior.

That said, stochastic noise does contribute to instability in the CMFD-MC simulation. As hypothesized in Section 3.5.1.1, cases which are near the infinite-particle stability limit can be “pushed” into the unstable regime by sufficient random noise. Thus, real CMFD-MC simulations are something of a balancing act: the coarse grid must be fine enough to maintain numerical stability, yet coarse enough to accumulate sufficient MC information.

3.6 Summary

In this chapter, we presented an overview of the existing CMFD method and its variants. We detailed new work that was performed to analyze the stability of the non-random CMFD-MC method, which demonstrates that the CMFD-MC equations are not unconditionally stable, even in the limit as the number of Monte Carlo particles approaches infinity. We presented numerical results to demonstrate the validity of the Fourier analysis, and also compared three existing variants of the CMFD-MC method for a homogeneous problem and several heterogeneous problems. One of these variants, the LJLS method, was shown to produce unrealistically low apparent RSD estimates for optically thick problems. In addition, we extended the Wolters variant of CMFD-MC to multidimensional geometry, and showed that use of the Wolters correction factor can be aid fission source convergence in 2-D problems (though its effectiveness is significantly diminished).

These findings lead to a set of recommendations for future CMFD-MC reactor core simulations. Specifically, we suggest that CMFD-MC calculations should (i) be run on a "reasonably fine" coarse grid (namely, less than an assembly), (ii) not use tally accumulation to ensure conservative estimates of solution error, and (iii) employ the Wolters correction to help stabilize fission source convergence.

CHAPTER 4

The LCMC Method

4.1 Introduction

In this chapter, we present a new alternative to the standard MC method for k-eigenvalue problems, in which the number of MC collisions per cycle is limited to a user-specified number. The result is an MC iteration strategy, with both a fission bank and a scattering bank, which we refer to as the Limited-Collision Monte Carlo (LCMC) method. Because CMFD acceleration is applied to LCMC in the same manner as standard MC, the full title of this new method is CMFD-LCMC. For succinctness, however, we refer to the full iteration strategy (LCMC with CMFD feedback) as simply the LCMC method.

The LCMC method is loosely patterned on the deterministic k-eigenvalue iteration strategy, in which a fixed number of "scattering sweeps" are performed per CMFD fission source update (this differs significantly from the standard MC iteration, which simulates particles from birth until leakage or absorption). In the standard deterministic strategy, the fission source is held fixed during scattering source sweeps. The initial implementation of LCMC was based on this algorithm, but we found the MC version to be inefficient. Instead, we allow the fission source to be updated as the MC "scattering sweeps" are performed– in the MC interpretation, this means that fission particles banked during a cycle are simulated during the same cycle. Fission and scattering banks for the next cycle are formed using only histories that fission or scatter, respectively, during the last permitted collision. In addition, coarse-grid quantities for the CMFD calculation are formed using only information from the last collision event.

By restricting the number of permissible collisions per history per cycle, the LCMC iteration strategy greatly reduces the simulation time per cycle. The user has far more control over LCMC histories than traditional MC histories; limiting the number of collisions eliminates the potential for particles to scatter a large number of times without contributing appreciably to the solution.

In the following section, we outline the LCMC iteration strategy, highlighting differences between LCMC and the standard MC method for k-eigenvalue problems. Then we linearize and Fourier-analyze the LCMC equations for both a monoenergetic and a two-group case, and we compare theoretical spectral radius predictions to numerical experiments. Finally, we present numerical results for the benchmark test problems introduced in Chapter 2.

Because the LCMC method is introduced as part of this thesis, all results in this chapter represent new research.

4.2 LCMC Iteration Strategy

To describe the LCMC simulation procedure, we begin with the high-order transport "sweep" equations. These equations differ from the standard MC system used in Chapters 2 and 3; here, the scattering source term appears (along with the fission source) as a lagged term on the right-hand side of the transport equation. We have introduced a new iteration index, m, to track the number of collisions. In addition, we introduce an initial condition for the LCMC sweep, in which the uncollided scalar flux [$\phi^{(\ell+1/2,0)}(x)$] is set equal to the CMFD-scaled flux from the previous iteration [$\phi^{(\ell)}(x)$].

$$\phi^{(\ell+1/2,0)}(x) = \phi^{(\ell)}(x)\,, \tag{4.1a}$$

$$\mu\frac{d}{dx}\psi^{(\ell+1/2,m)}(x,\mu) + \Sigma_t(x)\psi^{(\ell+1/2,m)}(x,\mu) = \frac{1}{2}\left(\Sigma_s(x) + \frac{\nu\Sigma_f(x)}{k^{(\ell)}}\right)\phi^{(\ell+1/2,m-1)}(x)\,, \tag{4.1b}$$

$$0 \le x \le X\,,\ -1 \le \mu \le 1\,,\ 1 \le m \le M\,,$$

$$\psi^{(\ell+1/2,m)}(0,\mu) = \psi^{(\ell+1/2,m)}(X,\mu)\,,\ -1 \le \mu \le 1\,, \tag{4.1c}$$

$$\phi^{(\ell+1/2,m)}(x) = \int_{-1}^{1}\psi^{(\ell+1/2,m)}(x,\mu)d\mu\,. \tag{4.1d}$$

In Eqs. (4.1), ℓ is the cycle iteration index, m is the collision index, and M is the maximum number of collisions allowed per cycle.

LCMC particles that survive M scattering events are stored in a collision bank for the next cycle. Fissions occurring when $m < M$ are stored in an "intermediate" bank and simulated during the cycle, whereas fissions occurring when $m = M$ are banked for the following cycle.

As usual, we impose a coarse grid on the continuous MC system, with J cells of size Δ_j ($1 \le j \le J$). The CMFD calculation itself (see Section 3.2, Eqs. (3.3a)–(3.3c)) is unchanged in the LCMC method; however, in keeping with the deterministic origin of the LCMC iteration scheme, coarse-grid quantities are now formed using only "M^{th}-collided" MC tallies:

$$\Phi_j^{(\ell+1/2)} = \frac{1}{\Delta_j}\int_{x_{j-1/2}}^{x_{j+1/2}} \phi^{(\ell+1/2,M)}(x)dx\,, \tag{4.2a}$$

$$\Phi_{1,j\pm1/2}^{(\ell+1/2)} = \int_{-1}^{1} \mu\psi^{(\ell+1/2,M)}(x_{j\pm1/2},\mu)d\mu\,, \tag{4.2b}$$

$$\Sigma_{a,j}^{(\ell+1/2)} = \frac{\int_{x_{j-1/2}}^{x_{j+1/2}} \Sigma_a(x)\phi^{(\ell+1/2,M)}(x)dx}{\int_{x_{j-1/2}}^{x_{j+1/2}} \phi^{(\ell+1/2,M)}(x)dx}\,, \tag{4.2c}$$

$$\Sigma_{t,j}^{(\ell+1/2)} = \frac{\int_{x_{j-1/2}}^{x_{j+1/2}} \Sigma_t(x)\phi^{(\ell+1/2,M)}(x)dx}{\int_{x_{j-1/2}}^{x_{j+1/2}} \phi^{(\ell+1/2,M)}(x)dx}\,, \tag{4.2d}$$

$$\nu\Sigma_{f,j}^{(\ell+1/2)} = \frac{\int_{x_{j-1/2}}^{x_{j+1/2}} \nu\Sigma_f(x)\phi^{(\ell+1/2,M)}(x)dx}{\int_{x_{j-1/2}}^{x_{j+1/2}} \phi^{(\ell+1/2,M)}(x)dx}\,, \tag{4.2e}$$

$$\tilde{D}_{j+1/2}^{(\ell+1/2)} = \frac{2}{3}\left(\frac{1}{\Sigma_{t,j}^{(\ell+1/2)}\Delta_j + \Sigma_{t,j+1}^{(\ell+1/2)}\Delta_{j+1}}\right)\,, \tag{4.2f}$$

$$\hat{D}_{j+1/2}^{(\ell+1/2)} = \frac{\Phi_{1,j+1/2}^{(\ell+1/2)} + \tilde{D}_{j+1/2}^{(\ell+1/2)}(\Phi_{j+1}^{(\ell+1/2)} - \Phi_j^{(\ell+1/2)})}{\Phi_{j+1}^{(\ell+1/2)} + \Phi_j^{(\ell+1/2)}}\,. \tag{4.2g}$$

In theory, we can form the CMFD system using tally data from all collisions (as is done in the CMFD-MC method). We expect the non-random spectral radius to be lower when only M^{th}-collided data is used, because this data should better represent the converged solution than information from previous collisions. However, using only M^{th}-collided tally data increases statistical error in the CMFD system. This tradeoff will be investigated in Section 4.4.2.2.

Once the CMFD calculation is complete, we obtain an updated estimate of the coarse-grid flux ($\Phi_j^{(\ell+1)}$) and eigenvalue ($k^{(\ell+1)}$). The updated coarse-grid solution is then used to scale both the LCMC fission and scattering source distributions for the following cycle:

$$\nu\Sigma_f(x)\phi^{(\ell+1)}(x) = \nu\Sigma_f(x)\phi^{(\ell+1/2,M)}(x)\left[\frac{\Phi_j^{(\ell+1)}}{\Phi_j^{(\ell+1/2)}}\right]\,, \tag{4.3a}$$

$$\Sigma_s(x)\phi^{(\ell+1)}(x) = \Sigma_s(x)\phi^{(\ell+1/2,M)}(x)\left[\frac{\Phi_j^{(\ell+1)}}{\Phi_j^{(\ell+1/2)}}\right]\,, \tag{4.3b}$$

$$x_{j-1/2} \le x \le x_{j+1/2}\ , \quad 1 \le j \le J\ .$$

The cross sections shown in Eqs. (4.3) cancel for the simple case shown here; however, we retain them to differentiate the scattering source distribution from the fission source distribution.

In summary, a single LCMC cycle consists of the following steps: (i) perform an LCMC calculation, where particles are sampled from fission and scattering banks and allowed to undergo a fixed maximum number (M) of collisions, (ii) bank particles surviving M collisions for the next cycle, (iii) form the CMFD system, using only "M^{th}-collided" tally data from the LCMC solve, (iv) solve the CMFD system to obtain an updated estimate of the coarse-grid flux and eigenvalue, and (v) use the updated CMFD solution to scale the LCMC fission and scattering banks for the next cycle.

The LCMC iteration differs from the CMFD-MC iteration (see Chapter 3) in a number of significant ways, which we briefly outline here. First of all, the user controls the maximum number of collisions per history, per cycle. In CMFD-MC, all histories are simulated from birth until death – there is no restriction on the number of collisions that a particle may have (unless the code sets an arbitrary cutoff). In theory, LCMC histories should be more "standardized" than standard MC histories; because they are allowed a limited number of collisions per cycle, no single history can claim a disproportionate share of computing time by scattering a large number of times. This may prove helpful in parallel simulations, where all processors must wait to synchronize after simulating a fixed number of histories.

As we show in Section 4.3, however, the convergence rate of the LCMC iteration (in the infinite-particle limit) depends strongly on the number of permitted collisions. As always, a balance must be struck between speed and stability. If the collision limit is set to a small value (M=1 or 2, for example), cycles will run very quickly; however, the fission and scattering distributions may take a large number of cycles to converge (or fail to converge altogether). This instability can usually be mitigated by refining the coarse grid, but in certain multigroup cases the LCMC spectral radius is independent of the coarse grid thickness (see Section 4.4.1.2).

This is roughly analogous to behavior observed in deterministic k-eigenvalue simulations, in which the convergence rate of the iteration scheme as a whole depends on the number of inner scattering sweeps performed per outer fission source update.

The presence of a scattering bank in LCMC provides an opportunity to apply CMFD feedback to the scattering source distribution (in addition to traditional fission source feedback). In general, the scattering source is a more complicated function of phase space than the fission source, potentially involving angular anisotropy and strong energy dependence.

Because the LCMC iteration must converge this complicated distribution, the overall source convergence rate may be slower than the CMFD-MC iteration.

Finally, we anticipate that coarse-grid tallies will be significantly noisier in the LCMC case, when compared to CMFD-MC tallies. While the standard CMFD-MC method uses tally information from every particle collision and boundary crossing, the LCMC method (in the form presented here) uses only tally information from the last collision. In theory, tallies formed using information from the last collision event should more closely represent the converged solution than tallies which are accumulated over the entire cycle. However, they will also contain significantly more random noise, because they contain less total information than full-cycle tallies. To address this, we also consider an alternate version of LCMC, where the CMFD system is formed using tallies that are averaged over all collisions during each cycle. This will be discussed in greater detail in Section 4.4.2.2.

4.3 Stability Analysis

In this section, we analyze the stability of the linearized non-random LCMC iteration equations. This analysis is valid only when statistical noise is negligible, and describes the convergence behavior of the linearized LCMC iteration in the limit as the number of histories per cycle approaches infinity.

Two cases are Fourier-analyzed: the monoenergetic iteration scheme, and the two-energy-group iteration scheme. These analyses are similar in structure, but they yield different types of information. While the monoenergetic Fourier analysis can be used to determine fundamental relationships between cross sections and grid sizes, the two-group case is more representative of realistic *k*-eigenvalue reactor core simulations (which involve energy dependence). We begin with the monoenergetic case in Section 4.3.1.

4.3.1 Monoenergetic Case

4.3.1.1 The Linearized Non-Random LCMC Method

Before the Fourier analysis can be carried out, we must first linearize the LCMC system defined in Section 4. To perform this linearization, we consider a 1-D, monoenergetic, homogeneous, isotropically-scattering problem with periodic boundaries:

$$\phi^{(\ell+1/2,0)}(x) = \phi^{(\ell)}(x) \, , \tag{4.4a}$$

$$\mu\frac{d}{dx}\psi^{(\ell+1/2,m)}(x,\mu) + \Sigma_t\psi^{(\ell+1/2,m)}(x,\mu) = \frac{1}{2}\left(\Sigma_s + \frac{\nu\Sigma_f}{k^{(\ell)}}\right)\phi^{(\ell+1/2,m-1)}(x) \, , \tag{4.4b}$$

$$0 \le x \le X\,,\ \ -1 \le \mu \le 1\,,\ \ 1 \le m \le M\,,$$

$$\psi^{(\ell+1/2,m)}(0,\mu) = \psi^{(\ell+1/2,m)}(X,\mu)\,,\ \ -1 \le \mu \le 1\,, \tag{4.4c}$$

$$\phi^{(\ell+1/2,m)}(x) = \int_{-1}^{1} \psi^{(\ell+1/2,m)}(x,\mu) d\mu\,. \tag{4.4d}$$

We assume a uniform coarse grid with J cells of width Δ. The coarse-grid cross sections and diffusivities ($\tilde{D}$) are known exactly for the homogeneous case, so we omit these expressions. The coarse-grid flux and current terms are tallied during the LCMC solve using:

$$\Phi_j^{(\ell+1/2)} = \frac{1}{\Delta}\int_{x_{j-1/2}}^{x_{j+1/2}} \phi^{(\ell+1/2,M)}(x)dx\,, \tag{4.5a}$$

$$\Phi_{1,j\pm1/2}^{(\ell+1/2)} = \int_{-1}^{1} \mu\psi^{(\ell+1/2,M)}(x_{j\pm1/2},\mu)d\mu\,. \tag{4.5b}$$

We reiterate that coarse grid data is composed of information from the last permitted LCMC collision event, as indicated by the flux superscript M in Eqs. (4.5). Coarse-grid flux and current values are then used to calculate the current correction ($\hat{D}$) terms:

$$\hat{D}_{j+1/2}^{(\ell+1/2)} = \frac{\Phi_{1,j+1/2}^{(\ell+1/2)} + \tilde{D}_{j+1/2}^{(\ell+1/2)}(\Phi_{j+1}^{(\ell+1/2)} - \Phi_j^{(\ell+1/2)})}{\Phi_{j+1}^{(\ell+1/2)} + \Phi_j^{(\ell+1/2)}}\,, \tag{4.5c}$$

which in turn are used to form the low-order system:

$$\Phi_{1,j+1/2}^{(\ell+1)} - \Phi_{1,j-1/2}^{(\ell+1)} + \Sigma_a\Phi_j^{(\ell+1)}\Delta = \frac{\nu\Sigma_f}{k^{(\ell+1)}}\Phi_j^{(\ell+1)}\Delta\,,\ \ 1 \le j \le J\,, \tag{4.5d}$$

$$\Phi_{1,j+1/2}^{(\ell+1)} = -\tilde{D}(\Phi_{j+1}^{(\ell+1)} - \Phi_j^{(\ell+1)}) + \hat{D}_{j+1/2}^{(\ell+1/2)}(\Phi_{j+1}^{(\ell+1)} + \Phi_j^{(\ell+1)})\,, \tag{4.5e}$$

$$\Phi_{1,1/2}^{(\ell+1)} = \Phi_{1,J+1/2}^{(\ell+1)}\,, \tag{4.5f}$$

$$1 = \frac{1}{J}\sum_{j=1}^{J}\Phi_j^{(\ell+1)}\,. \tag{4.5g}$$

Finally, the updated coarse grid fluxes are used to scale the Monte Carlo fission and scattering source banks for the next cycle:

$$\phi^{(\ell+1)}(x) = \phi^{(\ell+1/2,M)}(x)\left[\frac{\Phi_j^{(\ell+1)}}{\Phi_j^{(\ell+1/2)}}\right],\ \ x_{j-1/2} \le x \le x_{j+1/2}\,,\ \ 1 \le j \le J\,. \tag{4.5h}$$

(In Eq. (4.5h), we have cancelled out the cross sections shown in Eqs. (4.3). When this is done, Eqs. (4.3a) and (4.3b) reduce to a single expression.)

On convergence, this problem has the exact constant solution

$$\psi(x,\mu) = = \frac{1}{2}\ , \tag{4.6a}$$

$$\Phi_j = \phi(x) = 1\ , \tag{4.6b}$$

$$\Phi_{1,j+1/2} = 0\ , \tag{4.6c}$$

$$k = \frac{\nu\Sigma_f}{\Sigma_a}\ . \tag{4.6d}$$

To proceed, we define linear expansions around the exact solution (with $\epsilon << 1$):

$$\psi^{(\ell+1/2,m)}(x,\mu) = \frac{1}{2} + \epsilon\tilde{\psi}^{(\ell+1/2,m)}(x,\mu)\ , \tag{4.7a}$$

$$\phi^{(\ell+1/2,m)}(x) = 1 + \epsilon\tilde{\phi}^{(\ell+1/2,m)}(x)\ , \tag{4.7b}$$

$$\phi^{(\ell+1)}(x) = 1 + \epsilon\tilde{\phi}^{(\ell+1)}(x)\ , \tag{4.7c}$$

$$\Phi_j^{(\ell+1/2)} = 1 + \epsilon\tilde{\Phi}_j^{(\ell+1/2)}\ , \tag{4.7d}$$

$$\Phi_j^{(\ell+1)} = 1 + \epsilon\tilde{\Phi}_j^{(\ell+1)}\ , \tag{4.7e}$$

$$\Phi_{1,j+1/2}^{(\ell+1/2)} = 0 + \epsilon\tilde{\Phi}_{1,j+1/2}^{(\ell+1/2)}\ , \tag{4.7f}$$

$$\Phi_{1,j+1/2}^{(\ell+1)} = 0 + \epsilon\tilde{\Phi}_{1,j+1/2}^{(\ell+1)}\ , \tag{4.7g}$$

$$\hat{D}_{j+1/2}^{(\ell+1/2)} = 0 + \epsilon\hat{d}_{j+1/2}^{(\ell+1/2)}\ , \tag{4.7h}$$

$$\frac{1}{k^{(\ell+1)}} = \frac{\Sigma_a}{\nu\Sigma_f} + \epsilon\delta^{(\ell+1)}\ . \tag{4.7i}$$

The coarse-grid cross sections are known exactly for the homogeneous problem, so these quantities are not expanded. We insert Eqs. (4.7) into Eqs. (4.4a) - (4.5h). The $\mathcal{O}(1)$ terms cancel out, and we equate $\mathcal{O}(\epsilon)$ and ignore $\mathcal{O}(\epsilon^2)$ terms to obtain:

$$\tilde{\phi}^{(\ell+1/2,0)}(x) = \tilde{\phi}^{(\ell)}(x)\ ,\ \ 0 \le x \le X\ , \tag{4.8a}$$

$$\mu\frac{d}{dx}\tilde{\psi}^{(\ell+1/2,m)}(x,\mu)+\Sigma_t\tilde{\psi}^{(\ell+1/2,m)}(x,\mu) = \frac{\Sigma_t}{2}\tilde{\phi}^{(\ell+1/2,m-1)}(x) + \frac{\nu\Sigma_f}{2}\delta^{(\ell)}\ , \tag{4.8b}$$

$$-1 \le \mu \le 1\ ,\ \ 0 \le x \le X\ ,\ \ 1 \le m \le M\ ,$$

$$\tilde{\psi}^{(\ell+1/2,m)}(0,\mu) = \tilde{\psi}^{(\ell+1/2,m)}(X,\mu)\ ,\ \ -1 \le \mu \le 1\ , \tag{4.8c}$$

$$\tilde{\phi}^{(\ell+1/2,m)}(x) = \int_{-1}^{1}\tilde{\psi}^{(\ell+1/2,m)}(x,\mu)d\mu\ , \tag{4.8d}$$

$$\tilde{\Phi}_j^{(\ell+1/2)} = \frac{1}{\Delta}\int_{-1}^{1} \tilde{\phi}^{(\ell+1/2,M)}(x)dx\,, \tag{4.8e}$$

$$\tilde{\Phi}_{1,j+1/2}^{(\ell+1/2)} = \int_{-1}^{1} \mu\tilde{\psi}^{(\ell+1/2,M)}(x_{j+1/2},\mu)d\mu\,, \tag{4.8f}$$

$$\hat{d}_{j+1/2}^{(\ell+1/2)} = \frac{1}{2}\left[\tilde{\Phi}_{1,j+1/2}^{(\ell+1/2)} + \tilde{D}(\tilde{\Phi}_{j+1}^{(\ell+1/2)} - \tilde{\Phi}_j^{(\ell+1/2)})\right]\,, \tag{4.8g}$$

$$\frac{1}{\Delta}(\tilde{\Phi}_{1,j+1/2}^{(\ell+1)} - \tilde{\Phi}_{1,j-1/2}^{(\ell+1)}) = \nu\Sigma_f\delta^{(\ell+1)}\,, \tag{4.8h}$$

$$\tilde{\Phi}_{1,j+1/2}^{(\ell+1)} = -\tilde{D}(\tilde{\Phi}_{j+1}^{(\ell+1)} - \tilde{\Phi}_j^{(\ell+1)}) + 2\hat{d}_{j+1/2}^{(\ell+1/2)}\,, \tag{4.8i}$$

$$0 = \frac{1}{J}\sum_{j=1}^{J}\tilde{\Phi}_j^{(\ell+1)}\,, \tag{4.8j}$$

and

$$\tilde{\phi}^{(\ell+1)}(x) = \tilde{\phi}^{(\ell+1/2,M)}(x) + \tilde{\Phi}_j^{(\ell+1)} - \tilde{\Phi}_j^{(\ell+1/2)}\,, \tag{4.8k}$$

$$x_{j-1/2} \le x \le x_{j+1/2}\,,\quad 1 \le j \le J\,.$$

We note that several of Eqs. (4.8) differ in form from Eqs. (4.4a) - (4.5h). This occurs because the original equations contain nonlinear terms. Summing Eq. (4.8h) over all coarse cells, we immediately obtain:

$$\delta^{(\ell+1)} = 0\,. \tag{4.9}$$

Thus, after a single iteration the monoenergetic LCMC iteration scheme converges the $\mathcal{O}(\epsilon)$ component of the eigenvalue, but not the eigenfunction (this was also true for the linearized CMFD-MC equations). In the following section, we perform a Fourier analysis to estimate the eigenfunction convergence rate as a function of the coarse grid optical thickness and number of collisions allowed per cycle.

4.3.1.2 Fourier Analysis

Before we proceed with the monoenergetic LCMC Fourier analysis, we replace the original, continuous high-order iteration equations with a discrete-ordinates system. While this represents an approximation to the LCMC iteration, it greatly simplifies the Fourier analysis by permitting us to solve a block matrix equation for the spectral radius. The penalty in accuracy should be minimal if we solve the discrete ordinates problem on a very fine space-angle grid. This discretization was also carried out for the CMFD-MC Fourier analyses presented in Section 3.4.

We formulate the discrete ordinates problem on a space-angle grid with N discrete angles from $1 \leq n \leq N$ and K fine spatial cells $1 \leq k \leq K$, of thickness h.

The discretized high-order equations become:

$$\phi_k^{(\ell+1/2,0)} = \phi_k^{(\ell)} \, , \;\; 1 \leq k \leq K \, , \tag{4.10a}$$

$$\frac{\mu_n}{h}(\psi_{k+1/2,n}^{(\ell+1/2,m)} - \psi_{k-1/2,n}^{(\ell+1/2,m)}) + \Sigma_t \psi_{k,n}^{(\ell+1/2,m)} = \frac{1}{2}\left(\Sigma_s + \frac{\nu\Sigma_f}{k^{(\ell)}}\right)\phi_k^{(\ell+1/2,m-1)} \, , \tag{4.10b}$$

$$1 \leq n \leq N \, , \;\; 1 \leq k \leq K \, , \;\; 1 \leq m \leq M \, , \tag{4.10c}$$

$$\psi_{1/2,n}^{(\ell+1/2,m)} = \psi_{K+1/2,n}^{(\ell+1/2,m)} \, , \;\; 1 \leq n \leq N \, , \tag{4.10d}$$

$$\phi_k^{(\ell+1/2,m)} = \sum_{n=1}^{N} w_n \psi_{k,n}^{(\ell+1/2,m)} \, . \tag{4.10e}$$

To relate the cell-center and cell-edge fluxes, we again use the weighted-diamond auxiliary equations (introduced in Section 3.4.1.2):

$$\tilde{\psi}_{k,n}^{(\ell+1/2,m)} = \left(\frac{1+\alpha_n}{2}\right)\tilde{\psi}_{k+1/2,n}^{(\ell+1/2,m)} + \left(\frac{1-\alpha_n}{2}\right)\tilde{\psi}_{k-1/2,n}^{(\ell+1/2,m)} \, , \qquad 1 \leq n \leq N \, , \;\; 1 \leq k \leq K \, . \tag{4.11}$$

We also discretize the coarse-grid flux and current expressions (essentially converting integral terms to sums):

$$\tilde{\Phi}_j^{(\ell+1/2)} = \frac{1}{p}\sum_{k \in j} \tilde{\phi}_k^{(\ell+1/2)} \, , \tag{4.12a}$$

$$\tilde{\Phi}_{1,j+1/2}^{(\ell+1/2)} = \sum_{m=1}^{M} w_m \mu_m \tilde{\psi}_{(jp)+1/2,m}^{(\ell+1/2)} \, . \tag{4.12b}$$

The low-order system remains unchanged, while the discretized update equation becomes:

$$\tilde{\phi}_k^{(\ell+1)} = \tilde{\phi}_k^{(\ell+1/2,M)} + \tilde{\Phi}_j^{(\ell+1)} - \tilde{\Phi}_j^{(\ell+1/2)} \, , \;\; 1 \leq j \leq J \, , \;\; k \in j \, . \tag{4.12c}$$

We define a new, relative index to simplify the ansatz:

$$k = (j-1)p + r \, . \tag{4.13}$$

In Eq. (4.13), k is the fine cell index, j is the index of the coarse cell in which fine cell k resides, p is the coarse-grid parameter (introduced in Section 3.4.1.2), and r is the position of fine cell k within coarse cell j. Using this new indexing system, the Fourier ansatz can be expressed:

$$\tilde{\psi}^{(\ell+1/2,m)}_{k-1/2,n} = \omega^l A^{(m)}_{r,n} e^{i\Sigma_t \lambda x_j} \, , \tag{4.14a}$$

$$\tilde{\psi}^{(\ell+1/2,m)}_{k,n} = \omega^l B^{(m)}_{r,n} e^{i\Sigma_t \lambda x_j} \, , \tag{4.14b}$$

$$\tilde{\phi}^{(\ell+1/2,m)}_{k} = \omega^l F^{(m)}_{r} e^{i\Sigma_t \lambda x_j} \, , \tag{4.14c}$$

$$\tilde{\Phi}^{(\ell+1/2)}_{j} = \omega^l D e^{i\Sigma_t \lambda x_j} \, , \tag{4.14d}$$

$$\tilde{\Phi}^{(\ell+1/2)}_{1,j-1/2} = \omega^l K e^{i\Sigma_t \lambda x_j} \, , \tag{4.14e}$$

$$\tilde{\Phi}^{(\ell+1)}_{j} = \omega^l I e^{i\Sigma_t \lambda x_j} \, , \tag{4.14f}$$

$$\tilde{\phi}^{(\ell+1)}_{k} = \omega^{l+1} E_r e^{i\Sigma_t \lambda x_j} \, . \tag{4.14g}$$

The quantities that are updated during inner iterations ($\tilde{\psi}^{(\ell+1/2,m)}_{k-1/2,n}$, $\tilde{\psi}^{(\ell+1/2,m)}_{k,n}$, and $\tilde{\phi}^{(\ell+1/2,m)}_{k}$) depend on the collision iteration variable (m). We include this dependence in the Fourier ansatz by allowing the coefficients $A^{(m)}_{r,n}$, $B^{(m)}_{r,n}$ and $F^{(m)}_{r}$ to vary during the LCMC transport iterations. The transport error coefficients are also assumed to be periodic on the coarse grid, such that

$$\tilde{\psi}^{(\ell+1/2,m)}_{(k+p)-1/2,n} = \left(\tilde{\psi}^{(\ell+1/2,m)}_{k-1/2,n}\right) e^{i\Sigma_t \lambda \Delta} = \omega^l A^{(m)}_{r,n} e^{i\Sigma_t \lambda (x_j + \Delta)} \, . \tag{4.15}$$

Inserting the ansatz into the discretized version of Eqs. (4.8) and simplifying, we obtain:

$$F^{(0)}_r = E_r \, , \tag{4.16a}$$

$$\begin{cases} \frac{\mu_n}{\Sigma_t h}\left(A^{(m)}_{r+1,n} - A^{(m)}_{r,n}\right) + B^{(m)}_{r,n} = \frac{1}{2} F^{(m-1)}_r \, , & 1 \le r < p \, , \\ \frac{\mu_n}{\Sigma_t h}\left(A^{(m)}_{1,n} e^{i\Sigma_t \lambda \Delta} - A^{(m)}_{r,n}\right) + B^{(m)}_{r,n} = \frac{1}{2} F^{(m-1)}_r \, , & r = p \, , \end{cases} \tag{4.16b}$$

$$A^{(m)}_{1,n} = A^{(m)}_{1,n} e^{i\Sigma_t \lambda X} \, , \tag{4.16c}$$

$$\begin{cases} B^{(m)}_{r,n} = \left[\frac{1+\alpha_n}{2}\right] A^{(m)}_{r+1,n} + \left[\frac{1-\alpha_n}{2}\right] A^{(m)}_{r,n} \, , & 1 \le r < p \, , \\ B^{(m)}_{r,n} = \left[\frac{1+\alpha_n}{2}\right] A^{(m)}_{1,n} e^{i\Sigma_t \lambda \Delta} + \left[\frac{1-\alpha_n}{2}\right] A^{(m)}_{r,n} & r = p \, , \end{cases} \tag{4.16d}$$

$$F^{(m)}_r = \sum_{n=1}^{N} w_n B^{(m)}_{r,n} \, , \tag{4.16e}$$

$$D = \frac{1}{p} \sum_{r=1}^{p} F^{(M)}_r \, , \tag{4.16f}$$

$$2(I-D)(\cos(\Sigma_t\lambda\Delta)-1) = 3\Sigma_t\Delta\sum_{n=1}^{N} w_n\mu_n A_{1,n}^{(M)}(e^{i\Sigma_t\lambda\Delta}-1)\,, \tag{4.16g}$$

$$0 = \sum_{j=1}^{J} e^{i\Sigma_t\lambda x_j}\,, \tag{4.16h}$$

$$\omega E_r - F_r^{(M)} = (I-D)\,. \tag{4.16i}$$

In Eqs. (4.16), we have used Eq. (4.8f) to rewrite the coarse-grid current error in terms of the edge-centered angular flux error. The resulting coarse-grid equations [Eqs. (4.16f) - (4.16i)] depend on the total number of inner iterations per outer (M), but do not depend explicitly on the inner iteration variable (m).

To proceed, we first use the periodic boundary condition Eq. (4.16c) to determine the permissible discrete Fourier frequencies:

$$\lambda = \lambda_s = \frac{2\pi s}{\Sigma_t X},\;\; s = 1,2,3\,\ldots\,(J-1)\,. \tag{4.17}$$

These discrete frequencies depend on both the slab thickness (X) and number of coarse cells (J). When the discrete frequencies are applied to the Fourier ansatz, the normalization condition in Eq. (4.16h) is automatically satisfied.

Before a matrix system can be formed to solve for the theoretical spectral radius, we must express the final scalar flux error coefficients $F_r^{(M)}$ and coarse-grid current coefficient K in terms of the initial error coefficients E_r.

Beginning with Eqs. (4.16b), (4.16d), and (4.16e), we use Eq. (4.16d) to eliminate $B_{r,n}^{(m)}$ in Eq. (4.16b). The resulting equations are:

$$F_r^{(0)} = E_r\,, \tag{4.18a}$$

$$\begin{cases} \left(\left[\frac{1+\alpha_n}{2}\right]+\frac{\mu_n}{\Sigma_t h}\right)A_{r+1,n}^{(m)} + \left(\left[\frac{1-\alpha_n}{2}\right]-\frac{\mu_n}{\Sigma_t h}\right)A_{r,n}^{(m)} = \frac{1}{2}F_r^{(m-1)}\,, & 1 \le r < p\,, \\ \left(\left[\frac{1+\alpha_n}{2}\right]+\frac{\mu_n}{\Sigma_t h}\right)A_{1,n}^{(m)}e^{i\Sigma_t\lambda_s\Delta} + \left(\left[\frac{1-\alpha_n}{2}\right]-\frac{\mu_n}{\Sigma_t h}\right)A_{r,n}^{(m)} = \frac{1}{2}F_r^{(m-1)}\,, & r = p\,, \end{cases} \tag{4.18b}$$

$$\begin{cases} B_{r,n}^{(m)} = \left[\frac{1+\alpha_n}{2}\right]A_{r+1,n}^{(m)} + \left[\frac{1-\alpha_n}{2}\right]A_{r,n}^{(m)}\,, & 1 \le r < p\,, \\ B_{r,n}^{(m)} = \left[\frac{1+\alpha_n}{2}\right]A_{1,n}^{(m)}e^{i\Sigma_t\lambda_s\Delta} + \left[\frac{1-\alpha_n}{2}\right]A_{r,n}^{(m)} & r = p\,, \end{cases} \tag{4.18c}$$

$$F_r^{(m)} = \sum_{n=1}^{N} w_n B_{r,n}^{(m)}\,. \tag{4.18d}$$

We rewrite these equations in matrix form:

$$\mathbf{F}^{(0)} = \mathbf{E}\,, \tag{4.19a}$$

$$\mathbf{M_1}\mathbf{A}^{(m)} = \frac{1}{2}\mathbf{F}^{(m-1)} \tag{4.19b}$$

$$\mathbf{B}^{(m)} = \mathbf{M_2}\mathbf{A}^{(m)}\,, \tag{4.19c}$$

$$\mathbf{F}^{(m)} = \sum_{n=1}^{N} w_n \mathbf{B}^{(m)}\,. \tag{4.19d}$$

In Eqs. (4.19), $\mathbf{M_1}$ is an $Np \times Np$ matrix containing the coefficients of $A^{(n)}_{m,r}$ from Eq. (4.18b), while $\mathbf{M_2}$ is an $Np \times Np$ matrix containing the coefficients of $A^{(m)}_{n,r}$ from Eq. (4.18c). The size-Np column vector $\mathbf{A}^{(m)}$ contains the edge-centered angular flux error terms, while the size-Np column vector $\mathbf{B}^{(m)}$ contains the cell-centered angular flux error terms. The size-p column vectors $\mathbf{F}^{(m)}$ and $\mathbf{E}$ contain the updated and initial scalar flux error terms, respectively.

Next, we solve Eq. (4.19b) for $\mathbf{A}^{(m)}$, insert the result into Eq. (4.19c), and use the resulting expression for $\mathbf{B}^{(m)}$ in Eq. (4.19d) to obtain a recursive expression for $\mathbf{F}^{(m)}$:

$$\mathbf{F}^{(m)} = \sum_{n=1}^{N} w_n \mathbf{M_2}\mathbf{M_1}^{-1}\left(\frac{1}{2}\mathbf{F}^{(m-1)}\right). \tag{4.20}$$

Making the additional definition

$$\mathbf{H} = \frac{1}{2}\sum_{n=1}^{N} w_n \mathbf{M_2}\mathbf{M_1}^{-1}\,, \tag{4.21}$$

Eq. (4.20) becomes:

$$\mathbf{F}^{(m)} = \mathbf{H}\mathbf{F}^{(m-1)}\,. \tag{4.22}$$

Using Eq. (4.22) and the initial condition in Eq. (4.19a), we develop a simple formula for the updated scalar flux error coefficients after M iterations ($\mathbf{F}^{(M)}$) as a function of the initial scalar flux error coefficients ($\mathbf{E}$):

$$\mathbf{F}^{(M)} = \mathbf{H}^{M}\mathbf{E}\,. \tag{4.23}$$

In Eq. (4.23), $\mathbf{F}^{(M)}$ is a size-p column vector containing the scattering source flux error coefficients $F^{(M)}_r$, $\mathbf{E}$ is a size-p column vector containing the fission source flux error coefficients E_r, and $\mathbf{H}^M$ is a $p \times p$ matrix which relates the two flux error vectors.

The coarse-grid current error coefficients must also be rewritten in terms of the initial scalar flux coefficients ($\mathbf{E}$). These current coefficients were originally expressed in terms of the edge-centered angular flux error coefficients using

$$K = \sum_{n=1}^{N} w_n \mu_n A_{1,n}^{(M)} \, . \tag{4.24}$$

The coefficients $A_{1,n}^{(M)}$ are a size-N subset of the size-Np column vector $\mathbf{A}^{(M)}$. Using Eq. (4.19b), we solve for $\mathbf{A}^{(M)}$ and insert this expression into Eq. (4.24). Then, we use Eq. (4.23) to replace $\mathbf{F}^{(M-1)}$ in the resulting equation. This yields

$$\begin{aligned} K &= \sum_{n=1}^{N} w_n \mu_n A_{1,n}^{(M)} \\ &= \frac{1}{2} \sum_{r'=1}^{p} \left[\sum_{n=1}^{N} w_n \mu_n \mathbf{M_1}^{-1} \mathbf{H}^{M-1} \right]_{1,r'} E'_r \\ &= \sum_{r'=1}^{p} \tilde{A}_{1,r'}^{(M)} E'_r \, . \end{aligned} \tag{4.25}$$

Now that the updated flux and coarse-grid current error coefficients are expressed in terms of the initial flux error coefficients, we proceed to the low-order equations. Substituting Eqs. (4.23) and (4.25) into Eqs. (4.16g) - (4.16i) (with the exception of the normalization condition, which has already been satisfied), we obtain:

$$2(I - D)(\cos(\Sigma_t \lambda_s \Delta) - 1) = 3\Sigma_t \Delta \sum_{r'=1}^{p} \tilde{A}_{1,r'}^{(M)} E_{r'} (e^{i\Sigma_t \lambda_s \Delta} - 1) \, , \tag{4.26a}$$

$$\omega E_r - \sum_{r'=1}^{p} (H^M)_{r,r'} E_{r'} = (I - D) \, , \tag{4.26b}$$

where $(H^M)_{r,r'}$ are the components of $\mathbf{H}^M$ (see Eq. (4.23)). These two expressions can be combined to yield

$$2(\omega E_r - \sum_{r'=1}^{p} H_{r,r'}^{(M)} E_{r'})(\cos(\Sigma_t \lambda_s \Delta) - 1) = 3\Sigma_t \Delta \sum_{r'=1}^{p} \tilde{A}_{1,r'}^{(M)} E_{r'} (e^{i\Sigma_t \lambda_s \Delta} - 1) \, . \tag{4.27}$$

Moving all terms to one side of Eq. (4.27) and defining a lumped constant,

$$C = \frac{3\Sigma_t\Delta(e^{i\Sigma_t\lambda_s\Delta} - 1)}{2(\cos(\Sigma_t\lambda_s\Delta) - 1)} , \tag{4.28}$$

we arrive at the following eigenvalue system for ω:

$$C\sum_{r'=1}^{p}\tilde{A}^{(M)}_{1,r'}E_{r'} + \sum_{r'=1}^{p}(H^M)_{r,r'}E_{r'} - \omega E_r = 0 . \tag{4.29}$$

In matrix form, this can be expressed as

$$(\hat{\mathbf{H}} - \mathbf{I}\omega)\mathbf{E} = 0 , \tag{4.30}$$

where $\mathbf{I}$ is the $p \times p$ identity matrix, $\hat{\mathbf{H}}$ is a $p \times p$ matrix containing the coefficients of E_r from the first two terms of Eq. (4.29), and $\mathbf{E}$ is a size-p column vector which contains E_r.

Using Eq. (4.29), we calculate the eigenvalues ω_r numerically for $1 \leq r \leq p$ and permitted values of the discrete Fourier frequency, λ_s. Once the eigenvalues are known, the spectral radius (ρ) is determined using

$$\rho = \sup_{1\leq s<J}\left[\sup_{1\leq r\leq p}|\omega_r(\lambda_s)|\right]. \tag{4.31}$$

4.3.2 Two-group Case

4.3.2.1 The Linearized Two-group LCMC Method

To extend the LCMC Fourier analysis to a more realistic case, we also consider a two-group iteration scheme. The results of this Fourier analysis will allow us to investigate the effects of (simple) energy dependence on the stability of the linearized LCMC iteration equations. We employ the same assumptions that were made in the two-group CMFD-MC Fourier analysis; namely, that all fission neutrons are born in the fast group, all fission reactions occur in the thermal group, and no upscattering occurs from the thermal to the fast group. With these simplifications, the two-group LCMC iteration equations can be written in the following way (for a homogeneous, isotropic-scattering problem with periodic boundaries):

$$\phi_g^{(\ell+1/2,0)}(x) = \phi_g^{(\ell)}(x) , \tag{4.32a}$$

$$\mu\frac{d}{dx}\psi_1^{(\ell+1/2,m)}(x,\mu)+\Sigma_{t,1}\psi_1^{(\ell+1/2,m)}(x,\mu)=\frac{1}{2}\left(\Sigma_{s,1\to1}\phi_1^{(\ell+1/2,m-1)}(x)+\frac{\nu\Sigma_{f,2}}{k^{(\ell)}}\phi_2^{(\ell+1/2,m-1)}(x)\right)\,, \tag{4.32b}$$

$$\mu\frac{d}{dx}\psi_2^{(\ell+1/2,m)}(x,\mu)+\Sigma_{t,2}\psi_2^{(\ell+1/2,m)}(x,\mu)=\frac{1}{2}\left(\Sigma_{s,1\to2}\phi_1^{(\ell+1/2,m-1)}(x)+\Sigma_{s,2\to2}\phi_2^{(\ell+1/2,m-1)}(x)\right)\,, \tag{4.32c}$$

$$0\le x\le X\,,\ -1\le\mu\le1\,,\ 1\le m\le M\,,$$

$$\psi_g^{(\ell+1/2,m)}(0,\mu)=\psi_g^{(\ell+1/2,m)}(X,\mu)\,,\ -1\le\mu\le1\,, \tag{4.32d}$$

$$\phi_g^{(\ell+1/2,m)}(x)=\int_{-1}^{1}\psi_g^{(\ell+1/2,m)}(x,\mu)d\mu\,. \tag{4.32e}$$

Next, we introduce a uniform coarse grid with J cells of width Δ. Because the group-wise coarse-grid cross sections and diffusivities ($\tilde{D}$) are known exactly for the homogeneous case, we omit these expressions. The coarse-grid group-wise flux and current terms are tallied during the MC solve using:

$$\Phi_{j,g}^{(\ell+1/2)}=\frac{1}{\Delta}\int_{x_{j-1/2}}^{x_{j+1/2}}\phi_g^{(\ell+1/2,M)}(x)dx\,, \tag{4.33a}$$

$$\Phi_{1,j\pm1/2,g}^{(\ell+1/2)}=\int_{-1}^{1}\mu\psi_g^{(\ell+1/2,M)}(x_{j\pm1/2},\mu)d\mu\,. \tag{4.33b}$$

These flux and current values are then used to calculate the current correction ($\hat{D}$) terms:

$$\hat{D}_{j+1/2,g}^{(\ell+1/2)}=\frac{\Phi_{1,j+1/2,g}^{(\ell+1/2)}+\tilde{D}_g(\Phi_{j+1,g}^{(\ell+1/2)}-\Phi_{j,g}^{(\ell+1/2)})}{\Phi_{j+1,g}^{(\ell+1/2)}+\Phi_{j,g}^{(\ell+1/2)}}\,, \tag{4.33c}$$

which is used to form the coefficients of the low-order system:

$$\begin{gathered}\Phi_{1,j+1/2,1}^{(\ell+1)}-\Phi_{1,j-1/2,1}^{(\ell+1)}+\Sigma_{r,1}\Phi_{j,1}^{(\ell+1)}\Delta=\frac{\nu\Sigma_{f,2}}{k^{(\ell+1)}}\Phi_{j,2}^{(\ell+1)}\Delta\ ,\\ \Phi_{1,j+1/2,2}^{(\ell+1)}-\Phi_{1,j-1/2,2}^{(\ell+1)}+\Sigma_{r,2}\Phi_{j,2}^{(\ell+1)}\Delta=\Sigma_{s,1\to2}^{(\ell+1/2)}\Phi_{j,1}^{(\ell+1)}\Delta\,,\ 1\le j\le J\,,\end{gathered} \tag{4.33d}$$

$$\Phi_{1,j+1/2,g}^{(\ell+1)}=\tilde{D}_g(\Phi_{j+1,g}^{(\ell+1)}-\Phi_{j,g}^{(\ell+1)})+\hat{D}_{j+1/2,g}^{(\ell+1/2)}(\Phi_{j+1,g}^{(\ell+1)}+\Phi_{j,g}^{(\ell+1)})\,, \tag{4.33e}$$

$$\Phi_{1,1/2,g}^{(\ell+1)}=\Phi_{1,J+1/2,g}^{(\ell+1)}\,,\ g=1,2\,. \tag{4.33f}$$

In Eqs. (4.33d), we have defined the removal cross section:

$$\Sigma_{r,g}=\Sigma_{t,g}-\Sigma_{s,g\to g}\,. \tag{4.33g}$$

Finally, the updated coarse grid group-wise fluxes are used to scale the LCMC fission and scattering source distributions for the next cycle:

$$\phi_g^{(\ell+1)}(x) = \phi_g^{(\ell+1/2,M)}(x)\left[\frac{\Phi_{j,g}^{(\ell+1)}}{\Phi_{j,g}^{(\ell+1/2)}}\right] ,\ x_{j-1/2} \leq x \leq x_{j+1/2}\ ,\ 1 \leq j \leq J\ ,\ g = 1,2. \tag{4.33h}$$

Upon convergence, this problem has the exact solution

$$\psi_1(x,\mu) = \frac{1}{2}\ , \tag{4.34a}$$

$$\psi_2(x,\mu) = \frac{1}{2}\left(\frac{\Sigma_{s,1\to 2}}{\Sigma_{r,2}}\right) = \frac{\mathcal{C}}{2}\ , \tag{4.34b}$$

$$\Phi_{j,1} = \phi_1(x) = 1\ , \tag{4.34c}$$

$$\Phi_{j,2} = \phi_2(x) = \mathcal{C}\ , \tag{4.34d}$$

$$\Phi_{1,j+1/2,g} = 0\ ,\ g = 1,2\ , \tag{4.34e}$$

$$\frac{1}{k} = \frac{\Sigma_{r,1}\Sigma_{r,2}}{\nu\Sigma_{f,2}\Sigma_{s,1\to 2}} = \frac{1}{k_{ex}}\ . \tag{4.34f}$$

Next, we define linear expansions around the exact solution, using a small parameter ϵ ($\epsilon \ll 1$). These expansions take the form:

$$\psi_1^{(\ell+1/2,m)}(x,\mu) = \frac{1}{2} + \epsilon\tilde{\psi}^{(\ell+1/2,m)}(x,\mu)\ , \tag{4.35a}$$

$$\psi_2^{(\ell+1/2,m)}(x,\mu) = \frac{\mathcal{C}}{2} + \epsilon\tilde{\psi}^{(\ell+1/2,m)}(x,\mu)\ , \tag{4.35b}$$

$$\phi_1^{(\ell+1/2,m)}(x) = 1 + \epsilon\tilde{\phi}^{(\ell+1/2,m)}(x)\ , \tag{4.35c}$$

$$\phi_2^{(\ell+1/2,m)}(x) = \mathcal{C} + \epsilon\tilde{\phi}^{(\ell+1/2,m)}(x)\ , \tag{4.35d}$$

$$\phi_1^{(\ell+1,m)}(x) = 1 + \epsilon\tilde{\phi}^{(\ell+1,m)}(x)\ , \tag{4.35e}$$

$$\phi_2^{(\ell+1,m)}(x) = \mathcal{C} + \epsilon\tilde{\phi}^{(\ell+1,m)}(x)\ , \tag{4.35f}$$

$$\Phi_{j,1}^{(\ell+1/2)} = 1 + \epsilon\tilde{\Phi}_j^{(\ell+1/2)}\ , \tag{4.35g}$$

$$\Phi_{j,2}^{(\ell+1/2)} = \mathcal{C} + \epsilon\tilde{\Phi}_j^{(\ell+1/2)}\ , \tag{4.35h}$$

$$\Phi_{j,1}^{(\ell+1)} = 1 + \epsilon\tilde{\Phi}_j^{(\ell+1)}\ , \tag{4.35i}$$

$$\Phi_{j,2}^{(\ell+1)} = \mathcal{C} + \epsilon\tilde{\Phi}_j^{(\ell+1)}\ , \tag{4.35j}$$

$$\Phi_{1,j+1/2,g}^{(\ell+1/2)} = 0 + \epsilon\tilde{\Phi}_{1,j+1/2,g}^{(\ell+1/2)}\ , \tag{4.35k}$$

$$\Phi_{1,j+1/2,g}^{(\ell+1)} = 0 + \epsilon\tilde{\Phi}_{1,j+1/2,g}^{(\ell+1)}\ , \tag{4.35l}$$

$$\hat{D}_{j+1/2,g}^{(\ell+1/2)} = 0 + \epsilon\hat{d}_{j+1/2,g}^{(\ell+1/2)}\ , \tag{4.35m}$$

$$\frac{1}{k^{(\ell+1)}} = \frac{1}{k_{ex}} + \epsilon\delta^{(\ell+1)} \,. \tag{4.35n}$$

The coarse-grid cross sections are known exactly for the homogeneous case, so we do not expand these terms. Next, we insert the linear expansions (Eqs. 4.35) into the two-group iteration equations, equate $\mathcal{O}(\epsilon)$ terms, and neglect $\mathcal{O}(\epsilon^2)$ terms to obtain the linearized two-group LCMC system:

$$\tilde{\phi}_g^{(\ell+1/2,0)}(x) = \tilde{\phi}_g^{(\ell)}(x) \,, \;\; 0 \le x \le X \,, \tag{4.36a}$$

$$\mu\frac{d}{dx}\tilde{\psi}_1^{(\ell+1/2,m)}(x,\mu) + \Sigma_{t,1}\tilde{\psi}^{(\ell+1/2,m)}(x,\mu) = \frac{1}{2}\left(\Sigma_{s,1\to1}\tilde{\phi}_1^{(\ell+1/2,m-1)}(x) + \nu\Sigma_{f,2}\delta^{(\ell)}\mathcal{C} + \frac{\nu\Sigma_{f,2}}{k_{ex}}\tilde{\phi}_2^{(\ell+1/2,m-1)}(x)\right) \,, \tag{4.36b}$$

$$\mu\frac{d}{dx}\tilde{\psi}_2^{(\ell+1/2,m)}(x,\mu) + \Sigma_{t,2}\tilde{\psi}_2^{(\ell+1/2,m)}(x,\mu) = \frac{1}{2}\left(\Sigma_{s,1\to2}\tilde{\phi}_1^{(\ell+1/2,m-1)}(x) + \Sigma_{s,2\to2}\tilde{\phi}_2^{(\ell+1/2)}(x)\right) \,, \tag{4.36c}$$

$$-1 \le \mu \le 1 \,, \;\; 0 \le x \le X \,, \;\; 1 \le m \le M \,,$$

$$\tilde{\psi}_g^{(\ell+1/2,m)}(0,\mu) = \tilde{\psi}_g^{(\ell+1/2,m)}(X,\mu) \,, \;\; -1 \le \mu \le 1 \,, \tag{4.36d}$$

$$\tilde{\phi}_g^{(\ell+1/2,m)}(x) = \int_{-1}^{1} \tilde{\psi}_g^{(\ell+1/2,m)}(x,\mu)d\mu \,, \tag{4.36e}$$

$$\tilde{\Phi}_{j,g}^{(\ell+1/2)} = \frac{1}{\Delta}\int_{-1}^{1} \tilde{\phi}_g^{(\ell+1/2,M)}(x)dx \,, \tag{4.36f}$$

$$\tilde{\Phi}_{1,j+1/2,g}^{(\ell+1/2)} = \int_{-1}^{1} \mu\tilde{\psi}_g^{(\ell+1/2,M)}(x_{j+1/2},\mu)d\mu \,, \tag{4.36g}$$

$$\hat{d}_{j+1/2,g}^{(\ell+1/2)} = \frac{1}{2}\left[\tilde{\Phi}_{1,j+1/2,g}^{(\ell+1/2)} + \tilde{D}_g(\tilde{\Phi}_{j+1,g}^{(\ell+1/2)} - \tilde{\Phi}_{j,g}^{(\ell+1/2)})\right] \,, \tag{4.36h}$$

$$\tilde{\Phi}_{1,j+1/2,1}^{(\ell+1)} - \tilde{\Phi}_{1,j-1/2,1}^{(\ell+1)} + \Sigma_{r,1}\tilde{\Phi}_{j,1}^{(\ell+1)}\Delta = \nu\Sigma_{f,2}\Delta\left(\delta^{(\ell+1)}\mathcal{C} + \frac{1}{k_{ex}}\tilde{\Phi}_{j,2}^{(\ell+1)}\right) \,, \tag{4.36i}$$

$$\tilde{\Phi}_{1,j+1/2,2}^{(\ell+1)} - \tilde{\Phi}_{1,j-1/2,2}^{(\ell+1)} + \Sigma_{r,2}\tilde{\Phi}_{j,2}^{(\ell+1)}\Delta = \Sigma_{s,1\to2}\tilde{\Phi}_{j,2}^{(\ell+1)}\Delta \,, \tag{4.36j}$$

$$\tilde{\Phi}_{1,j+1/2,g}^{(\ell+1)} = -\tilde{D}_g(\tilde{\Phi}_{j+1,g}^{(\ell+1)} - \tilde{\Phi}_{j,g}^{(\ell+1)}) + 2\hat{d}_{j+1/2,g}^{(\ell+1/2)} \,, \tag{4.36k}$$

$$0 = \frac{1}{J}\sum_{j=1}^{J}\tilde{\Phi}_{j,g}^{(\ell+1)} \,, \tag{4.36l}$$

and

$$\tilde{\phi}_g^{(\ell+1)}(x) = \tilde{\phi}_g^{(\ell+1/2,M)}(x) + \tilde{\Phi}_{j,g}^{(\ell+1)} - \tilde{\Phi}_{j,g}^{(\ell+1/2)} , \tag{4.36m}$$

$$x_{j-1/2} \leq x \leq x_{j+1/2} , \; 1 \leq j \leq J .$$

Because the LCMC iteration scheme is nonlinear, several of Eqs. (4.36) differ in form from the original system in Eqs. (4.32)-(4.33). Summing the thermal and fast group coarse-grid balance equations [Eqs. (4.36i) and (4.36j)] over all coarse spatial cells, and then solving for $\delta^{(\ell+1)}$, we obtain:

$$\delta^{(\ell+1)} = 0 . \tag{4.37}$$

Thus, the two-group LCMC iteration scheme converges the $\mathcal{O}(\epsilon)$ component of the eigenvalue (but not the eigenfunction) after a single iteration. In the following section, we perform the Fourier analysis to estimate the eigenfunction convergence rate, as a function of the coarse grid thickness and number of permitted collisions per cycle.

4.3.2.2 Fourier Analysis

Following the procedure introduced for the monoenergetic case, we first approximate the continuous two-group LCMC equations with a two-group discrete ordinates system. While the two-group Fourier analysis proceeds in a fashion similar to the monoenergetic case, the details and results are sufficiently different that we feel it important to include both analyses in this thesis.

Discretizing the continuous LCMC iteration equations allows us to solve a block matrix system numerically for the spectral radius. To minimize the error introduced by this approximation, we assume the discrete ordinates problem is formulated on a very fine space-angle grid. We use the coarse-grid parameter $p = \frac{\Delta}{h}$ to denote the number of fine cells per coarse cell.

After the discrete approximation is introduced, the linearized high-order transport equations can be written:

$$\frac{\mu_n}{h}(\tilde{\psi}_{k+1/2,n,1}^{(\ell+1/2,m)} - \tilde{\psi}_{k-1/2,n,1}^{(\ell+1/2,m)}) + \Sigma_{t,1}\tilde{\psi}_{k,n,1}^{(\ell+1/2,m)} = \frac{1}{2}\left(\Sigma_{s,1\to 1}\tilde{\phi}_{k,1}^{(\ell+1/2,m-1)} + \frac{\nu\Sigma_{f,2}}{k_{ex}}\tilde{\phi}_{k,2}^{(\ell+1/2,m-1)}\right) , \tag{4.38a}$$

$$\frac{\mu_n}{h}(\tilde{\psi}_{k+1/2,n,2}^{(\ell+1/2,m)} - \tilde{\psi}_{k-1/2,n,2}^{(\ell+1/2,m)}) + \Sigma_{t,2}\tilde{\psi}_{k,n,2}^{(\ell+1/2,m)} = \frac{1}{2}\left(\Sigma_{s,1\to 2}\tilde{\phi}_{k,1}^{(\ell+1/2,m-1)} + \Sigma_{s,2\to 2}\tilde{\phi}_{k,2}^{(\ell+1/2,m-1)}\right) , \tag{4.38b}$$

$$1 \le n \le N,\ \ 1 \le k \le K\ ,\ 1 \le m \le M\ ,$$

$$\tilde{\psi}^{(\ell+1/2,m)}_{1/2,n,g} = \tilde{\psi}^{(\ell+1/2,m)}_{K+1/2,n,g}\ ,\ \ 1 \le n \le N\ ,\ g = 1,2\ . \tag{4.38c}$$

In Eqs. (4.38), we use Eq. (4.37) to eliminate the $\delta^{(\ell+1)}$ term. The discretized form of the linearized scalar flux expression becomes:

$$\tilde{\phi}^{(\ell+1/2,m)}_{k,g} = \sum_{n=1}^{N} w_n \tilde{\psi}^{(\ell+1/2,m)}_{k,n,g}\ . \tag{4.38d}$$

Finally, we introduce the weighted diamond auxiliary equations to close the system:

$$\tilde{\psi}^{(\ell+1/2)}_{k,n,g} = \left(\frac{1+\alpha_{n,g}}{2}\right)\tilde{\psi}^{(\ell+1/2)}_{k+1/2,n,g} + \left(\frac{1-\alpha_{n,g}}{2}\right)\tilde{\psi}^{(\ell+1/2)}_{k-1/2,n,g}\ ,$$

$$1 \le n \le N\ ,\ \ 1 \le k \le K\ ,\ g = 1,2\ . \tag{4.38e}$$

The $\alpha_{n,g}$ values are calculated using the *Step Characteristic* spatial discretization:

$$\alpha_{n,g} = \frac{1+e^{-\Sigma_{t,g}h/\mu_n}}{1-e^{-\Sigma_{t,g}h/\mu_n}} - \frac{2\mu_n}{\Sigma_{t,g}h}\ ,\ \ 1 \le n \le N\ ,\ g = 1,2\ . \tag{4.38f}$$

To simplify the ansatz, we again employ a relative cell index:

$$k = (j-1)p + r\ , \tag{4.38g}$$

where k is the fine cell index, j is the index of the coarse cell in which fine cell k resides, p is the coarse-grid parameter, and r is the position of fine cell k within coarse cell j. With this indexing scheme in place, we define the Fourier ansatz:

$$\tilde{\psi}^{(\ell+1/2,m)}_{k-1/2,n,g} = \omega^l A^{(m)}_{r,n,g} e^{i\lambda x_j}\ , \tag{4.39a}$$

$$\tilde{\psi}^{(\ell+1/2,m)}_{k,n,g} = \omega^l B^{(m)}_{r,n,g} e^{i\lambda x_j}\ , \tag{4.39b}$$

$$\tilde{\phi}^{(\ell+1/2,m)}_{k,g} = \omega^l F^{(m)}_{r,g} e^{i\lambda x_j}\ , \tag{4.39c}$$

$$\tilde{\Phi}^{(\ell+1/2)}_{j,g} = \omega^l D_g e^{i\lambda x_j}\ , \tag{4.39d}$$

$$\tilde{\Phi}^{(\ell+1/2)}_{1,j-1/2,g} = \omega^l K_g e^{i\lambda x_j}\ , \tag{4.39e}$$

$$\tilde{\Phi}^{(\ell+1)}_{j,g} = \omega^l I_g e^{i\lambda x_j}\ , \tag{4.39f}$$

$$\tilde{\phi}^{(\ell+1)}_{k,g} = \omega^{l+1} E_{r,g} e^{i\lambda x_j}\ . \tag{4.39g}$$

The quantities that are updated during inner iterations ($\tilde{\psi}^{(l+1/2,m)}_{k-1/2,n,g}$, $\tilde{\psi}^{(l+1/2,m)}_{k,n,g}$, and $\tilde{\phi}^{(l+1/2,m)}_{k,g}$)

depend on the inner iteration variable m. We include this dependence in the Fourier ansatz by allowing the coefficients $A^{(m)}_{r,n,g}$, $B^{(m)}_{r,n,g}$ and $F^{(m)}_{r,g}$ to vary during the high-order sweeps. The high-order error coefficients are also assumed to be periodic on the coarse grid, such that

$$\tilde{\psi}^{(\ell+1/2,m)}_{(k+p)-1/2,n,g} = \left(\tilde{\psi}^{(\ell+1/2,m)}_{k-1/2,n,g}\right) e^{i\lambda\Delta} = \omega^l A^{(m)}_{r,n,g} e^{i\lambda(x_j+\Delta)} \, . \tag{4.40}$$

The ansatz is then inserted into Eqs. (4.36). After some simplification, we obtain:

$$F^{(0)}_{r,g} = E_{r,g} \, , \tag{4.41a}$$

$$\begin{cases} \frac{\mu_n}{h}\left(A^{(m)}_{r+1,n,1} - A^{(m)}_{r,n,1}\right) + \Sigma_{t,1} B^{(m)}_{r,n,1} = \frac{1}{2}\left(\Sigma_{s,1\to1} F^{(m-1)}_{r,1} + \frac{\nu\Sigma_{f,2}}{k_e x} F^{(m-1)}_{r,2}\right) , & 1 \le r < p \, , \\ \frac{\mu_n}{h}\left(A^{(m)}_{1,n,1} e^{i\lambda\Delta} - A^{(m)}_{r,n,1}\right) + \Sigma_{t,1} B^{(m)}_{r,n,1} = \frac{1}{2}\left(\Sigma_{s,1\to1} F^{(m-1)}_{r,1} + \frac{\nu\Sigma_{f,2}}{k_e x} F^{(m-1)}_{r,2}\right) , & r = p \, , \end{cases} \tag{4.41b}$$

$$\begin{cases} \frac{\mu_n}{h}\left(A^{(m)}_{r+1,n,2} - A^{(m)}_{r,n,2}\right) + \Sigma_{t,2} B^{(m)}_{r,n,2} = \frac{1}{2}\left(\Sigma_{s,1\to2} F^{(m-1)}_{r,1} + \Sigma_{s,2\to2} F^{(m-1)}_{r,2}\right) , & 1 \le r < p \, , \\ \frac{\mu_n}{h}\left(A^{(m)}_{1,n,2} e^{i\lambda\Delta} - A^{(m)}_{r,n,2}\right) + \Sigma_{t,2} B^{(m)}_{r,n,2} = \frac{1}{2}\left(\Sigma_{s,1\to2} F^{(m-1)}_{r,1} + \Sigma_{s,2\to2} F^{(m-1)}_{r,2}\right) , & r = p \, , \end{cases} \tag{4.41c}$$

$$A^{(m)}_{1,n,g} = A^{(m)}_{1,n,g} e^{i\lambda X} \, , \tag{4.41d}$$

$$\begin{cases} B^{(m)}_{r,n,g} = \left[\frac{1+\alpha_{n,g}}{2}\right] A^{(m)}_{r+1,n,g} + \left[\frac{1-\alpha_{n,g}}{2}\right] A^{(m)}_{r,n,g} \, , & 1 \le r < p \, , \\ B^{(m)}_{r,n,g} = \left[\frac{1+\alpha_{n,g}}{2}\right] A^{(m)}_{1,n,g} e^{i\lambda\Delta} + \left[\frac{1-\alpha_{n,g}}{2}\right] A^{(m)}_{r,n,g} & r = p \, , \end{cases} \tag{4.41e}$$

$$F^{(m)}_{r,g} = \sum_{n=1}^{N} w_n B^{(m)}_{r,n,g} \, , \tag{4.41f}$$

$$D_g = \frac{1}{p} \sum_{r=1}^{p} F^{(M)}_{r,g} \, , \tag{4.41g}$$

$$K_1(e^{i\lambda\frac{\Delta}{2}} - e^{-i\lambda\frac{\Delta}{2}}) + \Sigma_{r,1} I_1 \Delta = \frac{\nu\Sigma_{f,2}}{k_{ex}} I_2 \Delta \, , \tag{4.41h}$$

$$K_2(e^{i\lambda\frac{\Delta}{2}} - e^{-i\lambda\frac{\Delta}{2}}) + \Sigma_{r,2} I_2 \Delta = \Sigma_{s,1\to2} I_1 \Delta \, , \tag{4.41i}$$

$$K_g = \frac{1}{3\Sigma_{t,g}\Delta}\left(e^{i\lambda\frac{\Delta}{2}} - e^{-i\lambda\frac{\Delta}{2}}\right)(D_g - I_g) + \sum w_n \mu_n A^{(M)}_{1,n,g} e^{i\lambda\frac{\Delta}{2}} \tag{4.41j}$$

$$0 = \sum_{j=1}^{J} e^{i\lambda x_j} \, , \tag{4.41k}$$

$$\omega E_{r,g} - F^{(M)}_{r,g} = (I_g - D_g) \, . \tag{4.41l}$$

The resulting coarse-grid equations [Eqs. (4.41g) - (4.41l)] depend on the total number of inner iterations per outer (M), but do not depend explicitly on the inner iteration variable (m).

Next, we use the periodic boundary condition Eq. (4.41d) to determine the permissible discrete Fourier frequencies:

$$\lambda = \lambda_s = \frac{2\pi s}{X}, \;\; s = 1,2,3 \, \dots \, (J-1) \, . \tag{4.42}$$

These discrete frequencies depend on the slab thickness (X) and number of coarse cells (J). As the coarse grid becomes infinitesmally fine, the λ_s values approach a continuous distribution. Also, when the discrete frequencies are applied to the Fourier ansatz, the normalization condition in Eq. (4.41k) is automatically satisfied.

In order to form and solve a block matrix system for the theoretical spectral radius, we must first express the group-wise fine grid scalar flux error coefficients $F^{(M)}_{r,g}$ and coarse-grid current coefficients K_g in terms of the initial error coefficients $E_{r,g}$.

First, we use Eq. (4.41j) to eliminate K_1 and K_2 from the low-order balance Eqs. (4.41h) and (4.41i). We also use Eq. (4.41g) to rewrite D_g in terms of $F_{r,g}$ in Eqs. (4.41h), (4.41i) and (4.41l), and convert exponential terms to trigonometric functions where possible. This yields:

$$\frac{2}{3\Sigma_{t,1}\Delta}\left(\frac{1}{p}\sum_{r=1}^{p} F^{(M)}_{r,1} - I_1\right)(\cos(\lambda_s\Delta) - 1) + \sum_{n=1}^{N} w_n\mu_n A^{(M)}_{1,n,1}(e^{i\lambda_s\Delta} - 1) + \Sigma_{r,1} I_1 \Delta = \frac{\nu\Sigma_{f,2}}{k_{ex}} I_2 \Delta \, , \tag{4.43a}$$

$$\frac{2}{3\Sigma_{t,2}\Delta}\left(\frac{1}{p}\sum_{r=1}^{p} F^{(M)}_{r,2} - I_2\right)(\cos(\lambda_s\Delta) - 1) + \sum_{n=1}^{N} w_n\mu_n A^{(M)}_{2,n,1}(e^{i\lambda_s\Delta} - 1) + \Sigma_{r,2} I_2 \Delta = \Sigma_{s,1\to 2} I_1 \Delta \, , \tag{4.43b}$$

$$\omega E_{r,g} - F^{(M)}_{r,g} + \frac{1}{p}\sum_{r'=1}^{p} F^{(M)}_{r',g} - I_g = 0 \, , \; g = 1,2 \, . \tag{4.43c}$$

Next, Eq. (4.41e) is used to eliminate $B^{(m)}_{r,n,g}$ from the high-order transport equations. Once this is done, we express the high-order system [Eqs. (4.41a)-(4.41f)] in matrix form, as was done in the monoenergetic case:

$$\mathbf{F}^{(0)} = \mathbf{E}\,, \tag{4.44a}$$

$$\mathbf{M_1}\mathbf{A}^{(m)} = \frac{1}{2}\mathbf{S}\mathbf{F}^{(m-1)} \tag{4.44b}$$

$$\mathbf{B}^{(m)} = \mathbf{M_2}\mathbf{A}^{(m)}\,, \tag{4.44c}$$

$$\mathbf{F}^{(m)} = \sum_{n=1}^{N} w_n \mathbf{B}^{(m)}\,. \tag{4.44d}$$

In Eqs. (4.44), $\mathbf{M_1}$ is a $2Np \times 2Np$ matrix containing the coefficients of $A_{n,r,g}^{(m)}$ from Eqs. (4.41b) and (4.41c), and $\mathbf{M_2}$ is a $2Np \times 2Np$ matrix containing the coefficients of $A_{n,r,g}^{(m)}$ from Eq. (4.41e). The size-$2Np$ column vector $\mathbf{A}^{(m)}$ contains the edge-centered angular flux error terms, while the size-Np column vector $\mathbf{B}^{(m)}$ contains the cell-centered angular flux error terms. The size-$2p$ column vectors $\mathbf{F}^{(m)}$ and $\mathbf{E}$ contain the updated and initial scalar flux error terms, respectively.

Eqs. (4.44) can be used to develop a recursion relation for the scalar flux error coefficients, which can then be rewritten in terms of the initial scalar flux error coefficients. This process is unchanged from the monoenergetic case, so we omit the algebra here for brevity (see Section 4.3.1.2 for details). The result is a simple formula for the updated scalar flux error coefficients after M iterations ($\mathbf{F}^{(M)}$), as a function of the initial scalar flux error coefficients ($\mathbf{E}$):

$$\mathbf{F}^{(M)} = \mathbf{H}^{M}\mathbf{E}\,, \tag{4.45}$$

where

$$\mathbf{H} = \frac{1}{2}\sum w_n \mathbf{M_2}\mathbf{M_1}^{-1}\mathbf{S}\,. \tag{4.46}$$

In Eq. (4.45), $\mathbf{F}^{(M)}$ is a size-$2p$ column vector containing the scattering source flux error coefficients after M inner iterations, $\mathbf{E}$ is a size-$2p$ column vector containing the fission source flux error coefficients $E_{r,g}$, and $\mathbf{H}^{M}$ is a $2p \times 2p$ matrix that relates the two flux error vectors (with M an exponent, not an iteration superscript).

The coarse-grid current error coefficients K_g must also be rewritten in terms of $\mathbf{E}$. These coefficients were originally expressed in terms of the edge-centered angular flux error coefficients using

$$K_g = \sum_{n=1}^{N} w_n \mu_n A^{(M)}_{1,n,g} \,, \tag{4.47}$$

where $A^{(M)}_{1,n,g}$ are a size-$2N$ subset of the size-$2Np$ column vector $\mathbf{A}^{(M)}$. As was done in the monoenergetic case, we solve Eq. (4.44b) for $\mathbf{A}^{(M)}$ and insert this expression into Eq. (4.47). Then, we use Eq. (4.45) to replace $\mathbf{F}^{(M-1)}$ in the resulting equation. This yields

$$\begin{aligned} K_g &= \sum_{n=1}^{N} w_n \mu_n A^{(M)}_{1,n,g} \\ &= \frac{1}{2} \sum_{r'=1}^{p} \left[\sum_{n=1}^{N} w_n \mu_n \mathbf{M_1}^{-1} \mathbf{H}^{M-1} \right]_{1,r',g} E_{r',g} \\ &= \sum_{r'=1}^{p} \tilde{A}^{(M)}_{1,r',g} E_{r',g} \,. \end{aligned} \tag{4.48}$$

In Eq. (4.48), $A^{(M)}_{1,n,g}$ are the groupwise edge-centered angular flux error coefficients for $r = 1$, and $\tilde{A}^{(M)}_{1,r',g}$ are the quantities which relate $E_{r',g}$ to the current error coefficient K_g.

We next proceed to the low-order equations (with the exception of the low-order normalization, which is automatically satisfied by λ_s). Substituting Eqs. (4.45) and (4.48) into Eqs. (4.43) and rearranging yields:

$$\frac{2}{3\Sigma_{t,1}\Delta} \left(\frac{1}{p} \sum_{r''=1}^{p} \sum_{r'=1}^{p} (H^M)_{r'',r',1} E_{r',1} - I_1 \right) (\cos(\lambda_s \Delta) - 1) + \\ \sum_{r'=1}^{p} \tilde{A}^{(M)}_{1,r',1} E_{r',1} (e^{i\lambda_s \Delta} - 1) = -\Sigma_{r,1} I_1 \Delta + \frac{\nu \Sigma_{f,2}}{k_{ex}} I_2 \Delta \,, \tag{4.49a}$$

$$\frac{2}{3\Sigma_{t,2}\Delta} \left(\frac{1}{p} \sum_{r''=1}^{p} \sum_{r'=1}^{p} (H^M)_{r'',r',2} E_{r',2} - I_2 \right) (\cos(\lambda_s \Delta) - 1) + \\ \sum_{r'=1}^{p} \tilde{A}^{(M)}_{1,r',2} E_{r',2} (e^{i\lambda_s \Delta} - 1) = -\Sigma_{r,2} I_2 \Delta + \Sigma_{s,1\to 2} I_1 \Delta \,, \tag{4.49b}$$

$$-\omega E_{r,g} + \sum_{r'=1}^{p} (H^M)_{r,r',g} E_{r',g} - \frac{1}{p} \sum_{r''=1}^{p} \sum_{r'=1}^{p} (H^M)_{r'',r',g} E_{r',g} + I_g = 0 \,, \tag{4.49c}$$

where $(H^M)_{r,r',g}$ are the components of $\mathbf{H}^M$ for group g (see Eq. (4.45)).

At this point, our system of equations is expressed in terms of two quantities: (i) the initial scalar flux error coefficients $E_{r,g}$, and (ii) the updated coarse-grid scalar flux coefficients I_g. To calculate the spectral radius, we solve the low-order balance equations [Eqs. (4.49a) and (4.49b)] for I_g as a function of $E_{r,g}$, then insert this result into Eq. (4.49c). This results in an eigenvalue system, which can then be solved numerically for the $2p$ values of ω. This process is repeated for each permissible value of the Fourier frequency λ_s. Once the eigenvalues are known, the spectral radius (ρ) is determined using

$$\rho = \sup_{g=1,2}\left[\sup_{1\le s<J}\left[\sup_{1\le r\le p}\left|\omega_{r,g}(\lambda_s)\right|\right]\right] . \tag{4.50}$$

In the next section, we present and discuss numerical results for both the monoenergetic and two-group LCMC Fourier analyses.

4.4 Numerical Results

In this section, we present numerical results for the LCMC method. We first use the Fourier analyses presented in this chapter to examine the convergence behavior of the LCMC method in the non-random limit. Numerical results are generated using both a surrogate deterministic code and direct LCMC simulations, and are then compared to theoretical predictions from the Fourier analysis. We also test the LCMC method on a set of benchmark problems, and use these results to investigate several features of the method. Specifically, we focus on aspects of LCMC which differ considerably from the standard MC and CMFD-MC methods presented earlier in this thesis.

4.4.1 Stability Analysis

4.4.1.1 Monoenergetic Case

First, we outline numerical results for the monoenergetic Fourier analysis. These results provide straightforward relationships between problem cross sections, coarse grid size, and convergence rate. We compare theoretical predictions to numerical experiment to demonstrate the validity of the Fourier analysis.

Because it is difficult to obtain accurate, low-noise spectral radius estimates from direct LCMC simulations, we also obtain estimates using a "surrogate" CMFD-S_N code. The surrogate code employs the same iteration strategy as the stochastic LCMC method, and is run on a suitably fine space-angle grid to minimize truncation error. Thus, it is effectively a non-random version of the stochastic LCMC method. For the results presented here, we use the S_{32} Gauss-Legendre quadrature set, with 50 fine cells per coarse cell (see parametric study in Section 3.5.1.2). The test problem is a homogeneous, 50 cm slab: surrogate CMFD-S_N simulations use vacuum boundaries, while LCMC calculations use periodic boundaries (see discussion below).

To calculate direct LCMC spectral radius estimates, we simulate the test problem in Table 4.1, using a large number of particles per cycle [$\mathcal{O}(10^6)$] to minimize statistical error. After four cycles, we use the numerical spectral radius expression introduced in Section 2.4.1 to calculate a single estimate of the spectral radius. In theory, an estimate of the spectral radius can be calculated after the third cycle; however, in practice this estimate is usually contaminated by the initial guess. Direct LCMC results are averaged over 25 independent simulations, and are reported along with their standard deviation.

Test problem parameters are reported in Table 4.1; these are the same as the CMFD-MC test problem, with the exception of the scattering cross section (which is allowed to vary in the CMFD-MC analysis).

Table 4.1: Test problem specifications

Σ_t (cm^{-1})	$\nu\Sigma_f$ (cm^{-1})	Σ_s (cm^{-1})	Δ (cm)	M
1.0	0.01	0.5	1.0 - 10.0	1, 2, 5, 10

As previously mentioned, our surrogate CMFD-S_N simulations use vacuum boundary conditions. While the numerical test problem could in theory be run with periodic boundaries, it is not guaranteed that the boundary conditions will be satisfied if the number of inner iterations per outer (M) is small. (The linearization procedure outlined in Section 4.3.1.1 requires that the exact solution of the theoretical problem be flat, which precludes the possibility of Fourier-analyzing the vacuum boundary case.)

This boundary condition mismatch introduces a slight difference between theoretical and CMFD-S_N numerical estimates of the LCMC Fourier analysis. However, the test problem is optically thick, which minimizes leakage. As a result, vacuum-boundary S_N numerical spectral radius estimates should be reasonably close to theoretical predictions for the periodic case. We note that stochastic LCMC simulations automatically satisfy the periodic boundary condition, so periodic boundaries can be used for LCMC numerical experiments.

Figures 4.1 and 4.2 compare theoretical and numerical LCMC spectral radius estimates as a function of the coarse grid size and number of collisions allowed per cycle (M). It is

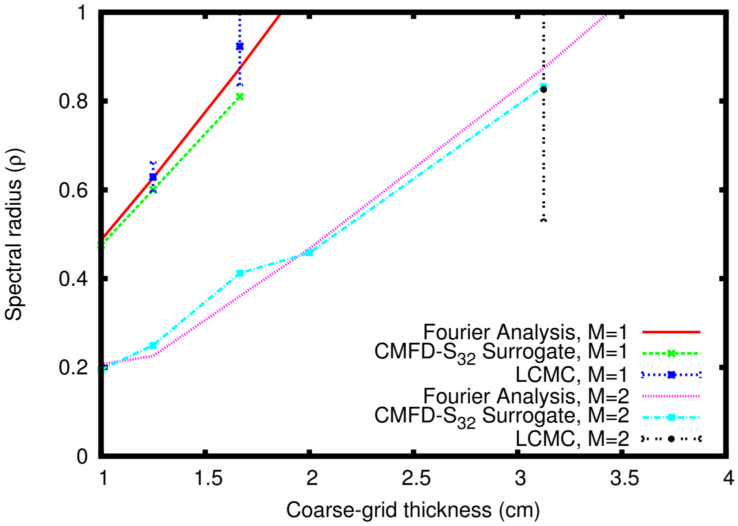

Figure 4.1: LCMC spectral radius estimates for M=1 and M=2

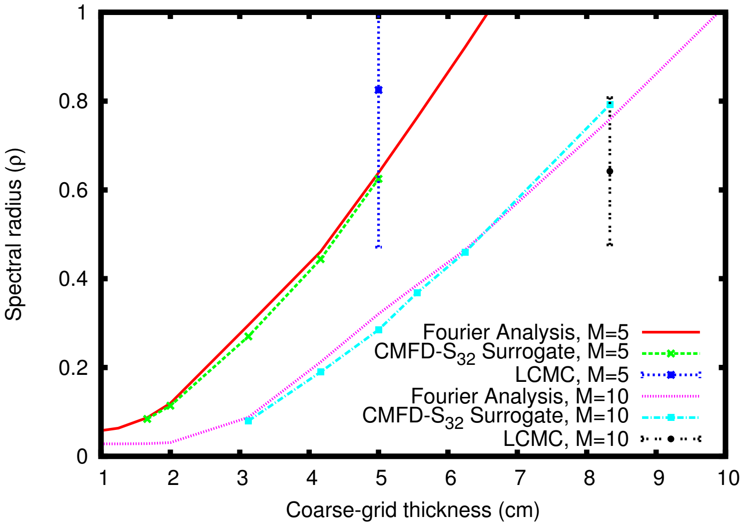

Figure 4.2: LCMC spectral radius estimates for M=5 and M=10

interesting to note that, unlike the CMFD-MC spectral radius, the LCMC spectral radius does not depend on the scattering cross section (Σ_s). (This is easily verified by examination of Eqs. (4.18); only the total cross section, Σ_t, appears in these equations.) This is in contrast to the CMFD-MC spectral radius (Section 3.5.1.2), which depends strongly on the scattering ratio (c).

Numerical spectral estimates from the CMFD-S_N LCMC surrogate show generally good agreement with theoretical estimates. In most cases, the numerical spectral radii are slightly lower than the theoretical predictions; this is likely due to the boundary condition mismatch between theory and simulation. As previously noted, the S_N numerical simulations use vacuum boundary conditions. This introduces leakage at problem boundaries, which lowers the spectral radius.

Direct spectral radius estimates from LCMC are very noisy; much noisier, in fact, than the direct CMFD-MC estimates presented in Section 3.5.1.2. It is exceedingly difficult to generate direct LCMC spectral radius estimates (with reasonble error bounds) on a personal computer. Thus, we conclude that the LCMC spectral radius is far more sensitive to random noise than the CMFD-MC spectral radius.

This observation can be explained in a very straightforward fashion. As detailed in Section 4, the LCMC low-order system is formed using only tally information from the last collision event in each cycle. As a result, considerably less MC information is used to calculate the LCMC CMFD coefficients; thus, we would expect these coefficients to be significantly noisier than tallies used in the standard CMFD-MC method. Unfortunately, we have no way to theoretically predict the quantitative effect that this additional noise will have on the spectral radius of real simulations. However, as mentioned earlier in this chapter, it is possible to use an alternate version of the LCMC method, where data from all collision events contribute to CMFD tallies. This will be discussed in Section 4.4.2.2.

The results in Fig. 4.1 indicate that, if an LCMC simulation is run with a small number of collisions per cycle (e.g. $M = 1$ or 2), the spectral radius is a steeply increasing function of the coarse grid optical thickness. In this case, special care must be taken to ensure that the coarse grid size is sufficiently thin (on the order of a mean free path), or the LCMC method may diverge. We hypothesize (and empirical results appear to support) that the presence of stochastic error can shift these curves to the left. If this is true, it is not only important to ensure that the "non-random" spectral radius is less than unity; the spectral radius must be *sufficiently* less than unity, to account for the potentially destabilizing effect of stochastic noise in real LCMC simulations.

In summary, the monoenergetic LCMC Fourier analysis reveals the following trends: the LCMC spectral radius (i) increases as the coarse grid size increases, (ii) decreases as the number of allowed collisions increases, and (iii) does not depend on the scattering ratio (in the monoenergetic case). The first two points provide some guidance in choosing a coarse grid size/collision limit combination for real simulations. If a small number of collisions per cycle is used, the coarse grid size should be kept reasonably fine to prevent the simulation from becoming unstable. Conversely, if a larger number of collisions per cycle is allowed, the simulation will remain stable for a larger range of coarse grid sizes.

4.4.1.2 Two-group Case

In this section, we present results from the two-group stability analysis of the non-random LCMC method. Theoretical predictions from the Fourier analysis are compared to numerical estimates obtained from a multigroup CMFD-S_N surrogate code. We emphasize that the surrogate code uses the same iteration strategy as the stochastic LCMC method, and is run with a fine space-angle grid (S_{16} quadrature, with 50 fine spatial cells per coarse cell) to minimize trunction error. The test problem is a 150-cm slab with periodic boundaries, though the surrogate CMFD-S_N results use vacuum boundaries (see discussion in the previous section).

As in Section 3.5.1.2, our test problem uses two-group flux-collapsed cross sections for the C5G7 UO_2 fuel material. These cross sections are collapsed from the original seven-group structure using an infinite-medium seven-group UO_2 spectrum (obtained from an S_N calculation). Problem cross sections can be found in Table 3.2, while other parameters are listed in Table 4.2.

We were not able to obtain two-group spectral radius results using direct LCMC. Estimates calculated using $\mathcal{O}(10^7)$ particles per cycle were too noisy to be useful, and memory constraints precluded the use of a larger source bank. As a result, we present only theoretical predictions and surrogate CMFD-S_{16} estimates for the two-group UO_2 spectral radius.

Table 4.2: UO_2 test problem specifications

Δ (cm)	M
1.25 - 30	1,2,5,10

Figures 4.3 and 4.4 plot spectral radius curves versus coarse grid size for the four values of the collision limit (M) listed in Table 4.2. We observe behavior similar to the monoenergetic case: the non-random LCMC spectral radius increases monotonically as the coarse grid size is increased. The two-group LCMC iteration is not unconditionally stable for the 150-cm two-group UO_2 fuel problem; regardless of the number of permitted collisions, there is a coarse grid size at which the simulation becomes unstable ($\rho > 1$).

Like the monoenergetic LCMC spectral radius, the two-group spectral radius is a monotonically decreasing function of M (for a fixed grid size). Thus, if an LCMC simulation is found to be unstable for a given value of M, it may be possible to stabilize the simulation by increasing the number of collisions permitted per cycle (at least, this is the case in the infinite-particle limit; we will show later that this may not be universally true for real LCMC simulations).

To better understand the dependence of the spectral radius on the energy group structure

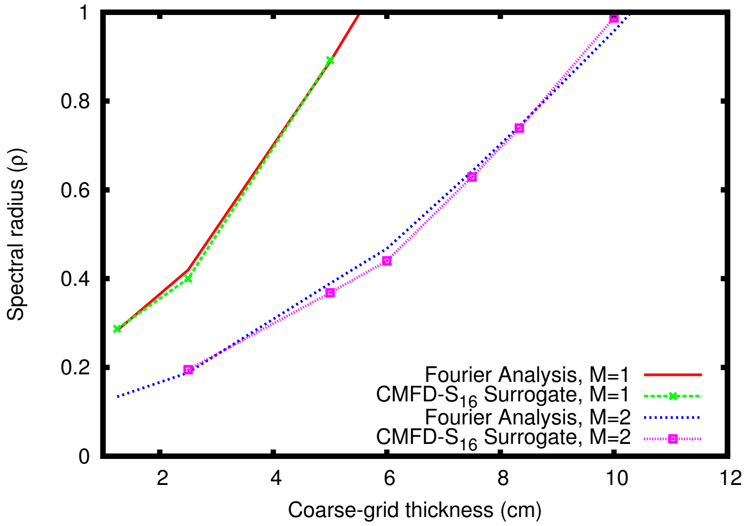

Figure 4.3: LCMC spectral radius (ρ) vs. coarse-grid size, group-collapsed UO_2, M=1 and M=2

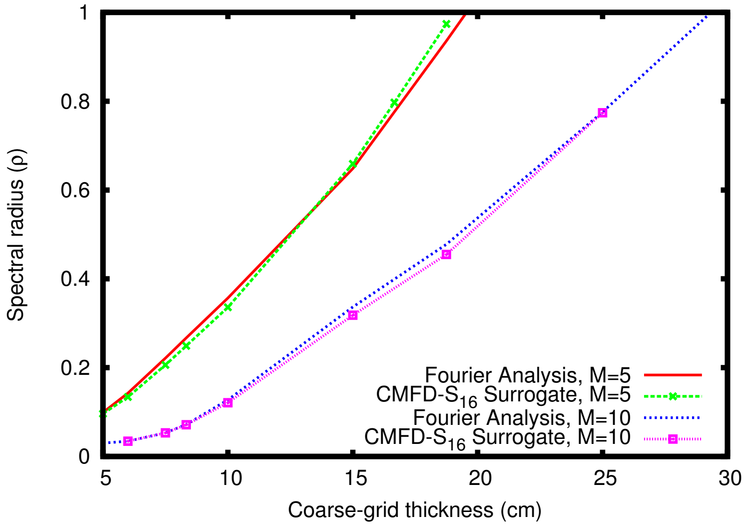

Figure 4.4: LCMC spectral radius (ρ) vs. coarse-grid size, group-collapsed UO_2, M=5 and M=10

of the problem, we also calculate numerical spectral radius estimates for a case in which the high-order (surrogate S_N) calculation uses seven energy groups, while the low-order CMFD calculation uses two (we refer to this as the 7g/2g LCMC iteration). We have not Fourier-analyzed this case; instead, our goal is to determine how well the two-group LCMC Fourier analysis predicts the convergence of an LCMC calculation with more than two transport energy groups. In Section 3.5.1.2, we noted that the multigroup calculation limits to continuous energy as the number of groups is allowed to approach infinity. Thus, it is important to understand how the LCMC iteration scheme behaves when the number of transport energy groups is larger than the number of CMFD energy groups.

Figures 4.5 and 4.6 show estimates of the 7g/2g LCMC spectral radius, which were calculated using our surrogate CMFD-S$_N$ code. The two-group LCMC Fourier analysis prediction (labeled “FA” in the figures) is included for comparison.

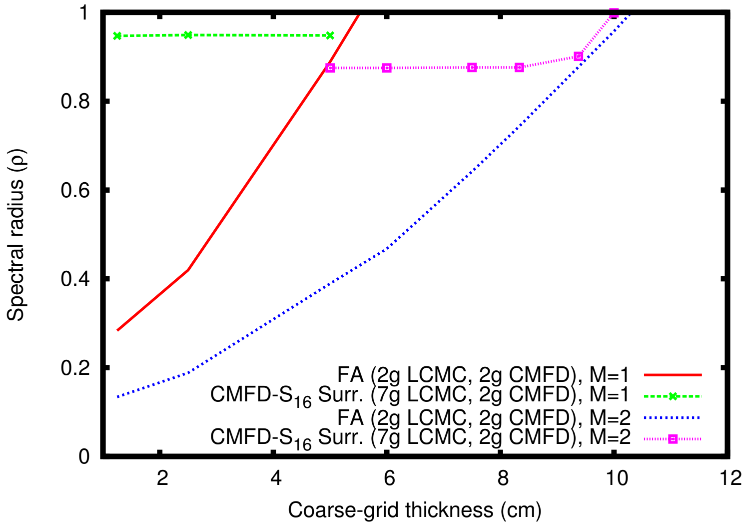

Figure 4.5: Spectral radius (ρ) vs. coarse-grid size, 7-group LCMC/2-group CMFD, M=1 and M=2

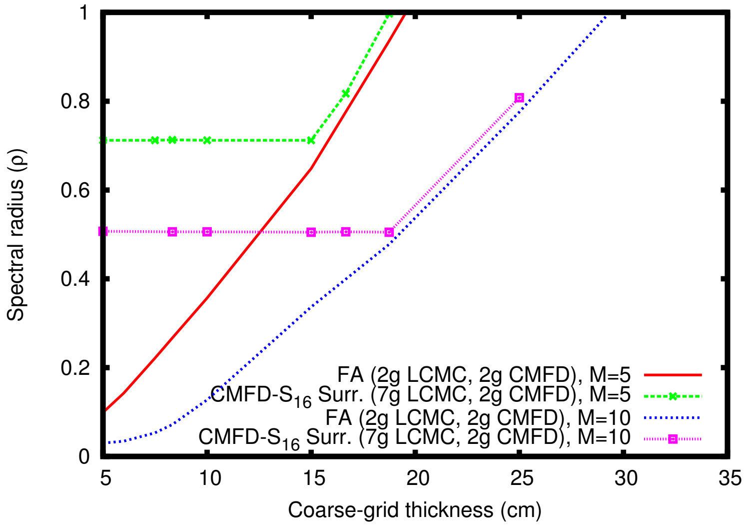

Figure 4.6: Spectral radius (ρ) vs. coarse-grid size, 7-group LCMC/2-group CMFD, M=5 and M=10

These figures reveal an interesting trend in the surrogate CMFD-S$_N$ estimates of the

7g/2g LCMC spectral radius. All of the spectral radius curves presented thus far in this thesis have been smoothly-increasing functions of the coarse grid size (or coarse-grid optical thickness, in the monoenergetic case). However, the spectral radius curves shown in Figures 4.5 and 4.6 are completely flat over a range of coarse-grid sizes. The magnitude of this flat spectral radius decreases as the number of permitted collisions increases.

The 7g/2g spectral radius "plateaus" suggest that performing a group collapse (from seven-group LCMC to two-group CMFD, in this case) introduces a Fourier mode that is (i) dominant when the coarse grid is reasonably fine, and (ii) independent of the coarse grid size. In other words, the convergence rate of the non-random 7g/2g LCMC iteration appears to be independent of coarse grid size when the coarse grid is "sufficiently fine." The upper limit of this spectral radius plateau occurs when the convergence rate of a spatially-varying mode becomes larger than the convergence rate of the spatially-flat mode.

We hypothesize that the spatially-varying modes of the 7g/2g iteration may converge at the rate predicted by the two-group Fourier analysis; this is supported by the fact that the numerical 7g/2g spectral radius curves in Figures 4.5 and 4.6 appear to roughly match the theoretical two-group prediction outside of the flat-spectral-radius range.

This feature of the 7g/2g spectral radius will likely prove very important in real LCMC simulations, where a many-group (or continuous-energy) LCMC energy group structure is used with few-group CMFD acceleration. If the non-random flat-mode spectral radius is sufficiently close to unity, it may not be feasible to run enough histories to converge the simulation for a given collision limit. If this is the case, a larger value of M should be used to reduce the convergence rate of the flat mode.

4.4.2 Benchmark Problem Performance

We now investigate the performance of the LCMC method for a set of benchmark test problems. These problems were originally introduced in Chapter 2; problem descriptions and other details can be found in Section 2.4.2. First, basic properties of LCMC are demonstrated using a homogeneous fissile slab. Then, the method is tested for a large, heterogeneous slab "reactor." We also use the slab reactor problem to investigate a modified tally strategy for the LCMC method, which increases the efficiency of the method and decreases statistical error. Finally, the LCMC method is used to simulate a 2-D quarter assembly problem, as well as a 2-D assembly problem. Due to memory limitations, we are unable to run the number of particles per cycle necessary to model the full C5G7 benchmark with LCMC.

4.4.2.1 Homogeneous Problem

In this section, we assess the performance of the LCMC method for the homogeneous problem introduced in Chapter 2 (problem #1). We use three variants of the LCMC method, with $M = 2$, 3, and 5 collisions per cycle.

All of our LCMC simulations employ CMFD feedback with the Wolters correction, which was introduced in Section 3.3.2. Other simulation parameters for problem #1 are listed in Table 4.3. We note that LCMC simulations require a larger number of inactive cycles than CMFD-MC simulations for problem #1, to ensure that the fission and scattering source distributions are adequately converged by the onset of active cycles. To determine when the source distributions are converged, we run a test case with a large number of cycles, then examine the Shannon entropy distributions. The source distribution is assumed to be converged when the Shannon entropy becomes largely stationary.

Table 4.3: Simulation parameters, problem #1

Case	Inactive Cyc.	Active Cyc.	Histories/Cyc.	Fine Grid (cm)	Coarse Grid (cm)
A	50	50	1e6	0.5	0.5
B	50	100	1e6	0.5	0.5
C	50	200	1e6	0.5	0.5

Figure 4.7 shows eigenfunction estimates for LCMC with $M = 2$, 3, and 5 collisions per cycle, with the S_N benchmark solution included for reference. All three LCMC cases show good agreement with the benchmark solution.

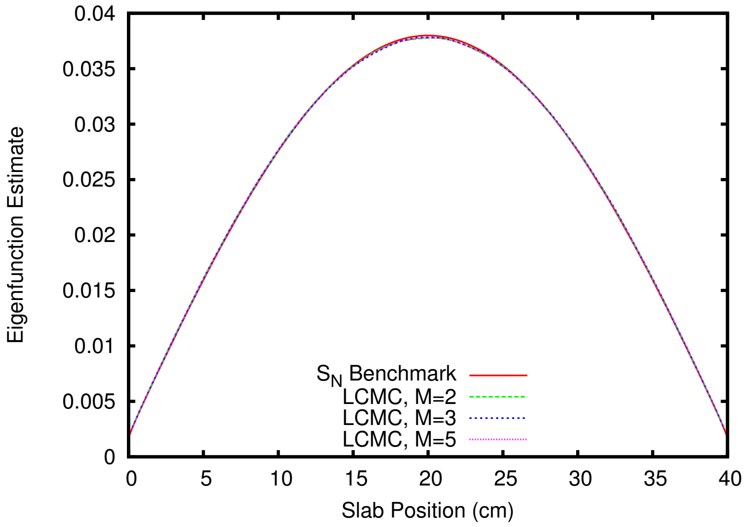

Figure 4.7: LCMC eigenfunction estimates, problem #1, case A

In keeping with results presented in Chapters 2 and 3, we consider the rate at which the apparent RSD decreases as the number of active cycles is increased. As previously mentioned, the Central Limit Theorem (CLT) predicts that the apparent RSD will decrease proportionally to $\frac{C}{\sqrt{N}}$, where C is some constant and N is the number of active batches simulated. Since we cannot prove theoretically that the LCMC method will behave as the CLT predicts, we instead show empirical behavior to support this hypothesis. To do this, we simulate cases A, B and C with each of the LCMC variants, then take ratios of the apparent RSDs for case A/case B, and again for case B/case C. Because the number of active cycles doubles between each case, we expect a corresponding factor of $\sqrt{2}$ reduction in the apparent RSD when these ratios are taken.

Figure 4.8 shows case A/case B and case B/case C apparent RSD ratios for the $M = 2$, 3, and 5 variants of LCMC.

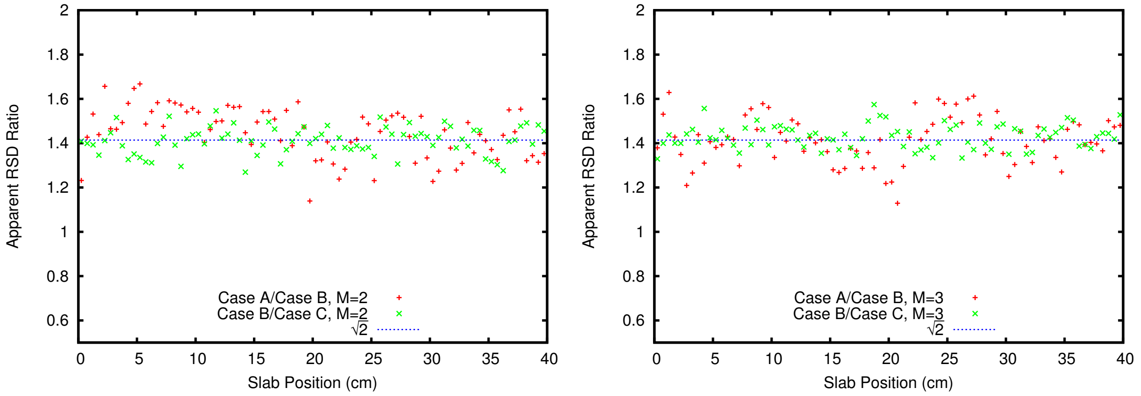

(a) $M = 2$ (b) $M = 3$

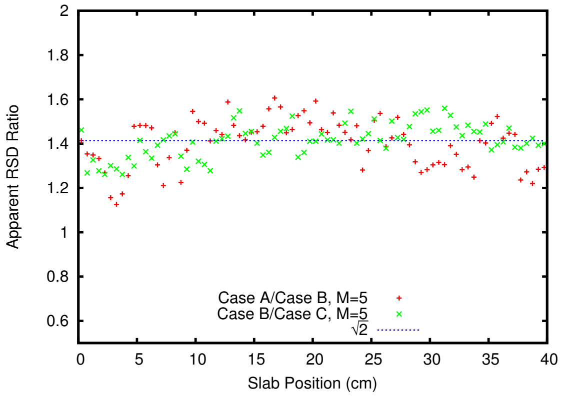

(c) $M = 5$

Figure 4.8: LCMC apparent RSD ratios, problem #1

LCMC apparent RSD ratios are, on average, close to the CLT-predicted value. In the

$M = 2$ and $M = 5$ plots, the case A/case B apparent RSD ratio has a slight trend across the spatial domain. This suggests that the LCMC method may be unable to completely converge the fission and scattering sources for the 0.5-cm coarse grid shown here. However, because the average ratio across the slab is very close to $\sqrt{2}$, LCMC cycles appear to be sufficiently independent to meet the requirements of the CLT.

Next, we use case A to estimate the real-to-apparent RSD ratio for each LCMC variant. To do this, 25 independent simulations are run, and statistics are calculated using eigenfunction solution estimates from all 25 runs. This yields an estimate of the real solution RSD, which can then be compared to the apparent RSD (calculated using active-cycle eigenfunction estimates from a single simulation). Real-to-apparent RSD results can be found in Figure 4.9; a line at unity is included for reference, and represents an exact match between apparent and real eigenfunction RSD.

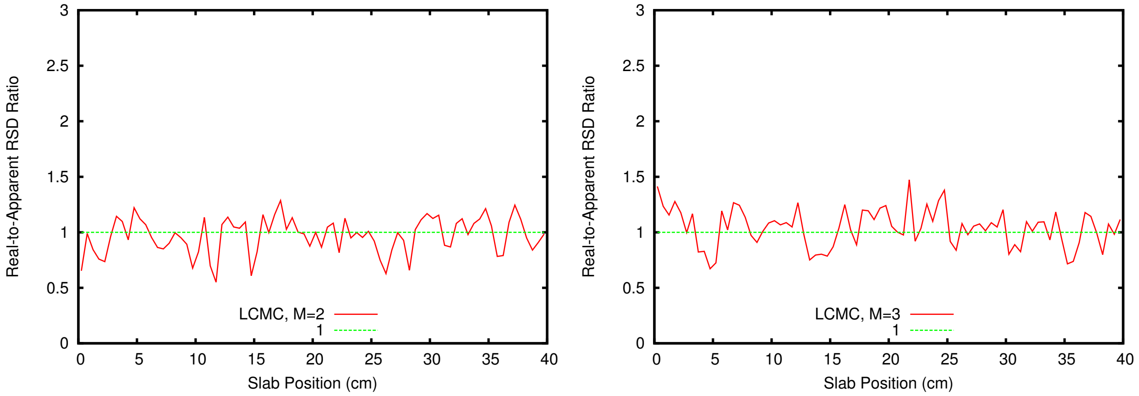

(a) $M = 2$ (b) $M = 3$

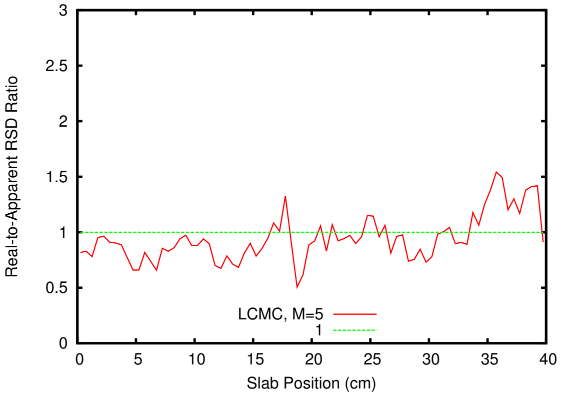

(c) $M = 5$

Figure 4.9: LCMC real-to-apparent RSD ratios, problem #1

Slab-average real-to-apparent RSD ratios are very close to unity for both the $M = 2$ and

$M = 3$ simulations. However, the $M = 5$ real-to-apparent RSD ratio appears to be slightly less than unity (on average). Similar behavior was seen in the CMFD-MC numerical results (see Section 3.5.2.1), and was determined to be the result of large (but stable) cycle-to-cycle oscillations in the coarse-grid solution. This is somewhat counter-intuitive, as the Fourier analysis predicts that the spectral radius of the LCMC iteration decreases monotonically as the number of permitted collisions increases. Thus, if we were to predict which of the cases in Figure 4.9 was most likely to be near the non-random stability limit, we would choose the $M = 2$ case.

However, there is another possible explanation that is not accounted for in the Fourier stability analysis. LCMC fission events occurring when $m < M$ are simulated in an analog fashion; they are not redistributed or reweighted using a low-order solution. Thus, when the LCMC iteration method is used for high dominance-ratio problems, the fission and scattering source solutions can fluctuate significantly within a cycle when the number of permitted collisions becomes large. When the CMFD system is formed using only data from the last collision event, this additional error results in decreased stability. In other words, even though tally information from the last collision is "more converged" in the infinite-particle limit than information from previous collisions, it may, in practice, contain significantly more error (as a result of the poor convergence properties of analog MC transport).

4.4.2.2 1-D Core Problem

Next, we consider the large, heterogeneous 1-D core problem introduced in Chapter 2 (problem #2). We again consider three values of the collision limit, $M = 2$, 3, and 5. LCMC simulation parameters for problem #2 are listed in Table 4.5. All of the problem #2 simulations employ a uniform 0.425-cm mesh for MC tallies. We consider three different total source weights (in histories per cycle) for the $M = 3$ case, to better understand how the fission bank scales with the number of histories simulated.

Numerical results from the Fourier analysis presented in Section 4.3 suggest that the LCMC method is less stable than CMFD-MC for a given grid size (when M is small); to counter this effect, we refine the coarse grid and increase the number of inactive cycles (relative to the CMFD-MC simulations in Section 3.5.2.2). This is done to ensure that the LCMC fission and scattering sources have adequate time to converge, and are sufficiently far from the non-random stability limit. Finally, we also increase the number of particles per cycle to ensure adequate tally information is available to form the low-order system during the last permitted collision.

In the course of simulating problem #2 with LCMC, we determined an alternate tally

Table 4.4: Simulation parameters, problem #2

Coll./Cyc. (M)	Inactive Cyc.	Active Cyc.	Coarse Grid (cm)	Histories/Cyc.
2	50	100	1.275	5e5
3	50	100	1.275	1.25e5, 2.5e5, 5e5
5	50	100	1.275	5e5

strategy that appears to increase the efficiency and stability of the LCMC method. In the original LCMC formulation, coefficients of the CMFD system are calculated using only tally data from the last permitted collision each cycle. As we show in Section 4.4.2.2.1, active-cycle eigenfunction estimates calculated using this strategy improve only marginally as the number of permitted collisions increases (assuming all other parameters are held constant). We observe this behavior because the CMFD solution contains roughly the same amount of statistical noise, regardless of the collision limit. As a result, apparent RSD estimates are dominated by noise in the CMFD solution; even though more stochastic information is tallied as M increases, this has little effect on solution error.

However, we hypothesize that the CMFD system can be formed using tally data from *all* collisions. We have not Fourier-analyzed this case, but we believe using tally data from all collisions increases the non-random spectral radius slightly. However, the corresponding reduction in statistical error appears to outweigh this increased spectral radius for real simulations.

We emphasize that use of the modified tally strategy has no drawbacks during active cycles. Because the fission and scattering sources are assumed stationary during the active-cycle phase, the LCMC flux iterates should all be "converged" in the infinite-particle limit (though stochastic noise will still be present in real simulations). In other words, during active cycles,

$$\phi^{(\ell+1/2,m)}(x) \approx \phi_{ex}(x)\ ,\ 1 \leq m \leq M\ , \tag{4.51}$$

where $\phi_{ex}(x)$ is the true flux solution. To demonstrate the benefit of using tally data from all collisions during active cycles, we split problem #2 results into two subsections. The first set of results, presented in Section 4.4.2.2.1, are generated with the original LCMC scheme (which uses data from the last permitted collision to form the CMFD system, for both inactive and active cycles).

The second set of results can be found in Section 4.4.2.2.2, and are generated using the modified tally strategy; that is, the CMFD system is formed using tally data from all collisions.

4.4.2.2.1 LCMC with Original Tallies

Figure 4.10 shows active-cycle eigenfunction estimates for the three LCMC collision limits considered here, with a zoomed-in view in Figure 4.11. A high-resolution S_N benchmark solution is included in both figures for reference.

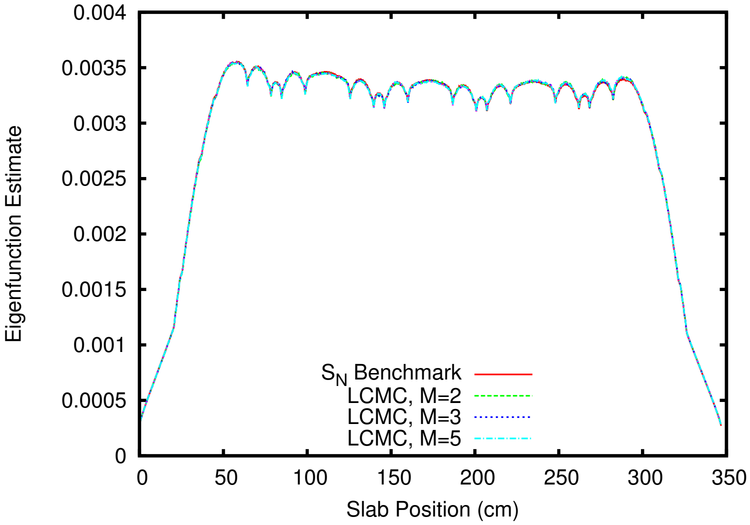

Figure 4.10: LCMC eigenfunction estimates, problem #2

The global LCMC eigenfunction shapes agree relatively well with the benchmark solution. Errors in the LCMC solution appear to be largely stochastic, suggesting that global solution wobble is minimal.

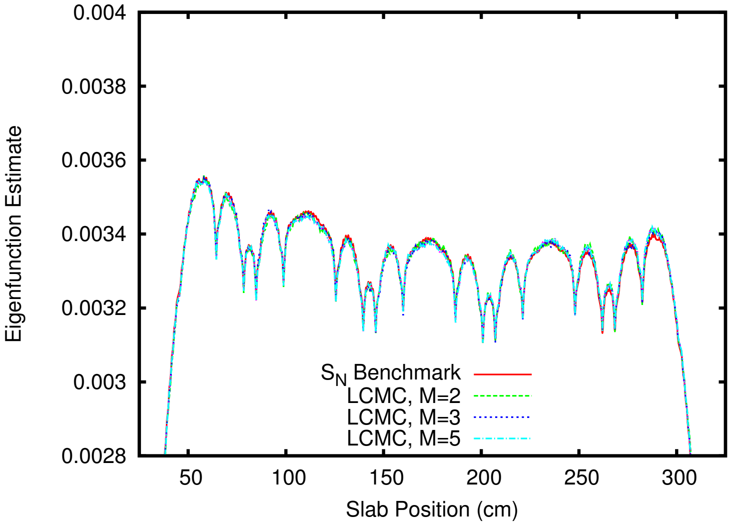

Figure 4.11: LCMC close-up of eigenfunction estimates, problem #2

In Figure 4.12 we plot close-up views of eigenfunction estimates for the three LCMC cases, averaged over cycles 50-100 and 100-150, respectively. While the overall solution averages shown in Figure 4.11 closely match the benchmark, the 50-cycle estimates show significantly more error, especially the $M = 2$ case. This is consistent with our understanding of non-random LCMC convergence behavior. Because the non-random spectral radius of the $M = 2$ case is higher than the $M = 3$ and $M = 5$ cases, it is logical to conclude that the spectral radius of the real simulation will also be higher. In addition, the presence of stochastic noise in the real simulation may drive the $M = 2$ spectral radius even closer to the stability limit.

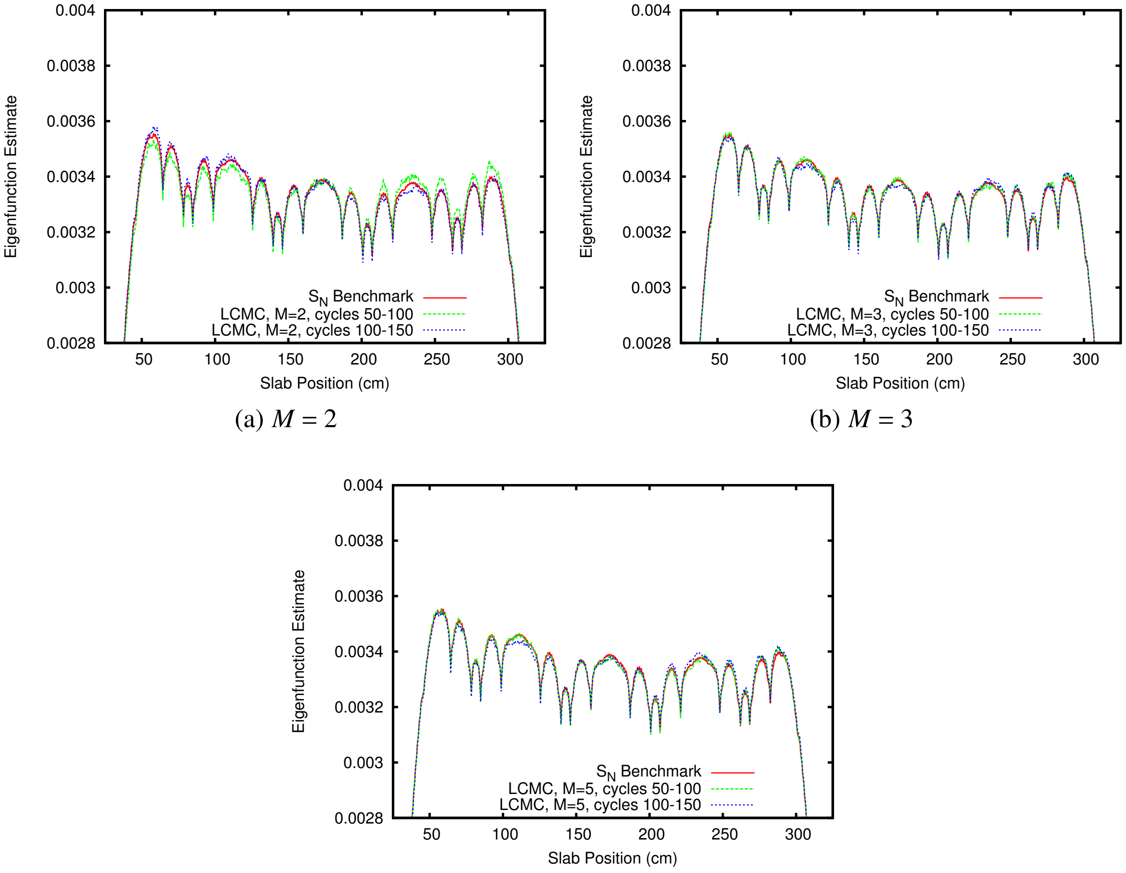

(a) $M = 2$

(b) $M = 3$

(c) $M = 5$

Figure 4.12: LCMC close-up of 50-cycle eigenfunction estimates, problem #2

Figure 4.13 plots the cycle-to-cycle variation in Shannon entropy for the LCMC simulations (using 500k particles per cycle for the $M = 3$ case). We note that there are two Shannon entropy distributions for the LCMC method, corresponding to the fission and scattering source distributions. The two plots shown in Figure 4.13 use different vertical

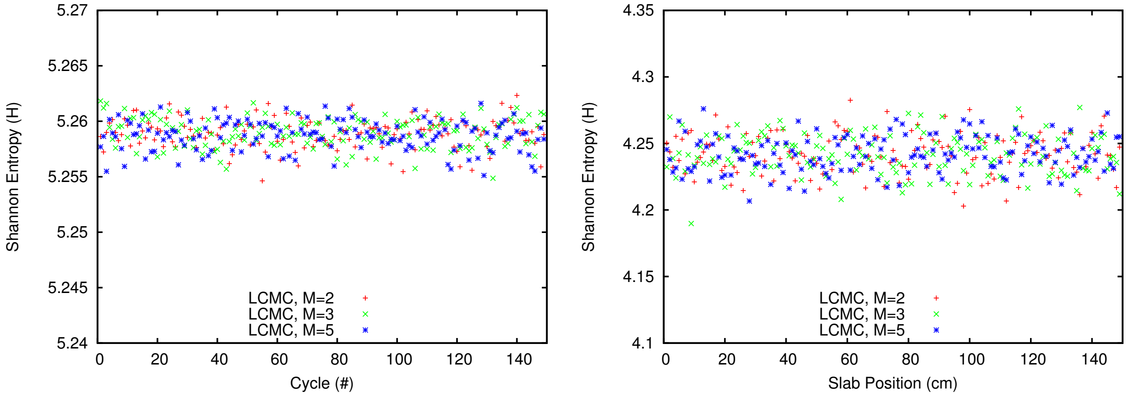

(a) Fission source

(b) Scattering source

Figure 4.13: LCMC Shannon entropy vs. cycle number, problem #2

scales; the scattering source distribution varies noticeably more from cycle to cycle than the fission source distribution. This is likely a result of the more complicated spatial dependence of the scattering source distribution. While the scattering source has no additional angular or energy dependence in problem #2 (which is 1-D and monoenergetic), every spatial cell has a non-zero scattering cross-section, while a considerable fraction of the domain is non-fissile.

We next compare LCMC apparent RSD distributions for problem #2, which are shown in Figure 4.14a. Actual relative solution error (with respect to the S_N benchmark) can be found in Figure 4.14b.

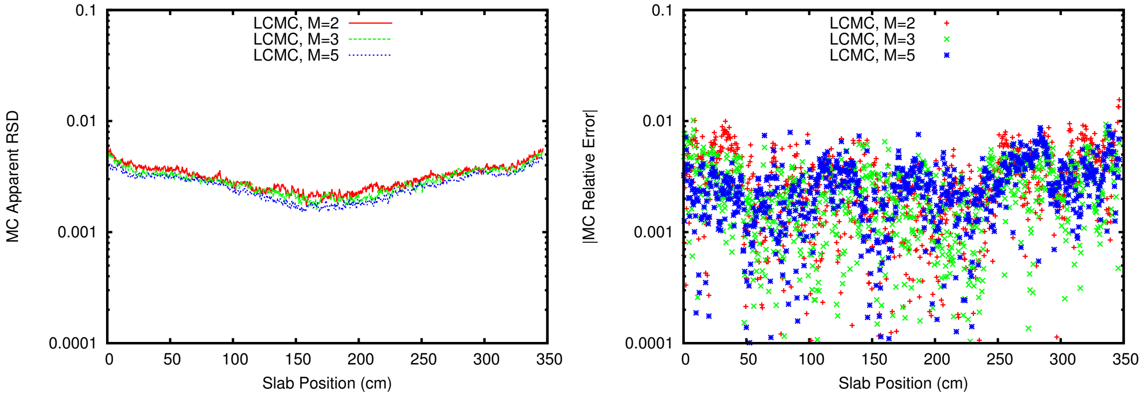

(a) Apparent RSD

(b) Relative error from benchmark

Figure 4.14: LCMC solution error curves, problem #2

The three apparent RSD curves, which correspond to different values of the collision limit (M), are very similar in shape. A decrease in magnitude is observed with increasing

M, though this decrease is very slight. In addition, the $M = 2$ curve shows more local high-freqency fluctuation than the higher collision limit cases.

At first glance, the curves in Figure 4.14a seem to defy standard wisdom regarding the behavior of MC solution error. In general, when the amount of information in a tally bin is doubled, the error in that quantity decreases by a factor of $\sqrt{2}$ (the rate predicted by the CLT). Thus, we might expect a significant decrease in the MC apparent RSD as the collision limit is increased from $M = 2$ to $M = 5$, as the total amount of MC information tallied per cycle increases by a factor of 2.5. However, we observe no such decrease.

There is a relatively simple explanation for this phenomenon. In the original LCMC method, we form the CMFD system using only tally information from the last permitted collision of the high-order calculation. This means that, regardless of the number of collisions allowed per cycle, the low-order CMFD system will be formed using the *same* amount of information! In turn, this causes error in the CMFD calculation to dominate total eigenfunction error. Because error in the CMFD calculation is roughly constant as a function of M, we observe very little decrease in the eigenfunction apparent RSD when the number of permitted collisions is increased.

Finally, in Figure 4.15 we investigate a parameter unique to the LCMC method: the size of the "intermediate" fission bank, which temporarily stores fission neutrons born during the LCMC cycle. For this parametric study, we use $M = 3$ and three different source bank sizes (1.25e5, 2.5e5, and 5e5 histories per cycle). We are chiefly concerned with two features of the intermediate fission bank: (i) how much the size of the bank changes from collision to collision, and (ii) how the size of the bank scales with the number of histories per cycle.

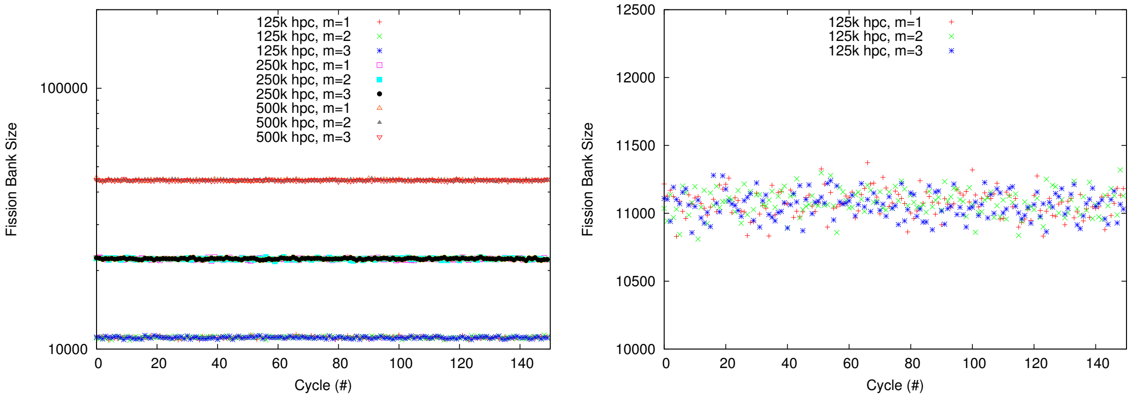

(a) Histories per cycle comparison

(b) Close-up, 125k hpc case

Figure 4.15: LCMC fission bank size vs. histories per cycle (hpc), problem #2

Because we scale fission neutron production by the *k*-eigenvalue, we expect the intermediate fission bank to reach an equilibrium size once the eigenvalue has converged (much like the fission bank in a standard MC calculation). Figure 4.15b demonstrates that this is indeed the case. The *k*-eigenvalue for problem #2 converges very quickly; as a result, intermediate fission bank sizes are well-behaved throughout the simulation, exhibiting only a small amount of fluctuation around a mean bank size of roughly 11k neutrons. In Figs. 4.15a and 4.15b, we also include the $m = 3$ case, which is the new source bank for the next cycle. It, too, is roughly 11k histories in size for the $M = 3$ case with 1.25e5 histories per cycle.

Figure 4.15a is plotted on a logarithmic scale to demonstrate the linear scaling of the intermediate fission bank with the number of histories per cycle. If the number of particles is doubled, the average size of the intermediate fission bank doubles as well. Conversely, if the number of particles is halved, the size of the intermediate fission bank is also halved. These relationships hold for all fission banks $m \leq M$, as shown in Figure 4.15a.

This linear scaling behavior is desirable for two primary reasons. First of all, it ensures that computation time will scale roughly linearly with the number of histories per cycle. This is of vital importance when running real-world simulations, as it allows for straightforward predictions of total runtime. In addition, linear scaling between source bank size and runtime allows us to use the same Figure of Merit (FOM) expression for LCMC that we use to assess the efficiency of other MC methods (this is discussed further in Chapter 5.5).

4.4.2.2.2 LCMC with Modified Tallies (LCMC-avg)

Figure 4.16 shows active-cycle eigenfunction estimates for the modified LCMC method, which we refer to as LCMC-avg. A close-up view of these estimates is shown in Figure 4.17, with an S_N benchmark solution included in both figures for reference. We emphasize that the CMFD system is formed using data from all collisions in the LCMC-avg method.

The global LCMC eigenfunction shapes agree reasonably well with the S_N benchmark. However, there appears to be a larger discrepancy between the LCMC-avg solution estimates and the benchmark, relative to the original LCMC results presented in Section 4.4.2.2.1. We believe that this is due to truncation error in the S_N benchmark solution, rather than systematic error in the LCMC-avg results (results from independent LCMC-avg runs and comparison with CMFD-MC results support this idea). In other words, the stochastic error in our LCMC-avg results is comparable to (or smaller than) the unknown truncation error in the S_N benchmark. As a result, detailed comparisons between LCMC-avg eigenfunction estimates and the S_N benchmark solution are not valid in this context.

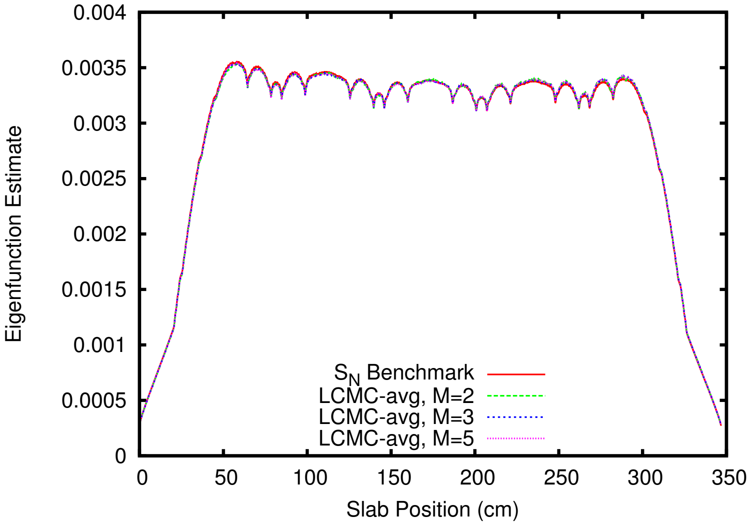

Figure 4.16: LCMC-avg eigenfunction estimates, problem #2

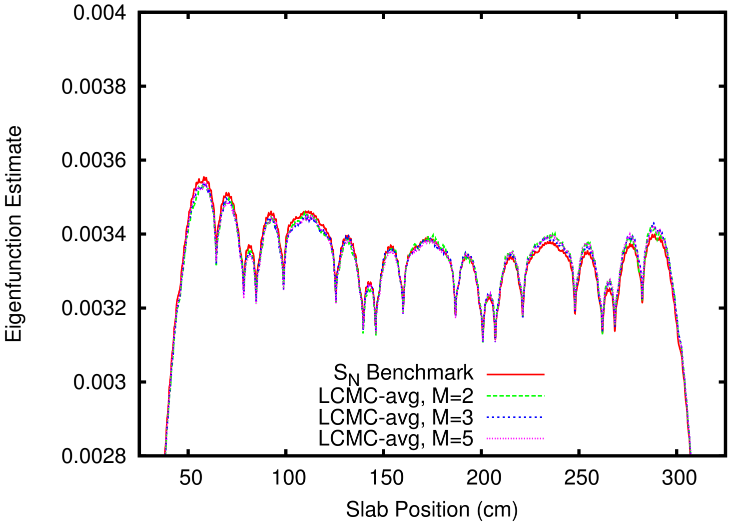

Figure 4.17: LCMC-avg close-up of eigenfunction estimates, problem #2

Quantities such as the Shannon entropy and fission bank size are not plotted for the LCMC-avg case, because these quantities are largely unchanged from the original LCMC trends presented in Section 4.4.2.2.1. (Shannon entropy values for the updated method are grouped more tightly about the mean value, but only slightly so.)

We do, however, plot apparent RSD distributions for the LCMC-avg method in Figure 4.18a. In addition, we calculate relative error with respect to the benchmark, and plot this in Figure 4.18b. As previously noted, our LCMC-avg results contain very little error; in fact, it is likely that truncation error in the benchmark solution is larger than stochastic noise in the updated LCMC-avg results. Thus, the error distributions presented in Figure 4.18b should not be considered an unbiased estimate of real solution error.

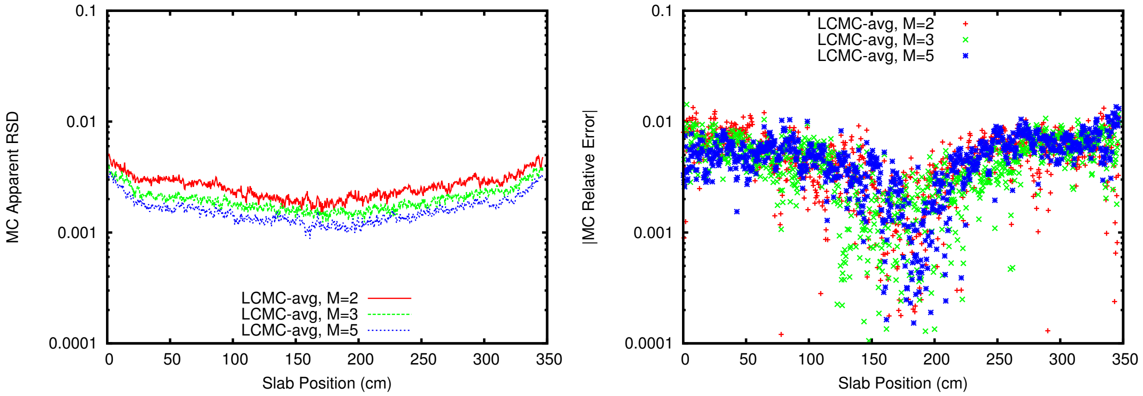

(a) Apparent RSD

(b) Relative error from benchmark

Figure 4.18: LCMC-avg eigenfunction error curves, problem #2

If the apparent RSD curves in Figure 4.18a are compared to those for the original LCMC method (Figure 4.14a), we observe three key differences. First, all of the curves in Figure 4.18a are smaller in magnitude than their counterparts in 4.14a. This verifies that the LCMC-avg tally method produces results with lower RSDs than the original LCMC method.

Second, the LCMC-avg apparent RSD curves depend more strongly on the value of the collision limit (M) than the original LCMC curves. In the original LCMC method, only tally information from the last permitted collision is used to form the coarse-grid coefficients. Thus, CMFD solution error is largely independent of the number of permitted collisions; it depends only on the number of histories per cycle. In the original LCMC curves shown in 4.14a, error in the coarse-grid solution is the dominant source of solution error. As a result, increasing the number of permitted collisions has little effect on the eigenfunction apparent RSD.

In the LCMC-avg tally method, the CMFD system is formed using tally information from all collisions. Thus, coarse-grid solution error is less dominant in the updated method, and decreases as the number of permitted collisions is increased.

Finally, the updated LCMC apparent RSD distributions are slightly flatter than the original LCMC distributions across most of the problem domain. This, again, indicates that error in the active-cycle CMFD solution (which manifests as global eigenfunction "wobble") is less dominant in the updated LCMC method. Consequently, the apparent RSD distribution is dominated by stochastic noise originating from the transport process.

In summary, after comparing the updated LCMC tally method to the original, we see that the updated version is indeed more accurate. Making use of additional tally data decreases the apparent RSD of the LCMC solution, and likely also helps prevent the CMFD calculation from destabilizing as a result of statistical fluctuations. Thus, we recommend the use of the updated tally LCMC method for real-world (multi-dimensional, energy-dependent) simulations. All LCMC results presented in the remainder of this thesis are generated using the modified LCMC-avg tally strategy.

4.4.2.3 2-D Quarter-Assembly Problem

In this section, we present LCMC results for the 2-D UO_2 quarter assembly problem introduced in Section 2.4.2 (problem #3). Problem #3 uses seven-group material cross sections from the C5G7 benchmark (see Appendix). The fuel region is surrounded by a quarter-assembly-thick reflector region.

Table 4.5: Simulation parameters, problem #3

Coll./Cyc. (M)	Inactive Cyc.	Active Cyc.	Coarse Grid (cm)	Histories/Cyc.
10	50	50	1.6065	1e6
12	50	50	1.071	1e6

LCMC simulation parameters for problem #3 can be found in Table 4.5. We use a larger number of inactive cycles for the LCMC cases than were used for the Wolters method case in Section 3.5.2.3. This ensures that the fission and scattering source distributions have adequate time to converge.

As listed in Table 4.5, we simulate problem #3 using two different values of the collision limit (M). These two cases use slightly different coarse grid sizes. The CMFD system for problem #3 is monoenergetic, and coarse-grid quantities are calculated using track-length tallies to reduce statistical noise. As noted in Section 4.4.1, the LCMC method is more sensitive to statistical noise than CMFD-MC. Thus, it is not feasible to run 2-D multigroup LCMC simulations with analog tallies on a personal computer.

Fast and thermal flux distributions for problem #3 are given in Figures 4.19 and 4.20 (for the $M = 10$ and $M = 12$ cases, respectively). These fluxes are tallied on a uniform 20×20 grid, which tends to "smear" fine spatial details around the guide tubes and fuel-reflector interface.

We observe excellent agreement between the $M = 10$ and $M = 12$ flux distributions, indicating that both simulations were run in a stable configuration.

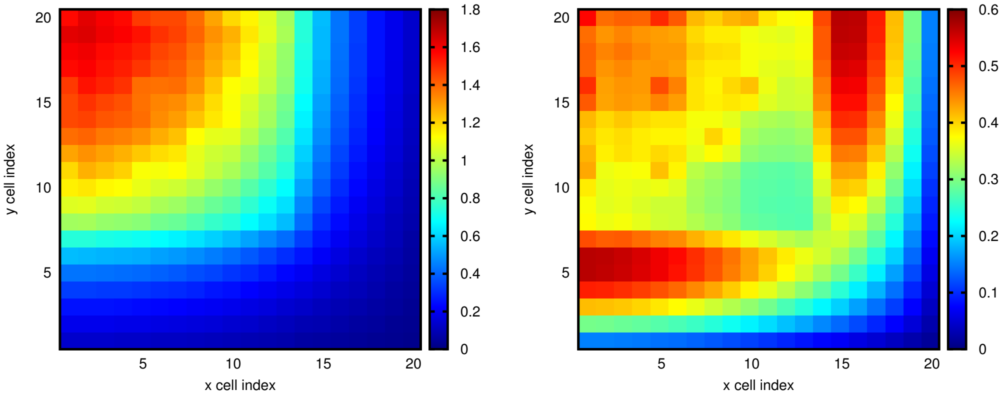

(a) Fast flux (C5G7 grp. 1-3)

(b) Thermal flux (C5G7 grp. 4-7)

Figure 4.19: LCMC fast and thermal flux distributions, M=10

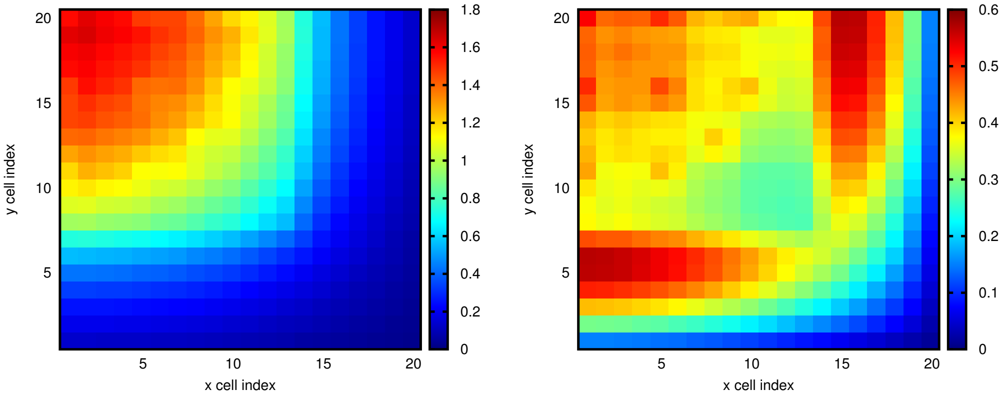

(a) Fast flux (C5G7 grp. 1-3)

(b) Thermal flux (C5G7 grp. 4-7)

Figure 4.20: LCMC fast and thermal flux distributions, M=12

Next, we compare quarter-pin power and quarter-pin power RSD distributions for the $M = 10$ and $M = 12$ cases. These plots are given in Figures 4.21 and 4.22, respectively.

Quarter-pin power distributions agree very closely between the $M = 10$ and $M = 12$ cases (this is expected, since the flux distributions also agree closely). The $M = 12$ quarter-pin power apparent RSD is slightly lower than the $M = 10$ apparent RSD, on average. Because more collisions per cycle are simulated in the $M = 12$ case than the $M = 10$ case, the $M = 12$ tallies contain a larger number of stochastic data points. As a result, statistical noise is less significant in the $M = 12$ case. From the Fourier analysis in Section 4.3, we also expect the $M = 12$ simulation to be more stable in the non-random limit.

Finally, we compare the use of analog and track-length tallies for the $M = 10$ case. Figure 4.23 shows LCMC k-eigenvalue estimates for the first 25 cycles. The red curve

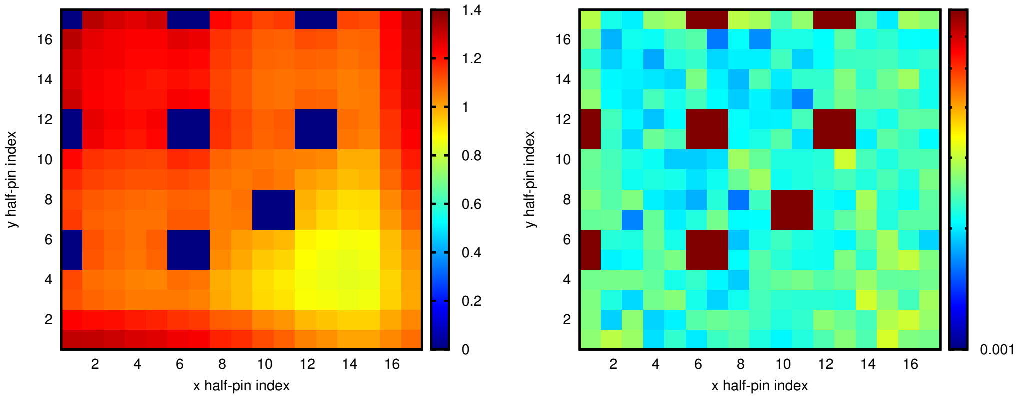

(a) Quarter-pin power (b) Apparent RSD

Figure 4.21: LCMC quarter-pin power and apparent RSD, M=10, problem #3

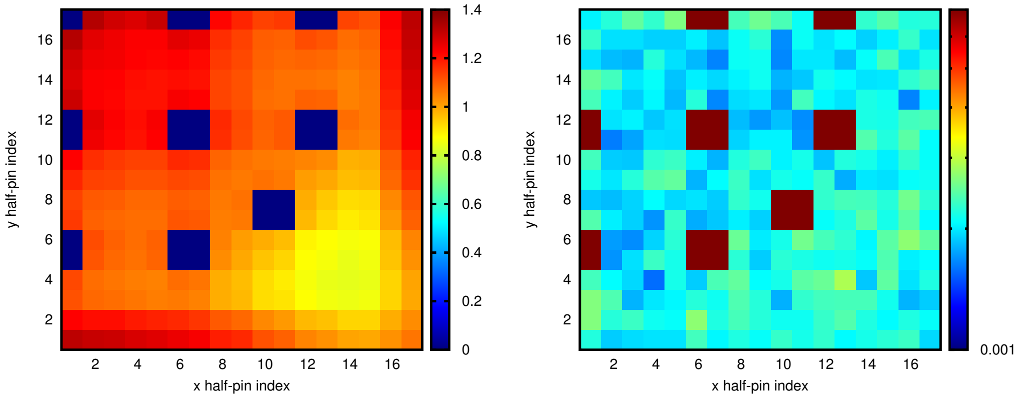

(a) Quarter-pin power (b) Apparent RSD

Figure 4.22: LCMC quarter-pin power and apparent RSD, M=12, problem #3

corresponds to the analog tally case, while the green curve corresponds to the track-length tally case.

In the track-length tally case, the LCMC *k*-eigenvalue estimate approaches a stationary value after ~ 6 cycles. By contrast, the LCMC *k*-eigenvalue estimate for the analog tally case exhibits large cycle-to-cycle oscillations. These oscillations appear to be dampened until cycle 10, when the *k*-eigenvalue estimate suddenly spikes. At cycle 14, code diagnostics terminate the analog tally simulation.

4.4.2.4 2-D Assembly Problem

In this section, we present results for the 2-D assembly problem introduced in Section 2.4.2.4 (problem #4). First, we list simulation parameters for problem #4 in Table 4.6.

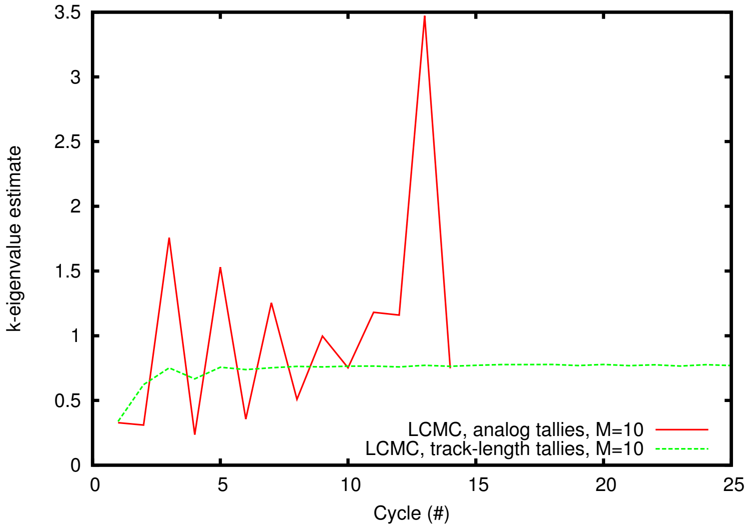

Figure 4.23: LCMC k-eigenvalue, analog vs. tracklength tallies, M=10, problem #3

While problem #3 was simulated using $M = 10$ and $M = 12$, the number of permitted collisions must be increased to $M = 12$ and $M = 14$ for problem #4 to achieve stability (see Figure 4.28). The number of particles per cycle is also increased to limit statistical error in the CMFD system.

Table 4.6: Simulation parameters, problem #4

Coll./Cyc. (M)	Inactive Cyc.	Active Cyc.	Coarse Grid (cm)	Histories/Cyc.
12	50	50	2.142	2e6
14	50	50	2.142	2e6

Fast and thermal flux distributions for the $M = 12$ and $M = 14$ LCMC simulations are shown in Figures 4.24 and 4.25.

Fast and thermal flux distributions agree reasonably well for the $M = 12$ and $M = 14$ cases, and also match closely with the standard MC problem #4 results shown in Chapter 2. The $M = 12$ simulation appears to slightly overpredict the thermal flux near the fuel-reflector interface, which may be an indication that this case is near the stability limit.

Next, Figures 4.26 and 4.27 show the pin power and pin power apparent RSD distributions for problem #4. We observe little difference between the $M = 12$ and $M = 14$ pin power distributions. On average, the pin power apparent RSD is slightly lower for the $M = 14$ case, because more collisions per cycle are simulated than in the $M = 12$ case.

Finally, we investigate an unstable case, where the collision limit (M) is set to 10. We use the same coarse grid and number of particles per cycle as the $M = 12$ and $M = 14$ cases

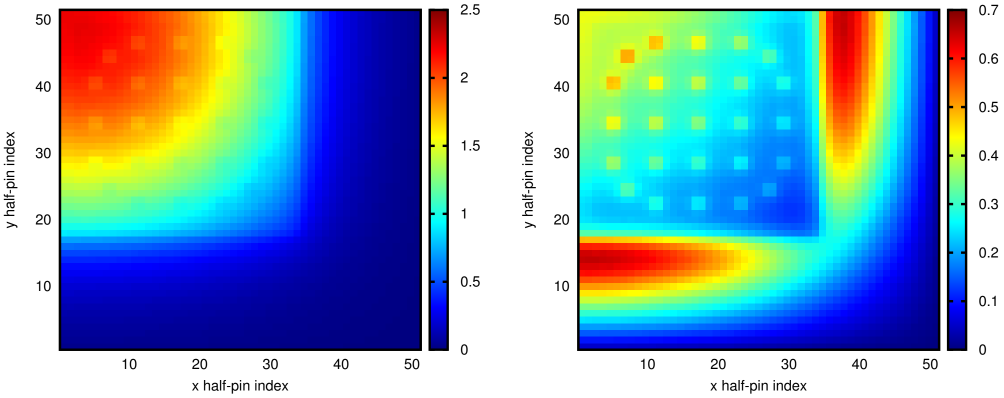

(a) Fast flux (C5G7 grp. 1-3)

(b) Thermal flux (C5G7 grp. 4-7)

Figure 4.24: LCMC fast and thermal flux distributions, M=12, problem #4

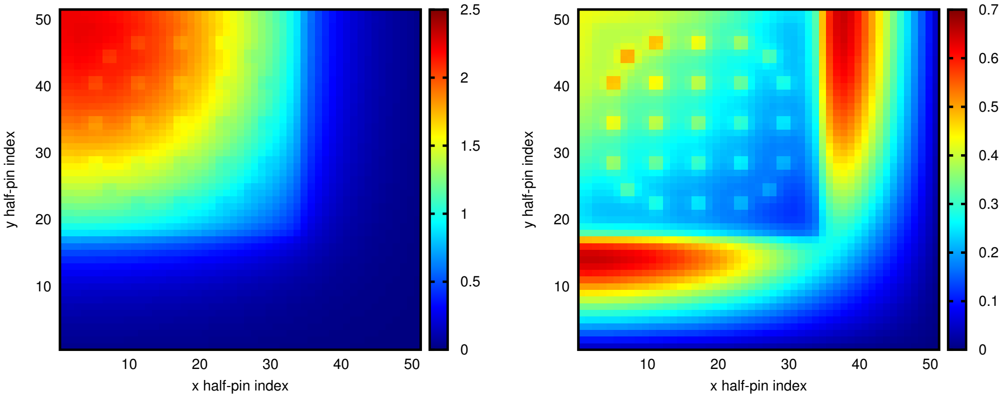

(a) Fast flux (C5G7 grp. 1-3)

(b) Thermal flux (C5G7 grp. 4-7)

Figure 4.25: LCMC fast and thermal flux distributions, M=14, problem #4

presented previously (see Table 4.6).

Figure 4.28 shows the CMFD *k*-eigenvalue estimate for the first 55 cycles of the $M = 10$ LCMC simulation. The standard MC *k*-eigenvalue estimate is also included for reference.

The $M = 10$ *k*-eigenvalue appears to be approaching a stationary value during the first ~ 15 cycles of the simulation. From this point onward, the eigenvalue estimate grows from cycle to cycle, slowly diverging from the standard MC curve. Around cycle 30, the growth rate accelerates, and the LCMC *k*-eigenvalue quickly becomes unphysical.

The behavior shown in Figure 4.28 is likely an example of the "flat-mode" LCMC instability first described in Section 4.4.1.2. This behavior occurs as a result of the energy group-collapse from seven-group LCMC to monoenergetic CMFD.

We do not observe analogous behavior in unstable CMFD-MC simulations, because the

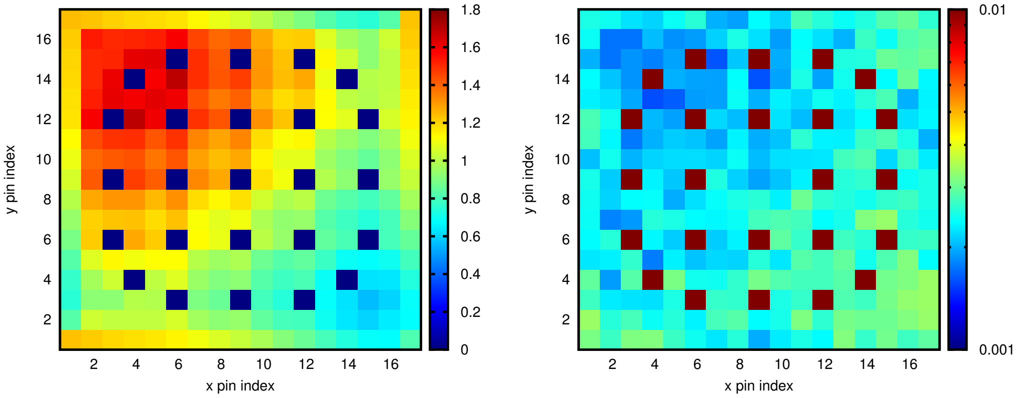

(a) Pin power (b) Apparent RSD

Figure 4.26: LCMC pin power and apparent RSD, M=12, problem #4

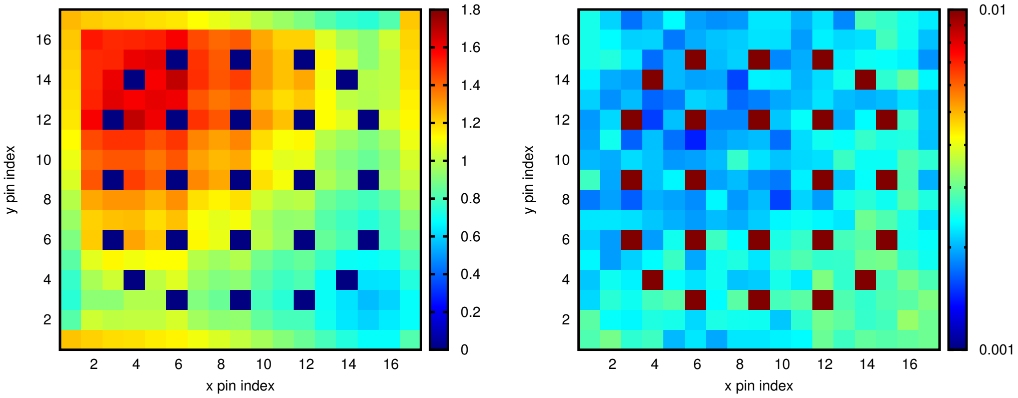

(a) Pin power (b) Apparent RSD

Figure 4.27: LCMC pin power and apparent RSD, M=14, problem #4

flat mode converges very quickly in the CMFD-MC method. Instead, unstable CMFD-MC simulations tend to exhibit large cycle-to-cycle flux oscillations.

Unfortunately, the presence of a flat mode instability is difficult to detect in practical LCMC simulations. As seen in Figure 4.28, the eigenvalue diverges very slowly for the first 30 cycles; in some problems, the eigenvalue may continue to diverge slowly throughout the simulation without reaching the rapid growth phase seen in the $M = 10$ case presented here. If this is the case, the solution will be inaccurate, but this inaccuracy will be difficult to detect without prior knowledge of the true k-eigenvalue of the system.

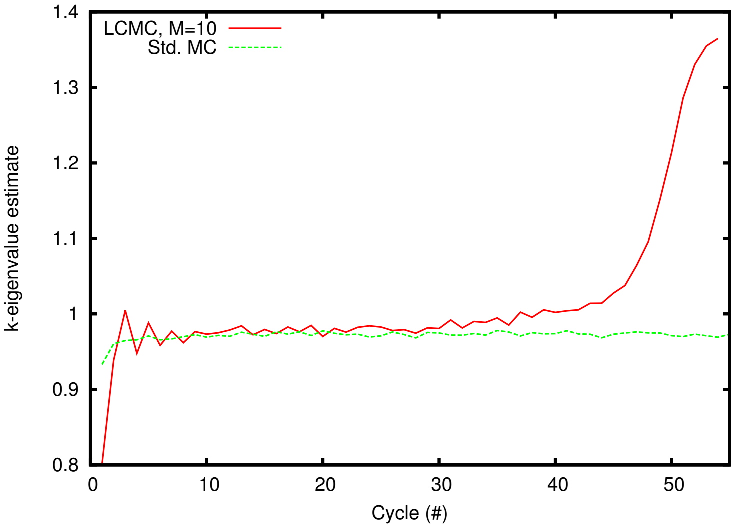

Figure 4.28: LCMC k-eigenvalue instability, M=10, problem #4

4.5 Summary

In this chapter, we introduced the LCMC method for reactor core *k*-eigenvalue calculations. The LCMC method limits Monte Carlo histories to a fixed maximum number of collisions per cycle, and was developed as part of this research to increase the active-cycle efficiency of MC reactor core simulations. The non-random LCMC equations were Fourier-analyzed to assess their stability. Predictions from the non-random Fourier analysis indicate that, for a given coarse grid size, the LCMC iteration scheme is generally less stable than the CMFD-MC method when the number of permitted collisions is small. Additionally, the existence of an energy group-collapse (from seven-group LCMC to two-group CMFD) introduces a spatially flat Fourier mode, which dominates problem convergence for small coarse grid sizes.

We then compared theoretical predictions from the Fourier analysis to numerical experiment. The Fourier analysis correctly reproduces qualitative trends in the LCMC spectral radius; that is, the LCMC spectral radius (i) decreases as the number of allowed collisions increases, (ii) increases as the coarse grid size increases, and (iii) does not depend on the scattering ratio (in the monoenergetic case). It was exceedingly difficult to obtain reasonable spectral radius estimates using direct LCMC simulations. As a result, we largely rely on estimates generated using a CMFD-S$_N$ "surrogate," which uses a discretized version of the non-random LCMC iteration equations.

Finally, we assessed the performance of the LCMC method for a set of benchmark problems. We are able to show that the LCMC method behaves roughly as the CLT predicts, provided the number of collisions per cycle is not too large. In addition, apparent RSD estimates closely resemble real RSD curves when the simulation is run in a stable configuration. We demonstrate that the size of the LCMC intermediate fission bank is roughly constant, once the *k*-eigenvalue is converged, and that it scales linearly with the number of histories per cycle.

CHAPTER 5

The Mixed Method

5.1 Introduction

In this chapter, we describe a new simulation procedure for MC reactor core *k*-eigenvalue calculations. This procedure combines the CMFD-MC and LCMC methods (described in Chapters 3 and 4, respectively) in a single simulation, in an effort to create a more optimal MC reactor core *k*-eigenvalue calculation. We refer to this new simulation procedure as the "mixed" method.

We motivate the mixed method in the following way. The MC *k*-eigenvalue simulation consists of two phases, which pose different computational challenges. During the inactive cycle phase, systematic error in the fission source shape is the dominant source of eigenfunction error. Thus, the purpose of the inactive-cycle iteration scheme is to converge the global fission source shape as quickly and efficiently as possible. As demonstrated in Chapter 3, the CMFD-MC method is capable of converging the fission source in a small number of cycles, provided the coarse grid is sufficiently fine. In addition, the Wolters correction factor method reduces cycle-to-cycle oscillation in the Shannon entropy during early inactive cycles. Thus, CMFD-MC with the Wolters histogram correction factor is well-suited for the inactive cycle phase of the *k*-eigenvalue calculation.

Once the global fission source shape has converged, the MC calculation enters the active cycle phase. During active cycles, statistical error originating from the random walk process dominates error in the eigenfunction. Hence, the iteration scheme used during active cycles should make efficient use of stochastic tally information. We believe the LCMC iteration is well-suited to this task; though LCMC requires a finer grid and a larger number of histories per cycle than CMFD-MC, each history can be simulated in significantly less time. In addition, CMFD feedback is applied to both the fission and scattering sources in the LCMC method, to mitigate cycle-to-cycle fluctuations in both sources.

5.2 The Mixed Method Iteration Strategy

In this section, we briefly outline the mixed iteration equations. Since the mixed method is a "hybrid" of the CMFD-MC and LCMC methods previously described in this thesis, we omit some details for brevity.

Before we proceed, we discuss the effect of transitioning from CMFD-MC to the LCMC method. In theory, we can transition from the CMFD-MC iteration to the LCMC iteration at the first active cycle. In practice, however, we must allow several cycles for the scattering source distribution to converge. Since histories are simulated from birth until death in the CMFD-MC method, histories for the first LCMC cycle will be sampled from a "converged" fission source bank, but without an accompanying scattering source bank.

The exact number of cycles required to converge the scattering source is problem-dependent, and in general is not known *a priori*. Therefore, an educated guess is made, based on user intuition and/or observation of test calculations (this is analogous to the way inactive cycles are set for standard MC k-eigenvalue simulations). In the mixed iteration equations below, we use N_{offset} to describe the number of cycles between the transition to LCMC and the beginning of active cycles.

To express the mixed iteration strategy mathematically, we begin with the monoenergetic CMFD-MC equations originally presented in Chapter 3. The CMFD-MC method is used for the first portion of inactive cycles ($1 \le \ell \le [N_{\text{inact}} - N_{\text{offset}}]$).

$$\mu \frac{d}{dx}\psi^{(\ell+1/2)}(x,\mu) + \Sigma_t(x)\psi^{(\ell+1/2)}(x,\mu) - \frac{\Sigma_s(x)}{2}\phi^{(\ell+1/2)}(x) = \frac{\nu\Sigma_f(x)}{2k^{(\ell)}}\phi^{(\ell)}(x)\,, \tag{5.1a}$$

$$0 \le x \le X\,,\ -1 \le \mu \le 1\,,\ 1 \le \ell \le [N_{\text{inact}} - N_{\text{offset}}]\,,$$

$$\psi^{(\ell+1/2)}(0,\mu) = \psi^{(\ell+1/2)}(X,\mu)\,,\ -1 \le \mu \le 1\,, \tag{5.1b}$$

$$\phi^{(\ell+1/2)}(x) = \int_{-1}^{1} \psi^{(\ell+1/2)}(x,\mu)d\mu\,. \tag{5.1c}$$

We impose a coarse grid with J cells of size Δ_j ($1 \le j \le J$). Once all MC histories have been run, cycle tallies are used to calculate the coarse grid flux-weighted cross sections ($\Sigma_{a,j}^{(\ell+1/2)}$, $\nu\Sigma_{f,j}^{(\ell+1/2)}$), diffusivities ($\tilde{D}_{j+1/2}^{(\ell+1/2)}$), and Fick's Law correction terms ($\hat{D}_{j+1/2}^{(\ell+1/2)}$). Expressions for these quantities are omitted here for brevity, but are the same as those defined in Eqs. (3.2c)-(3.2g). We then solve the following CMFD system:

$$\Phi_{1,j+1/2}^{(\ell+1)} - \Phi_{1,j-1/2}^{(\ell+1)} + \Sigma_{a,j}^{(\ell+1/2)}\Phi_j^{(\ell+1)}\Delta_j = \frac{\nu\Sigma_{f,j}^{(\ell+1/2)}}{k^{(\ell+1)}}\Phi_j^{(\ell+1)}\Delta_j\,,\ 1 \le j \le J\,, \tag{5.2a}$$

$$\Phi_{1,j+1/2}^{(\ell+1)} = \tilde{D}_{j+1/2}^{(\ell+1/2)}(\Phi_{j+1}^{(\ell+1)} - \Phi_j^{(\ell+1)}) + \hat{D}_{j+1/2}^{(\ell+1/2)}(\Phi_{j+1}^{(\ell+1)} + \Phi_j^{(\ell+1)})\,, \tag{5.2b}$$

$$\Phi_{1,1/2}^{(\ell+1)} = \Phi_{1,J+1/2}^{(\ell+1)} \,. \tag{5.2c}$$

The updated coarse grid fluxes are used to scale the fine grid fission source for the next cycle:

$$\phi^{(\ell+1)}(x) = \phi^{(\ell+1/2)}(x)\left[\frac{\Phi_j^{(\ell+1)}}{\Phi_j^{(\ell+1/2)}}\right], \; x_{j-1/2} \le x \le x_{j+1/2} \,, \; 1 \le j \le J \,. \tag{5.2d}$$

The equations described in Eqs. (5.1)–(5.2) are used to converge the fission source during inactive cycles.

During the first LCMC cycle, the total source weight is increased by an integer multiplier, and the standard MC iteration [Eqs. (5.1a)–(5.1c)] is replaced by the LCMC iteration described in Eqs. (5.3a)–(5.3e). The initial fission source guess comes from the last CMFD-MC cycle, while the initial scattering source guess is set to zero. Here, ℓ is the cycle iteration index, m is the collision index, M is the maximum number of collisions per cycle, and N_{cyc} is the total number of cycles:

$$\begin{cases} \Sigma_s(x)\phi^{(\ell+1/2,0)}(x) = 0 \,, & \ell = [N_{\text{inact}} - N_{\text{offset}} + 1] \,, \\ \Sigma_s(x)\phi^{(\ell+1/2,0)}(x) = \Sigma_s(x)\phi^{(\ell)}(x) \,, & \text{otherwise} \,, \end{cases} \tag{5.3a}$$

$$\nu\Sigma_f(x)\phi^{(\ell+1/2,0)}(x) = \nu\Sigma_f(x)\phi^{(\ell)}(x) \,, \tag{5.3b}$$

$$\mu\frac{d}{dx}\psi^{(\ell+1/2,m)}(x,\mu) + \Sigma_t(x)\psi^{(\ell+1/2,m)}(x,\mu) = \frac{1}{2}\left(\Sigma_s(x) + \frac{\nu\Sigma_f(x)}{k^{(\ell)}}\right)\phi^{(\ell+1/2,m-1)}(x) \,, \tag{5.3c}$$

$$0 \le x \le X \,, \; -1 \le \mu \le 1 \,, \; 1 \le m \le M \,, \; [N_{\text{inact}} - N_{\text{offset}}] < \ell \le N_{\text{cyc}} \,,$$

$$\psi^{(\ell+1/2,m)}(0,\mu) = \psi^{(\ell+1/2,m)}(X,\mu) \,, \; -1 \le \mu \le 1 \,, \tag{5.3d}$$

$$\phi^{(\ell+1/2,m)}(x) = \int_{-1}^{1} \psi^{(\ell+1/2,m)}(x,\mu)d\mu \,. \tag{5.3e}$$

As described in Chapter 4, LCMC particles that survive M scattering events are stored in a collision bank for the next cycle. Fissions occurring when $m < M$ are stored in an "intermediate" bank and simulated during the cycle, while fissions occurring when $m = M$ are banked for the following cycle. The low-order calculation [Eqs. (5.2] is unchanged in the LCMC method. The updated coarse grid solution is used to scale both the MC fission and scattering source banks for the following cycle:

$$\nu\Sigma_f(x)\phi^{(\ell+1)}(x) = \nu\Sigma_f(x)\phi^{(\ell+1/2,M)}(x)\left[\frac{\Phi_j^{(\ell+1)}}{\Phi_j^{(\ell+1/2)}}\right], \tag{5.4}$$

$$\Sigma_s(x)\phi^{(\ell+1)}(x) = \Sigma_s(x)\phi^{(\ell+1/2,M)}(x)\left[\frac{\Phi_j^{(\ell+1)}}{\Phi_j^{(\ell+1/2)}}\right], \qquad x_{j-1/2} \le x \le x_{j+1/2}\,,\ \ 1 \le j \le J\,. \tag{5.5}$$

This completes the description of the mixed method. Next, we discuss the stability considerations that must be taken into account when choosing parameters for a mixed method simulation.

5.3 Stability Considerations

Because the CMFD-MC and LCMC iteration schemes are both used in the mixed method simulation strategy, it is prudent to compare spectral radius curves between the two methods. This comparison can be found in Fig. 5.1 for the monoenergetic $c = 0.9$ CMFD-MC case. For clarity, we include only the theoretical spectral radius curves.

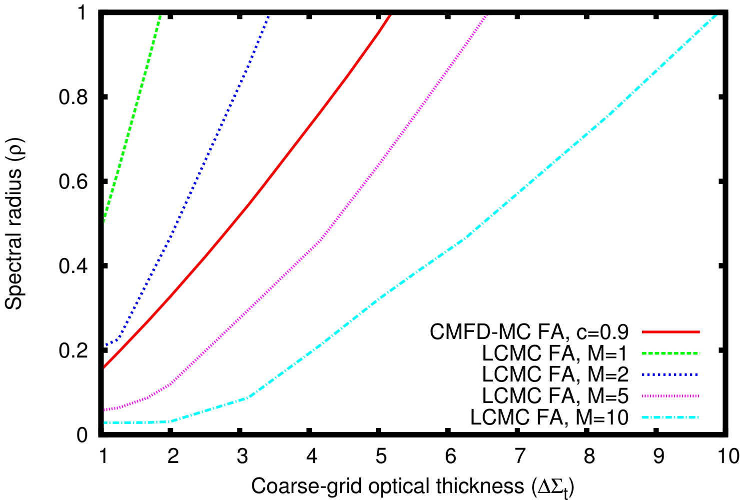

Figure 5.1: Spectral radius comparison, LCMC vs. CMFD-MC ($c = 0.9$ case)

The CMFD-MC spectral radius curve for $c = 0.9$ falls between the LCMC $M = 2$ and $M = 5$ curves. This can be interpreted in the following way: if the LCMC portion of a monoenergetic mixed method simulation is run with $M = 1$ or 2, the spectral radius of the LCMC phase (the active cycles) will be higher than the spectral radius of the CMFD-MC phase (the inactive cycles), regardless of the coarse grid optical thickness. This can lead to a scenario where the inactive cycles are stable, but the active cycles are not. For example, if a vertical line is drawn through $\Delta\Sigma_t = 4$ in Fig. 5.1, this line will intersect the CMFD-MC curve at $\rho \sim 0.75$. However, it will intersect the LCMC curve at $\rho > 1$, which is beyond the stability limit.

If, however, the LCMC (active cycle) portion of the simulation is run with a larger number of allowed collisions ($M = 5$ or 10, for example), the spectral radius of the LCMC iteration strategy will always be lower than the CMFD-MC spectral radius. That is, the LCMC spectral radius curves for $M = 5$ and $M = 10$ lie entirely to the right of the CMFD-MC curve. Simulations run in this configuration are unlikely to destabilize during active cycles.

Since the monoenergetic CMFD-MC spectral radius depends on the scattering ratio (while the LCMC spectral radius does not), the aforementioned relationships only hold for the $c = 0.9$ case. For some values of the scattering ratio, the CMFD-MC spectral radius curve will intersect one or more of the LCMC curves at a certain coarse grid size. In these cases, the LCMC iteration will be less stable than the CMFD-MC iteration for some range of coarse grid sizes, and more stable than the CMFD-MC iteration otherwise.

We also compare spectral radius estimates for the seven-group transport/two-group CMFD (7g/2g) iteration strategies, calculated using material cross sections for C5G7 UO_2 fuel. This comparison can be found in Figure 5.2. Since we have not Fourier-analyzed the 7g/2g iteration scheme, these spectral radii were estimated numerically using the multigroup surrogate CMFD-S_N codes described in Sections 3.5.1 and 4.4.1.

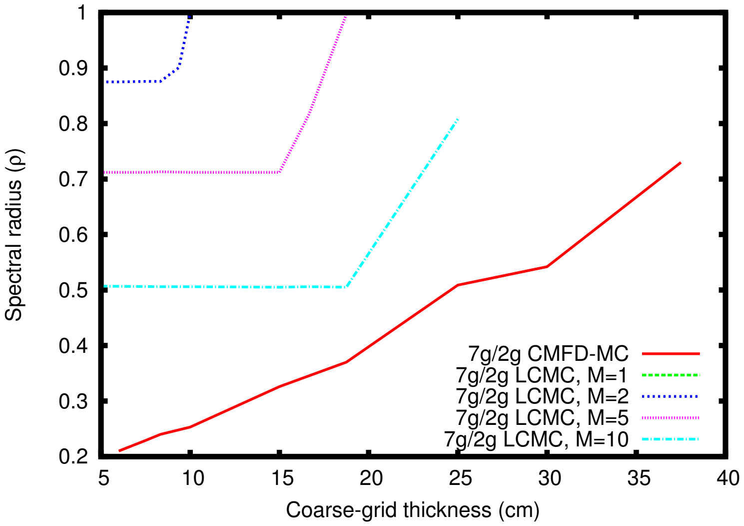

Figure 5.2: Spectral radius comparison, LCMC vs. CMFD-MC (UO_2 fuel, 7g/2g iteration)

Unlike the monoenergetic curves shown in Figure 5.1, the 7g/2g LCMC spectral radius for UO_2 fuel is higher than the corresponding CMFD-MC spectral radius for all $M \leq 10$. Thus, care must be taken to choose simulation parameters that ensure the mixed simulation remains stable after the transition from CMFD-MC to LCMC. As previously described, performing a group collapse from seven-group LCMC to two-group CMFD introduces a spatially-flat Fourier mode. This "flat mode" is visible in Figure 5.2 as a plateau region, where the spectral radius of the LCMC iteration is independent of the coarse grid size.

As a result of the 7g/2g LCMC flat mode, it is no longer certain that refining the coarse grid will reduce the spectral radius of the LCMC iteration (as was the case for monoenergetic simulations). Instead, the only reliable way to decrease the 7g/2g LCMC spectral radius is to increase the number of collisions per cycle, M (we believe this to be the case for any LCMC simulation which performs an energy group-collapse). Unfortunately, this diminishes the efficiency benefit of the LCMC iteration strategy.

5.4 Numerical Results

In this section, we present results for the mixed method developed as part of this research. In addition, we compare numerical results for the mixed method to other methods described in this thesis, including: (i) the LJLS variant of CMFD-MC (implemented in OpenMC, and considered the current "state of the art"), (ii) the Wolters variant of CMFD-MC (with histogram spatial weighting), and (iii) the LCMC method, and (iv) the standard MC method.

5.4.1 Benchmark Problem Performance

5.4.1.1 Homogeneous Problem

5.4.1.1.1 Mixed Method Results

The mixed method is first tested on problem #1, the homogeneous fissile slab introduced in Section 2.4.2.1. Parameters for problem #1 simulations are shown in Table 5.1. We consider two values of the collision limit, $M = 2$ and $M = 5$.

Table 5.1: Simulation parameters, problem #1

Case	Inactive Cyc.	Active Cyc.	Histories/Cyc.	Fine Grid (cm)	Coarse Grid (cm)
A	30	50	1e6	0.5	0.5
B	30	100	1e6	0.5	0.5
C	30	200	1e6	0.5	0.5

In Figure 5.3, we compare eigenfunction estimates for the $M = 2$ and $M = 5$ mixed method simulations to the S_N benchmark solution. Results from the mixed method simulations closely match the S_N benchmark.

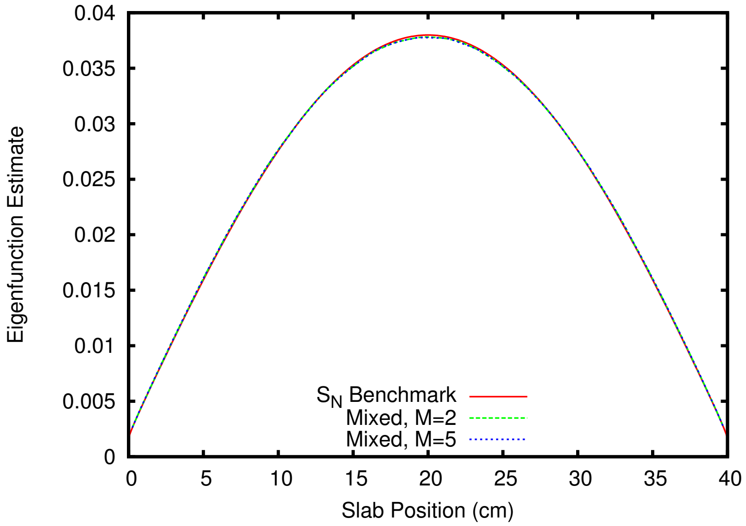

Figure 5.3: Mixed method eigenfunction estimate, problem #1, case A

Next, apparent RSD ratios for case A/case B and case B/case C are plotted for both values of the collision limit. These ratios are shown in Figure 5.4. As described in previous chapters, the CLT predicts an apparent RSD ratio of roughly 1.41 when the number of active cycles is doubled. On average, the RSD ratios in Figure 5.4 are very close to the CLT-predicted value.

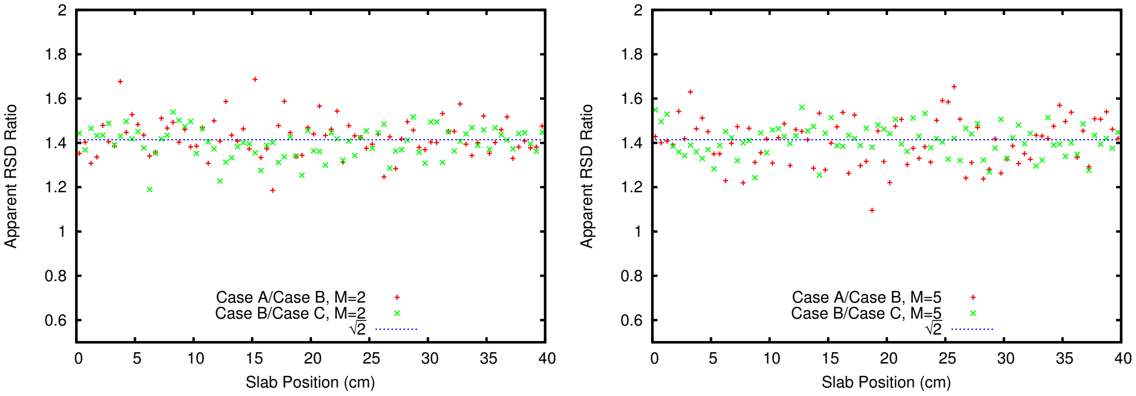

(a) M=2

(b) M=5

Figure 5.4: Mixed method apparent RSD ratios, problem #1

In Figure 5.5, we compare real-to-apparent RSD ratios for problem #1, with a line at unity for reference. Both the $M = 2$ and $M = 5$ real-to-apparent RSD ratios are close to unity, when averaged across the slab. This indicates that the apparent RSD for the mixed method provides a reliable estimate of the real RSD for the cases presented here. This

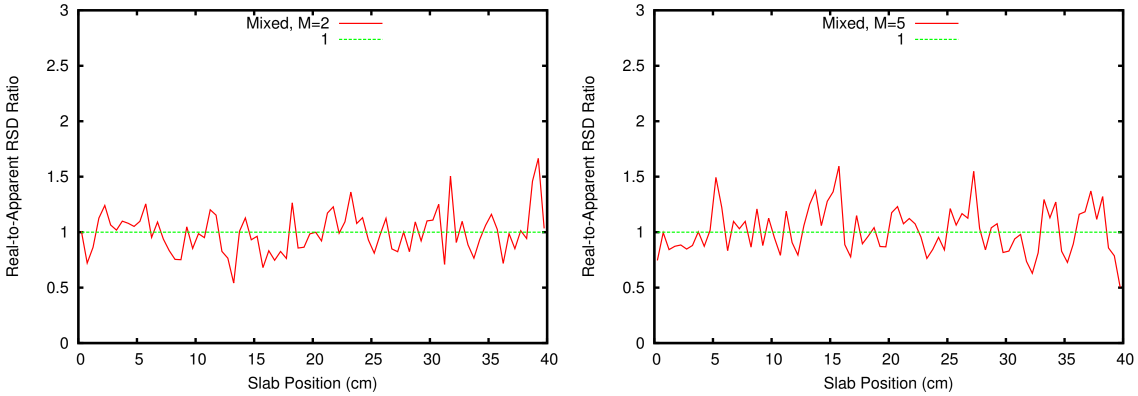

(a) M=2

(b) M=5

Figure 5.5: Mixed method real-to-apparent RSD ratios, problem #1

result should extend to any mixed simulation, provided the simulation is run in a stable configuration.

5.4.1.1.2 Comparison to Other Methods

Here, we compare results for problem #1 (the homogeneous fissile slab) across all methods considered in this thesis. For succinctness, we simply summarize our findings, and do not include the figures presented in previous chapters.

First, we discuss the behavior of the eigenfunction apparent RSD when the number of active cycles is increased. The CLT predicts that the apparent RSD of the eigenfunction should decrease by a factor of $\sim \sqrt{2}$ when the number of active cycles is doubled.

This prediction was tested numerically for each of the methods considered in this thesis. The apparent RSD decreases at roughly the expected rate for the CMFD-MC, Wolters, LCMC, and mixed methods. The standard MC eigenfunction RSD decreases more slowly than the CLT predicts, while the LJLS RSD decreases slightly more quickly than the CLT predicts. These deviations may be a result of inter-cycle correlation in the standard MC and LJLS methods.

Problem #1 was also used to investigate real-to-apparent RSD ratios for each method. A spatially-averaged ratio of unity indicates good agreement between the apparent RSD estimate and the real eigenfunction RSD. A ratio greater than unity means that the apparent RSD underpredicts the real RSD, while a ratio less than unity means that the apparent RSD overpredicts the real RSD.

The standard MC real-to-apparent RSD ratio for the homogeneous problem is roughly 4.5, indicating significant underprediction of the real eigenfunction RSD. The LJLS real-to-apparent RSD ratio is also larger than unity, but appears to decrease slightly as the coarse grid is refined.

Real-to-apparent RSD ratios for the CMFD-MC and Wolters methods are very close to unity when the coarse grid is sufficiently fine; however, both methods appear to overpredict the real eigenfunction RSD when the simulation is near the stability limit. As discussed in Chapter 3, we believe this is a result of oscillation in the low-order solution.

The average real-to-apparent RSD ratio for the LCMC and mixed methods is very close to unity for the case presented in this thesis. However, these methods may also overpredict the solution RSD in simulations near the stability limit.

5.4.1.2 1-D Core Problem

5.4.1.2.1 Mixed Method Results

We now present mixed method results for problem #2 (the heterogeneous 1-D reactor core). Problem #2 is simulated using two values of the collision limit, $M = 2$ and $M = 5$. Parameters for these simulations are listed in Table 5.5. Both the $M = 2$ and $M = 5$ cases transition from CMFD-MC to LCMC at cycle 25, which allows the scattering source five cycles to converge before the onset of active cycles. The source bank size is increased by a factor of five when the simulation transitions from CMFD-MC to LCMC (see column “LCMC Mult.” in Table 5.5).

Table 5.2: Simulation parameters, problem #2

Coll./Cyc. (M)	Inact. Cyc.	Act. Cyc.	Coarse Grid (cm)	Hist./Cyc.	LCMC Mult.
2	30	100	1.275	1e5	5
5	30	100	1.275	1e5	5

First, we compare mixed method eigenfunction estimates to the S_N benchmark solution in Figure 5.6. The global solution shape agrees relatively well, though we observe slight discrepancies near the edges of the core region. These are likely a result of truncation error in the S_N benchmark.

Figure 5.7 shows a close-up view of the problem #2 eigenfunction estimates. The $M = 2$ and $M = 5$ eigenfunctions agree relatively well across the problem domain. We again note the slight discrepancy between the mixed method and solution and the S_N benchmark, which we believe is a result of error in the benchmark solution.

In Figures 5.8a and 5.8b, we plot eigenfunction estimates averaged over cycles 50-100 and 100-150 for $M = 2$ and $M = 5$, respectively. 50-cycle eigenfunction estimates for

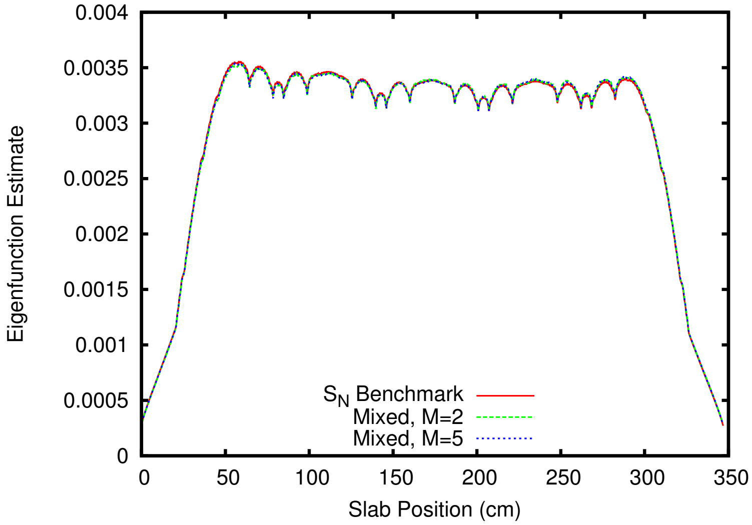

Figure 5.6: Mixed method eigenfunction estimates, problem #2

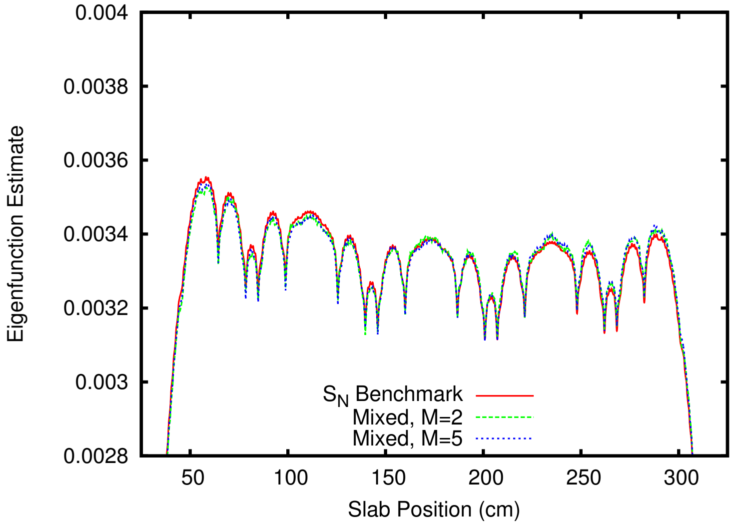

Figure 5.7: Mixed method close-up of eigenfunction estimates, problem #2

the $M = 5$ case show good agreement with the benchmark solution, while estimates for the $M = 2$ case exhibit significantly more error. This probably indicates that the $M = 2$ simulation is closer to the stability limit than the $M = 5$ simulation, which agrees with the predictions of the LCMC Fourier analysis.

We also consider scattering and fission source Shannon entropy for the mixed method. These plots are shown in Figure 5.9.

The fission source Shannon entropy is the same for both cases from cycle 1 through cycle 25, because both simulations employ the Wolters method to converge the fission source.

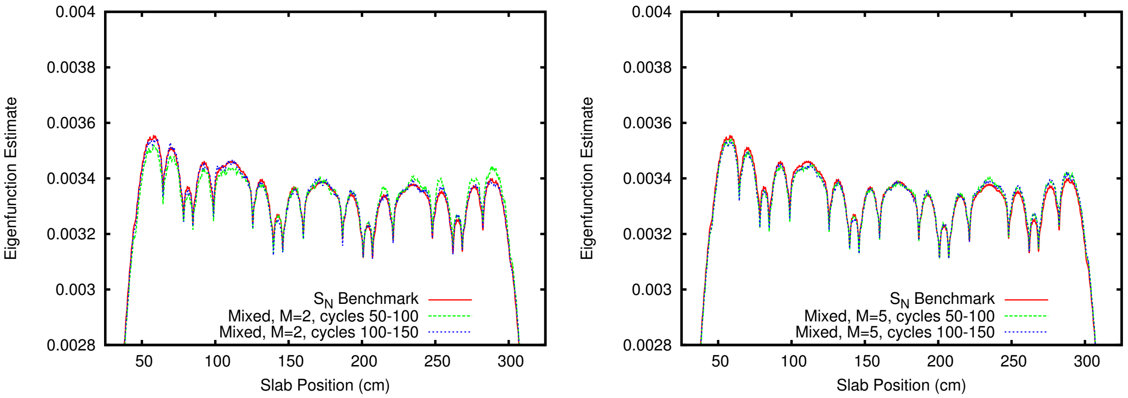

(a) M=2 (b) M=5

Figure 5.8: Mixed method close-up of 50-cycle eigenfunction estimates, problem #2

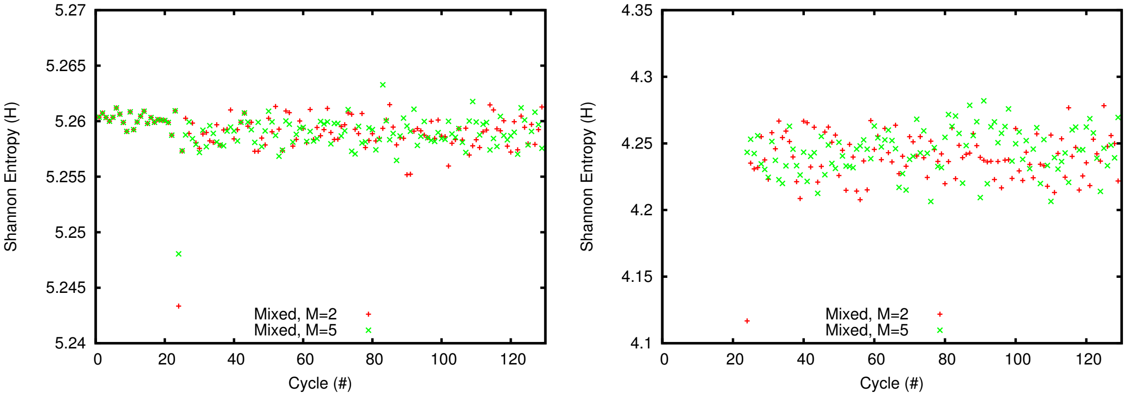

(a) Fission source (b) Scattering source

Figure 5.9: Mixed method shannon entropy vs. cycle number, problem #2

In cycles 26 and 27, we observe sudden fluctuation in the fission source Shannon entropy. This fluctuation is a result of the transition from CMFD-MC to LCMC, and quickly dies away as the scattering source distribution converges. From cycle 27 onward, the fission source Shannon entropy is roughly stationary. We note that the average Shannon entropy decreases very slightly after the transition from CMFD-MC to LCMC; we believe this occurs because fissile regions are more likely to bank zero fission sites in the LCMC method. We purposely exclude these zero-source regions from the Shannon entropy calculation because the expression involves a natural logarithm (see Eq. (2.21)), and the natural logarithm of zero is undefined. As a result, the average Shannon entropy drops slightly.

The scattering source Shannon entropy is significantly noisier than the fission source Shannon entropy, because the scattering source distribution is a more complicated function of phase-space than the fission source distribution. The $M = 2$ scattering source Shannon entropy takes a few cycles to converge, while the $M = 5$ scattering source Shannon entropy appears largely stationary after only one cycle.

Finally, we compare the apparent RSD distibution for problem #2 to the relative error with respect to the S_N benchmark. As was the case for the LCMC method, error in the mixed method eigenfunction is comparable to (or smaller than) error in the S_N benchmark. Thus, the relative error calculation is not valid for the mixed method. However, Figure 5.10a shows that the apparent RSD of the eigenfunction estimate decreases when the collision limit is increased from $M = 2$ to $M = 5$. This is consistent with previous findings for the LCMC method (see Section 4.4.2.2.2).

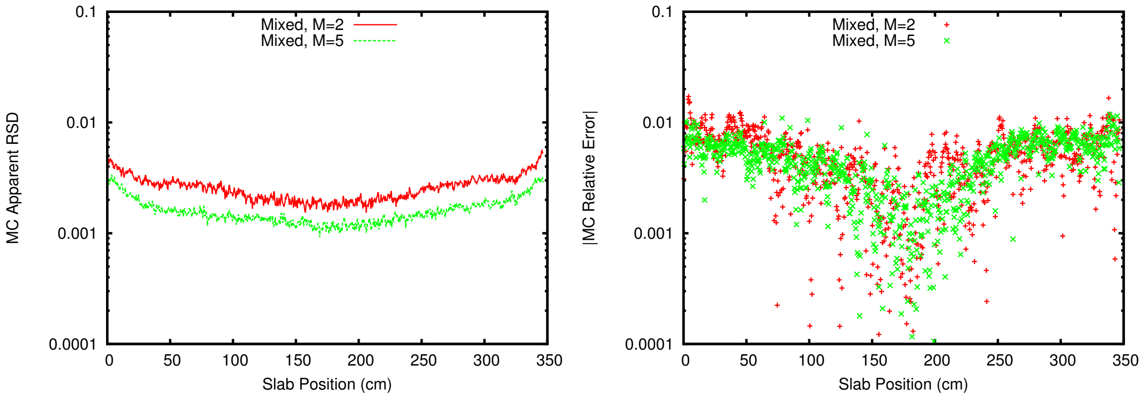

(a) Apparent RSD

(b) Relative error from benchmark

Figure 5.10: Mixed method eigenfunction error curves, problem #2

5.4.1.2.2 Comparison to Other Methods

Next, we compare the mixed method simulation of problem #2 to the methods introduced earlier in this thesis. For problem #2, the LJLS method employs assembly coarse grid CMFD feedback, while the Wolters method uses a quarter-assembly CMFD grid. Finally, the LCMC and mixed method cases are run with pin-cell CMFD feedback. These coarse grid sizes are chosen to ensure stability, and are consistent with our understanding of the stability characteristics of each method.

Table 5.3 summarizes simulation parameters for each of the cases. We present only the $M = 5$ collision limit case for the LCMC and mixed methods. In Table 5.3, the "LCMC Mult." column refers to the integer multiplier that is used to scale the mixed method source bank when the simulation transitions from the Wolters method to LCMC. As in Section 5.4.1.2.1, this transition occurs at cycle 25 (this allows 5 cycles for the scattering source to converge before active cycles begin).

Table 5.3: Comparison simulation parameters, problem #2

Method	Hist./cyc.	Coarse Grid (cm)	LCMC Mult.	Inact. cyc.	Active cyc.
Std. MC	1e5	–	–	150	100
LJLS	1e5	20.4	–	25	100
Wolters	1e5	5.1	–	25	100
LCMC, M=5	5e5	1.275	–	50	100
Mixed, M=5	1e5	1.275	5	30	100

In Table 5.4, we show timing data for the five methods compared here. The first data column shows the approximate source convergence time, while the second shows the total time spent simulating active cycles.

Table 5.4: Comparison simulation timing, problem #2

Method	Src. conv. time (s)	Act. cyc time (s)
Std. MC	155	105
LJLS	37	152
Wolters	17	170
LCMC, M=5	36	237
Mixed, M=5	22	241

The source convergence time is not a well-defined quantity, due to statistical noise in estimates of the Shannon entropy. As a result, we can only provide a rough estimate of this number, based on visual inspection of Shannon entropy curves.

In Figure 5.11, we compare fission source Shannon entropy for the first 50 cycles of each simulation. The Wolters method appears to reach a stationary Shannon entropy very

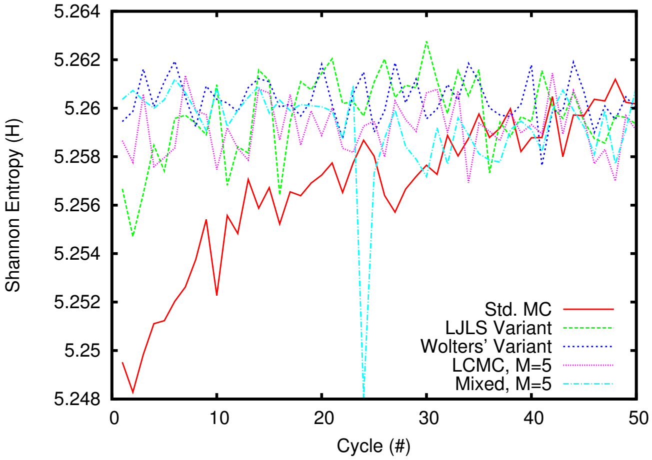

Figure 5.11: Close-up of Shannon entropy, problem #2

rapidly, while the LCMC method appears stationary after roughly 15 cycles. The LJLS Shannon entropy exhibits periodic fluctuations as a result of the multi-set strategy, but appears to approach fission source convergence after roughly 25 cycles. The standard MC Shannon entropy continues to fluctuate throughout the simulation, but the fluctuations become smaller in magnitude around cycle 150 (see Section 2.4.2.2). Finally, the mixed method Shannon entropy initially stabilizes after only a few cycles, but briefly fluctuates following the transition to LCMC at cycle 25. To estimate the source convergence time (shown in Table 5.4), we multiply the approximate number of cycles required to converge the fission source by the average simulation time per inactive cycle. A minimum value of 10 cycles is used for cases that appear to converge the fission source very quickly.

Since eigenfunction solutions have already been presented for all of the methods listed in Table 5.3, we omit these figures for brevity.

Next, we compare the eigenfunction Figure of Merit (FOM) for the five methods listed in Table 5.3. The FOM is a simple way to compare the active-cycle performance of different stochastic methods, and is calculated using the following expression:

$$FOM_k = \frac{1}{\sigma_{r,k}^2 T} \tag{5.6}$$

In Eq. (5.6), k is the fine-grid cell index, T is the active-cycle computation time, and $\sigma_{r,k}$ is the apparent RSD estimate for fine cell k. The FOM calculation yields a spatially-dependent distribution that can be used as a rough measure of the efficiency of the method.

This quantity should be relatively insensitive to the number of histories simulated, because the simulation time is directly proportional to the number of histories, while the quantity $\sigma^2_{r,k}$ is inversely proportional to the number of histories. Hence, their product should be roughly constant.

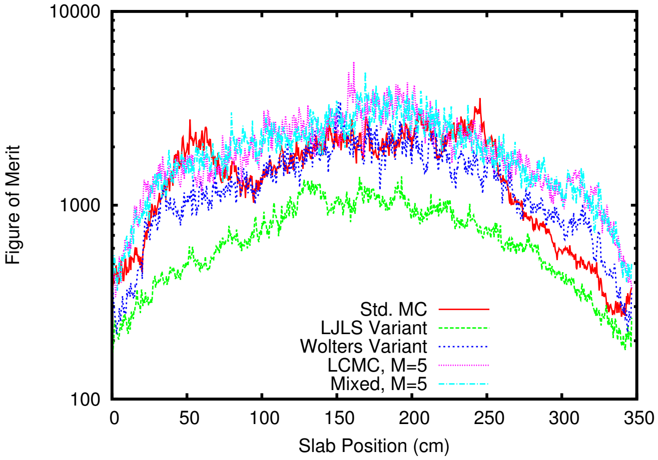

Figure 5.12: FOM comparison, problem #2

Figure 5.12 shows that the LJLS FOM is the lowest of the five cases presented here. The standard MC FOM appears comparable in magnitude to the Wolters, LCMC, and mixed method curves, but inspection of Shannon entropy verifies that the standard MC solution is not fully converged. Both the standard and LJLS apparent RSDs have been shown to significantly underpredict real error in the eigenfunction for high dominance-ratio problems; thus, we expect the "real" FOMs (those calculated using the real RSD) for these methods to be much lower than the curves shown in Figure 5.12.

The Wolters, LCMC, and mixed methods perform more comparably, with the LCMC and mixed methods producing slightly higher FOMs than the Wolters method. On average, FOMs for the LCMC and mixed methods are a factor of ~ 1.5 higher than the Wolters method FOM. The FCPI FOM distributions also appear to have slightly less high-frequency noise than the Wolters method, though this is difficult to see in Fig. 5.12.

Previously in this chapter, we described the motivation behind development of the mixed method for reactor core *k*-eigenvalue simulations. We believe that the two phases of the MC reactor core calculation (inactive and active cycles) can be treated using two separate iteration schemes, and that this "mixed" approach may be more efficient than the using a single iteration scheme for the entire calculation.

The problem #2 presented in this section support this theory. Though the overall benefit is modest, the mixed method (i) converges the fission source more efficiently than pure

LCMC, standard MC, or LJLS (and comparably to the Wolters method), and (ii) produces a FOM higher than the Wolters method, LJLS, and standard MC (and comparable to pure LCMC).

Next, we present mixed method results for the 2-D UO_2 quarter assembly problem (problem #3). We then compare the performance of the mixed method for problem #3 to other methods considered in this thesis.

5.4.1.3 2-D Quarter-Assembly Problem

5.4.1.3.1 Mixed Method Results

Here, we provide numerical results for mixed method simulations of problem #3, originally presented in Section 2.4.2.3. Problem #3 is a UO_2 quarter-assembly, surrounded by a reflector region one quarter-assembly in width. North and west boundaries are reflective, while south and east boundaries are vacuum. Mixed method simulations of problem #3 use monoenergetic CMFD feedback, and coarse-grid quantities are calculated using track-length tallies.

Table 5.5: Simulation parameters, problem #3

Coll./Cyc. (M)	Inact. Cyc.	Act. Cyc.	Coarse Grid (cm)	Hist./Cyc.	LCMC Mult.
10	35	50	1.6065	2e5	5
12	35	50	1.071	2e5	5

Table 5.5 lists simulation parameters for problem #3. Collision limits of $M = 10$ and $M = 12$ are used in our mixed method simulations of problem #3. We could not simulate problem #3 with small values of M on a personal computer, because the number of histories per cycle required for stability is too high.

In both simulations, the source bank is multiplied by a factor of five when the iteration scheme transitions from the Wolters method to LCMC. Ten cycles are performed between the iteration scheme transition and the onset of active cycles.

Figures 5.13 and 5.14 show the fast and thermal flux distributions for $M = 10$ and $M = 12$, respectively. Flux shapes for the two values of M agree closely, and also agree well with the problem #3 flux distributions presented in previous chapters.

In Figures 5.15 and 5.16, we plot quarter-pin power and quarter-pin power apparent RSD distributions for both values of the collision limit. As we expect, quarter-pin power distributions agree closely between the two cases. On average, the apparent RSD of the $M = 12$ case is slightly lower than the $M = 10$ case.

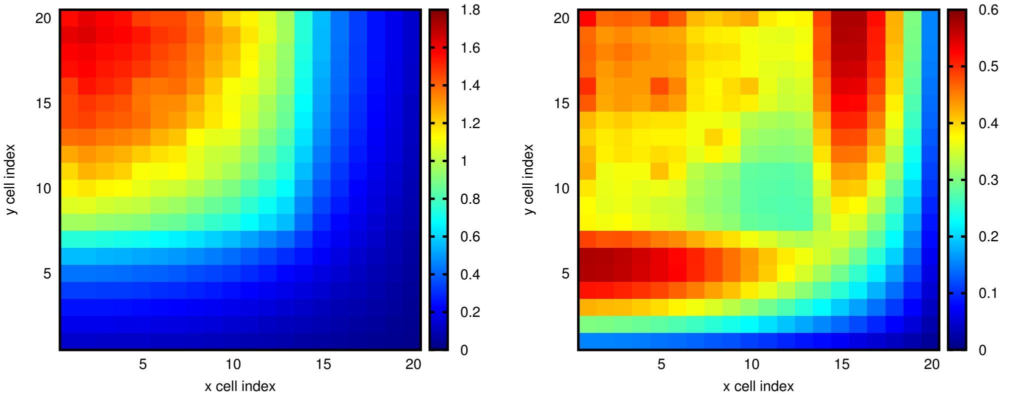

(a) Fast flux (C5G7 grp. 1-3)

(b) Thermal flux (C5G7 grp. 4-7)

Figure 5.13: Mixed method fast and thermal flux distributions, M=10, problem #3

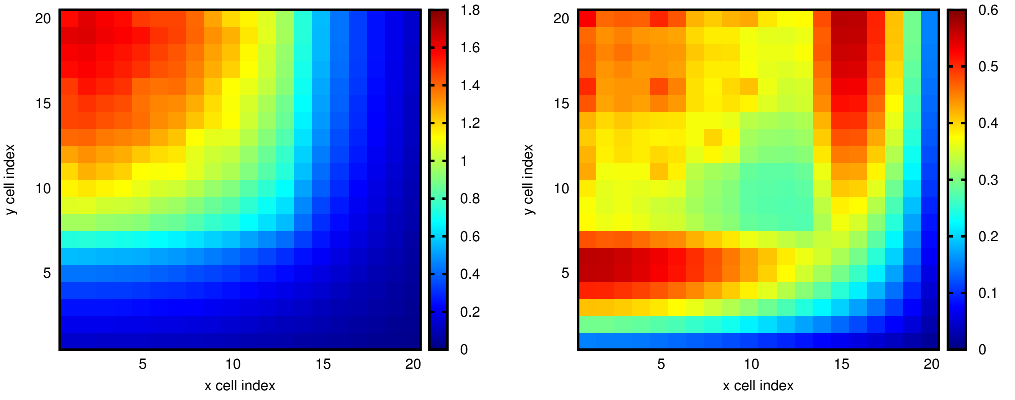

(a) Fast flux (C5G7 grp. 1-3)

(b) Thermal flux (C5G7 grp. 4-7)

Figure 5.14: Mixed method fast and thermal flux distributions, M=12, problem #3

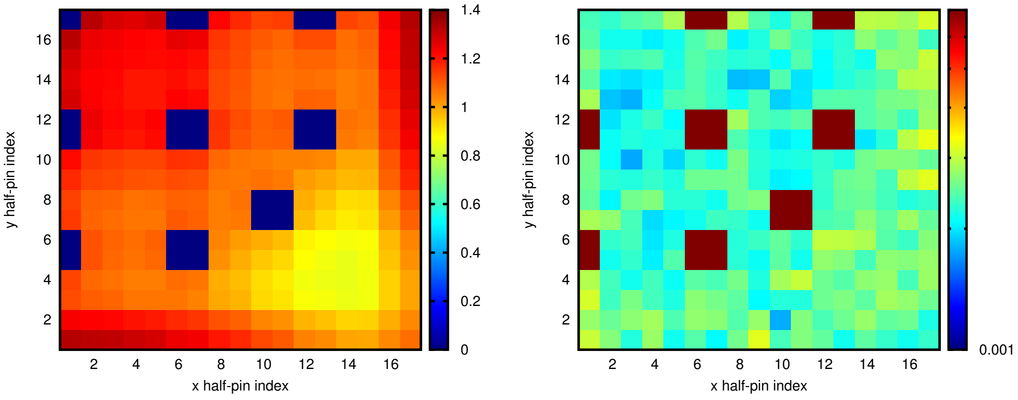

(a) Quarter-pin power

(b) Apparent RSD

Figure 5.15: Mixed method quarter-pin power and apparent RSD, M=10, problem #3

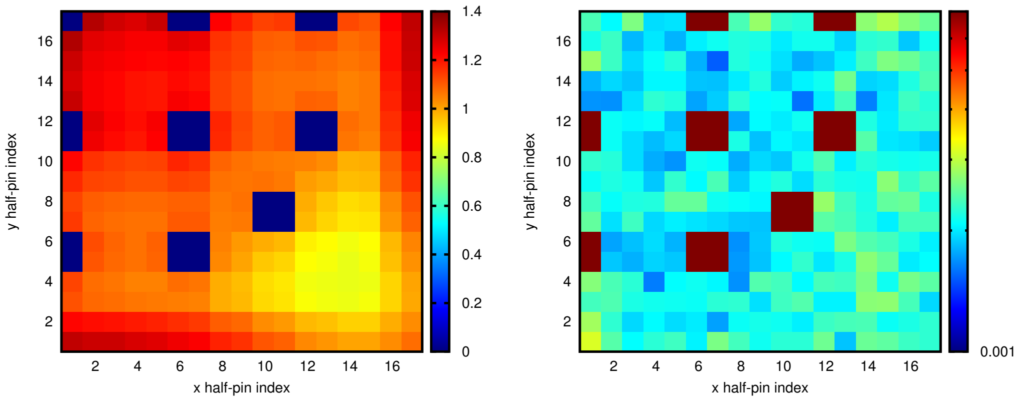

(a) Quarter-pin power (b) Apparent RSD

Figure 5.16: Mixed method quarter-pin power and apparent RSD, M=12, problem #3

In Section 5.4.1.3.2, we compare problem #3 results for the mixed method to other methods considered in this thesis.

5.4.1.3.2 Comparison to Other Methods

For problem #3, we compare the mixed method with $M = 10$ to standard MC, the Wolters method, and LCMC with $M = 10$. We choose only the smaller value of the collision limit for LCMC and the mixed method, because this case is more efficient. We also omit the LJLS method from our problem #3 comparison, because we expect all variants of CMFD-MC to perform comparably on a problem of this size.

As in problem #2, we ran each simulation with a "suitably fine" coarse grid, chosen according to the stability characteristics of the method. In the mixed method case, the source bank size is multiplied by a factor of five when the iteration scheme transitions from the Wolters method to LCMC.

Table 5.6: Comparison simulation parameters, problem #3

Method	Hist./cyc.	Coarse Grid (cm)	LCMC Mult.	Inact. cyc.	Active cyc.
Std. MC	2e5	–	–	50	50
Wolters	2e5	3.213	–	25	50
LCMC, M=10	1e6	1.6065	–	50	50
Mixed, M=10	2e5	1.6065	5	35	50

We present timing data for the four simulations in Table 5.7. The LCMC and mixed method simulations take considerably longer than the standard MC and Wolters method simulations, because the active-cycle source bank size is much larger for these cases. The

Table 5.7: Comparison simulation timing, problem #3

Method	Src. conv. time (s)	Act. cyc time (s)
Std. MC	173	1659
Wolters	352	2566
LCMC, M=10	1725	5683
Mixed, M=10	862	6027

source convergence times listed in Table 5.7 are estimated by visual inspection of the Shannon entropy curves in Figure 5.17. Once we determine the approximate number of cycles required for source convergence, this value is multiplied by the average time per inactive cycle to produce an estimate of the source convergence time. In the mixed method case, we include both the initial fission source convergence period and the temporary re-stabilization period that occurs following the transition from the Wolters method to LCMC. As in problem #2, we use a minimum value of 10 inactive cycles for simulations that converge the fission source very quickly. As shown in Figure 5.17, the standard MC method converges the fission source almost instantly. We expect this behavior when standard MC is used to model optically thin geometries like the quarter-assembly in problem #3, because the dominance ratio of problem #3 is not large. The Wolters method also converges the fission source in only a few cycles. By contrast, LCMC with $M = 10$ exhibits large oscillations for the first several cycles, and does not approach a stationary Shannon entropy until roughly cycle 20. The mixed method initially converges very quickly, but takes ~ 10 cycles to re-stabilize after the transition to LCMC at cycle 25.

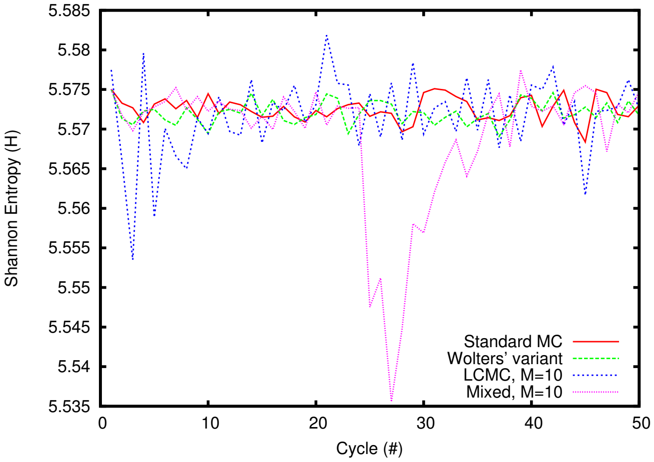

Figure 5.17: Close-up of Shannon entropy, problem #3

The mixed method converges the source distribution more efficiently than LCMC, but less efficiently than the Wolters method and standard MC. This is a result of the mixed method transition from the Wolters iteration scheme to LCMC. The source distribution takes roughly 10 cycles to re-stabilize after the LCMC phase begins; these cycles are computationally expensive because the source bank size has been increased (from the original 2e5 histories per cycle to 1e6).

Next, we compare pin-power FOM distributions for the standard MC, Wolters, LCMC and mixed methods. These distributions are presented in Figure 5.18, and are plotted on a logarithmic color scale. Not surprisingly, standard MC FOMs are significantly higher

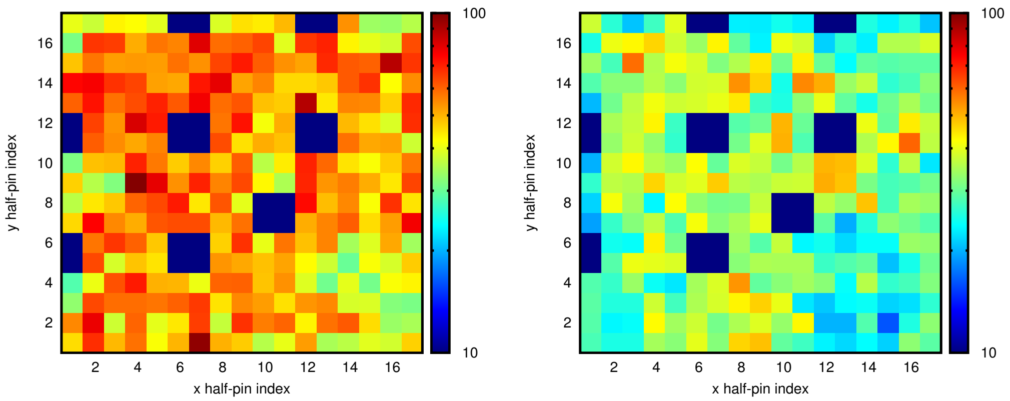

(a) Standard MC

(b) Wolters

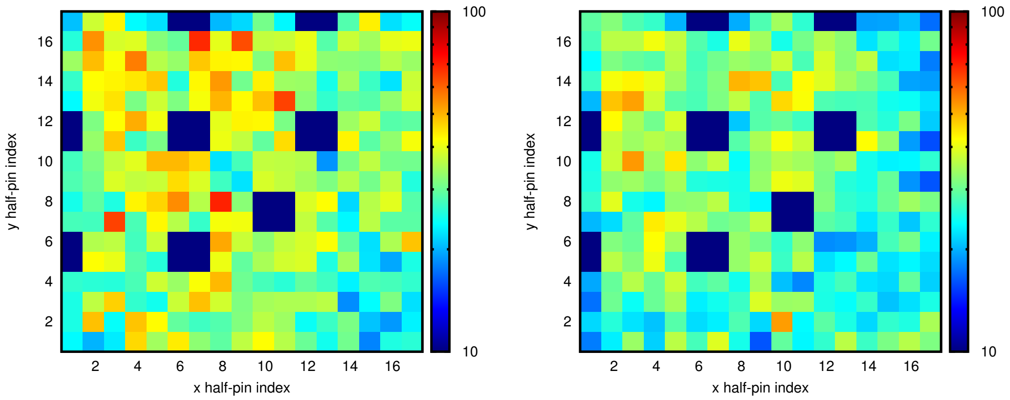

(c) LCMC, M=10

(d) Mixed, M=10

Figure 5.18: Quarter-pin power FOM, problem #3

than the other three methods for the quarter-assembly problem. Because problem #3 is not optically thick, the CMFD calculations performed by the Wolters, LCMC and mixed methods add to the computing time without providing any real benefit.

To enable straightforward comparison between the four cases, average pin-power FOM is reported in Table 5.8 (along with FOM standard deviation). Ideally, we desire a high average FOM with a low standard deviation. If this is the case, the method efficiently produces accurate pin-power results across the entire problem domain. The data presented in Table 5.8 shows that the Wolters, LCMC, and mixed methods are comparably efficient for the active-cycle portion of problem #3. This contrasts with results from problem #2, which showed the LCMC and mixed methods producing higher FOMs than the Wolters method by a factor of ∼ 1.5. This is likely due to the increased number of collisions per cycle used to simulate problem #3. As the number of collisions per cycle increases, the LCMC iteration becomes more stable in the infinite-particle limit; however, it also becomes less applicable for practical calculations on limited-memory computers.

Table 5.8: FOM average and std. deviation, problem #3

Method	Avg FOM	FOM SD
Std. MC	52.9	12.6
Wolters	32.9	7.96
LCMC, M=10	34.6	9.11
Mixed, M=10	29.6	7.13

If problem #3 were simulated using LCMC or the mixed method with a much larger number of histories per cycle (which would require more memory than we have available), the number of collisions per cycle could almost certainly be reduced. This, in turn, would increase the efficiency of the LCMC and mixed methods.

5.4.1.4 2-D Assembly Problem

5.4.1.4.1 Mixed Method Results

In this section, we show numerical results for mixed method simulations of problem #4 (the MOX assembly problem introduced in Section 2.4.2.4). Two values of the collision limit are tested (M = 12 and M = 14), with simulation parameters listed in Table 5.9. The total source bank is increased by a factor of 10 when the mixed method simulation transitions from the Wolters iteration scheme to LCMC; this transition occurs 10 cycles before the onset of the active cycle phase, to allow time for the scattering source to converge. Figures

Table 5.9: Simulation parameters, problem #4

Coll./Cyc. (M)	Inact. Cyc.	Act. Cyc.	Coarse Grid (cm)	Hist./Cyc.	LCMC Mult.
12	35	50	2.142	2e5	10
14	35	50	2.142	2e5	10

5.19 and 5.20 show thermal and fast flux distributions for the $M = 12$ and $M = 14$ cases, respectively. The $M = 12$ case appears to slightly overpredict thermal flux along the fuel-reflector interface, which is a sign that the $M = 12$ simulation is near the stability limit. Overall, flux distributions for the two cases agree well with one another, and also agree

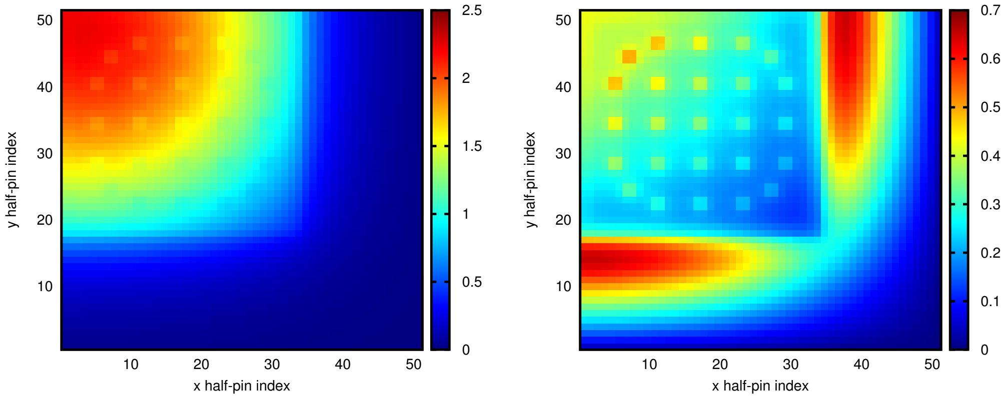

(a) Fast flux (C5G7 grp. 1-3)

(b) Thermal flux (C5G7 grp. 4-7)

Figure 5.19: Mixed method fast and thermal flux distributions, M=12, problem #4

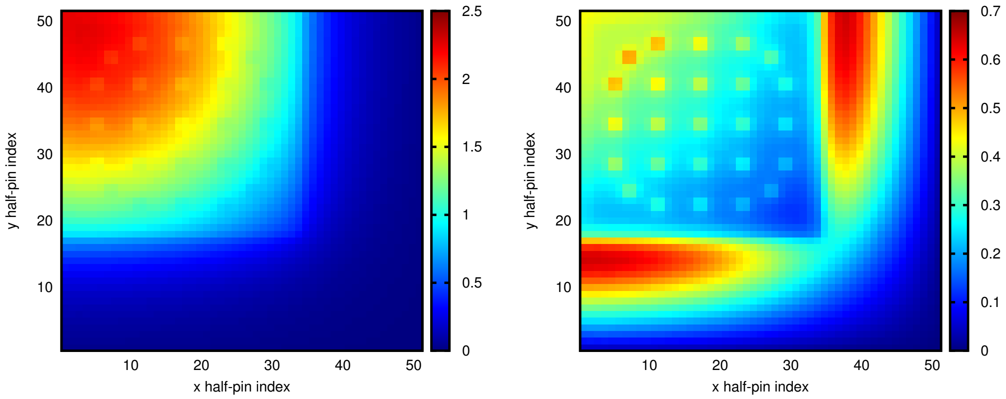

(a) Fast flux (C5G7 grp. 1-3)

(b) Thermal flux (C5G7 grp. 4-7)

Figure 5.20: Mixed method fast and thermal flux distributions, M=14, problem #4

with the problem #4 results presented in previous chapters.

Figures 5.21 and 5.22 show pin-power and pin-power apparent RSD distributions for mixed method simulations of problem #4. On average, the $M = 14$ pin power apparent RSD is slightly higher than the $M = 12$ case. Intuitively, we would expect the opposite trend, because more collisions are simulated in the $M = 14$ case. However, we reiterate that fissions occurring within each cycle (when the collision index $m < M$) are simulated

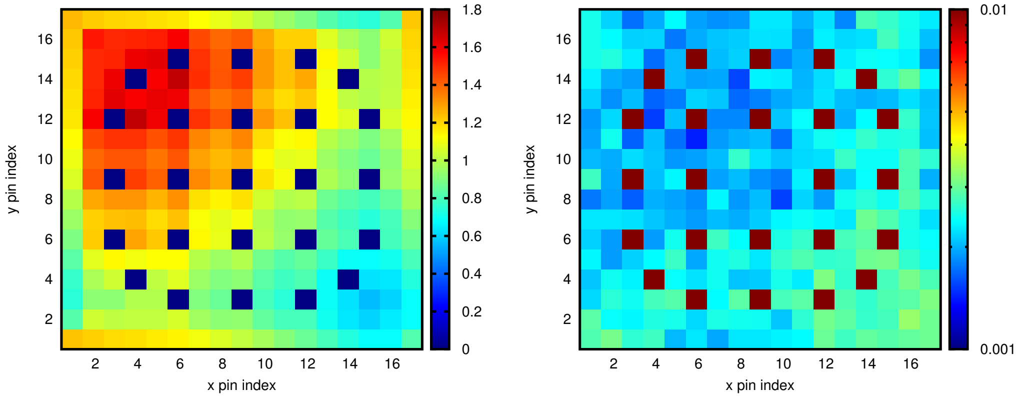

(a) Pin power (b) Apparent RSD

Figure 5.21: Mixed method pin power and apparent RSD, M=12, problem #4

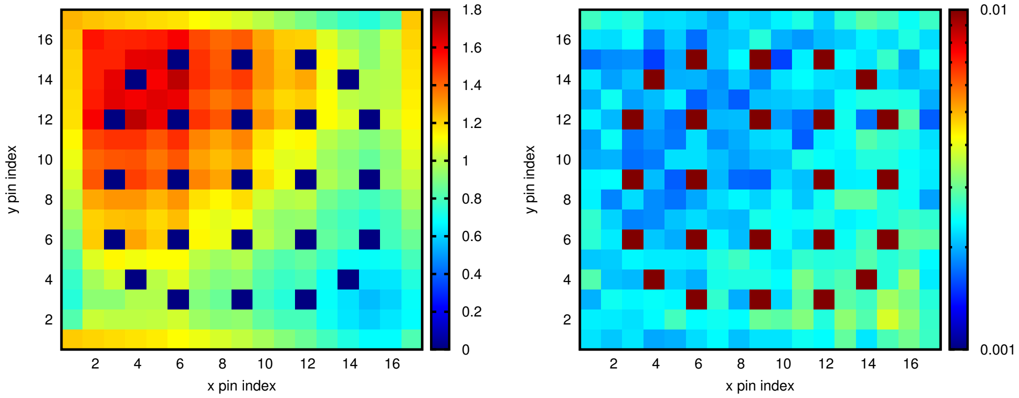

(a) Pin power (b) Apparent RSD

Figure 5.22: Mixed method pin power and apparent RSD, M=14, problem #4

using analog MC. When the collision limit is large, significant fission and scattering fluctuations can occur within a single cycle. This negatively affects the accuracy of the solution, resulting in increased apparent RSDs.

5.4.1.4.2 Comparison to Other Methods

We now compare mixed method results for problem #4 to the standard MC, Wolters and LCMC methods. Parameters for these methods are listed in Table 5.10. We consider only the $M = 12$ collision limit for LCMC and the mixed method, because this case proved more efficient than $M = 14$ for both methods.

Table 5.10: Comparison simulation parameters, problem #4

Method	Hist./cyc.	Coarse Grid (cm)	LCMC Mult.	Inact. cyc.	Active cyc.
Std. MC	2e5	–	–	50	50
Wolters	2e5	4.01625	–	25	50
LCMC, M=12	2e6	2.142	–	50	50
Mixed, M=12	2e5	2.142	10	35	50

In Table 5.11, we list timing results for the four methods. The source convergence time is estimated by visual inspection of the Shannon entropy, as described in Section 5.4.1.2.2. Active cycle times are highest for the LCMC and mixed methods, because these simulations are run using an order of magnitude more histories per cycle than the standard MC and Wolters methods. The standard MC method converges the fission source most efficiently, which is expected for a problem of this size. The mixed method converges the fission source more quickly than LCMC, but considerably more slowly than the Wolters method (as a result of the "re-stabilization" that occurs after the transition to LCMC).

Table 5.11: Comparison simulation timing, problem #4

Method	Src. conv. time (s)	Act. cyc time (s)
Std. MC	178	1804
Wolters	374	2668
LCMC, M=12	3228	14692
Mixed, M=12	1811	14088

In Figure 5.23, we plot Shannon entropy for the first 50 cycles of each simulation. The LCMC method exhibits the largest Shannon entropy fluctuations early in the simulation, but appears to reach a stationary fission source distribution around cycle 15. The standard MC Shannon entropy takes roughly 10 cycles to become stationary, while the mixed

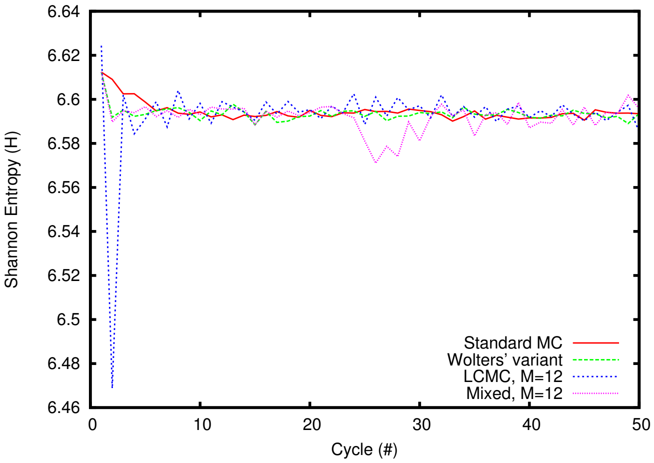

Figure 5.23: Close-up of Shannon entropy, problem #4

and Wolters methods converge the fission source very quickly. The mixed method Shannon entropy briefly fluctuates following the transition from the Wolters iteration scheme to LCMC, but returns to a stationary value after roughly 8 cycles.

In Figure 5.24, FOM distributions for the four methods are compared. Standard MC still produces the highest FOMs, but the difference between standard MC and the other methods is not as large in problem #4 as it was in problem #3. We observe this trend because problem #4 is more optically thick than problem #3; as the optical thickness of a problem increases, the dominance ratio increases and standard MC becomes less efficient.

Table 5.12 presents average FOMs and FOM standard deviation for the four methods. With the exception of standard MC, the mixed method has the highest average FOM for problem #4. The Wolters and LCMC average FOMs are comparable.

Table 5.12: FOM average and standard deviation, problem #4

Method	Avg FOM	FOM SD
Std. MC	19.3	6.41
Wolters	12.9	4.16
LCMC, M=12	12.3	4.08
Mixed, M=12	14.5	4.75

We expect that the LCMC and mixed method average FOMs would be considerably higher for smaller values of the collision limit (M). However, we were unable to simulate cases with small M on a personal computer, because the number of particles per cycle must be increased considerably to ensure stability.

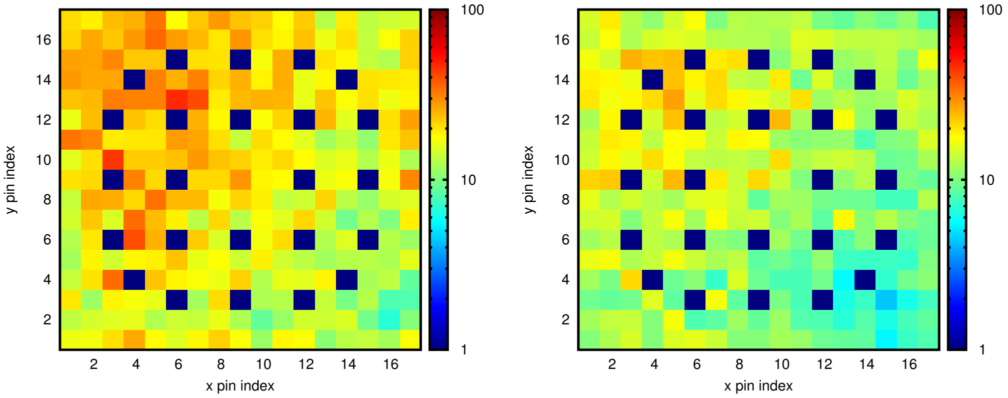

(a) Standard MC

(b) Wolters Method

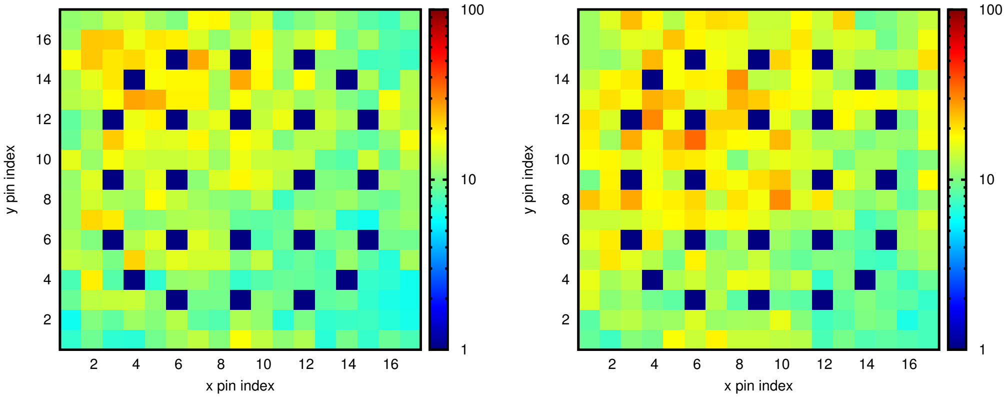

(c) LCMC, M=12

(d) Mixed, M=12

Figure 5.24: Pin power FOM, problem #4

5.5 Summary

In this section, we presented results for the new mixed method for reactor core *k*-eigenvalue calculations, and also carried out an overall comparison of the methods considered in this work.

First, we discussed the apparent RSD behavior of each method for problem #1, the homogeneous fissile slab. Next, we compared eigenfunction FOM and approximate source convergence time using problem #2, a large, monoenergetic, 1-D "core." The LJLS and standard MC methods had the lowest average FOM across the problem domain (in addition, FOM estimates for these methods likely overpredict real FOM, due to inter-cycle correlation). The LCMC and mixed methods produce the highest FOMs across the problem domain. The mixed method converges the source distribution faster than LCMC, but more slowly than the Wolters method.

We then carried out FOM and fission source convergence comparisons for a pair of 2-D multigroup problems (problems #3 and #4). The LCMC and mixed method cases required relatively large values of the collision limit (M) to maintain stability. Numerical results for problems #3 and #4 indicate that the LCMC and mixed methods produce pin power FOMs similar to the Wolters method when the collision limit is not small. We hypothesize that the LCMC and mixed methods become less efficient for large M; numerical results for problems #3 and #4 support this hypothesis. In the next chapter, we investigate how the mixed method FOM depends on both the collision limit and the number of histories per cycle.

CHAPTER 6

Mixed Method Figure of Merit Study

6.1 Introduction

In this chapter, we perform several parametric studies to investigate Figure of Merit (FOM) trends for the mixed method. We are especially interested in the way the mixed method FOM changes as a function of (i) the number of collisions permitted per cycle (M), and (ii) the number of histories per cycle. Since the FOM is a spatially-varying quantity, we average FOM results over all spatial cells to obtain a single value.

First, we examine FOM trends for problem #2, the large, heterogeneous 1-D core problem introduced in Section 2.4.2.2. This study provides insight into the mixed method FOM behavior for a large, high dominance-ratio problem.

Next, we introduce a 2-D pin-cell problem, which is modeled using both one and two-group cross sections. This allows us to evaluate the performance of the mixed method for a problem with simple energy dependence. We then compare two-group pin-cell results to the monoenergetic case.

In each section, FOM results for the mixed method are compared to FOM results for the Wolters method (introduced in Chapter 3). This provides a measure of the relative efficiency of the mixed method.

6.2 1-D Core Problem

In this section, we examine how the spatially-averaged mixed method FOM depends on both the collision limit and the number of histories per cycle. The test problem considered is problem #2, the large, 1-D, heterogeneous core used throughout this thesis.

Simulation parameters for the parametric study of problem #2 are listed in Table 6.1. All mixed method simulations use a pin-cell coarse grid for CMFD feedback, while Wolters method simulations use a quarter-assembly coarse grid; these grid sizes were chosen to ensure that the non-random spectral radius for each method is sufficiently below unity.

Table 6.1: Parametric simulation parameters, problem #2

Method	Inactive Cyc.	Active Cyc.	Coarse Grid (cm)
Wolters	15	25	5.1
Mixed	15	25	1.275

Four values of the mixed method collision limit ($M = 2$, 5, 10, and 20) are considered in the problem #2 parametric study. This allows us to investigate the mixed method FOM over a range of collision limits. All mixed method simulations increase the source bank by a factor of five at the transition from the Wolters iteration scheme to LCMC; this transition takes place five cycles before the onset of active cycles, to allow the scattering source to converge. The number of histories per active cycle ranges from 5e4 to 6e5 for each case.

In Figure 6.1, we plot the spatially-averaged problem #2 FOM for each of the five cases considered here, as a function of the number of histories per cycle. The vertical axis of Figure 6.1 uses a logarithmic scale.

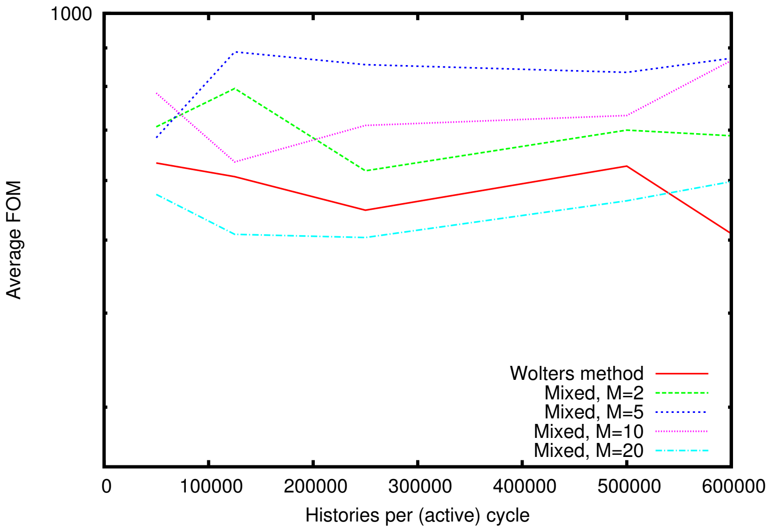

Figure 6.1: FOM vs. histories per cycle, problem #2

In Figure 6.1, the mixed method with $M = 5$ produces the highest average FOM for all but the 5e4 histories per cycle case.

Average FOM values for all cases appear to approach a constant value as the number of histories per cycle increases. As described in Section 5.5, the eigenfunction FOM *should* be nearly independent of the number of histories. However, FOM estimates become unreliable when the number of histories per cycle is small; since the FOM is calculated using the apparent RSD of the eigenfunction, it is only valid when the assumptions of the CLT are adequately satistfied.

To better visualize the relationship between the average FOM and the number of collisions per cycle, we plot the FOM as a function of M for the 2.5e5 histories per cycle case. We include simulations for additional values of M to improve the resolution of this curve.

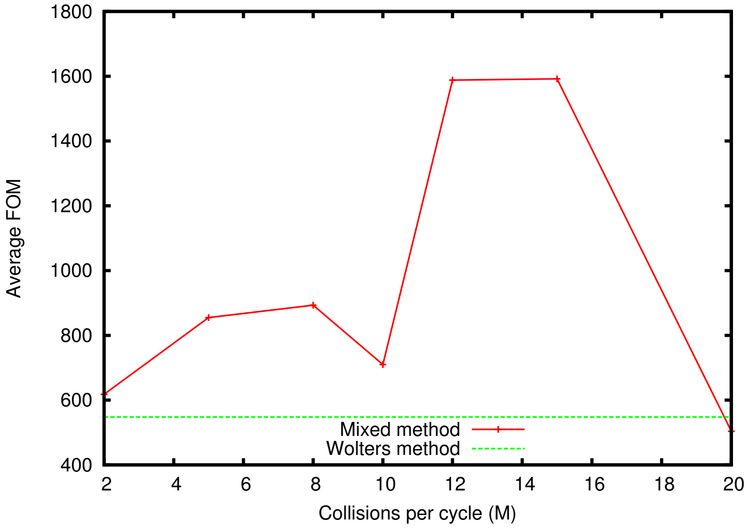

Figure 6.2: FOM vs. M, problem #2

The mixed method FOM is a non-monotonic function of the collision limit (M) for problem #2. The average FOM is low when the collision limit is small ($M \sim 2$ or 3), and also when it becomes sufficiently large ($M \geq 20$); peak average FOMs occur somewhere near $M = 15$. This behavior can be explained in the following way. As the collision limit decreases, the spectral radius of the non-random LCMC iteration increases. For a fixed number of histories per cycle, decreasing the collision limit moves the simulation closer to the stability limit. When M is small, error in the CMFD solution becomes dominant, which tends to decrease the FOM.

Conversely, when the collision limit becomes large, more computational effort shifts from the CMFD calculation to the LCMC solve. Fissions occurring during the LCMC cycle are simulated using standard MC, which is inefficient for high dominance-ratio problems (see Chapter 2). This negatively affects the accuracy of the coarse-grid tallies, which decreases the efficiency of the simulation.

In Figure 6.2, we observe a local decrease in the FOM around $M = 10$. We cannot fully explain this behavior at present. Further analysis is required to better characterize the relationship between average FOM, M, and problem geometry for the mixed method.

The optimal value of M for problem #2 appears to be somewhere near $M = 15$. The spatially-averaged FOM for the mixed method with $M = 15$ is a factor of ~2.9 higher than the Wolters method (for the 2.5e5 histories per cycle case presented in Figure 6.2). The mixed method cases with $M = 2$ and $M = 20$ are comparable in efficiency to the Wolters method, while all cases between $M = 2$ and $M = 20$ are more efficient than the Wolters method.

6.3 Pin-cell Problem

Next, we consider a single pin-cell, adjacent to a pin-cell-sized reflector region. Symmetry is used to reduce the size of the problem to a half pin-cell in height. The pin-cell problem geometry is shown in Figure 6.3, with the fuel pin colored blue and the water reflector region colored brown. All outer surfaces of the pin-cell problem use reflecting boundary conditions, and the total problem size is 2.52 cm × 0.63 cm. Simulation parameters for the pin-cell problem are given in Table 6.2. We emphasize that all mixed and Wolters method cases use the same coarse grid size for the pin-cell problem. Since the pin-cell geometry is optically thin, the non-random spectral radius of this problem should be small for both the LCMC and Wolters method iteration schemes.

Figure 6.3: Pin-cell geometry

Table 6.2: Parametric simulation parameters, pin-cell

Method	Inactive Cyc.	Active Cyc.	Coarse Grid (cm)
Wolters	15	25	0.63
Mixed	15	25	0.63

Each mixed method simulation begins with 1e5 particles per cycle, and transitions from the Wolters iteration to LCMC at cycle 10 (allowing 5 cycles for the scattering source to converge before active cycles begin). To modify the number of histories simulated during active cycles, we change the integer multiplier used to scale the source bank at the transition from the Wolters method to LCMC. (This differs slightly from the problem #2 parametric, in which the multiplier is held constant and the initial number of histories per cycle is adjusted.)

We investigate active cycle source bank sizes ranging from 1e5 histories per cycle to 2.5e6 histories per cycle for the pin-cell problem.

The pin-cell parametric is repeated twice, once for a problem with monoenergetic cross-sections, and once for a problem with two-group cross sections. In both cases, the CMFD system is monoenergetic, and coarse-grid tallies are calculated using track-length estimators. Since the two cases use identical geometry, differences in FOM trends can be attributed to the use of different energy group structures. First, we present results for the monoenergetic case.

6.3.1 Monoenergetic Case

Monoenergetic cross sections for the pin-cell problem are taken from the material cross-sections for problem #2, and are listed in Table 6.3. In the monoenergetic study, we consider collision limits of M = 2, 5, and 10 for the mixed method.

Table 6.3: Monoenergetic pin-cell cross sections (cm^{-1})

Material	Σ_t	$\nu\Sigma_f$	Σ_s	Σ_a
UO_2	0.332	7.98e-2	0.275	5.78e-2
H_2O	0.175	–	0.174	9.33e-4

First, we present the spatially-averaged FOM as a function of the number of histories per cycle for each value of the collision limit, M. Results for the Wolters method are included for comparison. This plot is given in Figure 6.4.

The Wolters method average FOM trend is noticeably smoother than the mixed method cases, especially when the number of particles per cycle is small ($\leq$1e6). This behavior is expected; previous results (see Section 4.4.1) show that the LCMC iteration scheme is considerably more sensitive to random noise than the Wolters method. Since the mixed method simulates active cycles using the LCMC iteration scheme, we expect the mixed method FOM to be noisier than the Wolters method FOM when the number of particles per cycle is relatively small.

In Figure 6.4, the M = 2 case produces the highest FOMs across the span of source bank sizes, ranging from a factor of roughly 1.25 to a factor of 2.5 higher than the Wolters method FOM. The M = 5 FOM is the lowest for all cases, while the M = 10 FOM is generally higher than the Wolters method FOM, but lower than the M = 2 FOM.

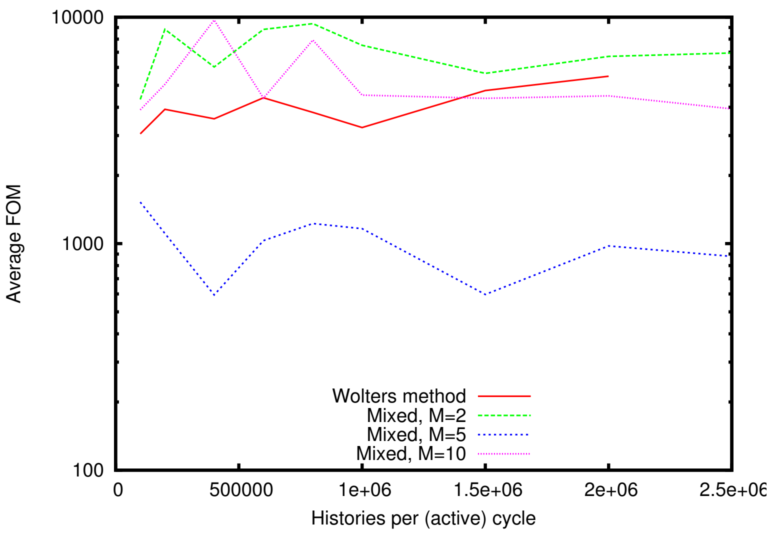

Figure 6.4: FOM vs. histories per cycle, monoenergetic pin-cell problem

Next, we consider the relationship between the collision limit M and the average FOM for the mixed method. This trend is shown in Figure 6.5 for the 1.5e6 histories per cycle case; the Wolters method FOM is included for comparison.

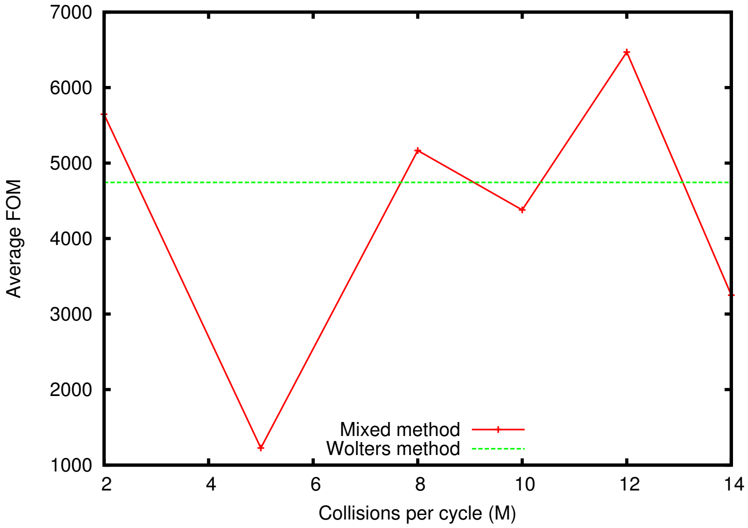

Figure 6.5: FOM vs. M, monoenergetic pin-cell problem

As in problem #2, the FOM versus M trend is non-monotonic for the monoenergetic pin-cell problem. However, trends in the monoenergetic pin-cell case are more difficult to interpret. The mixed method FOM is higher than the Wolters method value when $M = 2$, 8 and 12, and largest when $M = 12$. The mixed method FOM increases from $M = 5$ to

M = 12 (with a small decrease at M = 10); this agrees with the problem #2 trend. However, it is not clear why the FOM decreases sharply from M = 2 to M = 5.

While we do not fully understand these trends, we hypothesize that they may be somewhat problem-dependent. The pin-cell problem considered here is optically thin and reflected on all sides. Thus, it is possible that the reflecting boundaries influence the apparent RSD of the eigenfunction (and subsequently the FOM) for certain values of the collision limit.

Next, we consider the pin-cell problem geometry with two-group cross sections.

6.3.2 Two-group Case

Two-group cross sections for the pin-cell problem were taken from the C5G7 benchmark. To obtain these cross sections, the original seven-group UO_2 and H_2O reflector cross-sections were group-collapsed using the infinite-medium UO_2 spectrum.

Table 6.4: 2-group pin-cell cross sections (cm^{-1})

Material	$\Sigma_{t,1}$	$\Sigma_{t,2}$	$\nu\Sigma_{f,1}$	$\nu\Sigma_{f,2}$	$\Sigma_{s,1\to1}$	$\Sigma_{s,1\to2}$	$\Sigma_{s,2\to2}$	χ_1	χ_2
UO_2	0.328	0.524	3.81e-3	4.67e-2	0.323	1.32e-4	0.435	~1	1.17e-7
H_2O	0.406	0.608	–	–	0.393	1.27e-2	0.605	–	–

In the two-group case, we consider collision limits of M = 3, 5, and 10 for the mixed method.

Figure 6.6 shows the spatially-averaged FOM for each value of the collision limit, as a function of the number of histories per cycle. Average FOMs for the Wolters method are included for comparison; however, runtime considerations prevent us from simulating Wolters method cases with source banks larger than 8e5 histories per cycle. We anticipate that FOM results for these cases would be similar to the results shown in 6.6, because the trend should become roughly flat when the number of histories per cycle is large.

The mixed method with M = 3 is least efficient for all source bank sizes considered here, while the M = 5 case is most efficient for source banks ≥1e6 histories per cycle. FOM values for M = 10 generally lie between the M = 3 and M = 5 curves, which suggests that the mixed method FOM is a non-monotonic function of M for the two-group pin-cell problem. All of the mixed method cases shown in Figure 6.6 are less efficient than the Wolters method.

In Figure 6.7, we plot the spatially-averaged mixed method FOM as a function of M for the 1.5e6 histories per cycle case. Since we do not have an average FOM for the Wolters

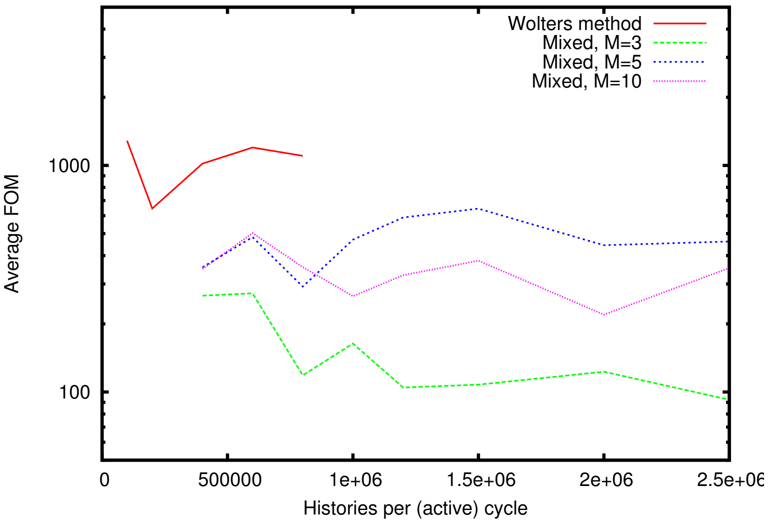

Figure 6.6: FOM vs. histories per cycle, two-group pin-cell problem

method with 1.5e6 histories per cycle, we instead use the FOM of the 8e5 histories per cycle case for comparison.

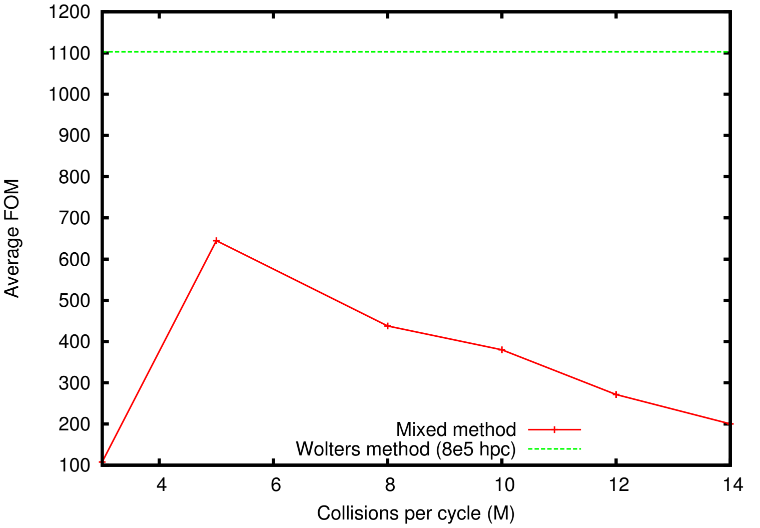

Figure 6.7: FOM vs. M, two-group pin-cell problem

The mixed method FOM trend in Figure 6.7 is non-monotonic, and agrees with our expectation for the LCMC iteration scheme. When M is small, the non-random LCMC spectral radius is large, and the simulation is inefficient. On the other hand, when M is sufficiently large, random fluctuations in the fission and scattering sources still occur; this also reduces the efficiency of the simulation. The "optimal" value of M for the two-group pin-cell problem appears to be near $M = 5$. However, all of the cases shown in Figure 6.7 are less efficient than the Wolters method.

This finding differs from the multigroup results presented in Section 5.5, in which the mixed method performs comparably to the Wolters method; this suggests that the relative efficiency of the mixed method is problem-dependent.

The optimal value of M also appears to be strongly problem-dependent. For problem #2, a collision limit of $M \approx 15$ produced the highest FOM. The monoenergetic pin-cell FOM was maximized for $M \approx 12$, while the two-group pin-cell FOM is maximized for $M \approx 5$. These results confirm that further research is needed to characterize the relationship between the mixed method FOM and the collision limit, M.

6.4 Summary

In this chapter, we performed parametric studies to better understand the FOM behavior of the mixed method. We first considered the heterogeneous 1-D core problem used throughout this work (problem #2). For problem #2, the mixed method FOM is a non-monotonic function of the collision limit, M. The mixed method is more efficient than the Wolters method for collision limits between $M = 2$ and $M = 20$, with a FOM peak at $M \approx 15$.

We also considered two 2-D pin-cell problems, one with monoenergetic cross sections and one with two-group cross sections. In the monoenergetic pin-cell case, the mixed method is more efficient than the Wolters method for some values of the collision limit. However, the relationship between the collision limit and the spatially-averaged FOM for this problem is not easily understood, and requires further study. We hypothesize that this relationship may be linked to the small size of the problem and the use of reflecting boundaries on all surfaces.

Mixed method FOM results for the two-group pincell case are a non-monotonic function of the collision limit, M. For small values of the collision limit, the mixed-method FOM is an increasing function of M. After reaching a peak around $M = 5$, the mixed method FOM decreases as M continues to increase. In the two-group pincell case, the Wolters method is more efficient than the mixed method for all values of the collision limit (M).

Finally, in this chapter we showed that the mixed method FOM behaves as expected as a function of the number of histories per cycle; the FOM is noisy for small source bank sizes, but becomes roughly constant as the source bank becomes large. The source bank size "threshold" (at which the FOM becomes roughly constant) is higher for the LCMC method than the Wolters method. This is consistent with our understanding of the two methods; numerical results throughout this thesis show that the LCMC iteration scheme is more sensitive to statistical error than the Wolters method.

CHAPTER 7

Conclusions and Future Work

7.1 Summary

Reactor core *k*-eigenvalue calculations provide important information about the space-angle-energy distribution of neutrons in an operating nuclear reactor. Flux solutions from *k*-eigenvalue simulations are used to calculate many quantities of interest to reactor physicists, including power profiles and reaction rates; this information can be used to assess the operating characteristics of an existing reactor, analyze the response of the core to accident scenarios, and design new systems.

However, detailed full-core neutron flux distributions are computationally expensive to obtain. To this end, considerable research is currently being performed to develop more efficient computational methods for *k*-eigenvalue calculations. Much of this research focuses on deterministic methods, which discretize the transport equation in space, angle, and energy (and in doing so introduce systematic error). Some deterministic codes also employ the diffusion approximation, which results in a more efficient simulation but may not be sufficiently accurate for all problems of interest in reactor physics.

In this work, we consider the Monte Carlo method, which simulates the transport process using random numbers for a large number of individual histories. The results from these histories are averaged to obtain a final eigenfunction estimate, which includes an estimate of statistical error. Monte Carlo calculations are often prohibitively expensive for full-core problems, and suffer from incomplete fission source convergence and inter-cycle correlation effects.

A major goal of this research is to better understand the behavior of several iteration strategies, all of which employ Monte Carlo random sampling. One such iteration strategy, the LCMC method, was developed as part of this research. In the LCMC method, Monte Carlo histories are restricted to a user-specified number of collisions per cycle.

A second goal of this research is to demonstrate that "non-random" versions of Monte

Carlo iteration equations, which represent the limit as the number of histories approaches infinity, can be linearized and Fourier-analyzed. While this analysis only applies to simulations in which statistical error is negligible, it can be used to glean information about real-world Monte Carlo simulations. It is our hope that this information will aid code users in selecting stable parameters for practical simulations.

Finally, we introduce a new, "hybrid" simulation procedure for large Monte Carlo *k*-eigenvalue simulations. This method is based on the idea that inactive and active Monte Carlo cycles pose different computational challenges; as a result, it may be optimal to treat the two calculation phases with different iteration schemes. Here, we employ the CMFD-MC method (with a sufficiently fine coarse grid) to efficiently converge the fission source, and then we transition to the LCMC scheme to accelerate active cycles. In this way, we attempt to leverage the strengths of both iteration schemes (while largely avoiding their respective drawbacks).

7.2 Conclusions

During the course of this research, we have reached a number of conclusions regarding the stabilization and acceleration of Monte Carlo *k*-eigenvalue simulations. First of all, we have verified that the standard Monte Carlo iteration scheme is unconditionally stable in the infinite-particle limit. Thus, any instabilities observed in real-world Monte Carlo simulations are the result of stochastic error, and can likely be resolved by running more histories. (We note that the number of histories required may prove intractable, especially for large systems.)

We have also shown that the CMFD-MC method, originally proposed by Lee et. al., is not unconditionally stable in the infinite-particle limit. The spectral radius of the CMFD-MC iteration depends on the coarse-grid optical thickness, as well as the scattering matrix. It was previously thought that the primary source of CMFD-MC instability came from stochastic noise in the low-order system, a belief which led to the development of two variants of CMFD-MC (LJLS and the Wolters method). We investigated these variants as part of this work, and verified that the LJLS multi-set method significantly underpredicts eigenfunction error for high dominance-ratio problems. We also extended the Wolters variant to multidimensional geometry, and concluded that the Wolters correction term provides a modest benefit. However, it is not sufficient to stabilize full-core simulations.

In this research, we also implemented and investigated an alternate deterministic-like iteration strategy for Monte Carlo reactor core calculations (the LCMC method), which limits the number of collisions per history per cycle. The LCMC method represents a significant departure from the traditional MC k-eigenvalue iteration scheme. We have analyzed the stability of the LCMC method, and shown that the spectral radius increases as the number of allowed collisions decreases. In addition, the spectral radius is a monotonically increasing function of the coarse grid size for the monoenergetic case. We concluded that the LCMC scheme does not efficiently converge the fission and scattering source distributions; however, it significantly decreases the cost of active cycles.

To develop a simulation that is efficient during both inactive and active cycles, we implemented the "mixed" method, which uses the CMFD-MC iteration equations to converge the fission source, and then transitions to LCMC to accelerate the active cycles. The mixed method produces higher Figure-of-Merit (FOM) values than the CMFD-MC method for the 1-D problems considered in this research. However, FOM results for 2-D multigroup simulations are very similar across all methods. We hypothesize that the presence of a spatially flat convergence mode decreases the efficiency of the LCMC iteration for multigroup problems. In addition, the LCMC iteration is significantly more sensitive to statistical noise than the CMFD-MC iteration (this effect is more noticeable in 2-D simulations, which have a larger tally space).

In general, we believe that the efficiency of the mixed method is problem-dependent for practical (multidimensional, multigroup) reactor core calculations. For most of the problems presented in this thesis, the mixed method is as efficient as (or more efficient than) the Wolters method over some range of collision limit/history per cycle combinations. We believe this range may be more limited in problems with energy dependence.

In conclusion, we have identified several ways to improve the current state-of-the-art for Monte Carlo reactor core k-eigenvalue calculations. We have shown that Fourier analysis can be applied to Monte Carlo calculations, to qualitatively assess the convergence rate of the fission source when statistical noise is negligible. Finally, we have developed and implemented the new LCMC method, which is loosely based on a deterministic iteration strategy. We have shown that the LCMC method can be combined with CMFD-MC in a single simulation (which we call the mixed method), and that this strategy yields higher FOMs for some problems.

7.3 Future Work

First and foremost, the LCMC and mixed methods should be extended to continuous energy problems. This should be a straightforward extension of the methods as they currently exist, and would allow for the simulation of more realistic MC benchmark problems.

In addition, it would be highly useful to develop a Fourier analysis technique that includes the effects of stochastic error in the spectral radius calculation. Presumably, the result of this Fourier analysis would be a mean spectral radius with some standard deviation. This would greatly improve the predictive capability of the Fourier analysis for real MC simulations, and would allow for more complete characterization of new methods.

A complicating factor in methods that employ CMFD feedback is the inevitable use of analog tallies to compute the low-order system. These tallies are inherently noisy, and they contribute to the instability of the CMFD-MC and LCMC methods when the coarse grid size is near the stability limit. In addition, they render the LCMC method infeasible for simulating large, multidimensional problems on personal computers.

Recent work by A.G. Nelson and W.R. Martin [26] has shown that multigroup cross sections can be calculated using modified track-length tallies, which are significantly more accurate than analog tallies. We believe that the use of track-length tallies to compute the low-order system would help stabilize simulations near the non-random stability limit. This is especially true for the LCMC method, which is highly sensitive to random noise.

We also emphasize that the CMFD system is by no means the only possible choice for the low-order feedback calculation. Recent work has shown that partial-current CMFD (PCMFD) acceleration outperforms CMFD acceleration for deterministic methods, and remains stable for larger coarse grid sizes. Preliminary results from our 1-D test code indicate that this result also holds for coarse-mesh acceleration of the Monte Carlo *k*-eigenvalue iteration. The PCMFD method should be implemented and tested alongside CMFD in OpenMC (or a similar multidimensional test code).

To improve the efficiency of the mixed method, the transition from CMFD-MC to LCMC should be streamlined. During the final CMFD-MC cycle, scattering source sites can likely be sampled in the same way that fission sites are sampled. If this is done, the first LCMC cycle will begin with both fission and scattering banks, which will largely eliminate the “re-stabilization” period observed in mixed method Shannon entropy plots. This would reduce the mixed method source convergence time considerably.

In general, we believe that further research should be performed to examine the ways in which deterministic insights can be used to guide the development of Monte Carlo methods (and vice versa). While determinstic and Monte Carlo methods are often viewed as distinct categories of computational methods, acceleration and stabilization strategies developed in one “camp” may prove beneficial to the other. For instance, we have implemented and tested the deterministic strategy of CMFD update relaxation to stabilize the CMFD-MC iteration. While this particular technique ultimately provided only minor benefits, it serves as an example of a deterministic technique that was easily adapted to Monte Carlo.

APPENDIX

The C5G7 Benchmark

In this section, we provide cross sections and geometry layouts for the C5G7 benchmark [27], which was originally created to benchmark the performance of deterministic codes. All scattering is isotropic; the benchmark description instructs users to run the code using the transport-corrected total cross section in place of the usual total cross section.

Figure 1 shows the C5G7 fuel assembly layout. All pin-cells use identical geometry, which is shown in Figure 2. Each pin-cell is 1.26 cm × 1.26 cm, with a centered fuel pin of radius 0.54 cm. (In Figure 2, the fuel-clad region is shaded dark gray, while the moderator region is light gray.) Finally, Figure 3 shows the full C5G7 geometry, which includes a ring of 5 reflector assemblies surrounding the fuel region.

Tables 1-14 list seven-group cross sections for the C5G7 benchmark.

Table 1: UO_2 fuel-clad macroscopic cross-sections

Group	Σ_t	Σ_{tr}	Σ_a	Σ_γ	Σ_f	ν	χ
1	2.12450E-01	1.77949E-01	8.02480E-03	8.12740E-04	7.21206E-03	2.78145E+00	5.87910E-01
2	3.55470E-01	3.29805E-01	3.71740E-03	2.89810E-03	8.19301E-04	2.47443E+00	4.11760E-01
3	4.85540E-01	4.80388E-01	2.67690E-02	2.03158E-02	6.45320E-03	2.43383E+00	3.39060E-04
4	5.59400E-01	5.54367E-01	9.62360E-02	7.76712E-02	1.85648E-02	2.43380E+00	1.17610E-07
5	3.18030E-01	3.11801E-01	3.00200E-02	1.22116E-02	1.78084E-02	2.43380E+00	0.00000E+00
6	4.01460E-01	3.95168E-01	1.11260E-01	2.82252E-02	8.30348E-02	2.43380E+00	0.00000E+00
7	5.70610E-01	5.64406E-01	2.82780E-01	6.67760E-02	2.16004E-01	2.43380E+00	0.00000E+00

Table 2: UO_2 fuel-clad scattering cross-sections

Group	→ 1	→ 2	→ 3	→ 4	→ 5	→ 6	→ 7
1	1.27537E-01	4.23780E-02	9.43740E-06	5.51630E-09	0.00000E+00	0.00000E+00	0.00000E+00
2	0.00000E+00	3.24456E-01	1.63140E-03	3.14270E-09	0.00000E+00	0.00000E+00	0.00000E+00
3	0.00000E+00	0.00000E+00	4.50940E-01	2.67920E-03	0.00000E+00	0.00000E+00	0.00000E+00
4	0.00000E+00	0.00000E+00	0.00000E+00	4.52565E-01	5.56640E-03	0.00000E+00	0.00000E+00
5	0.00000E+00	0.00000E+00	0.00000E+00	1.25250E-04	2.71401E-01	1.02550E-02	1.00210E-08
6	0.00000E+00	0.00000E+00	0.00000E+00	0.00000E+00	1.29680E-03	2.65802E-01	1.68090E-02
7	0.00000E+00	0.00000E+00	0.00000E+00	0.00000E+00	0.00000E+00	8.54580E-03	2.73080E-01

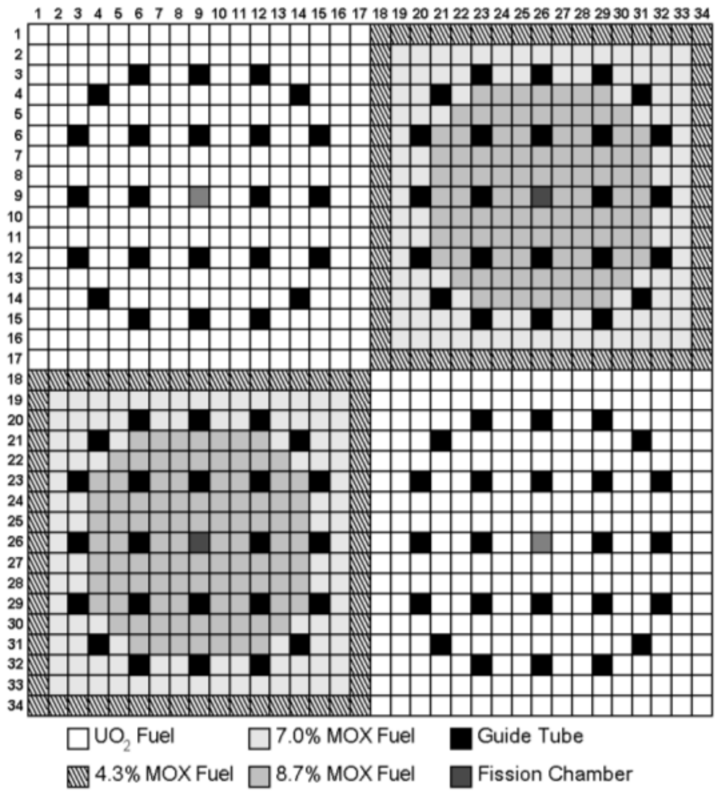

Figure 1: C5G7 fuel assembly geometry [27]

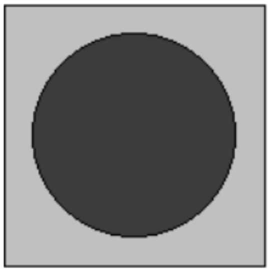

Figure 2: C5G7 pin cell geometry [27]

Table 3: 4.3% MOX fuel-clad macroscopic cross-sections

Group	Σ_t	Σ_{tr}	Σ_a	Σ_γ	Σ_f	ν	χ
1	2.11920E-01	1.78731E-01	8.43390E-03	8.06860E-04	7.62704E-03	2.85209E+00	5.87910E-01
2	3.55810E-01	3.30849E-01	3.75770E-03	2.88080E-03	8.76898E-04	2.89099E+00	4.11760E-01
3	4.88900E-01	4.83772E-01	2.79700E-02	2.22717E-02	5.69835E-03	2.85486E+00	3.39060E-04
4	5.71940E-01	5.66922E-01	1.04210E-01	8.13228E-02	2.28872E-02	2.86073E+00	1.17610E-07
5	4.32390E-01	4.26227E-01	1.39940E-01	1.29177E-01	1.07635E-02	2.85447E+00	0.00000E+00
6	6.84950E-01	6.78997E-01	4.09180E-01	1.76423E-01	2.32757E-01	2.86415E+00	0.00000E+00
7	6.88910E-01	6.82852E-01	4.09350E-01	1.60382E-01	2.48968E-01	2.86780E+00	0.00000E+00

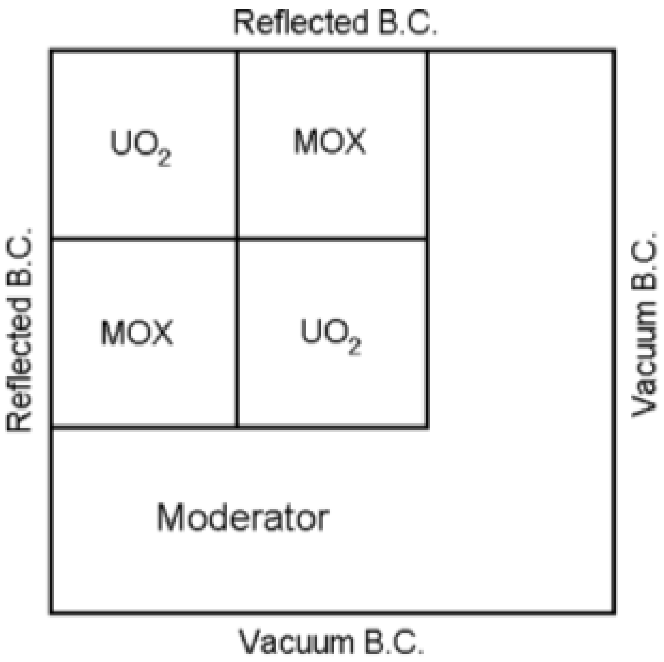

Figure 3: C5G7 problem layout [27]

Table 4: 4.3% MOX fuel-clad scattering cross-sections

Group	→ 1	→ 2	→ 3	→ 4	→ 5	→ 6	→ 7
1	1.28876E-01	4.14130E-02	8.22900E-06	5.04050E-09	0.00000E+00	0.00000E+00	0.00000E+00
2	0.00000E+00	3.25452E-01	1.63950E-03	1.59820E-09	0.00000E+00	0.00000E+00	0.00000E+00
3	0.00000E+00	0.00000E+00	4.53188E-01	2.61420E-03	0.00000E+00	0.00000E+00	0.00000E+00
4	0.00000E+00	0.00000E+00	0.00000E+00	4.57173E-01	5.53940E-03	0.00000E+00	0.00000E+00
5	0.00000E+00	0.00000E+00	0.00000E+00	1.60460E-04	2.76814E-01	9.31270E-03	9.16560E-09
6	0.00000E+00	0.00000E+00	0.00000E+00	0.00000E+00	2.00510E-03	2.52962E-01	1.48500E-02
7	0.00000E+00	0.00000E+00	0.00000E+00	0.00000E+00	0.00000E+00	8.49480E-03	2.65007E-01

Table 5: 7.0% MOX fuel-clad macroscopic cross-sections

Group	Σ_t	Σ_{tr}	Σ_a	Σ_γ	Σ_f	ν	χ
1	2.14540E-01	1.81323E-01	9.06570E-03	8.11240E-04	8.25446E-03	2.88498E+00	5.87910E-01
2	3.59350E-01	3.34368E-01	4.29670E-03	2.97105E-03	1.32565E-03	2.91079E+00	4.11760E-01
3	4.98910E-01	4.93785E-01	3.28810E-02	2.44594E-02	8.42156E-03	2.86574E+00	3.39060E-04
4	5.96220E-01	5.91216E-01	1.22030E-01	8.91570E-02	3.28730E-02	2.87063E+00	1.17610E-07
5	4.80350E-01	4.74198E-01	1.82980E-01	1.67016E-01	1.59636E-02	2.86714E+00	0.00000E+00
6	8.39360E-01	8.33601E-01	5.68460E-01	2.44666E-01	3.23794E-01	2.86658E+00	0.00000E+00
7	8.59480E-01	8.53603E-01	5.85210E-01	2.22407E-01	3.62803E-01	2.87539E+00	0.00000E+00

Table 6: 7.0% MOX fuel-clad scattering cross-sections

Group	→ 1	→ 2	→ 3	→ 4	→ 5	→ 6	→ 7
1	1.30457E-01	4.17920E-02	8.51050E-06	5.13290E-09	0.00000E+00	0.00000E+00	0.00000E+00
2	0.00000E+00	3.28428E-01	1.64360E-03	2.20170E-09	0.00000E+00	0.00000E+00	0.00000E+00
3	0.00000E+00	0.00000E+00	4.58371E-01	2.53310E-03	0.00000E+00	0.00000E+00	0.00000E+00
4	0.00000E+00	0.00000E+00	0.00000E+00	4.63709E-01	5.47660E-03	0.00000E+00	0.00000E+00
5	0.00000E+00	0.00000E+00	0.00000E+00	1.76190E-04	2.82313E-01	8.72890E-03	9.00160E-09
6	0.00000E+00	0.00000E+00	0.00000E+00	0.00000E+00	2.27600E-03	2.49751E-01	1.31140E-02
7	0.00000E+00	0.00000E+00	0.00000E+00	0.00000E+00	0.00000E+00	8.86450E-03	2.59529E-01

Table 7: 8.7% MOX fuel-clad macroscopic cross-sections

Group	Σ_t	Σ_{tr}	Σ_a	Σ_γ	Σ_f	ν	χ
1	2.16280E-01	1.83045E-01	9.48620E-03	8.14110E-04	8.67209E-03	2.90426E+00	5.87910E-01
2	3.61700E-01	3.36705E-01	4.65560E-03	3.03134E-03	1.62426E-03	2.91795E+00	4.11760E-01
3	5.05630E-01	5.00507E-01	3.62400E-02	2.59684E-02	1.02716E-02	2.86986E+00	3.39060E-04
4	6.11170E-01	6.06174E-01	1.32720E-01	9.36753E-02	3.90447E-02	2.87491E+00	1.17610E-07
5	5.08900E-01	5.02754E-01	2.08400E-01	1.89142E-01	1.92576E-02	2.87175E+00	0.00000E+00
6	9.26670E-01	9.21028E-01	6.58700E-01	2.83812E-01	3.74888E-01	2.86752E+00	0.00000E+00
7	9.60990E-01	9.55231E-01	6.90170E-01	2.59571E-01	4.30599E-01	2.87808E+00	0.00000E+00

Table 8: 8.7% MOX fuel-clad scattering cross-sections

Group	→ 1	→ 2	→ 3	→ 4	→ 5	→ 6	→ 7
1	1.31504E-01	4.20460E-02	8.69720E-06	5.19380E-09	0.00000E+00	0.00000E+00	0.00000E+00
2	0.00000E+00	3.30403E-01	1.64630E-03	2.60060E-09	0.00000E+00	0.00000E+00	0.00000E+00
3	0.00000E+00	0.00000E+00	4.61792E-01	2.47490E-03	0.00000E+00	0.00000E+00	0.00000E+00
4	0.00000E+00	0.00000E+00	0.00000E+00	4.68021E-01	5.43300E-03	0.00000E+00	0.00000E+00
5	0.00000E+00	0.00000E+00	0.00000E+00	1.85970E-04	2.85771E-01	8.39730E-03	8.92800E-09
6	0.00000E+00	0.00000E+00	0.00000E+00	0.00000E+00	2.39160E-03	2.47614E-01	1.23220E-02
7	0.00000E+00	0.00000E+00	0.00000E+00	0.00000E+00	0.00000E+00	8.96810E-03	2.56093E-01

Table 9: Fission chamber macroscopic cross-sections

Group	Σ_t	Σ_{tr}	Σ_a	Σ_γ	Σ_f	ν	χ
1	1.90730E-01	1.26032E-01	5.11320E-04	5.11315E-04	4.79002E-09	2.76283E+00	5.87910E-01
2	4.56520E-01	2.93160E-01	7.58130E-05	7.58072E-05	5.82564E-09	2.46239E+00	4.11760E-01
3	6.40700E-01	2.84250E-01	3.16430E-04	3.15966E-04	4.63719E-07	2.43380E+00	3.39060E-04
4	6.49840E-01	2.81020E-01	1.16750E-03	1.16226E-03	5.24406E-06	2.43380E+00	1.17610E-07
5	6.70630E-01	3.34460E-01	3.39770E-03	3.39755E-03	1.45390E-07	2.43380E+00	0.00000E+00
6	8.75060E-01	5.65640E-01	9.18860E-03	9.18789E-03	7.14972E-07	2.43380E+00	0.00000E+00
7	1.43450E+00	1.17214E+00	2.32440E-02	2.32419E-02	2.08041E-06	2.43380E+00	0.00000E+00

Table 10: Fission chamber scattering cross-sections

Group	→ 1	→ 2	→ 3	→ 4	→ 5	→ 6	→ 7
1	6.61659E-02	5.90700E-02	2.83340E-04	1.46220E-06	2.06420E-08	0.00000E+00	0.00000E+00
2	0.00000E+00	2.40377E-01	5.24350E-02	2.49900E-04	1.92390E-05	2.98750E-06	4.21400E-07
3	0.00000E+00	0.00000E+00	1.83425E-01	9.22880E-02	6.93650E-03	1.07900E-03	2.05430E-04
4	0.00000E+00	0.00000E+00	0.00000E+00	7.90769E-02	1.69990E-01	2.58600E-02	4.92560E-03
5	0.00000E+00	0.00000E+00	0.00000E+00	3.73400E-05	9.97570E-02	2.06790E-01	2.44780E-02
6	0.00000E+00	0.00000E+00	0.00000E+00	0.00000E+00	9.17420E-04	3.16774E-01	2.38760E-01
7	0.00000E+00	0.00000E+00	0.00000E+00	0.00000E+00	0.00000E+00	4.97930E-02	1.09910E+00

Table 11: Guide tube macroscopic cross-sections

Group	Σ_t	Σ_{tr}	Σ_a	Σ_γ
1	1.90730E-01	1.26032E-01	5.11320E-04	5.11320E-04
2	4.56520E-01	2.93160E-01	7.58010E-05	7.58010E-05
3	6.40670E-01	2.84240E-01	3.15720E-04	3.15720E-04
4	6.49670E-01	2.80960E-01	1.15820E-03	1.15820E-03
5	6.70580E-01	3.34440E-01	3.39750E-03	3.39750E-03
6	8.75050E-01	5.65640E-01	9.18780E-03	9.18780E-03
7	1.43450E+00	1.17215E+00	2.32420E-02	2.32420E-02

Table 12: Guide tube scattering cross-sections

Group	→ 1	→ 2	→ 3	→ 4	→ 5	→ 6	→ 7
1	6.61659E-02	5.90700E-02	2.83340E-04	1.46220E-06	2.06420E-08	0.00000E+00	0.00000E+00
2	0.00000E+00	2.40377E-01	5.24350E-02	2.49900E-04	1.92390E-05	2.98750E-06	4.21400E-07
3	0.00000E+00	0.00000E+00	1.83297E-01	9.23970E-02	6.94460E-03	1.08030E-03	2.05670E-04
4	0.00000E+00	0.00000E+00	0.00000E+00	7.88511E-02	1.70140E-01	2.58810E-02	4.92970E-03
5	0.00000E+00	0.00000E+00	0.00000E+00	3.73330E-05	9.97372E-02	2.06790E-01	2.44780E-02
6	0.00000E+00	0.00000E+00	0.00000E+00	0.00000E+00	9.17260E-04	3.16765E-01	2.38770E-01
7	0.00000E+00	0.00000E+00	0.00000E+00	0.00000E+00	0.00000E+00	4.97920E-02	1.09912E+00

Table 13: Moderator macroscopic cross-sections

Group	Σ_t	Σ_{tr}	Σ_a	Σ_γ
1	2.30070E-01	1.59206E-01	6.01050E-04	6.01050E-04
2	7.76460E-01	4.12970E-01	1.57930E-05	1.57930E-05
3	1.48420E+00	5.90310E-01	3.37160E-04	3.37160E-04
4	1.50520E+00	5.84350E-01	1.94060E-03	1.94060E-03
5	1.55920E+00	7.18000E-01	5.74160E-03	5.74160E-03
6	2.02540E+00	1.25445E+00	1.50010E-02	1.50010E-02
7	3.30570E+00	2.65038E+00	3.72390E-02	3.72390E-02

Table 14: Moderator scattering cross-sections

Group	→ 1	→ 2	→ 3	→ 4	→ 5	→ 6	→ 7
1	4.44777E-02	1.13400E-01	7.23470E-04	3.74990E-06	5.31840E-08	0.00000E+00	0.00000E+00
2	0.00000E+00	2.82334E-01	1.29940E-01	6.23400E-04	4.80020E-05	7.44860E-06	1.04550E-06
3	0.00000E+00	0.00000E+00	3.45256E-01	2.24570E-01	1.69990E-02	2.64430E-03	5.03440E-04
4	0.00000E+00	0.00000E+00	0.00000E+00	9.10284E-02	4.15510E-01	6.37320E-02	1.21390E-02
5	0.00000E+00	0.00000E+00	0.00000E+00	7.14370E-05	1.39138E-01	5.11820E-01	6.12290E-02
6	0.00000E+00	0.00000E+00	0.00000E+00	0.00000E+00	2.21570E-03	6.99913E-01	5.37320E-01
7	0.00000E+00	0.00000E+00	0.00000E+00	0.00000E+00	0.00000E+00	1.32440E-01	2.48070E+00

BIBLIOGRAPHY

[1] R. Blomquist, "Source Convergence in Criticality Safety Analyses, Phase II: Guidance for Analysts," Organization for Economic Cooperation and Development/Nuclear Energy Agency (2011).

[2] B. Collins, B. Kochunas, T. Downar, and A. Godfrey, "Assessment of the 2D MOC Solver in MPACT: Michigan Parallel Characteristics Transport Code," *Proc. Int. Conf. Mathematics and Comp. Meth. App. to Nucl. Sci. and Eng.*, Sun Valley, ID, May 5-9, 2013.

[3] T. Evans, A. Stafford, R. Slaybaugh, and K. Clarno, "Denovo: A New Three-Dimensional Parallel Discrete-Ordinates Code in SCALE," *Nucl. Tech.*, **171**, pp. 171 (2010).

[4] J. Cho and H. Joo, "Solution of the C5G7MOX Benchmark Three-dimensional Extension Problems by the DeCART Direct Whole Core Calculation Code," *Prog. Nucl. Energy*, **48**, pp. 456 (2006).

[5] J. Wagner, D. Peplow, and S. Mosher, "FW-CADIS Method for Global and Regional Variance Reduction of Monte Carlo Radiation Transport Calculations," *Nucl. Sci. Eng.*, **176**, pp. 37 (2014).

[6] M. Lee, H. Joo, D. Lee, and K. Smith, "A Feasibility Study of CMFD Acceleration in Monte Carlo Eigenvalue Calculation," *Trans. Kor. Nucl. Soc. Autumn Meeting*, Gyeongju, Korea, October 29-30, 2009.

[7] D. Zhang and F. Rahnema, "An Efficient Hybrid Stochastic/Deterministic Coarse Mesh Neutron Transport Method," *Ann. Nucl. Energy*, **41**, pp. 1 (2012).

[8] T. Sutton, "Wielandt Iteration as Applied to the Nodal Expansion Method," *Nucl. Sci. Eng.*, **98**, pp. 169 (1988).

[9] T. Yamamoto and Y. Miyoshi, "Reliable Method for Fission Source Convergence of Monte Carlo Criticality Calculation with Wielandt's Method," *Nucl. Sci. Tech.*, **41**, pp. 99 (2004).

[10] R. Blomquist and E. Gelbard, "Alternative Implementations of the Monte Carlo Power Method," *Nucl. Sci. Eng.*, **141**, pp. 85 (2002).

[11] D. She, K. Wang, and G. Yu, "Asymptotic Wielandt Method and Superhistory Method for Source Convergence in Monte Carlo Criticality Calculation," *Nucl. Sci. Eng.*, **172**, pp. 127 (2012).

[12] S. Carney, F. Brown, B. Kiedrowski, and W. Martin, "Theory and Applications of the Fission Matrix Method for Continuous-Energy Monte Carlo," *Ann. Nucl. Energy*, **73**, pp. 423 (2014).

[13] L. Pan, R. Wang, and S. Jiang, "Monte Carlo Fission Matrix Acceleration Method with Limited Inner Iteration," *Nucl. Sci. Eng.*, **180**, pp. 199 (2015).

[14] E. Wolters, *Hybrid Monte Carlo-Deterministic Neutron Transport Methods Using Nonlinear Functionals*, PhD thesis, Univ. of Michigan, 2010.

[15] T. Ueki, F. Brown, D. Parsons, and D. Kornreich, "Autocorrelation and Dominance Ratio in Monte Carlo Criticality Calculations," *Nucl. Sci. Eng.*, **145**, pp. 279 (2003).

[16] E. Wolters, E. Larsen, and W. Martin, "Hybrid Monte Carlo-CMFD Methods for Accelerating Fission Source Convergence," *Nucl. Sci. Eng.*, **174**, pp. 286 (2013).

[17] F. Brown, "Fundamentals of Monte Carlo Particle Transport," LA-UR-05-4983, Los Alamos National Laboratory (2005).

[18] "MCNP– A General Monte Carlo N-Particle Transport code, Version 5, Volume I: Overview and Theory," LA-UR-03-1987, X-5 Monte Carlo Team, Los Alamos National Laboratory (Revised 2008).

[19] M. Jessee, W. Wieselquist, T. Evans, and et. al, "POLARIS: A New Two-Dimensional Lattice Physics Analysis Capability for the SCALE Code System," *Proc. PHYSOR*, Kyoto, Japan, September 28-October 3, 2014.

[20] M. Young, F. Brown, B. Kiedrowski, and W. Martin, "Coarse Mesh Finite Difference in MCNP5," LA-UR-11-04384, Los Alamos National Laboratory (2011).

[21] M. Lee, H. Joo, D. Lee, , and K. Smith, "Monte Carlo Reactor Calculation with Substantially Reduced Number of Cycles," *Proc. PHYSOR 2012*, Knoxville, Tennessee, April 15-20, 2012.

[22] J. Hoogenboom and W. R. Martin, "A Proposal for a Benchmark to Monitor the Performance of Detailed Monte Carlo Calculation of Power Densities in a Full Size Reactor Core," *Proc. Int. Conf. Mathematics, Comp. Meth., and Reactor Phys.*, Saratoga Springs, New York, May 3-7, 2009.

[23] M. Lee, H. Joo, D. Lee, and K. Smith, "Coarse Mesh Finite Difference Formulation for Accelerated Monte Carlo Eigenvalue Calculation," *Ann. Nucl. Energy*, **65**, pp. 101 (2014).

[24] K. Keady and E. Larsen, "Stability of Monte Carlo *k*-Eigenvalue Simulations with CMFD Feedback," *J. Comp. Phys.* (Submitted Nov 2014).

[25] E. Larsen and B. Kelley, "The Relationship Between the Coarse-Mesh Finite Difference and the Coarse-Mesh Diffusion Synthetic Acceleration Methods," *Nucl. Sci. Eng.*, **178**, pp. 1 (2014).

[26] A. Nelson and W. Martin, "Improved Convergence of Monte Carlo Generates Multigroup Scattering Moments," *Proc. Int. Conf. Mathematics and Comp. Meth. App. to Nucl. Sci. and Eng.*, Sun Valley, ID, May 5-9, 2013.

[27] "Benchmark on Deterministic Transport Calculations without Spatial Homogenisation," ISBN 92-64-02139-6, Organization for Economic Cooperation and Development/Nuclear Energy Agency (2003).